

NORTHWESTERN UNIVERSITY

Shape Memory Alloy Based Micro-Meso Scale Manipulator

A DISSERTATION

SUBMITTED TO THE GRADUATE SCHOOL IN PARTIAL FULFILLMENT
OF THE REQUIREMENT

for the degree

DOCTOR OF PHILOSOPHY

Field of Mechanical Engineering

By

Kostyantyn Malukhin

EVANSTON, ILLINOIS

June 2008

UMI Number: 3307000

Copyright 2008 by
Malukhin, Kostyantyn

All rights reserved.

UMI[®]

UMI Microform 3307000

Copyright 2008 by ProQuest Information and Learning Company.
All rights reserved. This microform edition is protected against
unauthorized copying under Title 17, United States Code.

ProQuest Information and Learning Company
300 North Zeeb Road
P.O. Box 1346
Ann Arbor, MI 48106-1346

© Copyright by Kostyantyn Malukhin and Kornel F. Ehmann

All Rights Reserved

ABSTRACT

Shape Memory Alloy Based Micro-Meso Scale Manipulator

Kostyantyn Malukhin

The need for low-cost robust meso-scale “smart” robots (manipulators) that have no discrete parts (monolithic), no sensors (“self-sensing”) and can be used in space-constrained systems, e.g., in microfactories, biomedical applications, etc., was the motivation for the current research. This study describes the design, fabrication and analysis of such a smart robot – a monolithic Micro/Meso Scale Manipulator (mMM), fabricated from Shape Memory Alloy powders (NiTi) by means of the laser-based Direct Metal Deposition (DMD) process.

A first prototype, a functional part of the mMM – a SMA accordion spring type actuator was manufactured by DMD. The actuator provides a linear movement for the mMM due to the Shape Memory Effect (SME) property of SMAs. The One-Way SME was imposed on the spring actuator by a series of thermomechanical treatments. The SME drives the spring’s movements due to the property of the SMAs to change their crystallographic structure and, therefore, shape, during heating or cooling. The characterization of the DMD manufactured material was done.

SMAs change their crystallographic structure and/or shape (SME) when the phase transformation takes place in the material during its temperature and/or stress state change. A new mathematical model describing the phase transformation kinetics and a new analytical phase transformation function was developed.

The phase transformation in SMAs causes electrical resistance change in the material. The motion, caused by the SME, can be controlled using the electrical resistance change as a feedback signal with no need for separate motion sensors. In the current work this “self-sensing” concept was explored and evaluated in an SMA wire based actuator and applied to the SMA spring based actuator. The dynamics of the sub-millimeter and millimeter scale motion of the SMA actuators was identified using physical models of the SMA wire based actuators.

A new mathematical model of the motion of the SMA wire- and spring-based actuators was developed. This model can serve as a basis for SMA actuator control.. A prototype of the SMA spring actuator was manufactured from a commercially available SMA (NiTi) ingot to experimentally verify the models of motion.

ACKNOWLEDGEMENTS

I would like to acknowledge:

My scientific advisor, Professor Kornel F. Ehmann (Department of Mechanical Engineering, Northwestern University) for the significant academic and professional support (including the practice in research conferences, publications), for invaluable guidance through all the areas of this research study, especially in the measurements and automation area of all my experiments and for providing the equipment for conducting the experimental and numerical simulations in the frame of this research project.

My scientific committee member Professor Catherine L. Brinson (Department of Mechanical Engineering, Northwestern University) and her Ph.D. graduate Dr. Gao for help in understanding the fundamentals of the properties of Shape Memory Alloys (NiTi), their mathematical and Finite Element Modeling (FEM) modeling, included and presented in my Ph.D. candidacy qualifier report.

Professor Radovan Kovacevic and his colleagues Ph.D. Srdja Zekovic, engineer Michael Valant, Ph.D. Radjeev Dwivedy (Southern Methodist University/RCAM lab) for help with the Direct Metal Deposition (DMD) experiments, lending the necessary DMD equipment, teaching me the DMD basics and their expertise in the development of procedures for the DMD of NiTi powder.

My scientific committee member Professor Chi-Haur Wu (Department of Electrical Engineering, Northwestern University) for having such good publications on the “human

muscle” motion control model, that became a prototype for the motion control model of the SMA actuator.

Professor Ted Belytchko (Department of Mechanical Engineering, Northwestern University) and his former post-doctoral fellow Dr. Timon Rabzuk for help in the FEM of solid structures with SMA properties (included and presented in my Ph.D. candidacy qualifier report).

Professor Rod Ruoff and his Ph.D. graduate Geoffrey Dammett (Department of Mechanical Engineering, Northwestern University) for lending some of the equipment for my experiments, namely, hot plates.

Professor Ketterson (Department of Physics, Northwestern University, Evanston, IL) and his graduate student Weiqiang Mu (Department of Physics, Northwestern University, Evanston, IL) for help in developing the Selective Laser Annealing (SLA) procedure of NiTi alloys and lending the necessary equipment for it.

Professor Pfefferkorn (Department of Mechanical Engineering, University of Wisconsin-Madison) and his graduate student Yongho Jeon (Department of Mechanical Engineering, University of Wisconsin-Madison) for help in advancing the SLA processing of NiTi alloys and providing the necessary equipment for it.

Professor Jian Cao (Department of Mechanical Engineering, Northwestern University) for her comments on the FEM, included and presented in my Ph.D. candidacy qualifier report.

Professor Qian (Jane) Wang and her graduate student Aaron Greco (Department of Mechanical Engineering, Northwestern University) for help and training in optical profilometry.

The National Science Foundation (USA), for the financial support of this project under the grant #DMI-0400316.

Dr. James Hulvat (Department of Material Sciences, Northwestern University) for help in learning the Differential Scanning Calorimetry (DSC) method, training in the DSC equipment and performing some of the initial DSC measurements.

Senior lecturer Cathleen Stair (Department of Material Sciences, Northwestern University) for help and training in material preparation for analysis of its properties by means of optical microscopy imaging and for giving invaluable comments on some of the aspects of material science.

Network administrator Richard Marzek (Department of Mechanical Engineering, Northwestern University) for help and comments in electric circuits and some of the pieces of hardware.

Manager Rick Kraemer (Department of Material Sciences Department, Northwestern University) for giving advices and training in usage of ovens.

Tool-maker Robert Taglia (Department of Mechanical Engineering, Northwestern University) for help and training in machining.

I also gratefully acknowledge the permission to use equipment in the following laboratories: Scanning Electron Microscopes (SEM) in EPIC facility (Department of Material Sciences Department, Northwestern University), Secondary Ion Mass Spectroscopy (SIMS) equipment in Keck-11 facility (Department of Material Sciences, Northwestern University), DSC equipment in the laboratory of Professor Torkelson (Department of Material Sciences, Northwestern University), ovens in the laboratory of Professor Gregory Olson (Department of Material Sciences, Northwestern University), polishing laboratory (Department of Material Sciences, Northwestern University), optical profilometer in the laboratory of Professor Qian (Jane) Wang (Department of Mechanical Engineering, Northwestern University).

I would also like to thank various companies (Special Metals Corporation, NDC, Dynalloy, Vector Tool (thanks to Frank Mezzano), UNILOCK and others) for being collaborative and open.

Administrative assistants and secretaries in the Department of Mechanical Engineering, Northwestern University (Pat Dyess, Sinta Kulanda, Arlene Preus, Mariella Huber and others) deserve particular gratitude for the timely administration of the purchases for this research project and other paper work.

Special thanks to the administration of Northwestern University (The International Office, The Graduate School, The Office of the Dean of the McCormick School, The Office of the Registrar and others) for all kinds of support in making the administration of my research and academic activity to flow in a timely and minimal effort consuming manner.

Finally, but not the least, I lovingly acknowledge my parents and my friends for all their support that helped me to keep up the research enthusiasm, motivation and cheer.

And, many thanks to other people and organizations that made their contribution.

TABLE OF CONTENT

<i>ABSTRACT</i>	3
<i>ACKNOWLEDGEMENTS</i>	5
<i>TABLE OF CONTENT</i>	9
<i>LIST OF FIGURES</i>	16
<i>LIST OF TABLES</i>	28
1. Introduction	30
1.1 Background and motivation for shape memory alloy (SMA) based monolithic micro/meso-scale manipulator (mMM) development	30
1.2 Application of SMA mMMs, expected results and their significance	32
1.3 Conceptual embodiment of a plausible mMM	33
1.4 Outline of the dissertation	41
2. “State-of-the-art” review	44
2.1 SMA-based actuation	44
2.1.1 SMA properties	44
2.1.2 SMA actuators	48
2.2 Laser-based rapid prototyping processes	56
2.2.1 Equipment and process characteristics	58
2.2.2 Advantages of laser-based rapid prototyping processes	71

2.2.3 Drawbacks of laser-based rapid prototyping processes	10
2.2.3 Drawbacks of laser-based rapid prototyping processes	75
2.3 Direct metal deposition (DMD) of SMA (NiTi) powders	76
3. <i>Manufacture of SMA material</i>	81
3.1 DMD experimental apparatus	81
3.2 DMD fabrication of SMA bulk structures.....	83
3.3 DMD fabrication of SMA thin wall-structures	85
3.3.1 Heat transfer.....	86
3.3.2 Factorial design of experiments	93
3.3.3 Analysis of the influence of the DMD parameters	107
3.4 Concluding remarks	112
4. <i>Properties of SMA materials fabricated by DMD from SMA powder</i>	114
4.1 Sample preparation and microscopy	114
4.2 Thermo-mechanical treatment and differential scanning calorimetry (DSC).....	116
4.2.1 Effect of thermal treatment on TTRs with the use of quenching.....	121
4.2.2 Effect of thermal treatment on TTRs without the use of quenching.....	123
4.3 Energy dispersive spectrum (EDS) analysis.....	124
4.4 X-ray diffraction (XRD) analysis	125
4.5 Secondary ion mass spectroscopy (SIMS) analysis.....	126
4.6 Concluding remarks	130
5. <i>Fabrication of the SMA spring actuators - functional parts of mMM</i>	132

5.1 Fabrication of the SMA actuators by DMD using the DMD process parameters for building bulk structures	133
5.1.1 Fabrication of an accordion spring type actuator by DMD without further post-machining.....	134
5.1.2 Fabrication of an accordion spring type actuator by DMD with further post-machining using wire electro-discharge machining (EDM).....	139
5.1.3 One-way (OW) shape memory effect (SME) “training” of the accordion spring	144
5.2 Fabrication of SMA actuators by DMD using the DMD process parameters for building thin-wall structures.....	147
5.3 Concluding remarks	152
6. “Self-sensing” property of SMA actuators - resolution, sensitivity and dynamics	154
6.1 Control of “self-sensing” actuators	155
6.1.1 The “self-sensing” principle	156
6.1.2 mMM actuation.....	157
6.1.3 Working ranges of the sensor	162
6.2 Experimental setup and experimental procedure.....	163
6.2.1 Experimental set-up	164
6.2.2 Experimental procedure	169
6.3 Experiments with small displacement range sensing	171
6.3.1 Step response of the thermally non-insulated SMA wire actuator	171
6.3.2 Step response of the thermally insulated SMA wire actuator.....	173
6.3.3 Correlation analysis	175

6.3.4 Sensitivity analysis.....	12
6.3.4 Sensitivity analysis.....	181
6.3.5 Identification of the dynamics of motion of the SMA wire.....	185
6.3.6 Analysis of the feasibility of the “self-sensing” principle for small displacements ..	196
6.4 Experiments with large scale displacement sensing	197
6.5 Conclusions.....	199
7. <i>A new mathematical model of the kinetics of the austenite phase transformation in NiTi SMAs and its experimental verification</i>	201
7.1 Overview of existing phenomenological models of phase transformation kinetics in SMAs	203
7.2 Problem statement	205
7.3 Constitutive energy conservation equations for SMAs	206
7.4 Austenite phase transformation function	211
7.4.1 Stress independent formulation of the austenite phase transformation function	211
7.4.2 Stress dependent formulation of the austenite phase transformation function	215
7.4.3 Comparison of the suggested transformation function to a conventional existing transformation function.....	217
7.5 Experimental verification of the mathematical model of the stress-independent austenite phase transformation.	219
7.6 Concluding remarks	224
8. <i>Mathematical model of the motion of SMA actuators based on the new model of the kinetics of the phase transformation in SMAs.....</i>	225

	13
8.1 Description of the model of motion of a “muscle” after Wu et al., 1990.....	226
8.2 Formulation of the model of motion of the SMA actuator.....	230
8.3 Simulation model for the motion of the SMA wire actuator using “Simulink”	237
8.4 Verification of the suggested mathematical model of motion of the SMA wire actuator	241
8.4.1 Definition of model parameters	241
8.4.2 Determination of B_{SMA}	242
8.4.3 Comparative analysis of experimental and simulation results.....	250
8.5 Concluding remarks	255
9. <i>Experimental prototype of a linear stage of the mMM - SMA spring actuator.....</i>	256
9.1 Design of the linear stage.....	257
9.2 Characterization of the material of the linear stage	260
9.3 Development of the selective laser annealing (SLA) technique	264
9.4 Experimental investigation of the response of the 1DOF stage	272
9.4.1. Experimental setup.....	272
9.4.2 Experimental procedure	275
9.4.3 Experimental results.....	276
9.4.4 Analysis of the experiments.....	279
9.5 Mathematical model of the 1DOF stage.....	283
9.5.1 Formulation of the mathematical model of motion	283
9.5.2 Verification of the model	292

9.6 Concluding remarks	14 297
10. A gripper for mMMs with a short range gripping motion range.....	298
10.1 Conceptual design of the gripper.....	298
10.2 Fabrication of the gripper	302
10.3 Development of the TWSME training procedure for the SMA ring	305
10.3.1 Step #1 of the TWSME training	305
10.3.2 Step #2 of the TWSME training	307
10.3.2.1 FEM (UNIGRAPHICS) modeling of the NiTi ring	308
10.3.2.2 Experimental verification of step #2.....	310
10.4 Experimental testing of the gripper	312
10.5 Concluding remarks	315
11. Conclusions and future work	316
11.1 Conclusions.....	316
11.2 Future work.....	320
REFERENCES	325
APPENDIX A.....	336
APPENDIX B.....	357
APPENDIX C.....	363
APPENDIX D	368
APPENDIX E.....	370

APPENDIX F..... 372

LIST OF FIGURES

<i>Figure 1.1: Conceptual design of a monolithic X-Y-Z motion actuator with a microgripper.....</i>	<i>34</i>
<i>Figure 1.2: mMM X-Y motion actuator: (a) design, (b) wax prototype</i>	<i>38</i>
<i>Figure 1.3: FEM modeling of mMM (UNIGRAPHICS): (a) true scale, (b) relative scale.</i>	<i>39</i>
<i>Figure 2.1: Schematic of diffusionless martensite phase transformation (Weiming, 1998).....</i>	<i>45</i>
<i>Figure 2.2: SMA properties: (a) superelasticity; (b) shape memory effect (www.nitinol.com);(c) “superelastic” stress-strain curve; (d) SME stress-strain curve.....</i>	<i>47</i>
<i>Figure 2.3: SMA-based linear stage: (a) design; (b) actuation principle (Bellouard et al., 2001).</i>	<i>51</i>
<i>Figure 2.4: Monolithic microholder (a), microgripper (b) made of SMA (Ni-Ti-Nb) (Bellouard et al., 2001), and SMA microgripper (c) for scaffold assembly (Zhang et al., 2002).....</i>	<i>51</i>
<i>Figure 2.5: Feedback control system of an SMA actuator: a) control system of the bulk thin film actuator; b) experimental feedback results (Kuribayashi, 2000).</i>	<i>54</i>
<i>Figure 2.6: Directed light fabrication: (a) apparatus; (b) manufactured part (Mah, 1997; Milewski et al., 1998).....</i>	<i>59</i>
<i>Figure 2.7: Selective laser sintering (SLS) experimental setup. (www.arptech.com.au/slshelp.htm)</i>	<i>60</i>
<i>Figure 2.8: Microcladding examples: (a) one component (Ni); (b) two component microcladding (Cu/Sn) (Kathuria, 1999).....</i>	<i>60</i>
<i>Figure 2.9: Tooling made by SLS from 420 stainless steel powder infiltrated with 89/11 bronze: (a) heat exchanger; (b) rivet mandrels (Odonnchadha, Tansey, 2004).</i>	<i>61</i>

<i>Figure 2.10: SLS examples: (a) UNIGRAPHICS based STL file for the 1.75 mm x/y/z porous scaffold; (b) 1.75 mm x/y/z PCL scaffold made by SLS (Williams et al., 2005).</i>	61
<i>Figure 2.11: LDC laser head with a four-port nozzle system and a gas nozzle coaxial with the laser beam (Fearon et al., 2004).</i>	63
<i>Figure 2.12: Schematics of the direct metal deposition (DMD) process (www.trumpf.com/3.laserforming_proc_main.html).</i>	63
<i>Figure 2.13: DMD: (a) experimental setup, (b) forging tool repaired by DMD (www.twi.co.uk/j32k/getFile/dmd_index.html).</i>	64
<i>Figure 2.14: SMU/RCAM rapid prototyping equipment: (a) 3-DOF DMD and RP experimental setup; (b) 6-DOF LBAM experimental setup (Kovacevic, 2005).</i>	65
<i>Figure 2.15: DMD RP examples: (a) helical spring manufactured from tool steel powder, (b) vertical wall (Kovacevic, 2005).</i>	66
<i>Figure 2.16: LENS manufactured components:(a) turbine (www.optomec.com/html/aerospace-ro.htm); (b) blade processing (www.ca.sandia.gov/.../content.php?cid=50); (c) housing (www.ca.sandia.gov/.../content.php?cid=50).</i>	67
<i>Figure 2.17: Laser cladding process: (a) schematic (Hu et al., 1998); (b) example of a laser cladding process using a 10-axis laser (http://www.lasercladding.com/).</i>	68
<i>Figure 2.18: An example of a LasForm process (www.azom.com).</i>	69
<i>Figure 2.19: Examples of LasForm manufactured parts (www.azom.com).</i>	70
<i>Figure 2.20: Laser drilling (www.esi.com)(Nd:YAG feedback controlled system).</i>	73
<i>Figure 2.21: Comparison of microstructures of nickel-aluminum-bronze samples, made by: (a) conventional casting and (b) laser-based rapid prototyping (Wessel, 2004).</i>	75

<i>Figure 2.22: Defects in materials processed by laser-based rapid prototyping methods: (a) “Christmas tree” defect in a part with internal cavities made by DMD from tool steel powder (Kovacevic, 2005), (b) warping in a part made by DMD from Shape Memory Alloy (SMA) powder (one of our samples), (c) delamination and cracking defect in a part made by DMD from tool steel powder, part height is 50 mm, number of the deposited layers is 50 (Cooper, 1999).</i>	76
<i>Figure 3.1: DMD: (a) experimental setup (courtesy of Dr. R. Kovacevic at SMU/RCAM), (b).</i>	82
<i>Figure 3.2: NiTi samples, fabricated by DMD: (a) on Ti substrate, (b) on NiTi substrate.</i>	84
<i>Figure 3.3: Vertical thin wall: (a) DMD schematics (b) heat transfer schematics.</i>	87
<i>Figure 3.4: Dependence of the δ_m magnitude on: (a) coolant temperature, (b) heat exchanger wall thickness and (c) heat transfer coefficient between melt and solidified melt.</i>	91
<i>Figure 3.5: Vertical walls fabricated by DMD from NiTi powder on NiTi substrate: (a) batch #1, (b) batch #2, (c) side view of (a), (d) side view of (b).</i>	96
<i>Figure 3.6: Optical microscope micrographs of one of the 16 DMD NiTi walls: (a) left view, (b) top view, right- and left-hand side, (c) front view.</i>	98
<i>Figure 3.7: Wall halves: (a) digital camera image of the 32 wall halves on their substrates after wire-EDM, (b) optical micrograph of the wire-EDMed cross-section of one half of the non-polished wall #1 from batch #1 on its substrate</i>	100
<i>Figure 3.8: SEM micrograph of a non-polished, wire-EDMed wall’s half: (a) wall’s top edge area after wire-EDM, (b) zoom of (a), (c) wall body on its NiTi substrate.</i>	101
<i>Figure 3.9: Polished, wire-EDMed wall half: (a) optical micrograph, (b) SEM micrograph at magnification = 450, (c) SEM micrograph at magnification = 100.</i>	102
<i>Figure 3.10: Surface roughness of a wall measured by the optical profilometer: (a) 2-D view, (b) 3-D view.</i>	106

Figure 3.11: Distribution of the magnitudes of heights and widths the thin walls: (a) batch #1, (b) batch#2..... 110

Figure 3.12: Distribution of the magnitudes of the vertical diameters (axis) of the spherical build-ups located at the right-hand side corners of the thin walls. 111

Figure 3.13: Distribution of wall roughness values from measurements by the mechanical stylus method..... 111

Figure 4.1: As-annealed NITINOL sample: (a) turned cross-section; (b) optical microscope image of the ground and polished sample part of cylinder (a); (c) SEM micrograph of (b), Sample #1; (d) zoomed SEM micrograph of (c), Sample #1..... 115

Figure 4.2: DSC thermograms obtained under different heat treatment conditions (annealing temperatures) –

(a) as-is raw (pre-alloyed) NITINOL powder used for fabricating the samples;

(b) Sample#1: T=820 °C, time= 1hour, room temperature (t.) water quenched;

(c) Sample#2: T=500 °C, time – 1hour, room t. water quenched;

(d) Sample#2: T=450 °C, time – 1hour 30 min., room t. water quenched;

(e) Sample#2: T=424 °C, time – 1hour 30 min., room t. water quenched;

(f) Sample#2: T=408 °C, time – 1hour 30 min., room t. water quenched;

(g) Sample#2: T=396 °C, time – 1hour 30 min., room t. water quenched;

(h) Sample#2: T=358 °C, time – 1hour 30 min., room t. water quenched;

(i) Sample#2: T=331 °C, time – 1hour 30 min., room t. water quenched;

(j) Sample#2: T=309 °C, time – 1hour 30 min., room t. water quenched;

(k) Sample#2: T=282 °C, time – 1hour 30 min., room t. water quenched;

(l) Sample#2: $T=282$ °C, time – 1hour 30 min., no quenching;	
(m) Sample#2: $T=424$ °C, time – 1hour 30 min., no quenching.....	120
Figure 4.3: Cumulative annealing curves: TTRs versus annealing temperatures (T_m , T_a and T_r are the martensite, reverse martensite (austenite) and R- phase transformation temperatures).	
.....	122
Figure 4.4: EDS spectrum of the manufactured NiTi sample.....	125
Figure 4.5: XRD raw data of the cylinder annealed at 850 °C.	126
Figure 4.6: SIMS depth profiles: (a) commercially available (standard) NITINOL sample; (b) NiTi sample fabricated by means of DMD.	128
Figure 5.1: Accordion spring (UNIGRAPHICS): (a) 3-D model, (b) 2-D drawing.....	133
Figure 5.2: Digital camera images of the accordion springs, fabricated by DMD from NiTi powder on NiTi substrate with: (a) Ar flow rate 4.4...17.5 l/min and laser power 230...300 W, (b) Ar flow rate 17.5 l/min and laser power 300...350 W	135
Figure 5.3: Detailed view of accordion spring (1) (DMD parameters: Ar flow rate 4.4 l/min, and laser power 230...250 W): (a) digital camera image, (b) optical microscope image – enlarged view of a corner of the spring from (a).	136
Figure 5.4: Detailed view of accordion spring (2) (DMD parameters: Ar flow rate 17.5 l/min, and laser power 300 W): (a) digital camera image, (b) optical microscope image – enlarged view of a corner of the spring from (a).	137
Figure 5.5: Detailed view of accordion spring (3) (DMD parameters: Ar flow rate 17.5 l/min, and laser power 350 W...400 W): (a) digital camera image, (b) optical microscope image – enlarged view of a corner of the spring from (a).	137

<i>Figure 5.6: Accordion spring (4) fabricated by DMD from tool steel Crucible CPM 3V powder: (a) digital camera image; (b) optical microscope image – enlarged view of (a).....</i>	<i>138</i>
<i>Figure 5.7: Digital camera image of the block part fabricated by DMD from NITINOL powder on NiTi substrate (Ar flow rate = 17.5 l/min, laser power = 350...400 W).</i>	<i>140</i>
<i>Figure 5.8: Digital camera image of the NITINOL accordion spring.</i>	<i>141</i>
<i>Figure 5.9: Spring: (a) digital camera image of a side view of the spring, (b) optical microscope micrograph of a zoomed region of the spring (Fig. 5.8).</i>	<i>142</i>
<i>Figure 5.10: Optical microscope micrographs of: (a) SMA spring EDM cut into two halves: (b) porous and (c) non-porous.....</i>	<i>143</i>
<i>Figure 5.11: SME “trained” accordion spring: (a) optical microscope micrograph of the spring after “ training”; (b) optical microscope micrograph of the pre-stretched spring (c) DSC thermogram of the spring material.</i>	<i>146</i>
<i>Figure 5.12: Digital camera image of NiTi accordion springs deposited on NiTi substrate, using DMD process parameters for building thin wall structures.....</i>	<i>148</i>
<i>Figure 5.13: Optical microscope micrographs of the as-is NiTi accordion spring (4), not detached from its substrate: (a) side view, (b) top view.</i>	<i>149</i>
<i>Figure 5.14: Optical microscope micrographs of the NiTi accordion spring (4), detached from its substrate and polished: (a) top view, (b) side view.....</i>	<i>150</i>
<i>Figure 5.15: DSC thermogram of an SME trained thin wall actuator.....</i>	<i>151</i>
<i>Figure 6.1: Schematic of SMA-based sensing</i>	<i>155</i>
<i>Figure 6.2: Principle of the integral sensing (“self-sensing”) system.</i>	<i>157</i>
<i>Figure 6.3: mMM linear stage: (a) electrical layout; (b) electrical circuit diagram.....</i>	<i>159</i>
<i>Figure 6.4: DSC thermogram of the SMA wire.</i>	<i>163</i>

<i>Figure 6.5: The SMA wire based linear stage.</i>	165
<i>Figure 6.6: Electrical schematic</i>	166
<i>Figure 6.7: Calibration curves: (a) #1 (for small displacement) and (b) #2 (for large displacements)</i>	168
<i>Figure 6.8: Controlled recovery schematics.</i>	169
<i>Figure 6.9: Controlled strain recovery of the non-prestrained SMA wire: (a) SMA wire displacement, D, (b) amplified reference voltage, V_A, (c) SMA wire temperature, T</i>	172
<i>Figure 6.10: Controlled strain recovery of the initially pre-strained (2.77% strain) thermally insulated SMA wire: (a) SMA wire displacement, D, (b) amplified reference voltage, V_A, (c) SMA wire temperature, T, (d) zoom of (a), (e) zoom of (b), zoom of (c).</i>	174
<i>Figure 6.11: Statistical analysis: (a) correlation coefficients between: temperature and displacement, R_{TD}, temperature and voltage, R_{TV}, voltage and displacement, R_{VD}; (b) homoscedasticity test.</i>	178
<i>Figure 6.12: Cumulative correlation coefficients data: (a) as a function of pre-strain, (b) as a function of temperature</i>	181
<i>Figure 6.13: Displacement, D, vs. amplified voltage, V_A (from Fig.6.8): (a) step response at 330...399 sec, with the maximal displacement step (displacement range) 131 μm, (b) step response at 413...553 sec, with the maximal displacement step (displacement range) 200 μm</i>	183
<i>Figure 6.14: Characteristics of the “self-sensing” method: (a) sensitivity and (b) resolution versus displacement ranges.</i>	184
<i>Figure 6.15: Input and output data for the SMA wire step response with no thermal insulation: (a) output - displacement, (b) input - voltage.</i>	186

<i>Figure 6.16: Input and output data for the SMA wire step response with thermal insulation:</i>	
<i>(a) output - displacement, (b) input - voltage.</i>	<i>187</i>
<i>Figure 6.17: Frequency response data for the SMA wire step response with no thermal insulation: (a) amplitude, (b) phase.....</i>	<i>189</i>
<i>Figure 6.18: Frequency response data for the SMA wire step response with thermal insulation: (a) amplitude, (b) phase.....</i>	<i>190</i>
<i>Figure 6.19: Measured and simulated output of the thermally non-insulated SMA wire: (a) Exp. 27, (b) Exp. 32.....</i>	<i>190</i>
<i>Figure 6.20: Measured and simulated output of the thermally insulated SMA wire: (a) Exp. 45, (b) Exp. 41.....</i>	<i>191</i>
<i>Figure 6.21: Magnitudes versus average temperatures: (a) frequency response of the thermally non- insulated SMA wire and (b) frequency response of the thermally insulated SMA wire.</i>	<i>193</i>
<i>Figure 6.22: SMA wire heat balance diagram.</i>	<i>195</i>
<i>Figure 6.23: Step response from a large displacement experiment</i>	<i>198</i>
<i>Figure 7.1: Nodalized representation of an SMA wire.....</i>	<i>206</i>
<i>Figure 7.2: 3-D control volume.</i>	<i>206</i>
<i>Figure 7.3: Discrete representation of continua by (a) 0-D control volume and (b) its equivalent thermal node.</i>	<i>207</i>
<i>Figure 7.4: Austenite fraction evolution vs. temperature in NITINOL alloy for stress-independent conditions.....</i>	<i>214</i>
<i>Figure 7.5: Austenite fraction evolution vs. temperature in NITINOL alloy for stress-dependent conditions.....</i>	<i>217</i>

<i>Figure 7.6: Austenite fraction evolution vs. temperature in NITINOL alloy for stress-dependent conditions: (a) from equation 7.16, (b) from equation 7.18.....</i>	218
<i>Figure 7.7: FLEXINOL wire, attached to the air-bearing linear stage.</i>	221
<i>Figure 7.8: Experimental data from SMA wire heating cycle: (a) SMA wire displacement, (b) SMA wire temperature.</i>	222
<i>Figure 7.9: Austenite phase fraction vs. temperature in NiTi alloy under zero-stress conditions: (1) from the suggested equation (7.11), (2) from equation (7.18), (3) from experimental data in the plot in Figure 7.8 and Appendix F.</i>	223
<i>Figure 8.1: “Muscle” motion model (Wu et al., 1990).</i>	227
<i>Figure 8.2: Equivalent schematic of the experimental setup of the “load-muscle-wrist” system (Wu et al., 1990).</i>	228
<i>Figure 8.3: Simulation block for studying step disturbances to the “load-muscle-wrist” (Wu et al., 1990).</i>	228
<i>Figure 8.4: Displacement-time plot from the output of the step response simulations obtained from the “load-muscle-wrist” simulation model (Wu et al., 1990).</i>	230
<i>Figure 8.5: Experimental results from thermally insulated SMA wire step responses: (a) initial pre-strain = 5.55%, initial voltage $\approx 3V$, initial electric current $\approx 0.5 A$, (b) (initial pre-strain = 1.38%, initial voltage $\approx 2.9 V$, initial electric current $\approx 0.4 A$).....</i>	231
<i>Figure 8.6: Equivalent schematics of the mathematical model of the SMA wire actuator: (a) simplified schematics of the SMA wire actuator, (b) adapted schematics (c) final equivalent mathematical model of the SMA actuator.....</i>	233
<i>Figure 8.7: Block diagram (a), simulation block (b) for studying the step response of the SMA wire-based actuator, (c) nomenclature.....</i>	240

<i>Figure 8.8: Comparison of the experimental data and simulations: (a) temperature T_{SMA} of the SMA wire, (b) displacement of the SMA wire.</i>	252
<i>Figure 8.9: Comparison of experimental data and the corresponding simulations: (a) temperature T_{SMA} of the SMA wire, (b) displacement of the SMA wire.</i>	254
<i>Figure 9.1: UNIGRAPHICS drawing of the mMM linear stage: (a) 3-D view, (b) 2-D view.</i>	258
<i>Figure 9.2: 1-DOF mMM linear stage: (a) electrical schematic; (b) electrical circuit diagram.</i>	259
<i>Figure 9.3: DSC measurements of the “as-is” raw NiTi ingot.</i>	262
<i>Figure 9.4: DSC of the thermally treated NiTi ingot.</i>	263
<i>Figure 9.5: Experimental setup for selective laser annealing #1.</i>	265
<i>Figure 9.6: DSC thermograms: before and after selective laser annealing (SLA #1) of DMD fabricated material.</i>	266
<i>Figure 9.7: DSC thermograms: comparison of a laser annealed and oven annealed NiTi samples (DMD fabricated material).</i>	267
<i>Figure 9.8: Experimental layout of the method for selective laser annealing #2: (a) with NiTi sample, (b) with NiTi linear stage.</i>	269
<i>Figure 9.9: DSC thermograms of the NiTi samples after SLA #2: (a) DMD fabricated material, (b) commercially available material.</i>	271
<i>Figure 9.10: Linear stage: (a) UNIGRAPHICS NX3 drawing of the assembly of the 1-DOF linear stage, (b) digital camera photo of the experimental setup with the measurement system, (c) voltage divider circuit.</i>	275

Figure 9.11: Step response of the linear stage with the heat-treated spring (large pre-strain $\approx 3\text{mm}$, electrical current $\approx 10\text{ A}$, voltage $\approx 30\text{V}$): (a) temperature input, (c) voltage drop across the spring, (c) displacement output.....	277
Figure 9.12: Step response of the linear stage with the heat-treated spring (small pre-strain $\approx 0.25\text{ mm}$, electrical current $\approx 10\text{ A}$, voltage $\approx 30\text{ V}$): (a) temperature input, (c) voltage drop across the spring, (c) displacement output.....	278
Figure 9.13: Cumulative data of the heat loads versus corresponding displacement of the SLA heat-treated spring (curve 1 from Eq. 9.1 and curve 2 from Eq. 9.2)	282
Figure 9.14: Dependence between the heat load values $Q_{\Delta V}$ and $Q_{\Delta T}$	282
Figure 9.15: Voltage drop across the spring vs. the displacement of the spring	287
Figure 9.16: The model of motion of the spring actuator	289
Figure 9.17: The simulation block of the model of motion of the linear stage with the.....	291
Figure 9.18: Result of the numerical simulations of the open loop response of the model of motion of the spring actuator: (a) temperature of the SMA spring, T_{SMA} ; (b) fraction of austenite, ξ_A ; (c) recovery force, F_Q ; (d) voltage drop across the spring, U ; (e) reference and computed displacements, D_r and D_c	295
Figure 10.1: Conceptual design of gripper #1 (UNIGRAPHICS).....	299
Figure 10.2: Conceptual design of gripper #2 (UNIGRAPHICS): (a) assembly, (b) NiTi ring.	301
Figure 10.3: Schematic of the assembly of the NiTi ring and the steel spindle: (a) “hot” state, (b) “cold” state.....	302
Figure 10.4: Drawing of gripper #2 (UNIGRAPHICS): (a) stainless steel gripping element, (b) NiTi ring.....	304
Figure 10.5: Prototypes of the gripping element and NiTi rings – parts of the gripper.	305

	27
<i>Figure 10.6: TWSME “training” of a NiTi ring – Step #1</i>	306
<i>Figure 10.7: TWSME training of the NiTi ring – Step #2</i>	307
<i>Figure 10.8: Finite element modeling of the SMA ring (UNIGRAPHICS): (a) model, (b) results – view 1, (b) results - view 2.</i>	310
<i>Figure 10.9: Optical microscope images of the NiTi ring: (a) after the TWSME “training”, (b) heated, (c) cooled.</i>	312
<i>Figure 10.10: Optical microscope image of the SMA gripper - assembly of the NiTi ring and steel gripping element</i>	313
Figure 10.11: Tool (micro-mill)	314
<i>Figure 10.12: Clamping force due to the TWSME</i>	315

LIST OF TABLES

<i>Table 1.1: Target characteristics of the mMM</i>	35
<i>Table 2.1: Laser-based fabrication processes</i>	58
Table 2.2: Differences between the laser-based rapid prototyping processes	71
Table 2.3: Mechanical properties of Ti-6Al-4V alloy: comparison between some non-laser-conventional and laser-based rapid prototyping processes (Kobryn et al., 2000)	74
Table 3.1: Experimental parameters for DMD fabrication of SMA bulk structures	85
<i>Table 3.2: DMD heat transfer parameters</i>	89
<i>Table 3.3: Factorial design experimental parameters</i>	94
Table 3.4: Wall roughness measured by the mechanical stylus profilometer	103
Table 3.5: Wall surface roughness (half 1) measured by the optical profilometer	104
Table 3.6: Wall roughness (half 2) measured by the optical profilometer	104
Table 3.7: Influence of laser power, powder flow rate and coolant flow rate on top width of a wall at the left-hand side corner neck	107
Table 3.8: Influence of laser power, powder flow rate and coolant flow rate on wall roughness measured by the mechanical stylus	108
<i>Table 4.1: Chemical analysis of UDIMET NITINOL material provided by Special Metals Corporation</i>	129
<i>Table 5.1: Chemical analysis of UDIMET NITINOL powder provided by Special Metals Corporation</i>	134
Table 6.1: Correlation coefficients	177
<i>Table 6.2: Identification conditions and criteria</i>	187

Table 7.1: Physical properties of NITINOL (Brinson et al., 1996; Liang and Rogers, 1992)... 213

Table 8.1: Input parameters 242

Table 9.1: Material characteristics of the NiTi ingot provided by the NDC company 261

Table 9.2: Properties of the SMA NiTi material..... 292

CHAPTER 1

1. Introduction

The analysis of trends in manufacturing industries shows that the key technologies of the future are the emerging miniaturization technologies. The conclusion was based on the increasing number of conferences, workshops, and companies dealing with miniaturization technologies that are aimed at the production of small-scale (at the level of several millimeters) parts and mechanisms. Therefore, there is a pressing need for the theoretical understanding of the principles, devices and systems for micro/meso-manipulation that would deliver the necessary degree of reliability, longevity and predictability.

1.1 Background and motivation for shape memory alloy (SMA) based monolithic micro/meso-scale manipulator (mMM) development

A review of the needs of the emerging miniaturization industries and of the literature reveals that there is a lack of reliable, robust and effective approaches for the development of different manipulation systems for different functions. In this dissertation an effort will be made toward the development of micro/meso-scale manipulators (mMMs) for different purposes using a systematic model-based approach. The proposed manipulator will also represent a key building

block of the microfactory concept of the future whose development has already started, in particular in Japan, Korea and Europe (Bellouard et. al (2000), WTEC (www.wtec.org)).

A distinctive feature of the proposed device will be the use of advanced materials, i.e., Shape Memory Alloys (SMA). By combining the monolithic structure concept using SMAs (NiTi alloy in this study), whose feasibility has already been proven by a number of researchers (e.g., Bellouard et al., 2000; Huang et al., 1998), with the compliant structure concept in which a jointless mechanism uses elastic deformation as the source of motion (Kota, 2001) and with novel manufacturing technique - Direct Metal Deposition (DMD), which allows the creation of monolithic jointless metallic structures, an SMA based mMM will be developed. One of the advantages of the DMD technologies is in batch production that leads to a low cost of the manufactured devices. Given the fact, that some of the main requirements for mMMs are high force output, low degradation of mechanical properties under cyclic loads ($>10^5$ cycles), high repeatability and high precision, SMA proves to be an ideal material. Peirs et al. (2001) have reported that SMA based actuators have a much higher work density as compared to hydraulic and magnetic actuators. Their comparative analysis has shown, for example, that the work output per unit volume for SMA micro-actuators is 15 times larger than for hydraulic actuators, their response speed increases with miniaturization due to enhanced cooling, and that the force generated is 150 times higher than for hydraulic and 400 times higher than for magnetic actuators.

1.2 Application of SMA mMMs, expected results and their significance

The main research objective of this project is to develop design and fabrication methodologies, prototypes and mathematical models for self-sensing and self-actuating monolithic mMMs made from Shape Memory Alloys (SMAs) by Direct Metal Deposition (DMD). The mMM is to be capable of developing motions in the range from a fraction of a micron to several millimeters.

An advantageous property of the mMMs will be their biocompatibility and high corrosion resistance, due to the use of SMA (NiTi), making them compatible with biomedical needs (e.g., scaffold assembly in tissue engineering used as a matrix for human tissue (bones, organs, etc.) regeneration) as well as with applications that require handling of small objects in aggressive and hazardous environments. The work will also result in a substantial contribution toward the theoretical understanding of SMA properties as a result of the particular processes used in their manufacture.

The most consequential impact will be the creation of a fundamental scientific and technological base for micro/meso manipulation methods through the creation of mMMs for a spectrum of current and future needs. These systems will complement the traditional MEMS-based technologies.

A constitutive 0-D mathematical model that describes the kinetics of austenite transformation in SMAs will be suggested. The model will be aimed at the needs of mMM like structures. It will be used in modeling the dynamics of the mMM's motions and compared to conventional control theory based dynamics. The analytical expression of the dependence of the SMA's austenite fraction evolution on the SMA's temperature evolution (resulting from the applied heat load used

as an actuation factor) in the material will allow the definition of the stresses (forces) acting on the device. Therefore, the instantaneous state of the manipulator (position of the linear stages of the arm, exerted force by the grippers, etc.) will be predictable.

In the technological domain the principal contribution of the work will be the design and manufacture of a 2/3-DOF monolithic mMM using advanced DMD based rapid prototyping methods. Specifically:

- (a) Creation of DMD process “know how” and process optimization for the processing of SMA powder. Advanced DMD processes will be used to fabricate the mMM. DMD operates not at the sintering, but at the melting temperature, thus creating the needed thermal conditions for the production of complex SMA based structures;
- (b) Investigation of the properties of the SMA materials that will be processed by the newly established DMD processes for SMAs and comparison with similar SMAs made by conventional methods;
- (c) Performance metrics for monolithic mMMs for use in micro/meso manipulation;
- (d) Ability to batch manufacture mMMs. This will significantly impact industry.

1.3 Conceptual embodiment of a plausible mMM

A possible conceptual design of the suggested SMA mMM and of its functional components is schematically shown in Fig. 1.1. This design configuration will be used throughout this dissertation to explore, demonstrate and verify all the proposed scientific and technological advances that will be necessary to create the proposed monolithic mMM. The arrows in Fig. 1.1 show possible movements and corresponding functions of the mMM. The linear X-Y movement

of the manipulator will be accomplished by using an accordion spring structure, which results in high Z-directional rigidity. It also employs the “elastic hinge” concept at the corners of the springs. The Z vertical motion will be provided by the flexure spring (shaft) structure of the manipulator arm while the G grasping motion will be accomplished by the jaws of the microgripper.

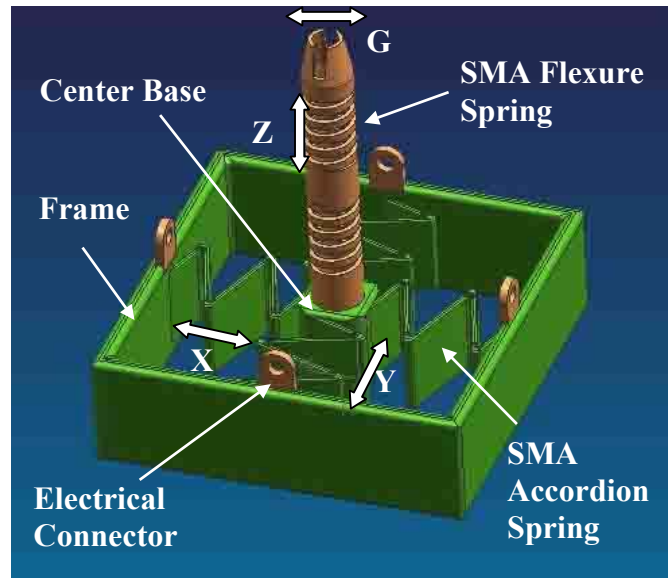


Figure 1.1: *Conceptual design of a monolithic X-Y-Z motion actuator with a microgripper.*

The mMM parameters (geometry, topology, etc.) will depend on actual mMM applications. In the current project the mMM will be designed to meet the requirements for micro/meso manipulation tasks in any application demanding handling of micro/meso scale objects in the meso-scale range of displacements.

The proposed mMM system will have a target size of about $40 \times 30 \times 30$ mm maximum, several millimeters of XYZ displacements with a micron-level resolution and up to a 5 N gripping force. It will be manufactured as a monolithic object using the laser-based DMD process. The possible cumulative target characteristics of the mMM are given in Table 1.1.

Table 1.1: *Target characteristics of the mMM*

Target mMM size	40 × 30 × 30 mm maximum
XYZ-displacements	several millimeters
Gripping range	2 - 3 mm
Material	NiTi (NITINOL)
Positioning accuracy	several microns
Feedback transient time	150 - 300 ms
Gripping force	1 mN - 5 N
Repeatability degradation	10% after 10 ⁵ cycles

The X-Y linear stage is represented by two pairs of “agonist-antagonist” actuators. The “agonist-antagonist” actuator is a pair of springs connected to each other in series, for example, in the X direction. One spring produces a bias force against the second spring that produces the active (pulling) force. When one of the springs is actuated it moves in the X direction (agonist), while the other one works as a bias to this movement (antagonist).

In order to provide all the mMM’s in-plane movements (X-Y direction) the one-way (OW) shape memory effect (SME) will be used in which the active SMA spring is previously thermo-mechanically processed or “trained” (as described in Perkins and Godgson, 1988) or selectively “annealed” (according to Bellouard et al., 2000) in a compressed state that corresponds to its minimal length. The OWSME can be combined with the R-phase transformation property that some SMAs possess, in order to significantly decrease the phase transformation hysteresis in the SMAs as it was done by Uchil et al. (2002). After the annealing procedure is done, the compressing force is removed. Afterwards, the annealed spring is

stretched back to its original (non-compressed, maximal) length. When a heat load is applied to the thermo-mechanically processed locations in the SMA structure, the shape memory effect (SME) forces the SMA spring – a part of the manipulator - to move to its original position (constrained recovery) that corresponds to the compressed (minimal) length of the spring. The places where heat will be applied to the manipulator are the accordion springs, flexure springs and the microgripper. Due to the presence of the bias force, upon cooling, the manipulator will restore its original shape at which it was compressed and annealed. The successful implementation of this idea was demonstrated by Bellouard et al. (2000) and Huang, et al. (1998) (e.g., an SMA satellite antenna) and many others. It is also possible to use the two-way (TW) SME, when a bias force is not required. The advantage of OWSME over TWSME is the several times larger recovery strain.

Several heating alternatives will be explored:

- (a) Indirect heating. The SMA element can be heated: 1) by applying an electrical current through an external heater consisting of a high resistance wire or tape wrapped around the SMA structures, 2) by externally placed mini ceramic heaters, 3) by the externally glued flexible heaters.
- (b) Direct heating (resistive). Heating can also be done by applying an electric current directly to the annealed part of the manipulator (e.g., springs) serving as a resistance. All the non-annealed parts of the mMM (case, center base and solid parts of the arms, excluding the flexural springs) will have an approximately 5-6 times larger magnitude of electrical resistance than the annealed parts (accordion, flexural springs and microgripper jaws) do, due to the crystallization of the material during the thermo-mechanical “training”.

Therefore, the non-annealed parts can be used/viewed as electrical insulators in the manipulator's design due to their low electrical conductivity. Electrical (highly conductive) connectors will be implemented in the mMM structure (Fig. 1.1) in order to provide electrical connections for the resistive heating method of actuation.

The actuation of the SMA mMM accordion springs occurs due to the shape memory effect (SME) imposed on them. Since the structure of the mMM will be experiencing heating/cooling cycles during actuation, it is advantageous to study the effect of heat on the structure. The SME driven actuation takes place at so-called transformation temperatures (TTRs) – the temperatures at which phase transformation occurs. The desired TTRs need to be close to room temperature due to the mMM's design requirements. For the current choice (chemical composition, level of contamination, previous thermal treatment history, etc.) of SMAs – NiTi – the TTRs should be in the range of 20...80 °C. To achieve these temperatures in the proposed mMM structure – a heat flux of approximately 10 W is needed (based on its geometry, thermal inertia, mass, etc.). Therefore, the thermo-mechanical response due to heating only was analyzed, using the finite element method (FEM) analysis software, “Structures” in UNIGRAPHICS.

For simplicity throughout this thesis only the XY-portion and the gripper of the mMM will be considered. The preliminary design (UNIGRAPHICS) and its was prototype made by 3D printer are shown in Figure 1.2.

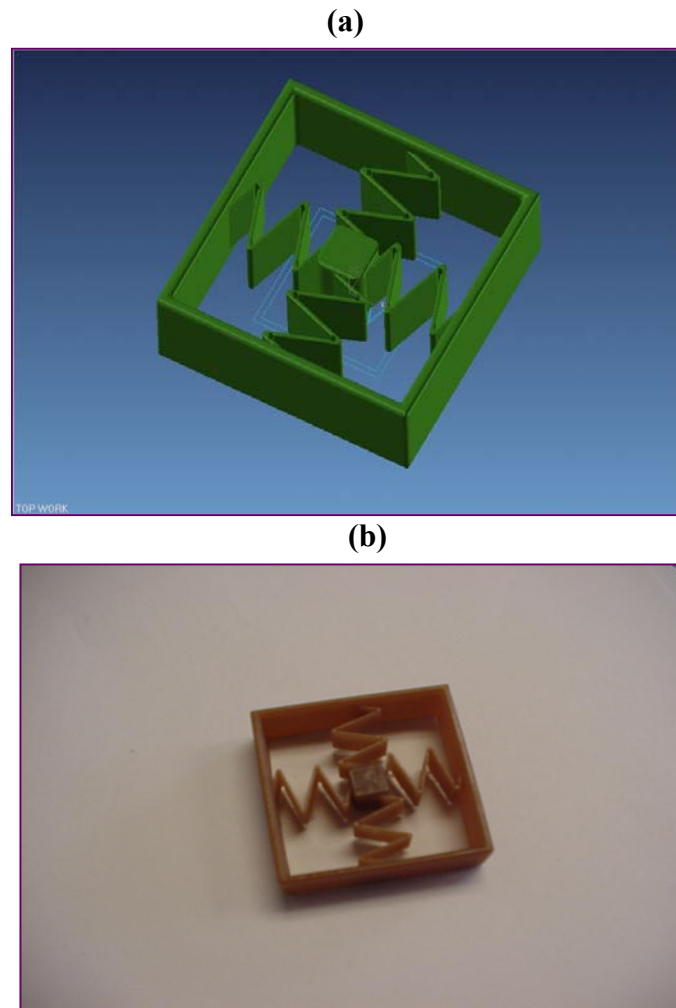


Figure 1.2: *mMM X-Y motion actuator: (a) design, (b) wax prototype*

In the FEM simulations, a distributed heat flux of $Q = 10 \text{ W}$ was applied to the right-hand side accordion spring of the mMM as shown in Fig. 1.3. The other elements of the structure were held at room temperature. To the best of our knowledge there is no commercially available FEM software that allows prediction of SME driven movements in complex 3-D structures such as the mMM.

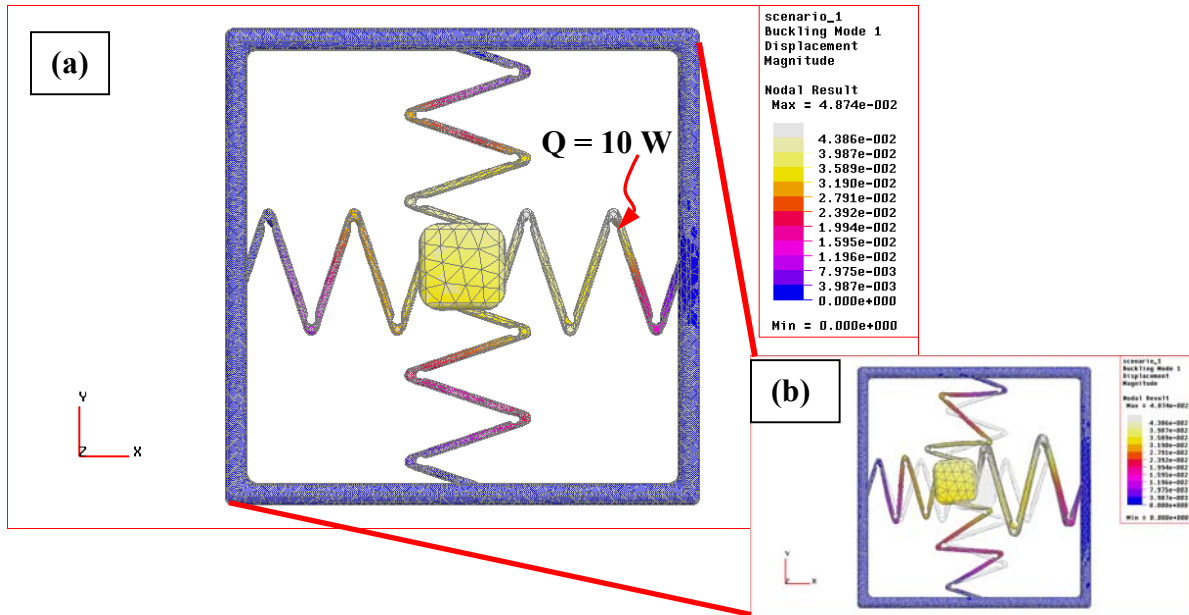


Figure 1.3: FEM modeling of mMM (UNIGRAPHICS): (a) true scale, (b) relative scale.

One can see that for this particular heating case the right-hand side spring insignificantly moves (actuates) to the left in the X-direction due to the thermal-expansion effect only (Fig. 1.3a). Figure 1.3b shows the movement due to the thermal expansion in at an exaggerated scale. In general, this thermal expansion driven movement may not be accounted for in the shape memory effect driven motion. The movement, shown in Fig. 1.3b, is not completely uniform due to the twist present in the middle piece of the structure. The non-uniformity of the movement is an effect of the layout of the four springs in the mMM, where the two vertical springs attenuate the motion of the heated (actuated) spring. The twist-effect is supposed to be eliminated when actuation takes place due to the shape memory effect rather than the thermal expansion effect. In this case, the force developed by the SME in the spring will be larger than the twisting forces in all other components of the mMM. This difference is characterized by the introduction of the effective stiffness of the material in the austenite and martensite states, although some

researchers has shown that a stiffness of martensite is almost equal to the stiffness of austenite (Rajagopalan, et al., 2005). The effective stiffness of the actuated (heated) spring will be considered to have almost three times larger value in comparison to the effective stiffness values of the other three springs. The change of the effective stiffness will resemble the reverse martensitic phase transformation effect, taking place during heating and providing the SME for the structure, and the assumption that the final material state of the phase transformation process is austenite, which has approximately three times higher effective stiffness than martensite for NiTi alloys. The material transformation and the corresponding SME details will be discussed later in this work.

The following are the major assumptions that will be used in all the experimental and numerical modeling techniques through this research:

- 1) Only the SMA material's response during heating (or reverse phase transformation) will be modeled. The material will be considered to have only two phases: detwinned (oriented) martensite and/or austenite.
- 2) Only simple loading histories of material will be explored.
- 3) The driving force for the shape memory effect driven motion will be based on the change in the effective stiffness (further – “stiffness”) of the austenite and martensite.
- 4) The driving forces, generated during the phase transformation (by transformation strain) will be lumped into an effective stiffness value for ease of modeling. This assumption is appropriate for simple loading paths of the material. Complex loading cycles with partial transformation cycles or R-phase will necessitate the use of more accurate and robust constitutive models.

- 5) The influence of the different phases of the material (R-phase, twinned martensite) and of the microstructural changes in the material (grain re-orientation, etc.) will not be accounted for in the modeling and experimental techniques of the shape memory effect driven motion.

1.4 Outline of the dissertation

Chapter 2 describes the current trends and issues in SMA based actuation, manipulation and manufacturing. Rapid prototyping processes that will be potentially considered for the fabrication of SMA based actuators are reviewed as well. An analytical description of the drawbacks and advantages of the described prototyping processes in using them in the processing of NITINOL powder is given and a choice of a direct metal deposition (DMD) process for the fabrication of mMMs from NITINOL powder is justified.

Chapter 3 contains an experimental study of the possibility of fabricating NiTi parts by the DMD process from NITINOL powder. The mMM is a predominantly thin-wall structure, containing some bulk sections. DMD parameters for the fabrication of high quality (non-cracked, non-porous) thin-wall and bulk structures are identified through factorial design of experiments. During the experimental studies several thin-wall and bulk structures were fabricated and analyzed.

The quality of the DMD fabricated material for both types of structures is assessed in Chapter 4. The influence of the DMD process and of the post-DMD thermal treatment on the properties of NITINOL fabricated structures was investigated by means of optical microscopy,

scanning electron microscopy energy, dispersive spectrum analysis, x-ray diffraction analysis, secondary ion mass spectroscopy and differential scanning calorimetry.

Chapter 5 is aimed at finding an optimal method for the fabrication of the mMM. It contains an experimental study of the fabrication of the mMM by DMD only and by a hybrid method - DMD plus conventional machining processes (wire electrical discharge machining (wire-EDM) and milling). Several functional parts of the mMM, namely, NITINOL accordion spring actuators, were fabricated using the above-mentioned machining processes. The ability of the actuators' material to undergo a temperature-induced phase transformation, that is a prerequisite for the shape memory effect (SME) driven motion, is studied here as well. A one-way shape memory effect (OWSME) "training" procedure is developed in order to impart the phase transformation property on the DMD fabricated NiTi parts. The OWSME "training" procedure is applied to the fabricated actuators and their ability to develop a linear motion due to this temperature-induced OWSME "training" process is studied.

Chapter 6 is devoted to studying the dynamics of the SMA actuators during their sub-millimeter and millimeter-scale SME driven motion. This study is undertaken by using an SMA wire actuator and a conventional system identification procedure. The resolution and accuracy of the sub-millimeter scale motion of the actuator is estimated as well. The so-called "self-sensing" principle is explored that will be used for the motion control of the SMA actuators.

The known difficulties with the motion control of SMA actuators due to hysteresis were the motivation of the research undertaken in Chapter 7. A new mathematical model that predicts the kinetics of the temperature-induced phase transformation in SMAs is developed. The model predicts the evolution of the austenite fraction in the SMA material with the increase of its temperature. The model can be used in the development of a mathematical model of motion of

an SMA actuator and its corresponding motion control model. For simplicity, this model was developed for an SMA wire actuator. Its extension to other structures is addressed in later chapters.

Chapter 8 describes a new mathematical model of motion of the SMA actuator based on the suggested model of the kinetics of the temperature-induced phase transformation in SMAs given in Chapter 7. The model of motion also uses an already existing model of motion of a “human muscle” developed by Wu et al., 1990.

An SMA spring based actuator, corresponding to the linear stage of the mMM is designed, fabricated and tested in Chapter 9. The linear stage is fabricated by wire-EDM from a NiTi ingot. A conventional system identification of the linear stage is performed in addition to the modeling of the step response behavior of the linear stage of the mMM. Another goal of Chapter 9 is to develop the motion model of the spring actuator. Therefore, a model of motion of the linear stage, based on the model for the kinetics of phase transformation in SMAs, is formulated. The model uses the same approach as for the modeling of the motion of the SMA wire actuator in Chapter 7 and Chapter 8. The model is used to study the sub-millimeter and millimeter scale motion of the linear stage.

Chapter 10 describes the design, manufacture and development of the mMM’s NiTi gripper. The gripping motion is achieved by means of the Two-Way Shape Memory Effect (TWSME). The TWSME “training” procedure is developed specially for the design of grippers suggested in this Chapter.

In Chapter 12 conclusions are drawn and possible directions for future work are suggested.

CHAPTER 2

2. “State-of-the-art” review

Chapter 2 describes current trends and issues in SMA based actuation, manipulation and manufacturing. Rapid prototyping processes that can be potentially considered for the fabrication of SMA based actuators will be reviewed here as well. The drawbacks and advantages of the described prototyping processes will be analyzed.

2.1 SMA-based actuation

2.1.1 SMA properties

SMAs belong to a class of “smart” materials with particular mechanical and thermal responses. These materials have the ability to undergo diffusionless martensite and reverse martensite (austenite) phase transformations under certain temperature and stress conditions (Fig. 2.1).

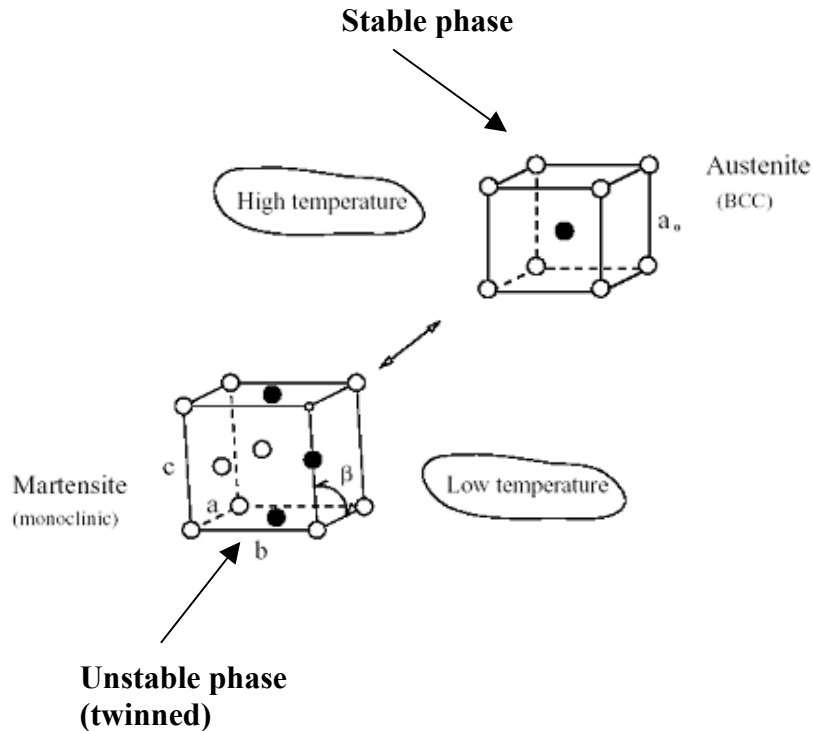


Figure 2.1: Schematic of diffusionless martensite phase transformation (Weiming, 1998).

Four phase transformation temperatures (TTRs) characterize the direct and reverse martensite phase transformations in the SMA material: martensite start – M_s , martensite finish – M_f , austenite start – A_s , and austenite finish – A_f (Weiming, 1998). When the SMA materials are under particular stress and temperature conditions, M_s – is the temperature of the material at which the martensite phase starts to form, M_f – is the temperature of the material at which the martensite phase stops to form, A_s – is the temperature of the material at which the austenite phase starts to form, and A_f – is the temperature of the material at which the austenite phase starts to form. The TTRs are usually defined by Differential Scanning Calorimetry (DSC).

Austenite is considered to be a thermodynamically stable phase of the material and has a BCC crystal structure. Martensite possesses a monoclinic (e.g., HCP) crystal structure and represents an unstable phase of the SMA material.

The SMA transformations manifest themselves in two properties (Fig. 2.2): “superelasticity” and Shape Memory Effect (SME). “Superelasticity” is characterized by the ability of the material to recover large elastic strains (uniaxial strains up to 8.5%) if these exist, i.e., when the material is deformed and above its austenite finish transformation temperature. For example, if an SMA wire (the closest example to uniaxial strain recovery) is above its A_f temperature and a large external force is applied to the wire thus stretching it, the wire recovers its pre-stretched length (like “rubber”) when the external force is removed.

The SME property allows the wire to fully recover the externally induced apparently plastic strains with great force due to the reverse martensite transformation. For example, if the SMA wire is in its martensite phase and its temperature is below the M_f temperature, a large apparently “plastic” deformation (uniaxial strain) can be imposed on it, thus stretching the wire and leaving it in this stretched state when the deforming force is removed. The pre-stretched length of the SMA wire can be recovered afterwards, when the wire is heated above its A_s temperature. Therefore, SMAs can produce extremely large recovery microstrains that are on the order of 10^4 according Wuttig et al. (1999), as well as large forces. The stress-strain curve that corresponds to the “superelastic” state of the SMA material is shown in Fig. 2.2c. The SME state of the material is represented by the stress-strain curve in Fig. 2.2d.

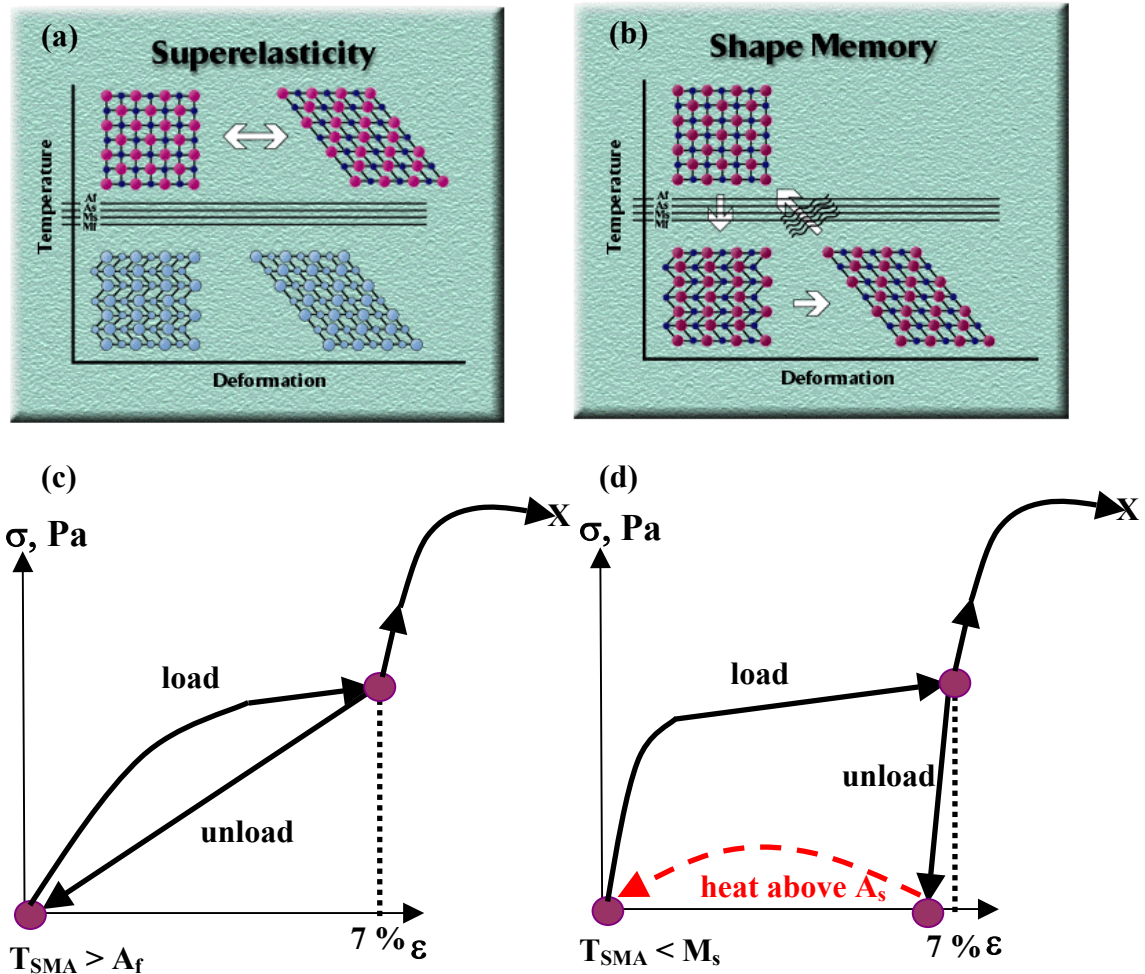


Figure 2.2: SMA properties: (a) superelasticity; (b) shape memory effect (www.nitinol.com); (c) “superelastic” stress-strain curve; (d) SME stress-strain curve.

The SME driven strain recovery property of SMAs is used in actuators and grippers manufactured from SMAs. SMAs, in particular NiTi, are useful in many applications: due to their biocompatibility (Chu et al., 2003), corrosion resistance (Cui et al., 2003; Rocher et al., 2003) and fatigue behavior (Duerig et al., 1999; Eggeler et al., 2004; Gall et al., 2002; Gall et al., 2001). SMA’s are widely used in biomedical applications and orthodontics; (Chu et al., 2003; Duerig et al., 1999). Their enhanced damping makes them applicable in seismic design to absorb seismic energy.

2.1.2 SMA actuators

SMA actuators can be actuated by heating them through: 1) direct application of electric current through the SMA structure (resistive heating) or 2) application of heat through externally located heaters.

Peirs et al. (2001) have shown that SMA actuators, when compared to hydraulic and magnetic actuators, have the highest work density and that with the miniaturization of the actuators their power density increases. They have also pointed out the drawbacks of the particular SMA systems they have considered: low effective work density on the order of $1\mu\text{J}/\text{mm}^3$ (except for SMA based grippers - $50\mu\text{J}/\text{mm}^3$), control difficulties and high magnitudes of the electric current and power required. However, they have considered only a limited variety of systems characterized by the low volume of SMA material compared to the total actuator volume. One of the major reasons for the observed problems was in the low electrical resistivity of the particular SMAs (in the “resistive” heating case) and in the fact that the considered actuators contained only a small portion of their structure made from SMA. Therefore, the largest problem encountered was the high amount of current required for heating, for example, of the SMA wire-based actuators, to achieve the needed actuation temperature due to their low resistivity. This problem was overcome by the “Nanomuscle” company that invented a 30 mm long SMA linear actuator with a linear stroke in the range from 17 μm to 4 mm, requiring an actuation electrical current of 80 mA. The “nanomuscle” actuator consists of bundles of 30 μm diameter SMA wires that contract after heat is applied. The major drawback of such a device is its high cost - around \$2,000 per batch (25 pieces) because of the sophisticated digital control

interface embedded into the system and because of the manufacturing problems connected with the fabrication of the small, 30 μm diameter SMA wires.

So far, the SMA wire-based actuators have shown the largest recovery displacements (e.g., the linear stage by Bellouard et al., 2000). Their advantage is that their resistivity can be affected by merely increasing their length. Resistivity, in turn, is the key parameter in achieving the required transformation temperature of the SMA. Another way to overcome the resistivity problem is to use low transformation temperature SMAs (Fu et al, 2001). Finally, one of the very successful works, done in the area of micro-gripper design, uses Micro Electro Mechanical System (MEMS) manufacturing techniques (Fu et al., 2001). The SMA (NiTi alloy) was deposited as a thin film on a Si substrate, micromachined beforehand in the form of a freestanding cantilever. This solution also facilitates the possible integration of a heating system inside of the substrate thus overcoming the “heating” problem of an SMA since the SMA is deposited on the top of the substrate. The additional heaters, embedded into the substrate, are capable of achieving greater heat fluxes due to their high resistivity in comparison to the SMA itself. The authors have achieved a reasonable agreement (less than 15 % error) between their numerical and experimental simulations of this SMA thin film structure thus improving the SMA micro-gripper characteristics (e.g., robustness, repeatability, and precision) and its gripping motion control properties.

Control related difficulties in SMA based actuators and manipulators can be overcome by stabilizing the SMA transformation temperatures and decreasing their hysteresis. In addition, the Shape Memory Effect (SME) can be significantly increased by using rapid quenching procedures described by Furuya, 2000. For example, conventional binary SMAs (NiTi) can be modified by adding a stabilizer like Cu or Nb. Kennedy and Straub (2000) have used Cu to stabilize the

transformation temperature in their SMA based actuator. Ni-Ti-Nb alloys have similar advantageous properties. Bellouard et al. (2000) have shown that in the case of Cu addition, the degradation of the strain recovery characteristic of an SMA based manipulator is 10% after 10^5 actuation (heating/cooling) cycles and reaches a level of 20% after 2×10^5 actuation cycles. Besides, additions like Cu or Nb decrease the existing phase transformation hysteresis in SMAs, thus facilitating an easier control of the actuators. The author has achieved a 1 μm positioning accuracy of his small scale SMA linear stage (50 mm long, 17 mm wide and 0.05 mm thick) (Fig. 2.3). The same research group has also developed a monolithic 2 mm SMA gripper (Fig. 2.4 a and b) able to provide a grasping motion of 160 μm . This monolithic micro-gripper contains both passive (no SME) and active (with SME) parts made of SMAs thus decreasing the number of moving parts in the whole structure. The gripper is used for optical micro-lens (diameter = 0.3 mm) handling (Bellouard et al., 1997; Bleuler et al., 2001) and for the 3-D assembly of an artificial scaffold for tissue engineering purposes (Zhang et al., 2002). The artificial scaffold is a biocompatible matrix (armature) used for regeneration of human tissues (bones, human organs, cartilages, nerves, etc.). Zhang et al. (2002) used an SMA (NiTi) monolithic microgripper to assemble a scaffold by manipulating 100 μm polymer building blocks (Fig. 2.4c).

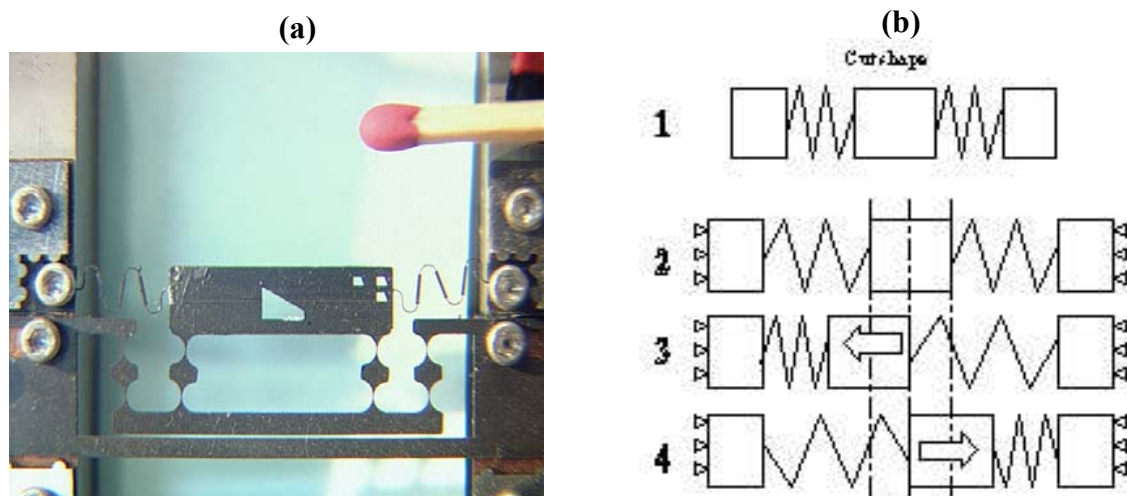


Figure 2.3: SMA-based linear stage: (a) design; (b) actuation principle (Bellouard et al., 2001).

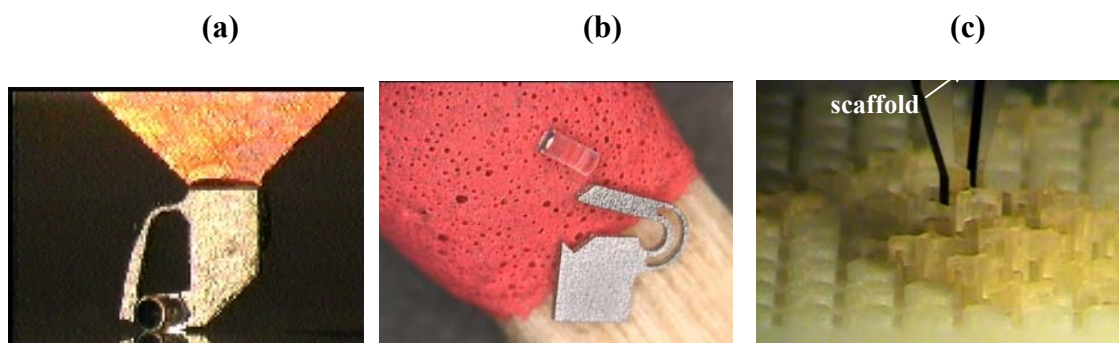


Figure 2.4: Monolithic microholder (a), microgripper (b) made of SMA (Ni-Ti-Nb) (Bellouard et al., 2001), and SMA microgripper (c) for scaffold assembly (Zhang et al., 2002).

Roch et al. (2003) have created a monolithic SMA thin film microgripper to safely transport electronic microparts for MEMS purposes. The existence of a large SMA phase transformation hysteresis in the widely used closed loop control systems (e.g., proportional-integral-derivative (PID) control) of macro scale SMA based actuators is not favorable. The additional problem here lies in the large thermal inertia (large mass) of such systems and cooling difficulties, contributing to the control issues related to the hysteresis. After the application of an electric current to the SMA structure in order to heat it and initiate the SMA driven actuation of an SMA macro scale

actuator, a certain amount of time is needed for the reverse martensite phase transformation related strain recovery (actuation) to occur. The reverse phase transformation, when martensite transforms into austenite starts at the A_s and stops at the A_f temperatures. To return, for example, an SMA wire based actuator, to its initial, pre-recovered position, the SMA structure needs to be cooled. In this case the austenite phase of the SMAs transforms back into the martensite phase at the M_s and M_f temperatures, that are different from the A_s and A_f temperatures. Therefore, the difference in the TTRs creates the hysteresis in the control of the motion of the SMA actuator if it uses the SMA temperature as a feedback signal. In addition to this, if cooling the SMA actuator is achieved by natural convection only, then the phase transformation time increases, which represents a problem in PID controlled systems. The solution proposed by Elahinia (2001) was to use a Variable Structure Controller that proved to be reliable in the motion control of their SMA based actuator. In contrast to macro-scale SMA actuators or certain micro-scale SMA devices, some investigators were able to meet very tight control system requirements (precision, resolution) for controlling the motion of the micro-scale SMA actuators. For instance, Kuribayashi (2000) designed a NiTi thin film micro-scale device that responded within 200 ms to an applied heat flux and was capable of achieving a reference force of 4N in such a short period of time using a regular PI control scheme (Fig. 2.5). The repeatability of this system is, however, questionable, since no data on the number of cycles before the start of degradation of the SMA strain recovery properties was given. One can assume, based on the information given above, that it is advantageous to use the SMAs like NiTi-Cu, with the Cu stabilizer, in order to achieve high operational cycling characteristics, i.e., a maximal number of heating/cooling cycles before the magnitude of the maximal recovery uniaxial strain of the SMAs starts decreasing.

The electrical resistance of the SMAs is used as a feedback signal in controlling the SMA structures' movements by a number of researchers. For instance, Lee et al. (2001) used electrical resistance measurements of an SMA structure as a feedback signal in their neural-fuzzy control algorithm. They were able to precisely control the angular motion of their SMA active catheter. Since the catheter was actuated by resistive heating (with an electric current), the only additional information needed was the change in the corresponding voltage drop across the catheter. They have shown that the dependence between the applied electric power (heat flux) and the measured voltage drop change (resistance change) across the SMA structure is linear. Another example is described by Lei and Yam (2000). They have successfully created a model-based position control and a neural-fuzzy logic based position control for a SMA wire actuator.

According to some researchers, the control difficulties related to the phase transformation hysteresis do not pose a major problem in the motion control of SMA actuators as long as the corresponding control parameters (applied voltage/current, force and stress) are continuous functions. This was shown to be the case in the SMA-based thin film-micro-manipulators fabricated by Kuribayashi (2000). He has shown that continuity of the controlled functions (stress or strain vs. the applied voltage/current) is necessary and enough to maintain the efficiency of the corresponding control system. One just needs to make the functions linear.

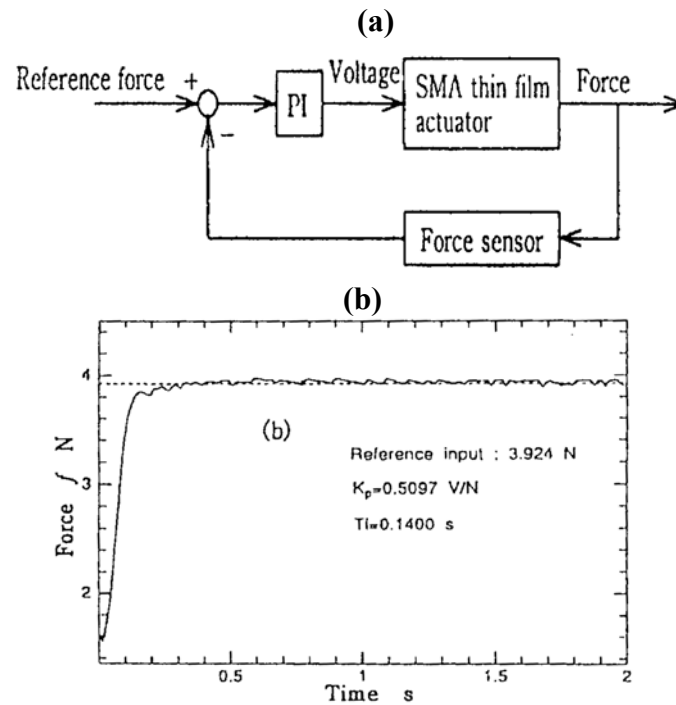


Figure 2.5: Feedback control system of an SMA actuator: a) control system of the bulk thin film actuator; b) experimental feedback results (Kuribayashi, 2000).

A way of decreasing the effect of phase transformation hysteresis is to use the so-called R-phase transformation (rhombohedral phase), according to (Miyazaki and Otsuka (1986), instead of the martensite phase transformation, though it decreases the maximal magnitude of the uniaxial strain recovery by a factor of 10. This was done in a $2 \text{ mm} \times 5.8 \text{ mm} \times 0.23 \text{ mm}$ monolithic SMA microgripper system (Kohl et al., 2001) with a positioning accuracy of $2 \text{ }\mu\text{m}$ and a maximal gripping force of $35 \text{ }\mu\text{N}$. Uchil et al. (2002) have also designed a spring-like SMA actuator combining the two-way SME with the R-phase transformation property. The authors achieved a 4 cm stroke (strain recovery) over 10^6 of heating/cooling cycles with no degradation in the stroke length.

In addition, the SMA structure itself can be used as a thermistor, because the electrical resistance of SMAs is proportional to their temperature according to Tohyama et al., 2001. This property eliminates the need for a separate temperature sensor. The slight hysteresis in the temperature dependence versus the electrical resistance (Otsuka and Ren, 2002) can be decreased by a number of methods, for example, by heat treatment of the SMAs as in Otsuka and Ren, 2002. Ikuta et al. (1988) and Lind et al. (2000) have also shown that the electric resistance based motion control of an SMA actuator is a quite precise and reliable method of positioning in similar systems. After a system identification procedure, the authors proved that the SMA resistance controlled actuator behaves as a linear first order dynamic system. The system required a relatively small control effort (up to 0.25 A) to achieve a zero steady-state error with a transient of about 1-3 sec.

In comparison to the already existing experiments with SMA wire-based actuators (Lee et al., 2001) where the SMA wires developed large (on the order of several millimeters) displacements, the first objective of our SMA wire based actuator is to develop sub-millimeter displacements under different initial temperatures and strain conditions in the SMA wire. The second objective is to conduct system identification tests on the SMA wire actuator's step response at different heat sink conditions, i.e., when the SMA wire is thermally non-insulated and thermally insulated. In order to exhibit the SME the SMA wire has to be pre-strained. In most cases the amount of the pre-strain is proportional to the displacement the SMA wire can recover when heated afterwards. Strain recovery is possible due to the OWSME. The SMA wire, used in the current work, may also exhibit the so-called TWSME. The TWSME can be imposed on the SMA wire by different thermal training techniques (Lei et al., 2000; Lind et al., 2000; Wu et al., 2000). Usually, the TWSME driven shape change, characterized by wire

contraction/extension, is about ten times smaller than the conventional OWSME driven shape change. The TWSME can recover approximately 0.6% of uniaxial strain.

2.2 Laser-based rapid prototyping processes

The trade-off between the cost, efficiency and size of SMA actuators requires an innovative solution related to the development of an actuator that has a minimal number of moving parts thus substantially decreasing its cost. This is the reason why during the last decade research in manipulation and actuation was aimed at the development of monolithic devices where all the active moving parts are integrated into one structure with no assembly. Therefore, it is also important to identify the manufacturing processes that allow the building of such structures in a cost effective manner, e.g., batch production. One of the challenges in the identification of a proper manufacturing process for the purposes of this research, i.e., the development of an SMA-based monolithic manipulator, is the fact that SMAs are intermetallics that are difficult to machine without influencing the quality of the material and degrading its properties.

Contemporary industrial requirements impose significant restrictions on the produced parts, e.g., in the aircraft industry, medical industry, etc. The produced parts are constrained in weight, size and load (www.azom.com). Moreover, assembly of products, especially at the micro- and meso-scales, introduces significant errors. Therefore, it is desirable to make them monolithic, completely avoiding the assembly process. Conventional machining methods, such as casting or “one-piece” machining can be used to fabricate monolithic structures, e.g., turbine blades, housings, medical stents, etc. The advantage of using casting is in the production of near net-

shape structures requiring minimal finish machining, while the drawbacks are high tooling costs for large components and the inability to fabricate structures with complex geometry due to restrictions in aspect ratios and section thickness changes (www.azom.com).

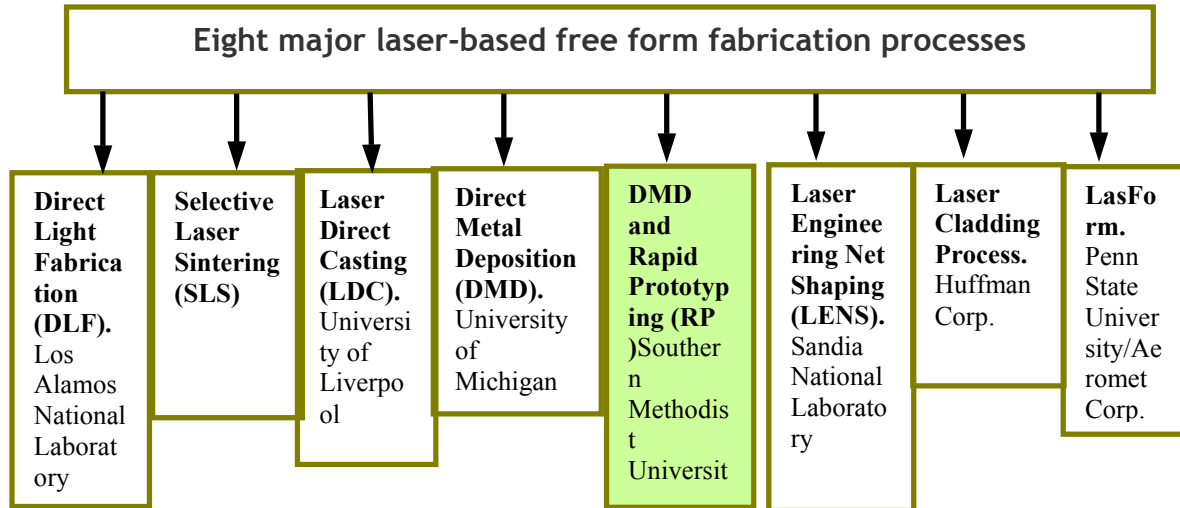
Large material waste, tools wear and long turnaround times are the drawbacks of the conventional machining processes used for monolithic structures. Up to 90% of the machined material can be wasted if the part is machined from a single ingot. Forging improves the material waste parameter, but it significantly increases the processing and tooling costs because it has to be done at high temperatures in several cycles. It also increases the turnaround times.

A solution to the above-mentioned manufacturing problems that arise in the manufacture of monolithic structures, is to use laser-based manufacturing processes. These processes build only the necessary geometry (net-shape) thus decreasing material waste to about 15%...50% (www.azom.com, Kalpakjian and Schmidt (2006)).

2.2.1 Equipment and process characteristics

Eight major laser-based free-form fabrication processes can be distinguished according to Wessel (2004). The processes are listed in Table 2.1.

Table 2.1: *Laser-based fabrication processes*



Directed Light Fabrication (DLF) (Mah, 1997). DLF is a rapid fabrication process that melts the metal powder deposited in layers on a substrate and fuses them together, layer by layer, into a pre-defined geometry. It was developed at the Los-Alamos National Laboratory. The DLF apparatus developed by (Mah, 1997) consists of a Nd:YAG laser, a powder delivery system, and a laser head positioning system controlled by a computer NC program. The author designed a five-axis DLF apparatus with two orthogonal motion axes (x and y) and a tilt axis to move the laser head, one rotary axis in the horizontal plane to move the part, and a vertical axis. The DLF apparatus is shown in Fig. 2.6a. Examples of parts created by the DLF apparatus are shown in Fig. 2.6b (Milewski et al., 1998).

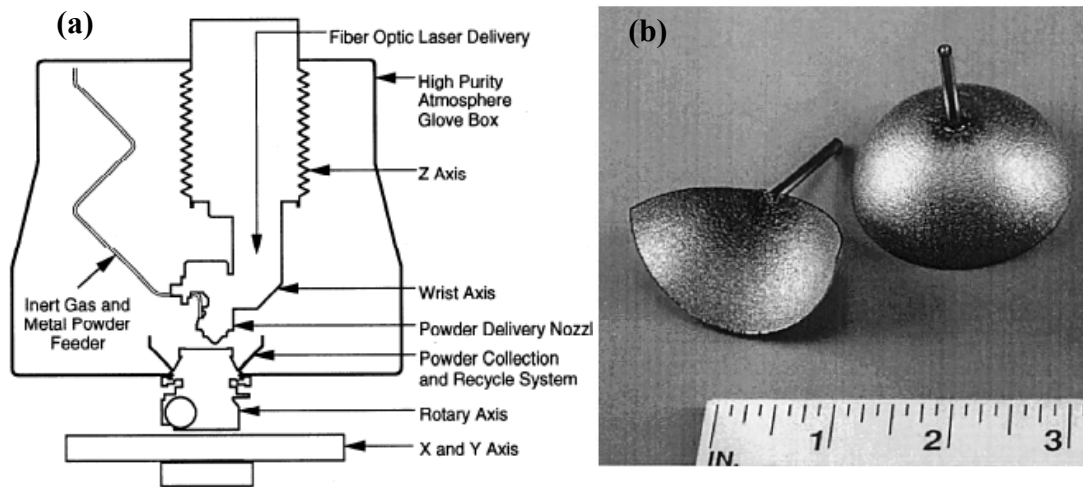


Figure 2.6: *Directed light fabrication: (a) apparatus; (b) manufactured part (Mah, 1997; Milewski et al., 1998).*

Selective Laser Sintering (SLS). SLS uses metallic, plastic or ceramic powders to create 3-D structures (Bourell et al., 1992). An SLS experimental setup is shown in Fig. 2.7. The main peculiarity of SLS is that the particles of the material being processed by the laser are not melted, but attached to each other along their boundaries, thus forming a porous structure. During the next step of manufacturing, thermal (non-laser) processing can remove or significantly decrease the porosity if needed. Kathuria, (1999) describes several techniques of 3D micro-forming by means of the SLS process. The author states that the interaction time of the laser beam with the material plays a major role in the quality of the end product built up by laser sintering. Examples of the microcladding process (SLS) are shown in Figs. 2.8 a, b. Further sintering of the already made structure removes porosity and solidifies the manufactured object.

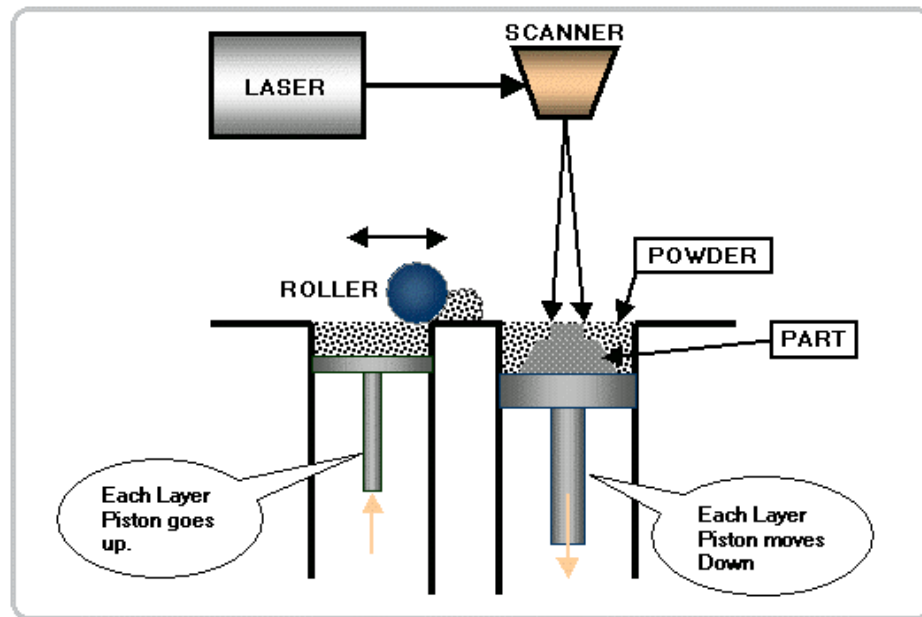


Figure 2.7: Selective laser sintering (SLS) experimental setup. (www.arptech.com.au/slshelp.htm)

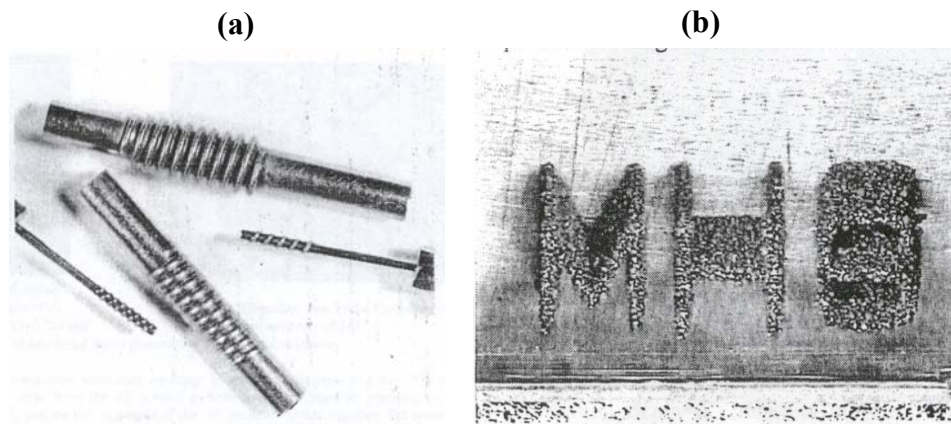


Figure 2.8: Microcladding examples: (a) one component (Ni); (b) two component microcladding (Cu/Sn) (Kathuria, 1999).

An example of metal composite tooling made by SLS is shown in Fig. 2.9 (Odonnchadha, Tansey, 2004).

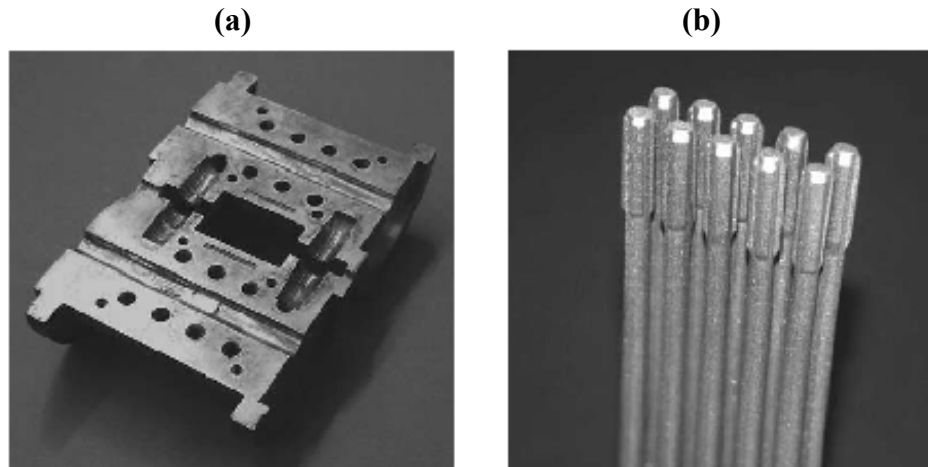


Figure 2.9: Tooling made by SLS from 420 stainless steel powder infiltrated with 89/11 bronze: (a) heat exchanger; (b) rivet mandrels (Odonnchadha, Tansey, 2004).

It is also possible to SLS manufacture porous polycaprolactone (PCL) based scaffolds (Williams et al., 2005) for bone and cartilage repair (Fig. 2.10). PCL is a bioresorbable polymer powder, which is sintered at about 50 °C. The authors show that the compressive modulus of such structures ranges from 52 to 67 MPa.

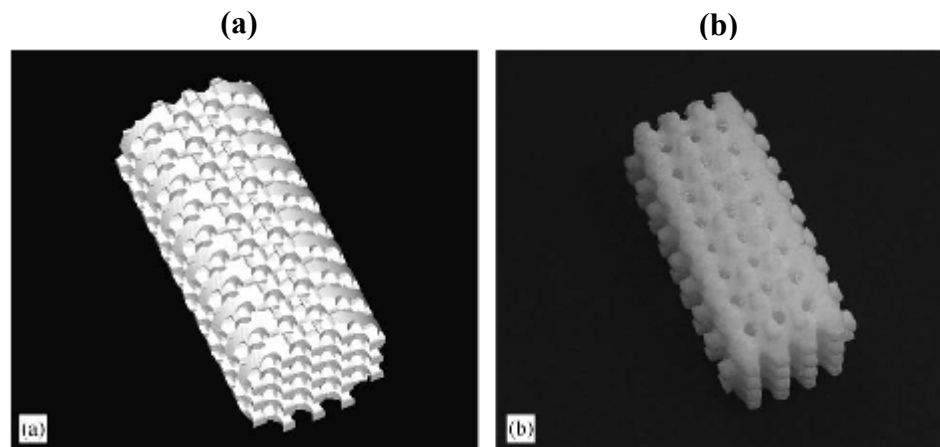


Figure 2.10: SLS examples: (a) UNIGRAPHICS based STL file for the 1.75 mm x/y/z porous scaffold; (b) 1.75 mm x/y/z PCL scaffold made by SLS (Williams et al., 2005).

The main problem in SLS is in maintaining the part's net-shape geometry throughout the manufacturing process and the insufficient resolution of the STL (stereolithography) numerical format used to approximate the geometry of the part from its CAD model. The accuracy of the laser-sintered parts was reported to be about 0.05% of the part's nominal size plus the average particle size of the powder (Petzoldt et al., 1997).

Laser Direct Casting (LDC). LDC is a laser-based melting process that was developed at the University of Liverpool (Odonnchadha, Tansey, 2004; Irving, 1999). The LDC apparatus consists of a 6-axis computer controlled machine that uses a 1.5 kW CO₂ laser. The process can produce fully dense, porosity free complex 3-D parts requiring no integral support with about 15% powder loss. The laser head of the LDC apparatus is equipped with a four-port nozzle system and a gas nozzle coaxial with the laser beam (Fig. 2.11). The main difference between the LDC system and the other laser-based manufacturing systems is the presence of the gas nozzle directing the metallic powder streams from the four angled nozzles into a more uniform powder flow. One of the advantages of LDC is in the deposition layer height control capability of the LDC apparatus. It is possible to limit the height of the deposited layer by controlling only the physical height (z-axis) of the powder feed nozzle independently of the other deposition parameters (like speed of the laser head, heat transfer conditions, etc.). The error of such a height control method is about 300 μm (Fearon et al., 2004). Another advantage of the method is the reduction in the attenuation of the powder stream as a consequence of a greater angle between the laser beam and the powder streams than in the other laser based rapid prototyping systems. For example, in Fearon et al. (2004) the LDC system has a 60 degree angle (Fig. 2.11) that is two times larger than in other analogous systems.

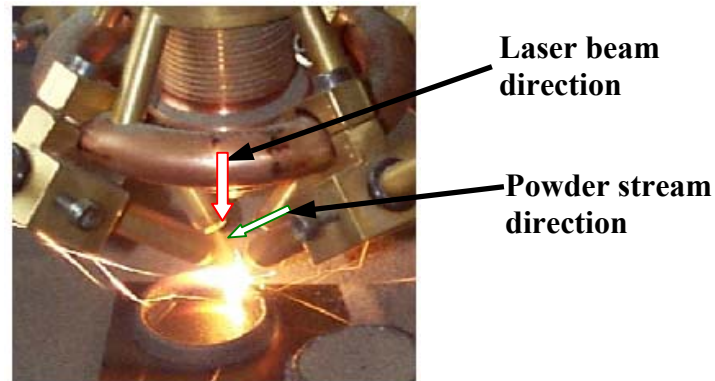


Figure 2.11: LDC laser head with a four-port nozzle system and a gas nozzle coaxial with the laser beam (Fearon et al., 2004).

Direct Metal Deposition (DMD). Researchers from the University of Michigan developed the DMD process (Wessel, 2004). The generalized DMD process schematic is shown in Fig. 2.12.

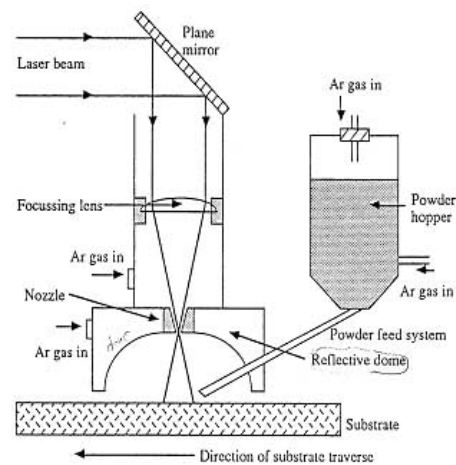


Figure 2.12: Schematics of the direct metal deposition (DMD) process (www.trumpf.com/3.laserforming_proc_main.html).

DMD is similar to the above-described rapid prototyping processes. It is used in the manufacture of parts, molds, dies, etc. from metallic powders melted by the laser. The originally built DMD

setup included a 5-kW CO₂ laser. Post-DMD heat treatment is required to improve the structure (Wessel, 2004). An experimental DMD setup is shown in Fig. 2.13a, while an example of a part fabricated by DMD is shown in Fig. 2.13b. DMD is used in the low-volume production of precision parts (e.g., artificial hip joints, space shuttle parts).



Figure 2.13: *DMD: (a) experimental setup, (b) forging tool repaired by DMD* (www.twi.co.uk/j32k/getFile/dmd_index.html).

Direct Metal Deposition (DMD) and Rapid Prototyping (RP). The DMD and RP process was developed by researchers from Southern Methodist University (SMU/RCAM). The DMD and RP experimental setup represents a 3-axis motion controlled machine equipped with a Nd:YAG laser (Fig. 2.14a) (Labudovic et al., 2003). The laser head moves in the Z-direction. The pre-heated substrate, where the metallic powder deposition and melting takes place, moves in the X-Y direction. The heat transfer conditions of the deposition process can be controlled by using a flat copper heat exchanger beneath the substrate. Furthermore, the authors modified their DMD and RP experimental setup by introducing a 6-DOF robotic hand (Fig. 2.14b) (Kovacevic, 2005). This advanced DMD process was named Laser Based Additive Manufacturing (LBAM).

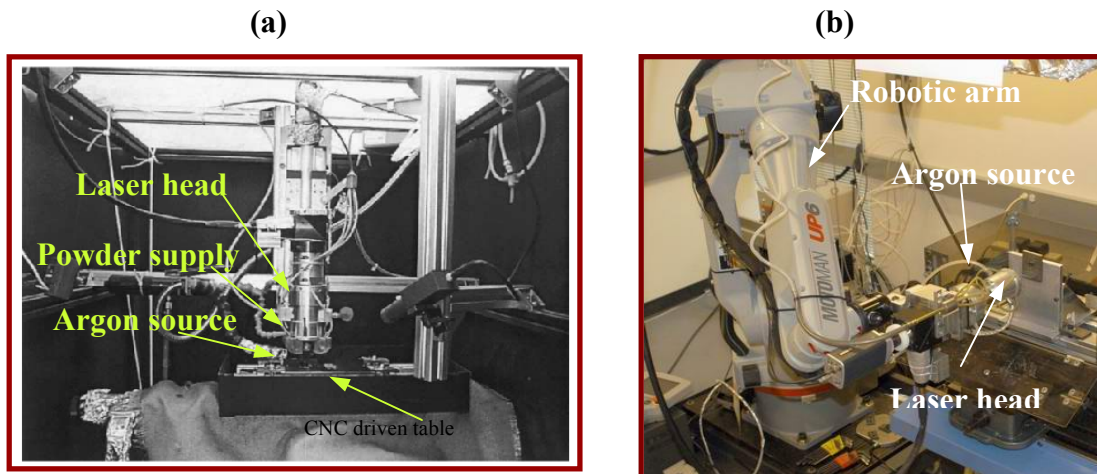


Figure 2.14: SMU/RCAM rapid prototyping equipment: (a) 3-DOF DMD and RP experimental setup; (b) 6-DOF LBAM experimental setup (Kovacevic, 2005).

Some examples of 3-D objects manufactured by the LBAM process are shown in Fig. 2.15. The LBAM experimental setup is capable of creating 3-D solid structures that possess complicated geometries (with undercuts, internal cavities, etc.) without using a sacrificial support deposition layer due to the 6-DOF functionality. It can be used in both 2.5-D layered or 3-D layered deposition; it can also be used in continuous deposition. The smallest feature that can be built (deposited) by such a system is about 1mm in size.

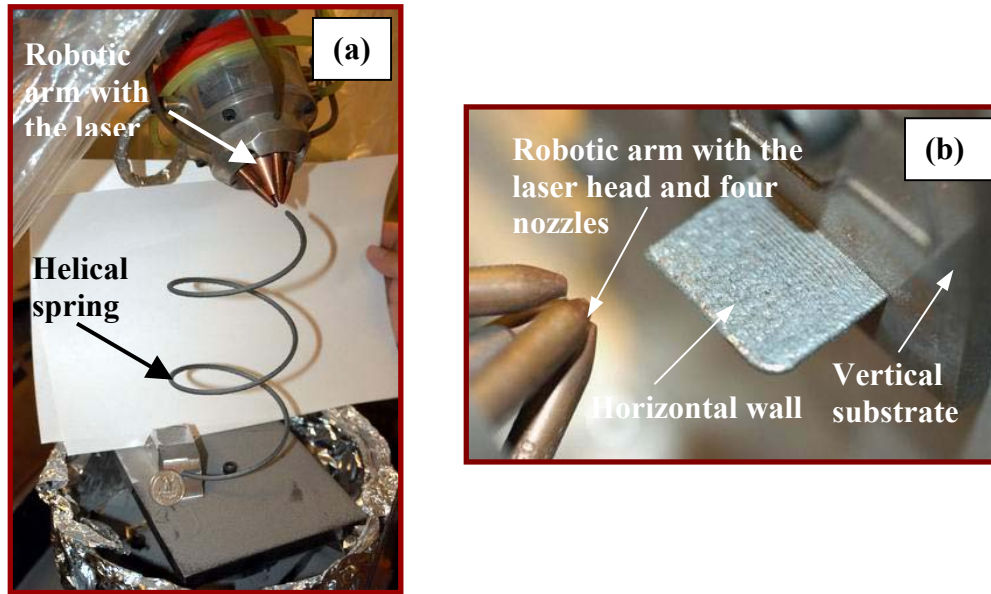


Figure 2.15: DMD RP examples: (a) helical spring manufactured from tool steel powder, (b) vertical wall (Kovacevic, 2005).

Laser Engineered Net Shaping (LENS). Scientists from the Sandia National Laboratories developed the LENS apparatus and the LENS technique. The apparatus is equipped with a 1.8 kW continuous wave Nd:YAG laser, a 4-axis positioning system, and a powder feeder (Smugersky et al., 1997). In order to obtain a high quality material (low contamination level and low oxygen level), a glove box is used to create an inert (Argon gas) atmosphere. A nominal oxygen level of 2-3 parts per million is maintained inside the glove box. The laser head is stationary and the positioning system controls the movement of the substrate. Several examples of LENS manufactured parts are shown in Fig. 2.16.

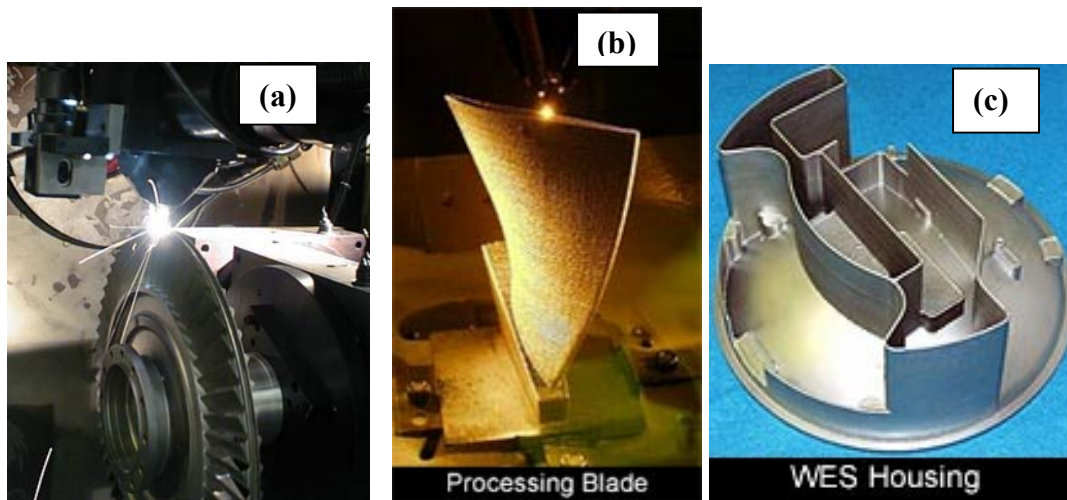


Figure 2.16: LENS manufactured components: (a) turbine (www.optomec.com/html/aerospace-ro.htm); (b) blade processing (www.ca.sandia.gov/content.php?cid=50); (c) housing (www.ca.sandia.gov/content.php?cid=50).

Typical materials used in the LENS process, include: Ti-6-4; Inconel 617, 625, and 718; 15-5PH, 17-4PH, and 420 SS; H13 tool steel, titanium alloy (6Al-4V), and other materials (www.rpmandassociates.com/index_files/Page1557.htm, mfgshop.sandia.gov/1400_ext_LENS.htm). The minimal feature size the process is capable of achieving is around 0.76 mm (0.03 inch) with a typical build rate of 0.5 inch³/hour.

Laser Cladding Process (LCP). LCP was invented by the Huffman Corporation (Wessel, 2004). The process is used in repairing parts. This process extends the working life of the part. Cladding material is applied to the damaged section while the laser bonds the material to the part. The originally invented LCP consisted of a 5-axis controlled machine with a 1...2 kW CO₂ laser. A simplified schematic of the process is shown in Fig. 2.17 (Hu et al., 1998). LCP increases the surface hardness and improves corrosion resistance of the damaged parts (<http://www.lasercladding.com/>). The process provides low heat input and, therefore, low distortion and a minimal area affected by heat in the repaired part due to the rapid solidification

of the bonded deposited and base materials. An advantage of the process is the low dilution (chemical transformation) of the base material. An example of the cladding material (deposit) is a combination of a matrix material and of spherical cast tungsten carbide (<http://www.lasercladding.com/>). The examples of some matrix materials are: 1) Cr-Ni-B-Si self-fluxing alloys (have good welding and wear characteristics); 2) different stainless steels (improve anti-fretting and anti-corrosion properties); 3) stellite (improves anti-galling and anti-corrosion properties); 4) special steels (reduce wear); 5) inconel (reduces stress and control wear due to corrosion). Contemporary LCP machines use 10-axis laser heads with 6-axis coordinates (<http://www.lasercladding.com/>). An example of the LCP process is shown in Fig. 2.17.

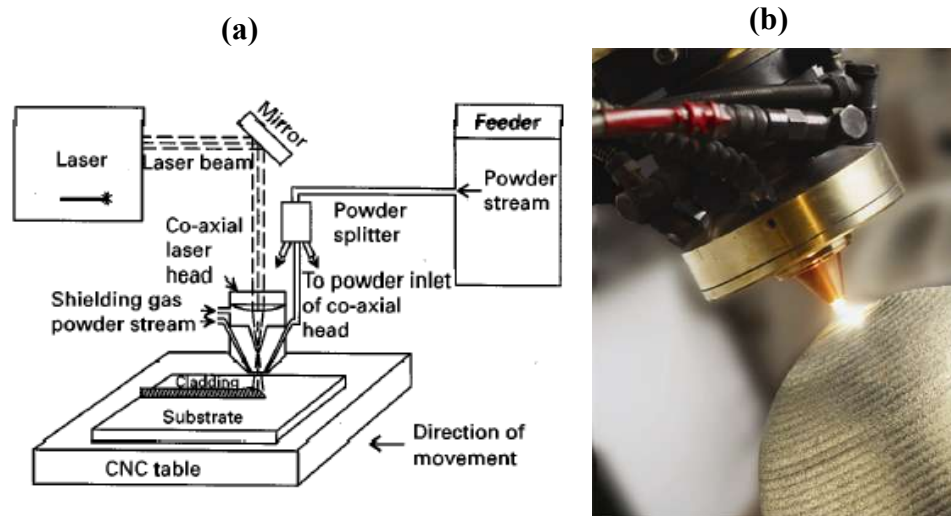


Figure 2.17: Laser cladding process: (a) schematic (Hu et al., 1998); (b) example of a laser cladding process using a 10-axis laser (<http://www.lasercladding.com/>).

LasForm. The Laser Forming (LasForm) process was developed by Penn State University and Aeromet Corporation. This is process similar to some of the previously described laser based prototyping processes. It is based on the “art-to-part” concept, when a part is

fabricated directly from a customer's CAD file using layer-by-layer deposition. The process schematic and LasForm apparatus are shown in Fig. 2.18.

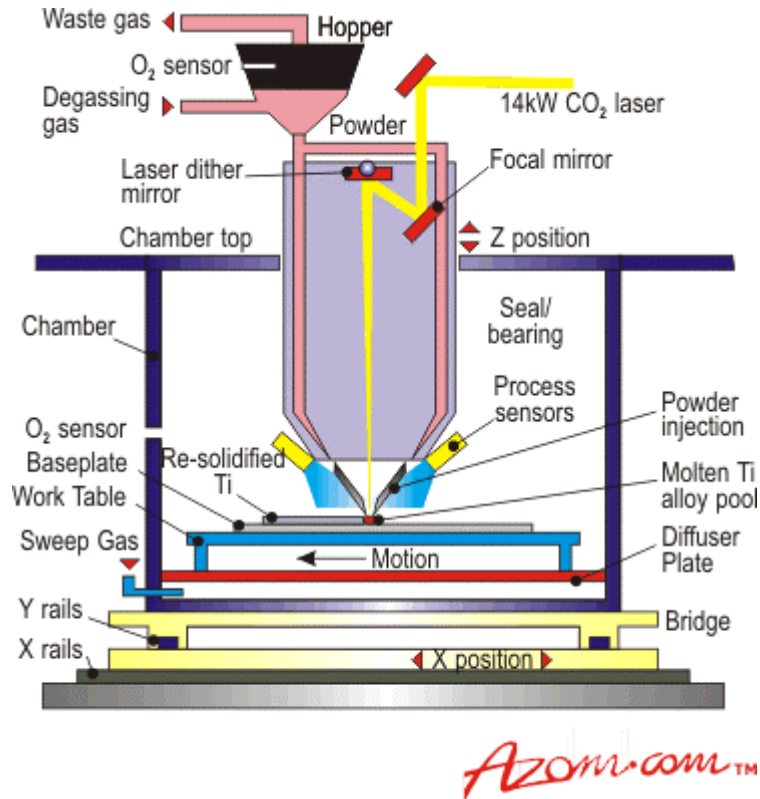


Figure 2.18: An example of a LasForm process (www.azom.com).

The LasForm apparatus is equipped with a high power 14-kW CO₂ laser. The original experimental setup contains a laser head moving in the XYZ directions, while the deposition substrate together with the deposited part is stationary (Wessel, 2004). An alternative LasForm experimental setup, shown in Fig. 2.18 (www.azom.com), has another layout, with the stationary laser head and a CNC driven XYZ-controlled moving deposition substrate. Deposition of the metallic powder onto the substrate takes place inside an inert gas filled chamber, where the oxygen content is maintained at a level below 50 ppm (www.azom.com). The process can produce fully dense high quality parts (Fig. 2.19) that require some post-machining to achieve

the final dimensions of the parts. The LasForm process is restricted to parts with very complex geometry and is limited in the choice of the deposition materials. Ti-6Al-4V powders are the most frequently used deposition materials due to their easy weldability property.



Figure 2.19: *Examples of LasForm manufactured parts (www.azom.com).*

The major differences between the above-described laser-based rapid prototyping processes are given in Table 2.2. It can be seen that the processes differ in the laser types, operating temperatures (melting or sintering), the number of DOF with which the material is deposited onto the deposition substrate, the laser power, existence of support structures and heat sink conditions (heat exchangers, etc.).

Table 2.2: *Differences between the laser-based rapid prototyping processes*

(1) DLF: metallic powder; melting point temperature; part moves in XY directions; laser head moves in Z direction; fine optics based Nd:YAG laser; deposition layer thickness 0.075...0.25mm; porosity.
(2) SLS: polymer-coated metal powder; sintering temperature (lower than metal melting point).
(3) LDC: metallic powder; 6-axis controlled machine; no limitation in building angle; no integral support; 1.5 kW CO ₂ laser; fully dense, porosity free; 15 % powder loss; fine grains.
(4) DMD: metallic powder; melting point temperature; 5-kW CO ₂ laser; post-DMD heat treatment is required.
(5) DMD and RP: metallic powder; 3-axis machine; Nd:YAG laser; part moves in XY directions; laser head moves in Z direction; pre-heated substrate; inert atmosphere; heat transfer and FEM model controlled deposition process.
(6) LENS: metallic powder; melting point temperature; Nd:YAG laser; 3-axis controlled machine; inert atmosphere; part moves in XY; laser head moves in Z direction.
(7) Laser cladding: 5-axis controlled machine; 1...2-kW CO ₂ laser; used in repairing of metallic parts.
(8) LasForm: high power 14-kW CO ₂ laser; different layouts: 1) part is stationary and the laser head moves in XYZ directions; 2) part moves in XYZ directions and the laser head is stationary.

2.2.2 Advantages of laser-based rapid prototyping processes

The common advantages of the 8 laser based prototyping processes are listed below.

These are:

- 1) Most of the processes can produce fully dense, near-net-shape metallic parts without conventional machining, forming, pressing, forging, etc. and without using molds or dies.
- 2) The part design can be easily changed by modifying its CAD model only.

- 3) There is no bulk segregation effect of the deposited material because only a small amount of the material is melted at a time. The segregate is limited to the size of the laser beam focal spot.
- 4) Homogeneity of the material is insured because the laser spot and the melting pool sizes remain constant.
- 5) The input material (metallic powder), that is wasted during the deposition and melting processes, can be recycled after each deposition run, thus minimizing material loss.
- 6) There is almost no contamination of the working space in the laser-based rapid prototyping machines with lubricants or oxides during the rapid prototyping process, in comparison to the level of contamination present during the fabrication process using conventional machining equipment (mills, lathes, etc.). As a consequence, there is no need for chemical cleaning of the working space.
- 7) Some of the laser-based rapid prototyping processes, which produce parts at the melting temperature, require very minimal post-machining.
- 8) Cost and time of parts production, associated with the above-listed advantages, is reduced.
- 9) The product gets to the consumer market faster.

As it can be seen from Table 2.2, the most popular lasers used in the rapid prototyping equipment are CO₂ gas lasers and Nd:YAG solid-state lasers (Ready, 2001). The lasers can work in continuous wave or pulsed wave modes. Increase in the frequency, at which a laser operates, (e.g., up to femto-second level) can improve the quality of the laser processed material. For example, laser drilling of holes in a material decreases the laser-affected zone adjacent to the

hole. This, in its turn, increases the strength of the corresponding material surrounding the hole (decreased material damage) and improves the surface roughness of the hole. Figure 2.20 shows an example of a hole, drilled by a laser in epoxy resin. The insignificant amount of damage, done to the material surrounding the hole, lets us assume that a high frequency laser was used in this process.

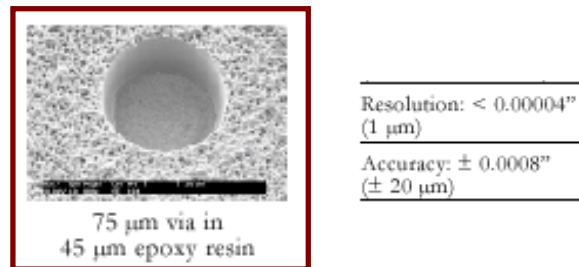


Figure 2.20: *Laser drilling (www.esi.com)(Nd:YAG feedback controlled system).*

A comparison of the performance of some non-laser based conventional machining processes and laser-based rapid prototyping processes, which used Ti-6Al-4V material to fabricate a part, is shown in Table 2.3 (Kobryn et al., 2000), where, for example, the LENS rapid prototyping process (process #6 in Table 2.1) gives a greater strength to the processed material, then the conventional casting process, without any further machining or heat treatment of the material.

Table 2.3: Mechanical properties of Ti-6Al-4V alloy: comparison between some non-laser-conventional and laser-based rapid prototyping processes (Kobryn et al., 2000)

Process	Reference	Condition	Test Direction	UTS (MPa)	YS (MPa)	% Elong.	% R of A
LENS	24	As-deposited	Z	1172	1067	11	N/R
SLS/HIP	36	As-HIP'ed	N/R	1117	N/R	5	N/R
DLF	29	Mill annealed	N/R	1027	958	6.2	N/R
Aeromet	28	N/R	N/R	896-1000	827-896	9-12	18-22
Penn State	ARL-Penn State	Aged	Y	995	850	10.7	23.8
Penn State	ARL-Penn State	Mill annealed	Y	979	848	8.5	14.3
Press and Sinter	28	As-sintered	N/A	945	868	15	25
Cast (typical)	35	Annealed	N/A	1015	890	10	16
Cast (min)	ASTM B367 CS	Annealed	N/A	896	827	6	N/R
Wrought bar (typical)	35	Annealed	N/A	1000	925	16	34
Wrought (Armor, min)	Mil-A-40677	Annealed	N/A	896	827	12	30

Another example, showing the advantages of the laser based rapid prototyping processes versus the conventional manufacturing methods is shown in the micrograph in Fig. 2.21. The micrograph of a sample, manufactured from a Nickel-Aluminum-Bronze material by conventional casting (Fig. 2.21a), shows the existence of larger grains and a less uniform grain structure than those of a sample fabricated by laser-based rapid prototyping from Nickel-Aluminum-Bronze powder (Fig. 2.21b).

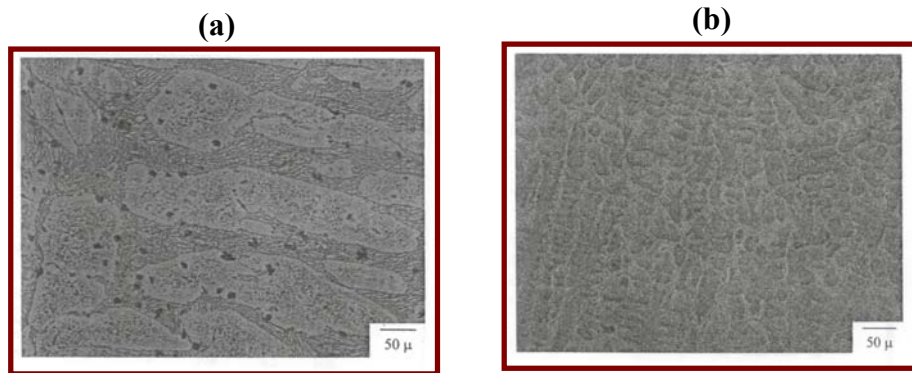


Figure 2.21: Comparison of microstructures of nickel-aluminum-bronze samples, made by: (a) conventional casting and (b) laser-based rapid prototyping (Wessel, 2004).

2.2.3 Drawbacks of laser-based rapid prototyping processes

The common drawbacks of some of the laser-based rapid prototyping processes are low surface finish and accuracy of the processed material in comparison to the material processed by conventional machining methods. Therefore, post-machining is required to achieve the final dimensions of the manufactured parts. Conventional machining processes achieve a surface roughness of $0.5\ \mu\text{m}$, which is relatively higher in comparison, for example, to Selective Laser Sintering (SLS), which gives a $2.6\text{--}6.1\ \mu\text{m}$ roughness (Cooper, 1999).

Another issue, which is to be considered in laser-based rapid prototyping is material defects present in the manufactured parts. Cooper (1999) underlines the most frequently encountered defects: (a) “christmas tree” defect (saw-tooth geometry), (b) warping, (c) delamination and cracking, (d) porosity due to oxidation and gassing of the powder. The examples of these defects are shown in Fig. 2.22.

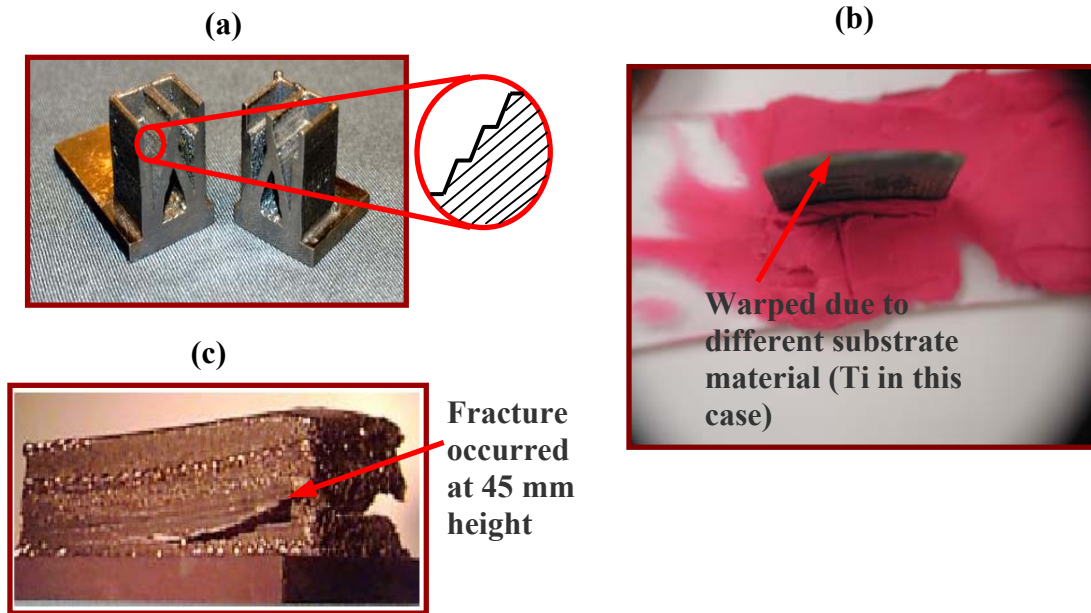


Figure 2.22: Defects in materials processed by laser-based rapid prototyping methods: (a) “Christmas tree” defect in a part with internal cavities made by DMD from tool steel powder (Kovacevic, 2005), (b) warping in a part made by DMD from Shape Memory Alloy (SMA) powder (one of our samples), (c) delamination and cracking defect in a part made by DMD from tool steel powder, part height is 50 mm, number of the deposited layers is 50 (Cooper, 1999).

2.3 Direct metal deposition (DMD) of SMA (NiTi) powders

The laser-based DMD process was chosen in the current research for the fabrication of the mMM from SMA (NiTi) powder. The choice was driven by the availability of the necessary DMD equipment. The two major challenges in the DMD processing of NiTi powder into solid structures were identified as: 1) the achievement of high quality non-porous non-cracked NiTi alloy monolithic parts and 2) the ability of the DMD fabricated and processed NiTi alloy to possess the phase transformation property, namely the shape memory effect, needed for the actuation of the mMM.

The first challenge is the consequence of the NiTi alloy's property of being an intermetallic with a low amount of dislocations in it due to its close-packed crystal structure (martensite phase) that also leads to a low elastic modulus (high brittleness). Therefore, the non-mechanical processing (machining) methods, such as DMD, offer a better alternative in processing NiTi alloys than the conventional machining methods (milling, turning, drilling, etc.)

The second challenge lies in the fact that one of the properties of the conventionally fabricated and processed NiTi alloy is the material's property to undergo the diffusionless phase transformation, as explained in Section 2.1.1. To the best of our knowledge it was not known how this property is altered in the material fabricated by DMD from NiTi powder. The phase transformation property is characterized by the presence of the phase transformation temperatures (TTRs). TTRs are the pre-requisite for an SMA structure to exhibit the SME driven actuation. They also define the proper application (medical, industrial, etc.) for NiTi alloys, which depends on a certain composition of Ni and Ti in them. The TTRs are dependent on the manufacturing method by which the SMA is fabricated and/or processed. Therefore, it is important to understand how the DMD affects the TTRs and how to achieve a certain level of the TTRs in the SMA.

Conventionally, SMAs are made by high frequency induction-, argon arc-, plasma arc- or electron beam-melting (Otsuka and Wayman 1998). Melting is performed several times in sequence to ensure the homogeneity of the manufactured material. Melting is followed by hot/cold working and thermal treatment (annealing and quenching) (Otsuka and Wayman, 1998). Otsuka and Ren (2002), Ren and Otsuka (2000), Otsuka and Ren (1999) classified NiTi alloys using their Ni content as an indicator of their performance range. Using a Landau-type model, they state that the higher the elastic modulus (larger amount of Ni) of the material the lower the

TTR's are. In addition, quenching of NiTi alloys increases point defects, which can be viewed as an equivalent to a compositional change in the NiTi alloy. The compositional change in a material contributes to the change in its elastic modulus – in this case, it increases the elastic modulus of the NiTi alloy. Since the “elastic modulus” is a property of a material that can be treated as an effect caused by a change in the material's “composition”. Both terms (“composition” and “elastic modulus”) are used as synonyms in this study. Hence, quenching lowers the TTRs, since it increases the elastic modulus of the material. For example, a 1 at.% (atomic percent) composition change of Ni content (plus or minus) in a NiTi alloy can result in an approximately 10% change in the elastic modulus (minus or plus accordingly) of the material and a decrease or increase of the TTRs by as much as several tens of degrees.

The other factors that affect the composition of SMAs and, therefore, their Ni content, are the level of impurities and the level of precipitation in the SMA material, fabricated and processed by the laser-based rapid prototyping process. The level of impurities in the material is greatly affected by the high reactivity of Ti with oxygen at high temperature levels (Otsuka and Wayman, 1998), which are present during the melting process of NiTi. The precipitates (additional stable phases such as NiTi₂ and Ni₃Ti according to the NiTi phase diagram) affect not only the composition of the NiTi alloy, but also its SME property. Their presence alters the alloy composition, and therefore influences the TTRs. Bram et al. (2002) believe that metastable precipitates Ni₄Ti₃ (ultimately transforming into Ni₃Ti precipitates) mediate martensite phase transformation. This conclusion came from the fact that the authors did not achieve any TTRs, according to their Differential Scanning Calorimetry measurements, in solid-solution treated NiTi samples, but the TTRs were achieved in precipitation-hardened NiTi samples. In this case, solid solution treatment was used to achieve better homogeneity of the material. Finally, it

appeared that with an increase of Ni content in the NiTi (50at.%-50at.%) alloy, the martensite phase transformation TTRs decrease almost linearly. This characteristic allows the use of NiTi alloys in medical, biological and other applications that require very low actuation temperatures (TTRs).

Bram et al. (2002) used Metal Injection Molding (MIM) and Hot Isostatic Pressing (HIP) to fabricate their NiTi samples from NiTi powder. They explored the possibility of achieving SMA properties in the manufactured samples, namely, the ability to undergo the phase transformation. The level of homogeneity of the material was not high enough, which can be seen from their DSC thermograms, where the TTR peaks were not smooth and pronounced. The possible reasons for having non-smooth peaks are contamination and the initial level of homogeneity of the starting powders (Ni and Ti). Another RP technique for producing NiTi SMA by means of a thermal explosion mode of combustion synthesis was tested by Yi and Moore (1988). In their case, the impurities present in the fabricated material due to the combustion reactions significantly increased the brittleness of the NiTi SMA.

As a consequence of the above reasons, it was decided to use a novel manufacturing technique – laser based Direct Metal Deposition (DMD) - to process NiTi powder in the current work. DMD alleviates the material contamination problems, present during processing by MIM, HIP, and combustion synthesis. According to the research done by Kovacevic et al. (2005), DMD allows the creation of monolithic jointless metallic structures from metallic powders. Another advantage of the DMD technologies lies in their ability to batch produce parts leading to a decrease in the cost of the manufactured devices. Batch production requires minimal post-machining of the DMD fabricated parts: milling, grinding, drilling, etc., in comparison to the conventional manufacturing processes. A technique similar to the DMD, as pointed out earlier, is

Laser Engineered Net Shaping (LENS). The DMD and LENS processes allow the creation of fully dense metallic structures from computer aided design (CAD) solid models (Griffith et al., 1996; Lewis and Schlienger, 2000; Mazumder et al., 1999). The DMD process is aimed at processing metallic powders, while LENS can process non-metallic components as well. It should, however, be noted that the influence of DMD processing of NiTi powder on the final material quality was not explored so far.

One of the major goals of the present research is to study how the DMD process can be modified in order to fabricate high quality NiTi parts from pre-alloyed NiTi powder. A subsequent heat treatment procedure (annealing and quenching) to impose the SME on the fabricated parts needs to be established as well. The physical properties, characterizing the SME in the part and the quality of the material must also be investigated. A subsidiary objective of this work is the achievement of a specific set of TTRs - to be close to room temperature as explained before. The preferred values of the TTRs are: the finish temperature of the martensite phase transformation at about 9 °C, the start temperature of the martensite phase transformation at about 18 °C, the start temperature of the austenite phase transformation (reverse martensite phase transformation) at about 34 °C, and the finish temperature of the austenite phase transformation at about 49 °C.

CHAPTER 3

3. Manufacture of SMA material

Since the goal of this work is to fabricate the mMMs by the DMD process from SMA powders, it is necessary to identify the optimal set of DMD process parameters to build high quality structures that are non-porous, non-cracked and have low amounts of contaminations. It is also important to understand how the DMD process affects the SME properties of SMAs, since mMMs are devices driven by the SME.

The primary goal of the current chapter is to present a systematic experimental study aimed at identifying suitable DMD process parameters. The DMD parameters will be identified for manufacturing bulk- and thin-wall structures from NiTi powder. The identified DMD parameters will be further applied for the fabrication of the mMM prototype.

3.1 DMD experimental apparatus

A DMD machine, equipped with an Nd:YAG laser and a feedback control system, was used (courtesy of Prof. Dr. R. Kovacevic at Southern Methodist University (SMU), RCAM laboratory). The experimental DMD setup is shown in Fig. 3.1.

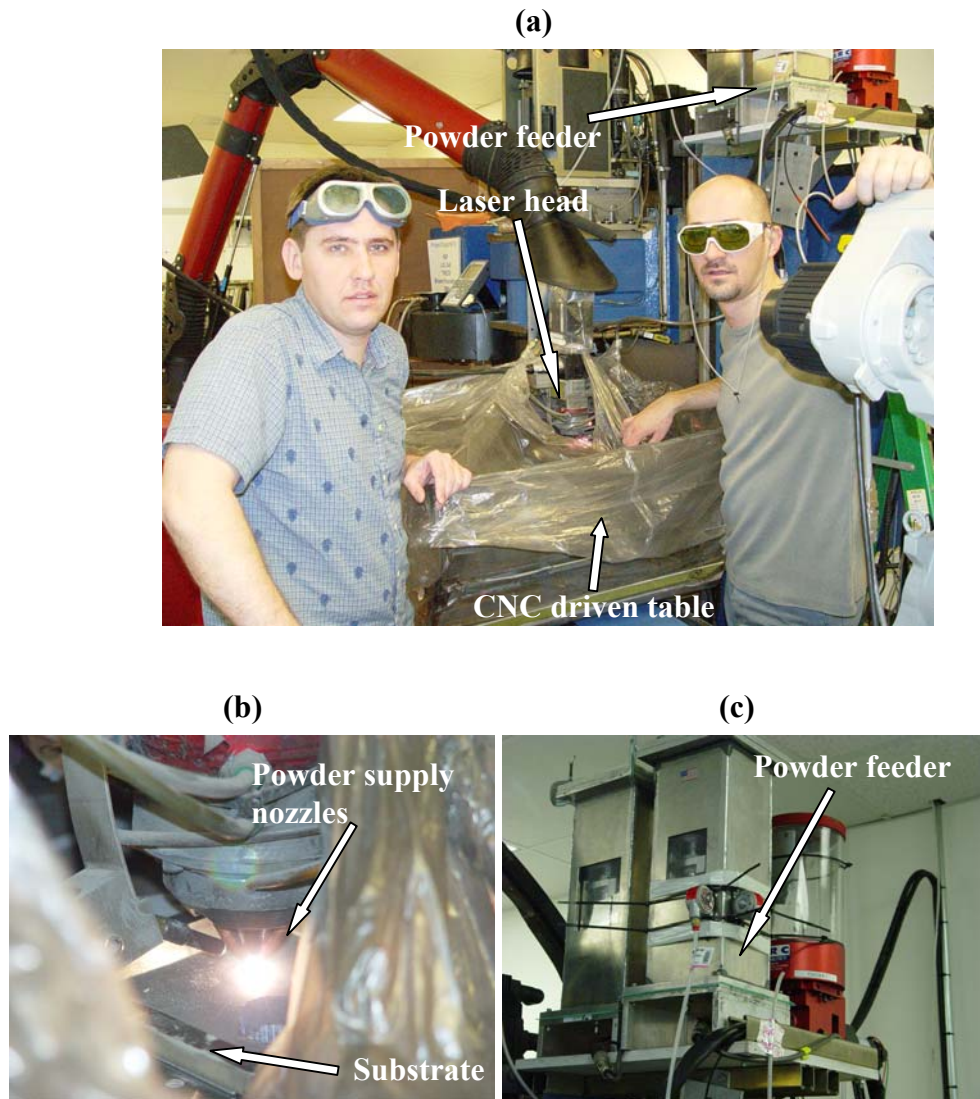


Figure 3.1: DMD: (a) experimental setup (courtesy of Dr. R. Kovacevic at SMU/RCAM), (b) laser head, (c) powder feeder.

The DMD apparatus (Fig. 3.1a) consists of a laser head, a powder supply system, 3-axis CNC driven table and an argon protective atmosphere delivery system.

The powder supply system consists of a powder feeder (Fig. 3.1c), located at the top of the DMD apparatus, 4 powder supply nozzles (Fig. 3.1b) and an Ar delivery manifold. The

powder feeder is equipped with a mechanical shaker that is used to enhance powder supply rate. The feeder is connected to the powder supply nozzles through the Ar delivery manifold. The powder in the feeder is supplied to the manifold under its weight and with the help of the shaker. Further, it is delivered to the deposition substrate by the Ar flow through the nozzles.

The laser head is attached to the supply nozzles such that the powder is melted as soon as it reaches the substrate. The argon protective atmosphere delivery system creates an Ar shield around the deposited and melted powder to prevent oxidation and contamination of the solidified melt. Ti is known for its high affinity to oxygen, therefore, it is important to create a proper shielding environment during the deposition and melting process of the NiTi powder and the further solidification of the melt.

3.2 DMD fabrication of SMA bulk structures

Preliminary experiments have been conducted to assess the feasibility of using the DMD process in the fabrication of bulk structures. Six cylindrical objects were DMD fabricated from a pre-alloyed UDIMET NITINOL (NiTi) powder. According to the powder manufacturer specification, the NiTi powder contained 55.5-56wt.% of Ni and balance Ti. The particle size was in the range of 10-180 μm .

The fabricated cylinders were 25.4 mm in diameter and 2.54 mm in height. Five out of the six NiTi samples were deposited on a horizontal Ti substrate (Fig. 3.2a) at laser power levels ranging between 300 - 600 W. Due to the difference in the thermal expansion coefficients of the solidified NiTi melt (deposit) and Ti substrate, the samples debonded from the Ti substrate at the

end of the deposition process. No melting pool in the Ti substrate was formed. The sixth NiTi sample (Fig. 3.2b) was deposited on one of the five previously manufactured NiTi samples (similar to the one shown in Fig. 3.2a) using it as the substrate (instead of the Ti substrate) at a laser power level of 250 W. Consequently, no debonding occurred in this case. The advantage of using the pure Ti substrate (in addition to Ar as the shielding gas), is that it insures a minimal oxygen contamination of the deposited NiTi, since the oxygen is absorbed by the Ti substrate, rather than by the NiTi melt (Otsuka, and Wayman, 1998).

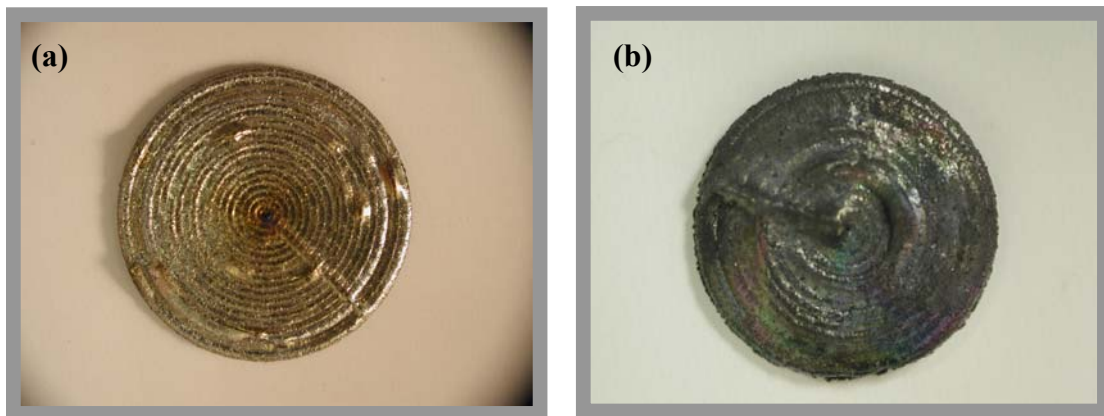


Figure 3.2: *NiTi samples, fabricated by DMD: (a) on Ti substrate, (b) on NiTi substrate.*

The DMD process parameters for the fabrication of bulk structures were identified during several experimental DMD runs (Table 3.1). The identified parameters have allowed the fabrication of apparently solid non-porous samples from NiTi powders by the DMD process. A detailed analysis of the quality of the fabricated material will be given later.

Table 3.1: *Experimental parameters for DMD fabrication of SMA bulk structures*

Laser power	250W - 600W for different samples
Beam spot size	Not more than 1 mm
Traverse speed (scan speed)	10.16 mm/s
Z-incremental (layer thickness)	0.381 mm
Shielding gas	Ar, at 17.5 l/min
Carrier gas	Ar, @ ΔP (pressure difference) of 13.7895 kPa
Flow rate of powder (set point)	6.7 g/min
Number of layers	20 layers \times 0.381 mm, or 12 layers \times 0.635 mm

3.3 DMD fabrication of SMA thin wall-structures

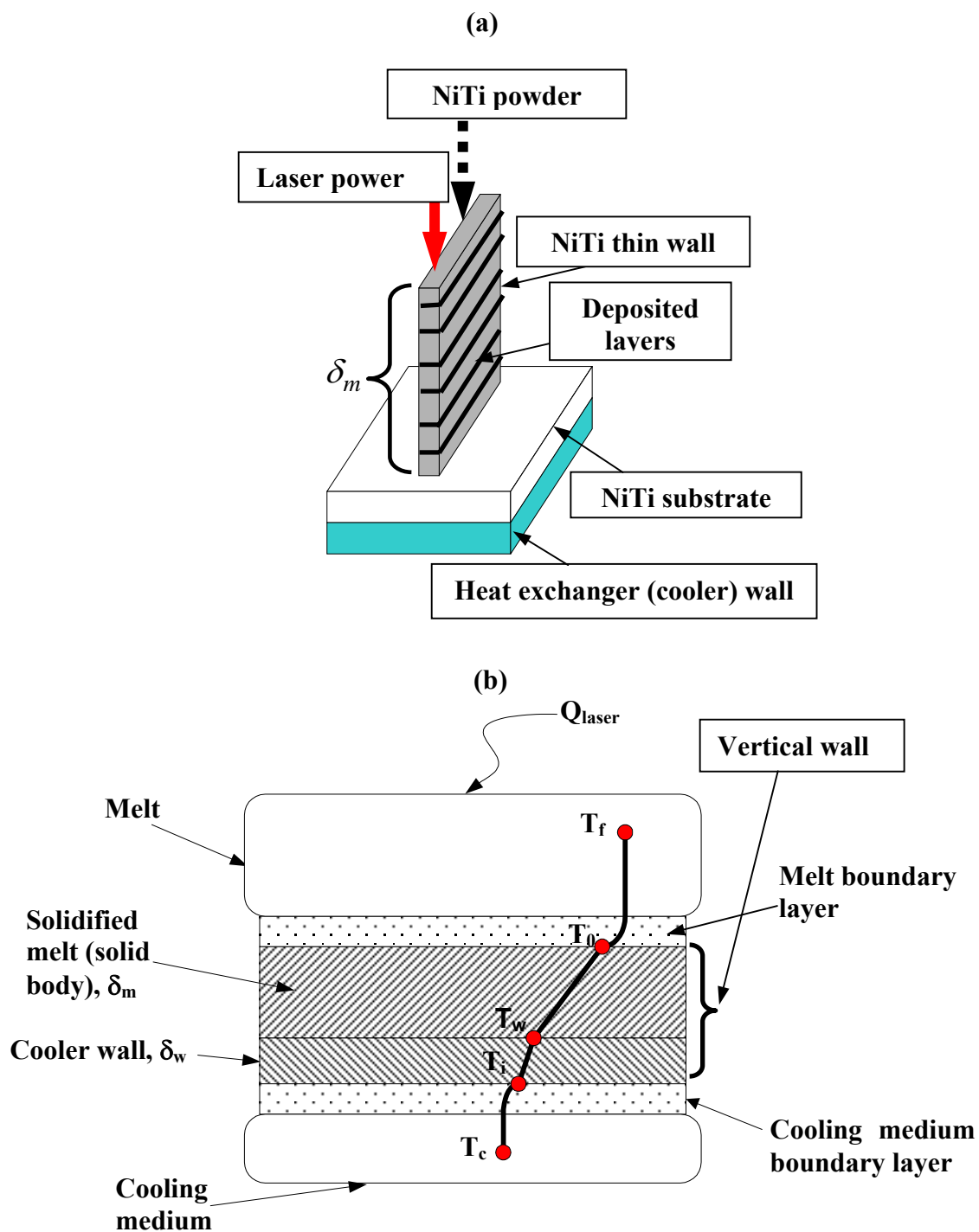
The mMM represents a component that consists of both bulk- and thin-wall sections. The goal of this part of the study is to identify DMD process parameters for the fabrication of thin wall structures from SMA powder. The DMD parameters previously identified for fabrication of the bulk structures are not suitable for thin-wall structures, as it will be shown later. The major problem is that during the DMD process, the heat transfer conditions in thin wall structures are worse than in bulk structures. This occurs due to the fact that NiTi has a relatively high heat capacitance and low heat conductance values resulting in excessive heat accumulation in the

material (as opposed to, for example, tool steel). To remove the extra amount of the accumulated heat in a thin-wall structure, an additional heat sink needs to be used.

3.3.1 Heat transfer

Since DMD is a thermal process, it is advantageous to investigate the effect of heat transfer on the quality of thin-wall structures (Fig. 3.3 a) to properly identify the DMD process parameters. In this research study a thin-wall structure is defined as a structure that has an aspect ratio (width/thickness) in the range of 6 to 10. The heat transfer diagram in DMD fabricated thin-walls is schematically shown in Fig. 3.3.

The heat transfer during the DMD process is composed of convective, conductive and radiation heat transfer. Only convective and conductive heat transfer will be considered in this study, since the surface area of the mMM is relatively small and the radiation heat transfer is therefore much smaller than the heat transfer due to the convection and conduction. The diagram in Fig. 3.3b describes the heat transfer during the melting of the deposited powder during the DMD process. Raw powder is delivered onto the substrate, melted by the heat flux \dot{Q}_{laser} and solidified. The substrate can be cooled by a flat heat exchanger (copper cold plate). The maximal achievable thickness of the solidified melt defines the height of the wall (or “limiting layer thickness” according to Van’t Land (2005), beyond which the melt does not solidify and stays in the molten condition. This occurs because the higher the deposited wall the larger the amount of heat accumulates in the wall and the heat sink conditions become worse. After the solidification of the newly molten material, the heat is removed from the structure mainly by heat conductance.



According to the heat transfer schematics in Fig. 3.3b and the corresponding stationary heat balance equations, a so-called limiting layer thickness δ_m (or maximal achievable height of the wall) can be defined as follows (Van't Land, 2005):

$$\delta_m = \frac{\lambda_s}{\alpha_0} \cdot \frac{(T_0 - T_c)}{(T_f - T_0)} - \lambda_s \left(\frac{1}{\alpha_c} + \frac{\delta_w}{\lambda_w} \right) \quad (3.1)$$

where:

λ_s - coefficient of thermal conductivity in the solidified melt, W/(m·°C);

λ_w - coefficient of thermal conductivity in the cooler wall, W/(m·°C);

α_0 - convective heat transfer coefficient between the solidified melt and melt, W/(m²·°C);

α_c - convective heat transfer coefficient between the heat exchanger wall and the cooling medium, W/(m²·°C);

T_0 - melting point temperature, °C;

T_f - temperature of melt, °C;

T_c - coolant temperature, °C;

δ_w - thickness of the cooler/substrate wall, °C.

A sample set of variables, used in equation (3.1) for the calculation of the limiting layer thickness, is given in Table 3.2. They were chosen according to: 1) the specified geometry of the mMM, 2) geometry of the DMD setup, 3) magnitude of the heat flux computed from the

magnitude of the laser power supplied by the DMD setup, 4) the NiTi powder's physical properties and 5) the heat sink conditions during the DMD process. The parameters for the heat sink conditions present during the melting process of metallic powders, such as α_0 and T_f are difficult to identify due to the lack of deterministic correlations and experimental data, especially for melting processes of NiTi powders. For example, experimental studies done by Shestakov and Shichkov (1984) show that α_0 for molten lead is about $500 \text{ W}/(\text{m}^2 \cdot ^\circ\text{C})$ and for steel is about $2500 \text{ W}/(\text{m}^2 \cdot ^\circ\text{C})$.

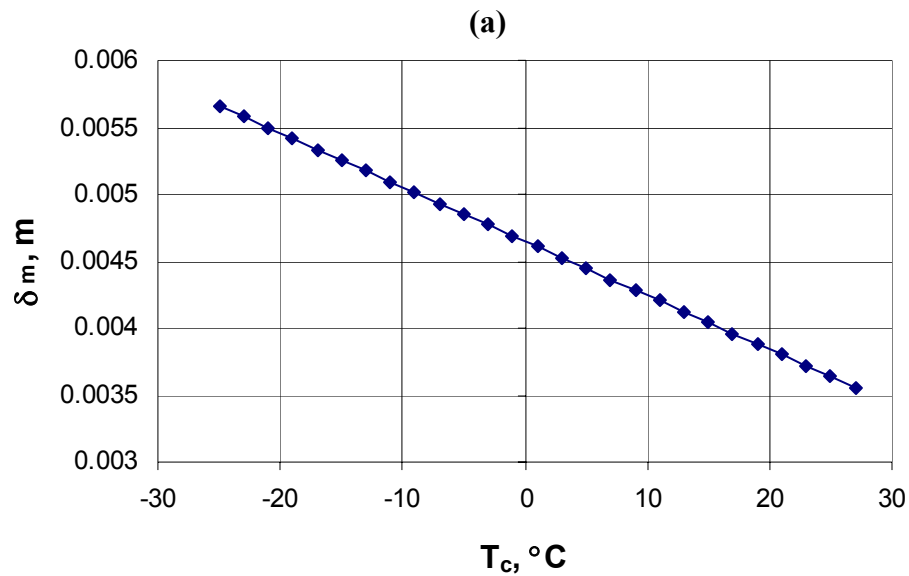
In this study, α_0 and T_m were estimated (Table 3.1) based on the available literature (Shestakov, and Shichkov, 1984; Labudovic et al., 2003), and the mMM's geometry. Therefore, the maximal achievable height of the thin wall can be computed as $\delta_m = 12 \text{ mm}$ from Eq. (3.1).

Due to the ambiguity in the determination of α_0 , it is important to estimate its effect on the magnitude of δ_m , to account for possible errors in α_0 .

Table 3.2: DMD heat transfer parameters

$\lambda_s, \text{ W}/(\text{m} \cdot ^\circ\text{C})$	18	$T_0, ^\circ\text{C}$	1310
$\lambda_w, \text{ W}/(\text{m} \cdot ^\circ\text{C})$	295	$T_m, ^\circ\text{C}$	2300
$\alpha_0, \text{ W}/(\text{m}^2 \cdot ^\circ\text{C})$	450	$\delta_w, \text{ m}$	0.0025
$\alpha_c, \text{ W}/(\text{m}^2 \cdot ^\circ\text{C})$	450		

The influence of some of the heat transfer parameters (Table 3.2) on the height δ_m can be identified from Eq. (3.1) as well. For example, the effect of the coolant temperature T_c , thickness of the wall of the heat exchanger/substrate δ_w , and of the convective heat transfer coefficient α_0 between the melt and solidified melt on the magnitude of δ_m is shown in Fig. 3.4 a, b and c. By changing all three of the above-mentioned values within their possible physical limits, it is possible to identify the parameter that has the largest influence on the magnitude of δ_m .



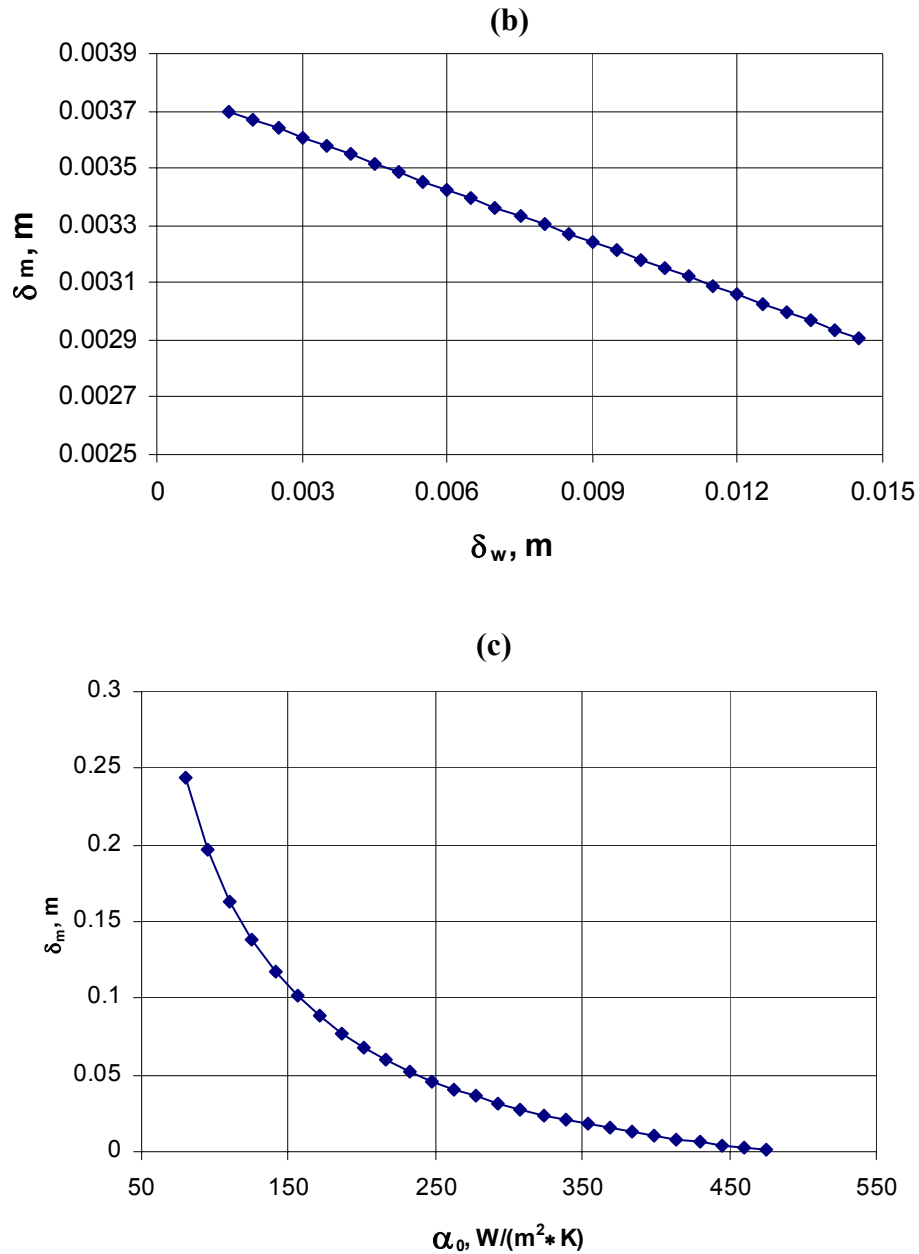


Figure 3.4: Dependence of the δ_m magnitude on: (a) coolant temperature, (b) heat exchanger wall thickness and (c) heat transfer coefficient between melt and solidified melt

The analysis of the results presented in the plots in Fig. 3.4 shows that δ_m is most sensitive to the value of α_0 (Fig. 3.4c), rather than to the values of T_c and δ_w (Fig. 3.4 a and

b). For instance, the change of coolant temperature T_c from +25 °C down to -25 °C changes δ_m from 3.5 mm up to 5.5 mm respectively, while the other variables in Equation (3.1) were kept constant. Similarly, a decrease of substrate thickness (heat exchanger wall thickness) from 15 mm to 1.5 mm, increases δ_m from 2.9 mm to 3.7 mm. Meanwhile, a decrease in the heat transfer coefficient α_0 from 470 W/(m²°C) to 70 W/(m²°C) increases δ_m from 1mm to 250 mm. Therefore, the magnitude of the heat transfer coefficient α_0 plays a major role in the determination of the magnitude of δ_m . The lower the value of α_0 , the higher δ_m , such that the maximal possible height of the thin wall can be achieved at the minimal possible magnitude of α_0 . It can be concluded that, α_0 is the key parameter in controlling the height of thin-wall structures built by DMD.

It is known, that α_0 is difficult to measure and control since the heat flux, \dot{Q}_{laser} , created by the laser power and delivered to the raw powder, has to be always at a level high enough to maintain the melting process of the powder. Melting is one of the parameters that insures that the molten material will be continuous (e.g., no voids) after its solidification. Effective heat removal from the melt and from the solidified structure insures that the structure will be flawless (e.g., non-porous and non-cracked). Since melting and solidification occur at a much faster rate than heat transfer does (Labudovic et al., 2003), it is advantageous to increase the heat removal rate from the already molten and solidified structure, for example, by placing a flat heat exchanger underneath the deposition substrate. The heat exchanger will also allow a better and more accurate control of the geometry and of the quality of the DMD built structures by effectively controlling the heat sink conditions. The effect of heat sink conditions on the geometry of thin

wall structures (height, width, thickness) built by DMD from SMA powders will be experimentally explored further.

3.3.2 Factorial design of experiments

The purpose of this study is to find out the parameters of the DMD process aimed at the fabrication of thin-wall structures from SMA powder and to study the effect of heat sink conditions on the structure's geometry and quality.

A 2^3 factorial design and statistical estimates of experiments was conducted (according to Montgomery, 2001). Laser power (A), coolant flow rate (B) through the heat exchanger and powder flow rate (C) were chosen as the three factors/variables, whose values were varied between their maximal and minimal levels. Laser power had two levels of 250 W (min) and 350 W (max), coolant flow rate was 378.54 l/h (min) and 757.08 l/h (min) and powder flow rate was 8 l/h (min) and 17.5 l/h (max). The experimental parameters are given in Table 3.3. The coolant flow rate through the heat exchanger was chosen such, that the maximal wall height (limiting layer thickness), δ_m , calculated in Section 3.3.1, would approach 12 mm.

Sixteen (16) vertical walls were built by DMD from SMA powder on a 3 mm thick NiTi substrate. Each wall was built using a particular set of DMD parameters varied according to the standard order - column #1 in Table 3.2. Two separate DMD runs (two batches) were manufactured and 8 walls in each run were deposited. They are shown in Fig. 3.5.

The geometry of each wall was measured as shown in the optical microscope micrographs depicted in Fig. 3.6. The width of each wall of the 16 walls was measured in 5 to 7

cross-sections (Fig. 3.6a), starting from the bottom of the wall (at the substrate) up to its top, thus showing how the width varies with the wall's height. The wall's height was measured at its maximum (Fig. 3.6a).

The thickness of the wall was measured at several points (Fig. 3.6b). Since each wall had small spherical build-ups at its ends (top view, Fig. 3.6b), the diameters of the spheres were measured as well (Fig. 3.6b). Finally, Fig. 3.6c shows that the distribution of heights along the wall length at different locations was estimated, by taking measurements at 5 to 7 cross-sections. The other 15 walls with their measured geometries are shown in Appendix A.

Table 3.3: Factorial design experimental parameters

Standard order	Coolant flow rate, l/h	Laser power, W	Powder flow rate, l/min
1	378.54 (-)	250 (-)	8 (-)
2	757.08 (+)	250 (-)	8 (-)
3	378.54 (-)	350 (+)	8 (-)
4	757.08 (+)	350 (+)	8 (-)
5	378.54 (-)	250 (-)	17.5 (+)
6	757.08 (+)	250 (-)	17.5 (+)
7	378.54 (-)	350 (+)	17.5 (+)
8	757.08 (+)	350 (+)	17.5 (+)

For example, the maximal height of the wall shown in Fig. 3.6a is 10.86 mm. It can also be noticed that the width of the wall changes along its height: the width near the substrate (bottom

width) is smaller than the width at the top of the wall (top width) - 2.29 mm versus 2.56 mm.

This is the consequence of the heat removal during the heat transfer process from the top part of the wall to the bottom part of the wall (surface of the substrate). Heat removal deteriorates significantly as the height of the wall increases during the deposition, melting and solidification process. This is why the thin wall structure becomes tapered along its height or, in other words, the thickness of the wall increases with increase of the wall's height.

The thickness of the wall does not change noticeably along the length of the wall during the DMD process (Fig. 3.6b). It was measured to be 2.15 mm, although, it becomes thinner at the very corners (around 1.74 mm) in the top part of the wall, forming a neck between the corner (spherical build-up) and the rest of the wall.

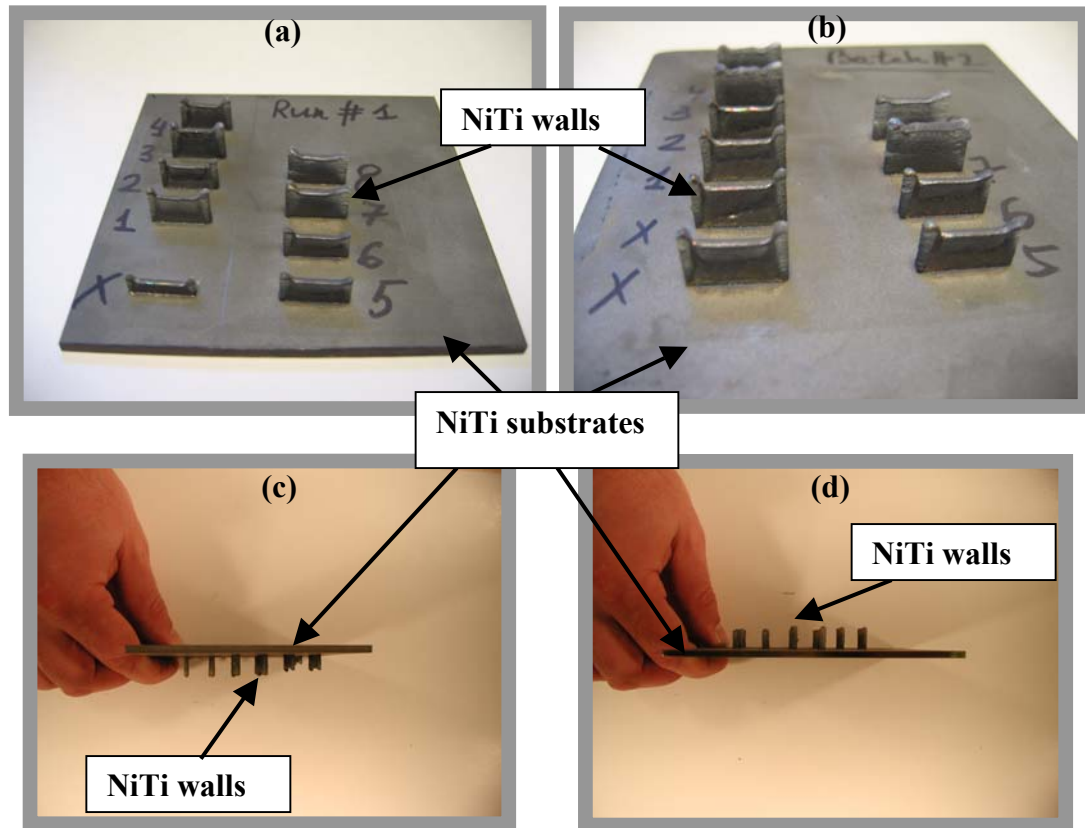
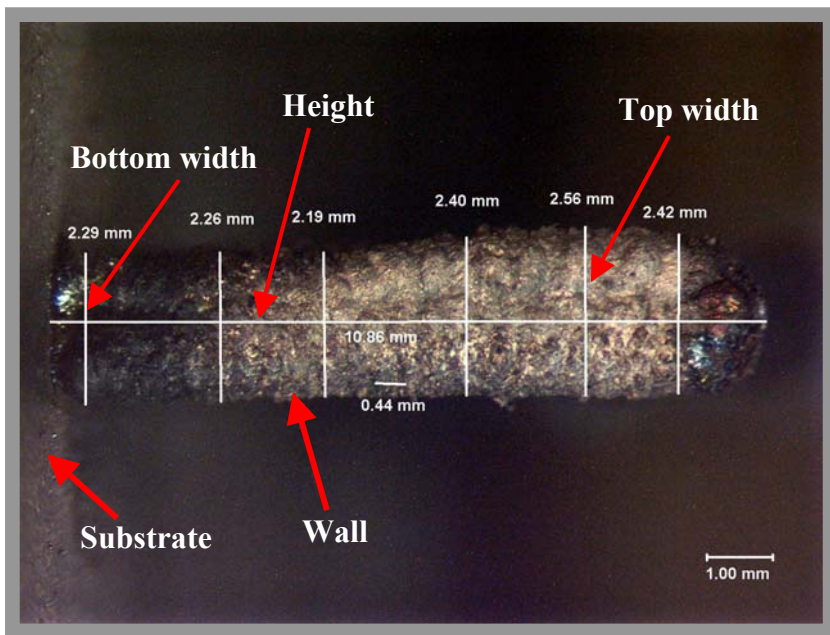


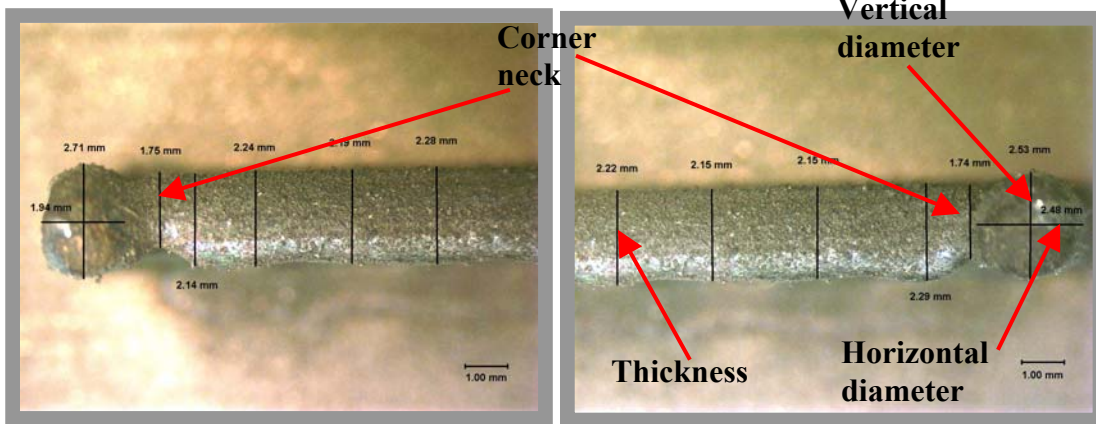
Figure 3.5: Vertical walls fabricated by DMD from NiTi powder on NiTi substrate: (a) batch #1, (b) batch #2, (c) side view of (a), (d) side view of (b)

Figure 3.6c shows that at the corners of each wall the amount of material is larger than between the corners. This occurs due to the fact that the laser head stops at the wall corners during the deposition process each time the direction of the deposition is reversed. Therefore, spherical build-ups were formed (Fig. 3.6b). Both, the horizontal and vertical diameters of the spheres were measured and for the current wall they were equal to 2.48 mm and 2.53 mm respectively (Fig. 3.6c).

(a)



(b)



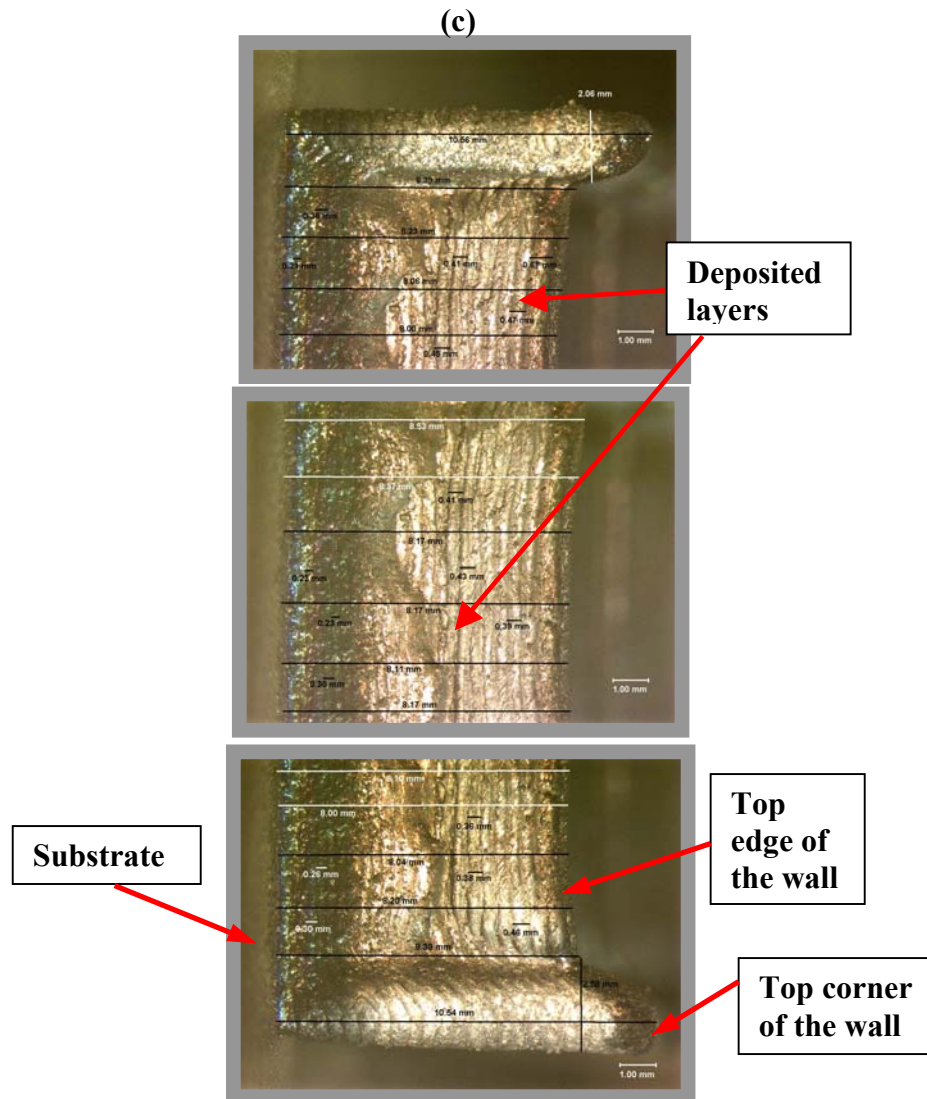


Figure 3.6: Optical microscope micrographs of one of the 16 DMD NiTi walls: (a) left view, (b) top view, right- and left-hand side, (c) front view.

It can also be noticed that the height (thickness) of each deposition layer gradually increases from the bottom of the wall up to its top – from 0.21 mm up to 0.61 mm. This effect can also be attributed to the fact that heat sink conditions become worse when approaching the top of the thin-wall structure during the deposition process.

Figure 3.6c clearly shows the boundaries of the deposition layers formed during the DMD process. It is advantageous to estimate the homogeneity or bonding between the layers of

the deposited material in a wall and between the wall itself (or its first deposited layer) and its deposition substrate. All of the 16 walls were separated from each other and cross-sectioned along their lengths into two identical halves by wire-EDM (without detaching them from the NiTi substrate) (Fig. 3.7). Finally, 32 separate wall halves, each attached to its separate piece of the substrate, were obtained. Afterwards, one of the wall halves (with a piece of the substrate attached to it) was ground and polished on the side, where the wire-EDM cut took place. The SEM micrographs of the non-polished and polished wall halves are shown in Figures 3.8 and 3.9 respectively.

The optical (Fig. 3.7b) and the SEM micrographs (Fig. 3.8a) of the non-polished wall show that there is no visible indication of the boundaries between the adjacent deposition layers from the DMD process, meaning that the bonding (or degree of homogeneity) between the layers is excellent. This suggests that the mechanical properties of the DMD processed NiTi alloy are non-significantly affected by the fact that the thin wall structure was built by the layer-by-layer deposition process. Moreover, Fig. 3.8c shows no visible indication of bonding between the deposited NiTi wall and its NiTi substrate. Figure 3.9 shows the optical and SEM micrographs of the polished wall (Fig. 3.8). It is seen from Fig. 3.9 that there are no apparent cracks in the material. The apparent porosity of the material was estimated by taking the actual area of all the visible pores and dividing it by the area of the SEM image window (Fig. 3.9). The porosity constituted 3.92 % (based on Fig. 3.9 b). The average pore size was approximately 10 μm .

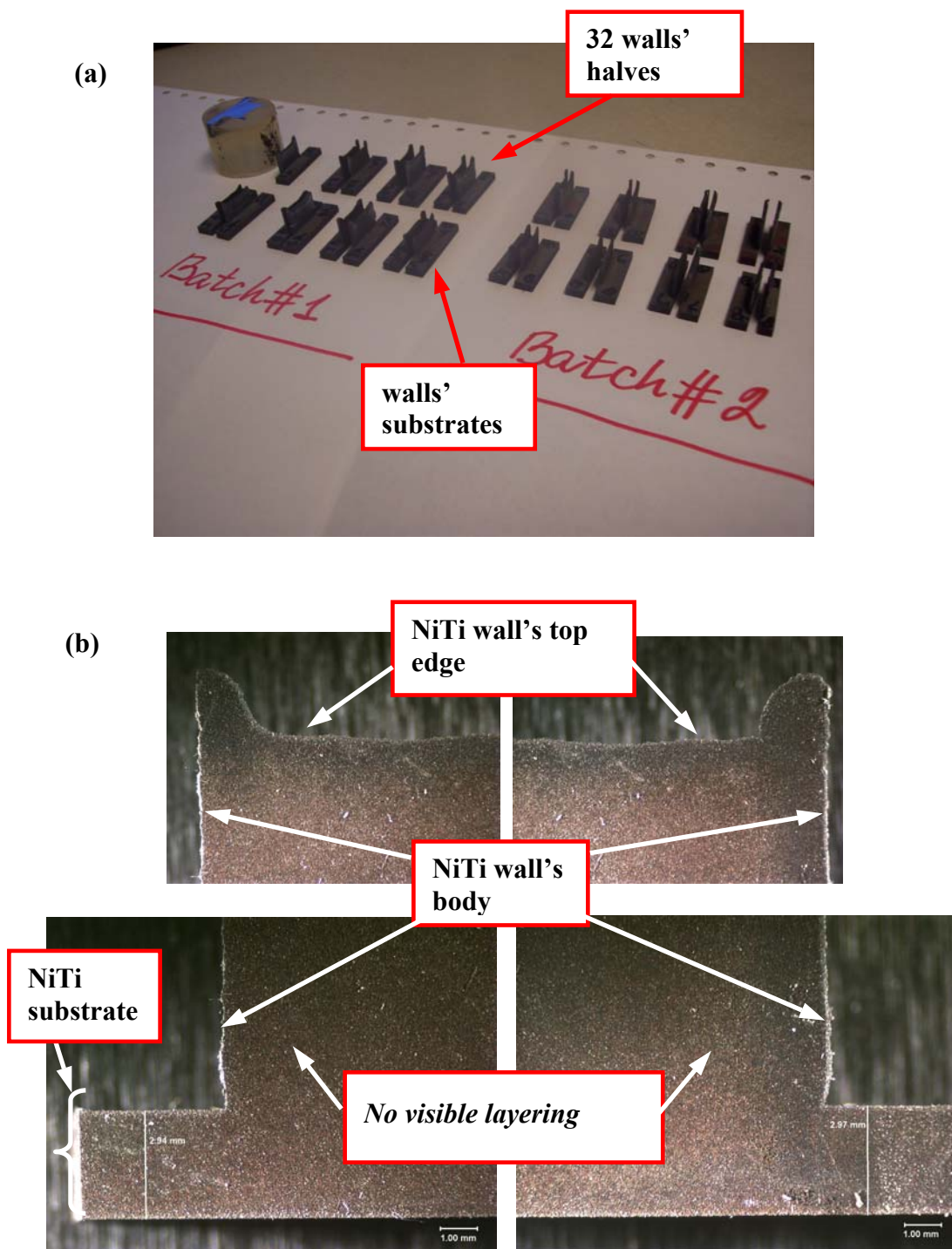


Figure 3.7: Wall halves: (a) digital camera image of the 32 wall halves on their substrates after wire-EDM, (b) optical micrograph of the wire-EDMed cross-section of one half of the non-polished wall #1 from batch #1 on its substrate

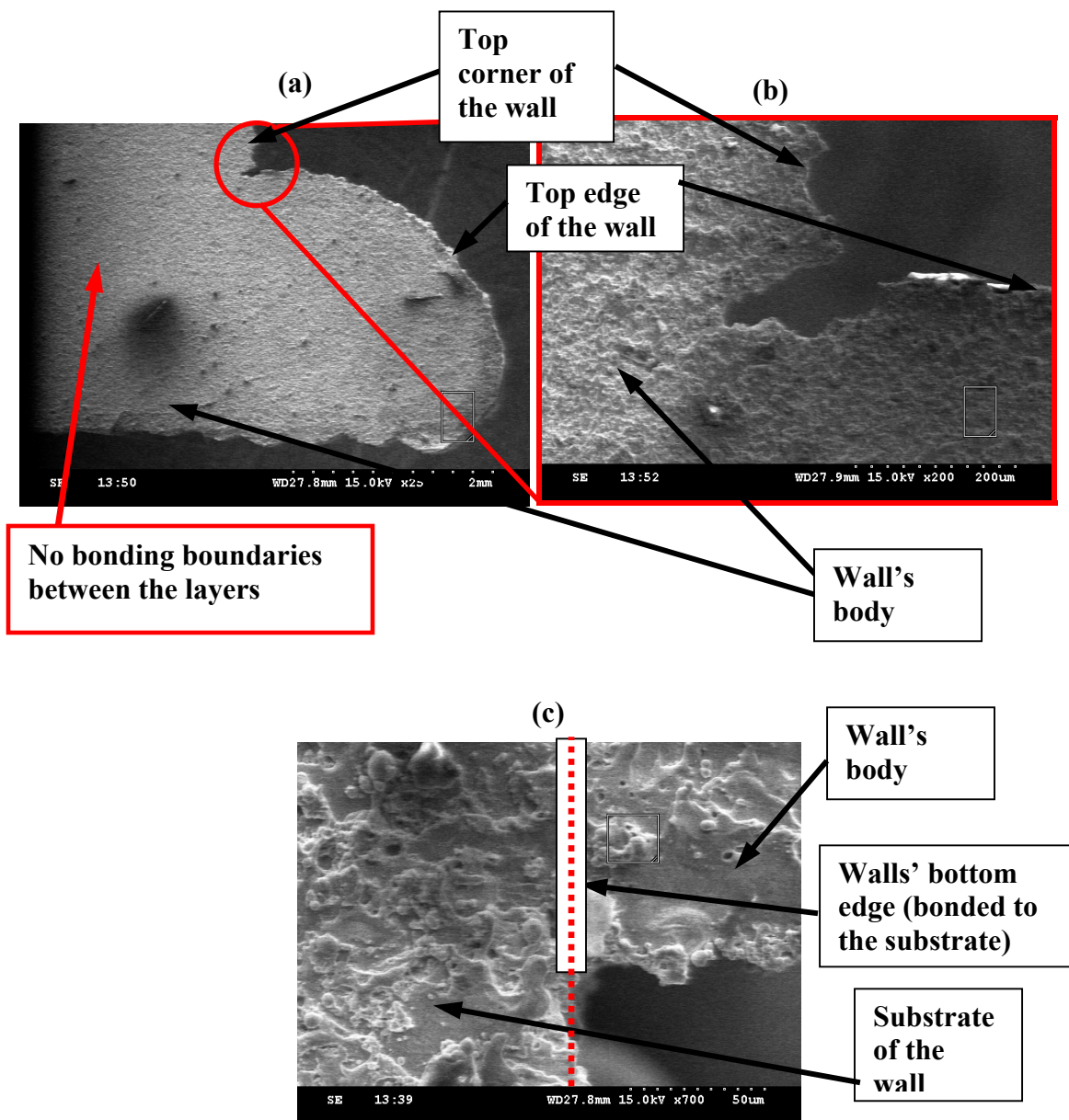


Figure 3.8: SEM micrograph of a non-polished, wire-EDMed wall's half: (a) wall's top edge area after wire-EDM, (b) zoom of (a), (c) wall body on its NiTi substrate.

Since during the grinding and polishing, a substantial part of the material was removed, the layers' boundaries, visible on the outside surface, not machined by wire-EDM of the wall

(Fig. 3.6 c), became visible after polishing on the inside, machined surface (wire-EDMed cross-section) of the wall (Fig. 3.9 a).

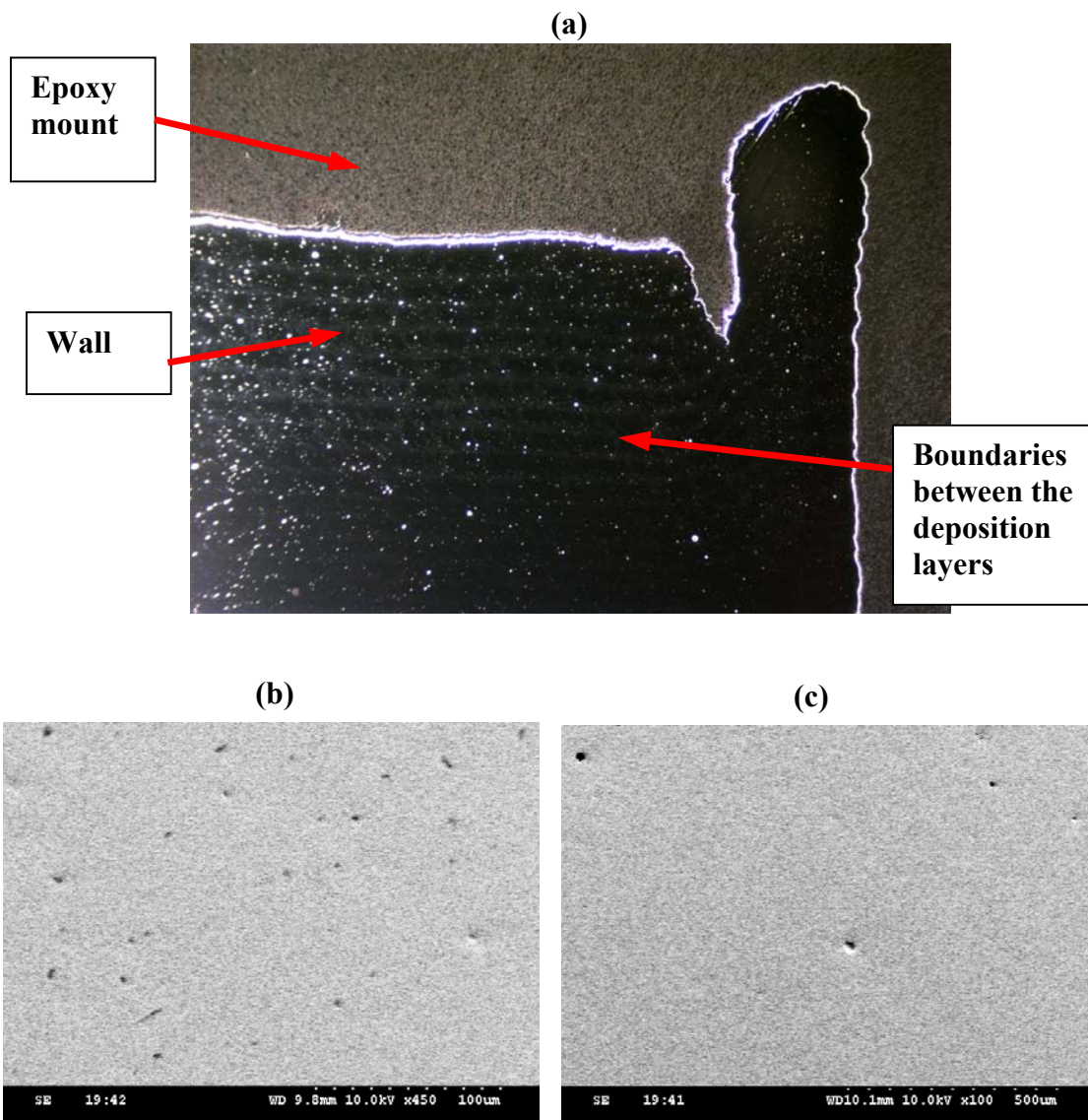


Figure 3.9: Polished, wire-EDMed wall half: (a) optical micrograph, (b) SEM micrograph at magnification = 450, (c) SEM micrograph at magnification = 100.

Another geometrical parameter – wall roughness – was measured using a mechanical stylus profilometer ("Surftest-211", Mitutoyo) and an optical profilometer ("MicroXAM", ADE

Phase Shift). The mechanical stylus profilometer was used to measure the roughness of each wall from one of its sides only, i.e., only 16 wall halves were measured. Data from the mechanical stylus profilometer measurements are given in Table 3.4, where the roughness, R_a , of the deposits varies from 10 to 21 μm .

Table 3.4: *Wall roughness measured by the mechanical stylus profilometer*

Wall #	Wall Roughness, R_a, μm. Batch #1	Wall Roughness, R_a, μm. Batch #2
1	10.342	14.986
2	10.714	16
3	16.872	16.356
4	17.232	15.528
5	13.056	13.848
6	16.138	15.58
7	21.538	19.622
8	19.52	21.79

An optical profilometer was used for the measurements on both halves of each of the 16 walls, i.e., all the 32 wall halves were measured. The surface roughness data are given in Tables 3.5 and 3.6, marked as half 1 and half 2 correspondingly for each of the 16 walls (8 walls in batch #1 and 8 walls in batch #2).

Table 3.5: *Wall surface roughness (half 1) measured by the optical profilometer*

Wall #	Wall Roughness (half 1), R_a, μm. Batch #1	Wall Roughness (half 1), R_a, μm. Batch #2
1	9.381	13.48
2	15.09	6.914
3	8.039	9.388
4	11.47	11.34
5	10.88	12
6	11.59	10.62
7	8.046	13.48
8	8.685	9.563

Table 3.6: *Wall roughness (half 2) measured by the optical profilometer*

Wall #	Wall Roughness (half 2), R_a, μm. Batch #1	Wall Roughness (half 2), R_a, μm. Batch #2
1	10.353	10.353
2	8.4003	10.328
3	12.429	9.2617
4	9.4733	11.218
5	8.1767	11.102
6	7.9007	9.4033
7	12.392	11.891
8	8.126	10.967

Roughness values measured by the optical profilometer show lower values, than the roughness measured by the mechanical profilometer. For example, for wall #8 in batch #1, the mechanical profilometer shows $R_a = 19.52 \mu\text{m}$ (Table 3.4) while the optical profilometer shows $R_a = 8.685 \mu\text{m}$ (Table 3.5). This can be explained by the fact that the mechanical profilometer stylus uses an about 10 times larger area for gathering the roughness data while the optical profilometer uses an area approximately equal to 1 mm^2 . A sample roughness measurement from one of the walls by means of the optical profilometer is shown in Fig. 3.10.

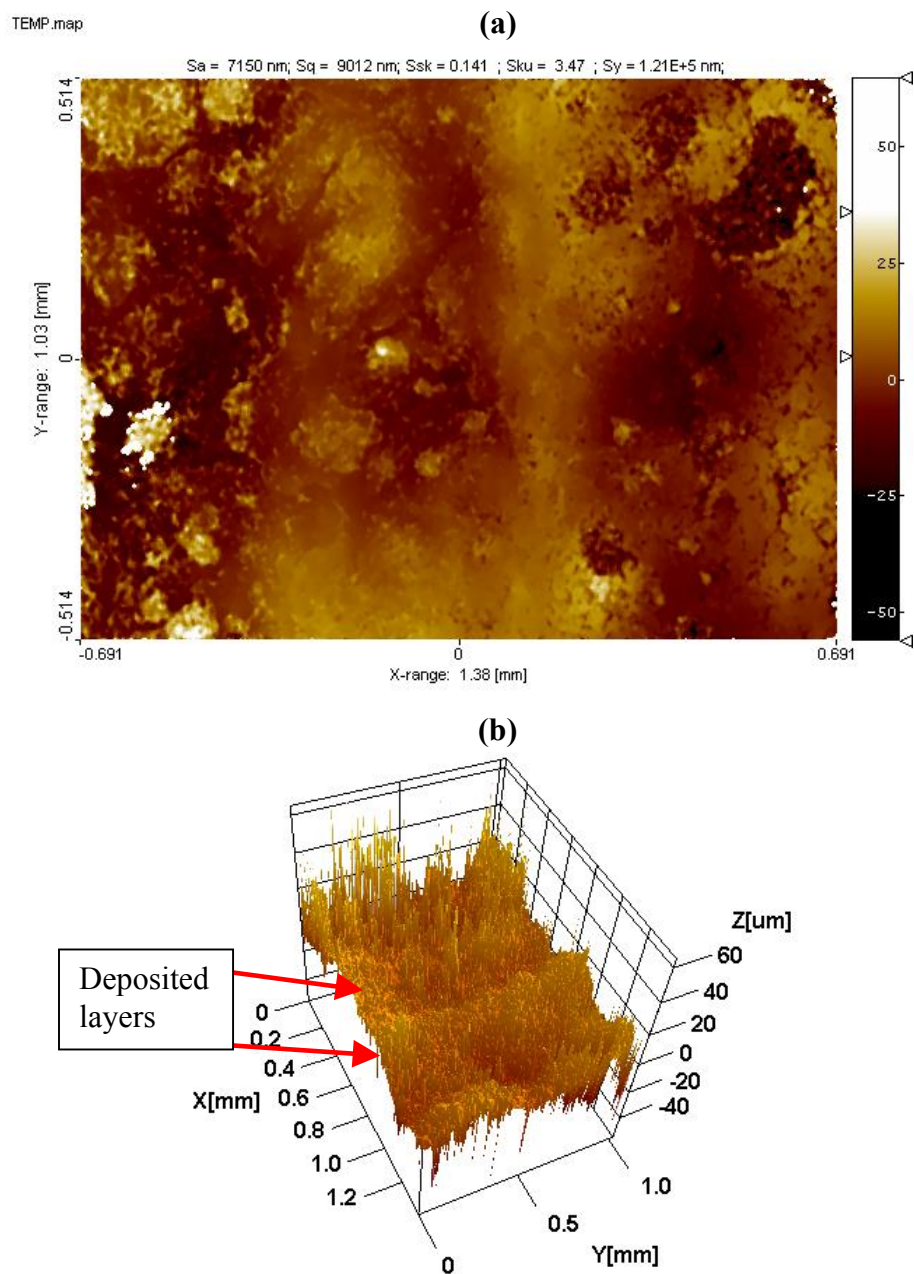


Figure 3.10: Surface roughness of a wall measured by the optical profilometer: (a) 2-D view, (b) 3-D view.

3.3.3 Analysis of the influence of the DMD parameters

Statistical estimates of the influence of each factor (A – laser power, B – coolant flow rate and C – powder flow rate) on the wall roughness, thickness, width, height, and spherical build-up diameters at the walls' right- and left-hand side corners were done, based on the factorial design of experiments. Table 3.7 shows the effects of the factors on wall top width at a corner neck. This geometrical parameter was chosen to appear in the main text of this chapter rather than in Appendix B (where the data on all other geometrical parameters are cited), because it shows the most sensitive reaction to the change in the factors' values (laser power, powder feeding rate and coolant flow rate) during the experiments.

Table 3.7: *Influence of laser power, powder flow rate and coolant flow rate on top width of a wall at the left-hand side corner neck*

Factor	Effect Estimate	Sum of Squares, SS	Percent Contribution, %
A (cooler)	-0.155	0.0961	2.820684038
B (laser)	0.76	2.3104	67.81382311
C (powder rate)	0.2725	0.297025	8.718144395
AB	0.0225	0.002025	0.05943689
AC	-0.01	0.0004	0.01174062
BC	-0.09	0.0324	0.950990248
ABC	0.0525	0.011025	0.323600848
Pure error		0.6576	19.30157985
Total		3.406975	100

In the other example, in Table 3.8, the effect of the DMD process parameters on the wall roughness magnitude, measured by the mechanical profilometer, is shown. The effects of the factors (DMD parameters) on all other geometrical parameters are given in Appendix B.

Table 3.8: *Influence of laser power, powder flow rate and coolant flow rate on wall roughness measured by the mechanical stylus*

Factor	Effect Estimate	Sum of Squares, SS	Percent Contribution, %
A (cooler)	0.73525	2.16237025	1.301080666
B (laser)	4.72425	89.27415225	53.71553436
C (powder rate)	2.88275	33.24099025	20.00083461
AB	-0.81475	2.65527025	1.597654604
AC	0.50575	1.02313225	0.615610388
BC	1.23775	6.12810025	3.687228288
ABC	-0.35125	0.49350625	0.296938714
Pure error		31.220494	18.78511838
Total		166.1980158	100

According to Table 3.7, laser power contributes 67% to the DMD fabrication of a vertical wall, namely, to its top width. While the other two factors – heat exchanger coolant flow rate and powder flow rate – contribute 3% and 9%, respectively. Therefore, the choice of the laser power is the determining parameter for the DMD of thin wall structures. If the exchanger efficiency would increase – it could contribute more to the DMD process. Ultimately, the heat exchanger would allow the building of non-tapered thin-wall structures.

Table 3.8 shows that the roughness of the DMD built thin-wall structures is affected by laser power at 53%, powder feeding rate at 20% and coolant flow rate at 1.3%. Comparing this data to Table 3.7, it can be concluded that different geometrical parameters of a thin wall are affected differently by the DMD process parameters, though the largest impact still comes from the laser's power. The general trends in geometry distribution among the different walls fabricated with different DMD parameters is shown in Fig. 3.11, depicting the change of the walls' heights and of the top and bottom widths versus wall number corresponding to the standard order in Table 3.3.

Walls 3 and 4 as well as walls 7 and 8 were fabricated using the maximal values (according to Table 3.3) of laser power - 350 W. This is why, Fig. 3.11 a and b show that, these walls have the maximal heights and widths in both separately fabricated batches #1 and #2.

A more pronounced, repetitive and stable influence of the laser power on the wall's geometry can be shown in the distribution of the diameter values of the spherical build-ups at the corners of each wall (Fig. 3.12), namely the horizontal and vertical diameters of the spheres. Walls 3, 4, 7, and 8 show the maximal values in the distribution of sizes of the vertical diameters of each sphere at the corners of the wall.

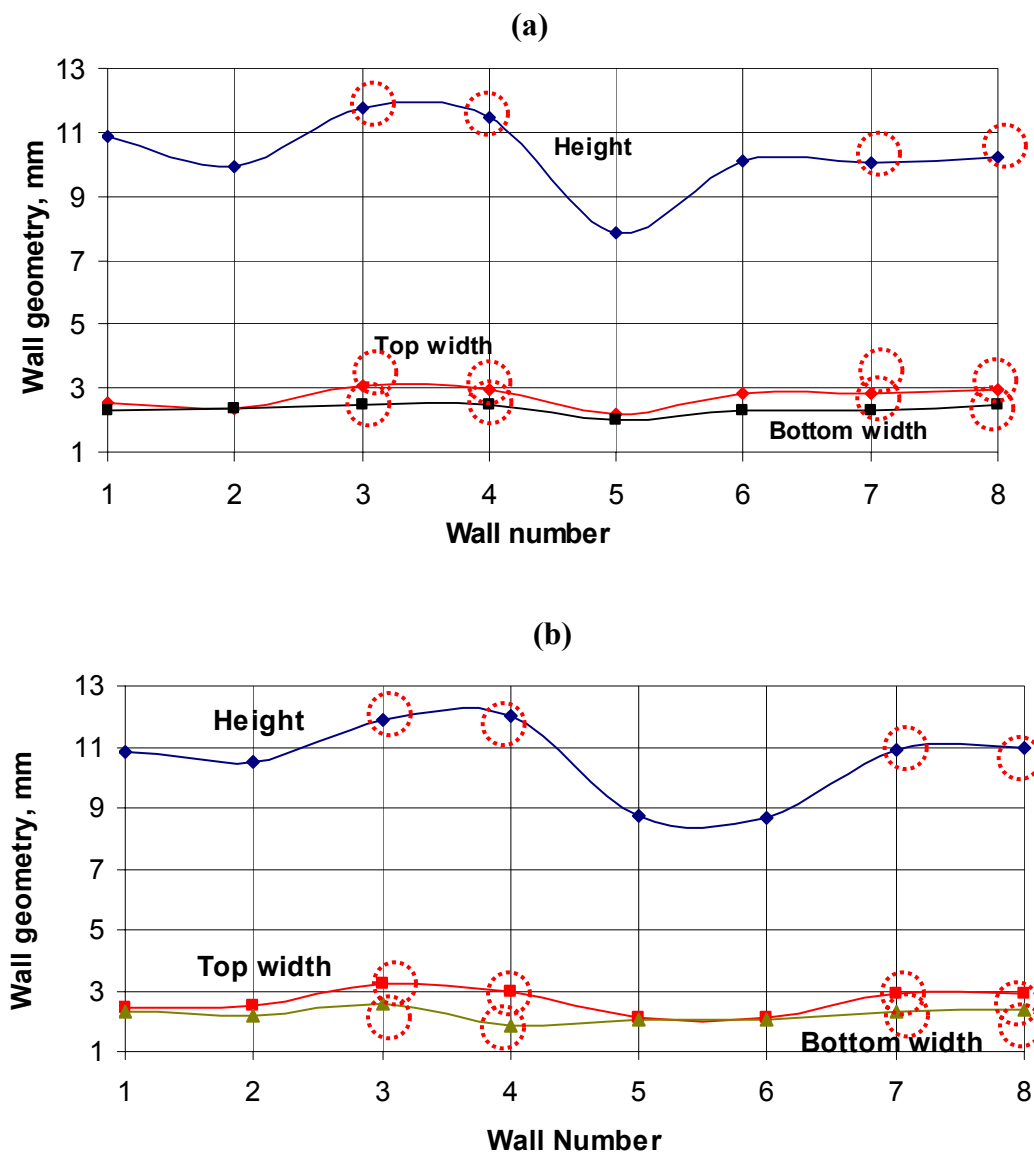


Figure 3.11: *Distribution of the magnitudes of heights and widths the thin walls: (a) batch #1, (b) batch#2.*

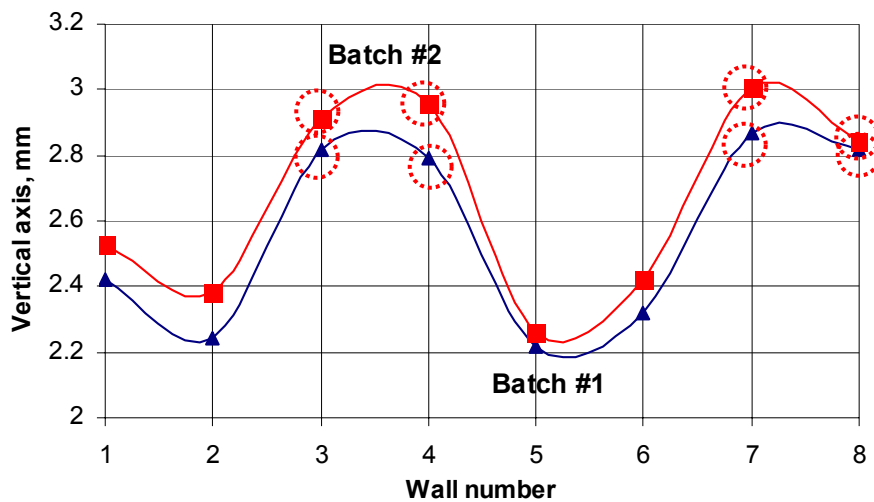


Figure 3.12: Distribution of the magnitudes of the vertical diameters (axis) of the spherical build-ups located at the right-hand side corners of the thin walls.

Wall roughness distribution is shown in Fig. 3.13. The trend is similar to the one in Figures 3.11 and 3.12.

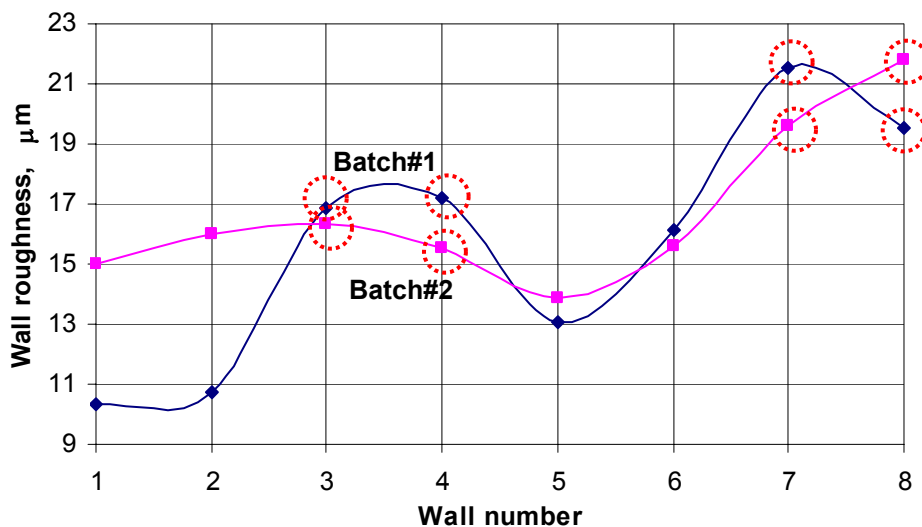


Figure 3.13: Distribution of wall roughness values from measurements by the mechanical stylus method.

The trends in the distribution of the other geometrical parameters of the vertical walls are shown in Appendix C. They all show similar behavior as above, i.e., maximal peaks correspond to the maximal laser power values.

3.4 Concluding remarks

Two sets of the DMD process parameters were identified during this experimental study: 1) for the fabrication of bulk structures from NiTi powder, 2) for the fabrication of thin wall structures from NiTi powder.

The experimental study has proven the feasibility of using laser assisted manufacturing processes such as DMD for the fabrication of bulk- and thin-wall structures. High quality (non-porous, non-cracked) 2.5-D and 3-D solid objects were successfully fabricated during the experimental studies aimed at the identification of the DMD parameters.

The effect of heat transfer on the DMD process was experimentally and theoretically investigated. Theoretical studies show that the height of a wall, based on the so-called “limiting layer thickness” defined by Van’t Land (2005), can be used as an estimator of the maximal achievable height of thin wall structures made by DMD. Finally, based on the wall’s height estimate, it was concluded that the heat transfer coefficient between the melt and the solidified material is the most influential parameter affecting the quality of the DMD build thin wall structures. The height can be controlled by adjusting the heat sink conditions of the DMD process by the proper choice of the heat exchanger, laser power and powder flow rate.

It was found that there are no visible bonding boundaries (or that the homogeneity degree was excellent) between the adjacent deposition layers in the thin walls. Therefore, it can be

concluded, that the homogeneity of the molten and solidified material of a thin-wall structure is very little affected by the fact that it was built on a “layer-by-layer” basis by the DMD process, provided that the overall thickness (height of the wall in this case) of the molten material does not exceed the “limiting layer thickness”.

The factorial design of experiments has shown that the choice of laser power plays a major role in the DMD manufacture of thin-wall structures. By analyzing the experimental data, it was concluded that the geometrical parameters of the walls – height, width, thickness, and roughness – have their maximal magnitudes at the maximal laser power level of 350 W. The other DMD parameters, i.e., the powder flow rate and heat exchanger coolant flow rate was shown to have a lesser effect on the walls’ quality.

CHAPTER 4

4. Properties of SMA materials fabricated by DMD from SMA powder

An investigation of the properties of the DMD fabricated SMA material will be accomplished in this chapter. For these purposes, a sample of the fabricated ingot will be prepared (ground and polished) and studied under the optical and scanning electron microscopes. X-ray Diffractometry, Secondary Ion Mass Spectroscopy, and Differential Scanning Spectroscopy analyses will be undertaken to investigate the properties of the fabricated material.

4.1 Sample preparation and microscopy

In order to study the materials' properties, the raw DMD manufactured 25.4 mm dia. cylindrical sample (Chapter 3, Fig. 3.2b) was annealed at 850°C in an Ar atmosphere and then, first, quenched in an Ar filled vessel at room temperature. This was done to homogenize the material, since according to the phase diagram for NiTi (55.5 wt% Ni, balance – Ti) this is the solid-solution region. After that, two identical 5 mm diameter and 0.5 mm thick round samples (Sample #1 and Sample #2) were wire-EDM cut from the bigger DMD manufactured NiTi cylinder (Fig. 4.1a). Sample #1 (Fig. 4.1c) was polished and its surface was investigated by

optical microscopy and scanning electron microscopy (SEM) imaging. All heat treatments were done in a vertical oven with a protective Ar atmosphere to prevent oxidation of the material.

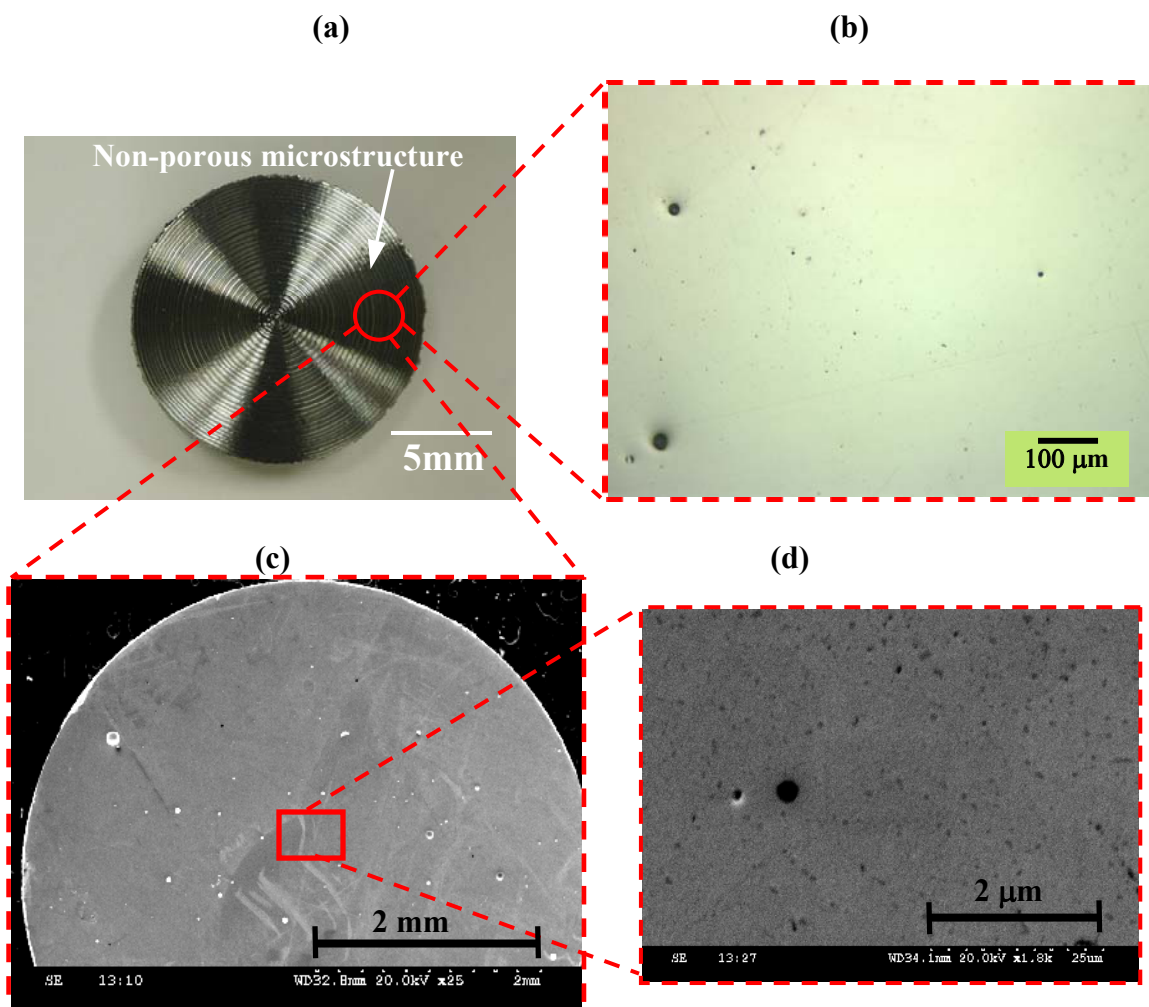


Figure 4.1: As-annealed NITINOL sample: (a) turned cross-section; (b) optical microscope image of the ground and polished sample part of cylinder (a); (c) SEM micrograph of (b), Sample #1; (d) zoomed SEM micrograph of (c), Sample #1.

Optical microscopy has been performed on Sample #1. Figures 4.1 b, c, d show an apparently solid and non-porous microstructure of the sample. After grinding and polishing the

sample, microscopy at a higher resolution revealed a negligible amount of pores in the material (Fig. 4.1b). The largest pore had a diameter of approximately 15 μm . In the area of interest ($500\mu\text{m} \times 700\mu\text{m}$ in Fig. 4.1b) the amount of area porosity was about $300 \mu\text{m}^2$ of pores per $350000 \mu\text{m}^2$ of the area or 0.086%. Scanning electron microscopy (SEM) on Sample #1 was done using a Hitachi S-3500N variable-pressure scanning electron microscope. The SEM micrographs corresponding to the circled part on the optical microscopy image (Fig. 4.1a) are shown in Fig. 4.1 c, d.

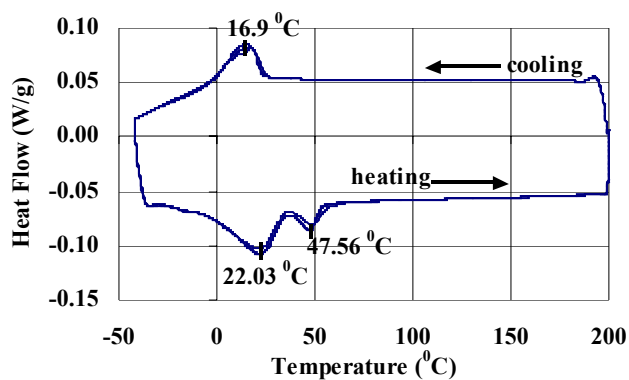
4.2 Thermo-mechanical treatment and differential scanning calorimetry (DSC)

The differential scanning calorimetry (TA Instruments 2920 DSC) method was used to determine the TTRs in the manufactured NiTi (NITINOL) samples under no stress conditions. For this purpose, both samples were subject to a secondary annealing process to achieve the needed TTRs. Since the thermo-mechanical treatment procedure was previously not established for this kind of material (DMD processed NiTi powders) – one of the intermediate goals of this research was to identify the proper heat treatment parameters. The NiTi phase diagram was used in the identification process. Two ranges of heat treatment temperatures were explored: (1) from 630 °C and above that corresponds to the solid-solution region according to the NiTi phase diagram and (2) below 630 °C that corresponds to the precipitation-hardening region.

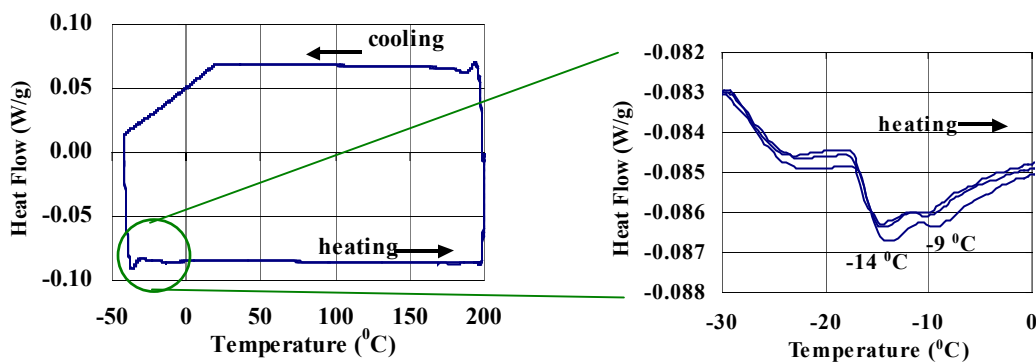
Sample #1 was annealed at temperatures above 630 °C (in an Ar atmosphere) and quenched in room temperature water. Sample #2 was annealed eleven times under different

experimental conditions to achieve the phase transformation heat flux peaks on the DSC thermogram. The different annealing temperatures, falling between 282 °C and 500 °C, different annealing times and quenching conditions are shown in the annotation to Fig. 4.2. The resulting DSC thermograms for different samples and different heat treatment conditions are also shown in Fig. 4.2.

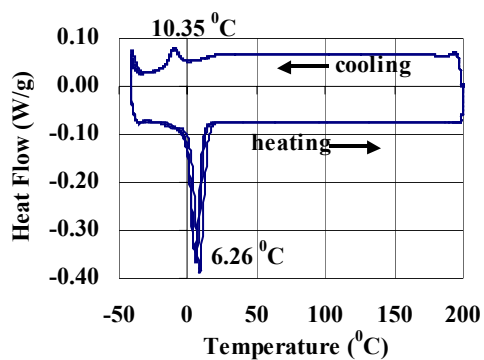
(a)



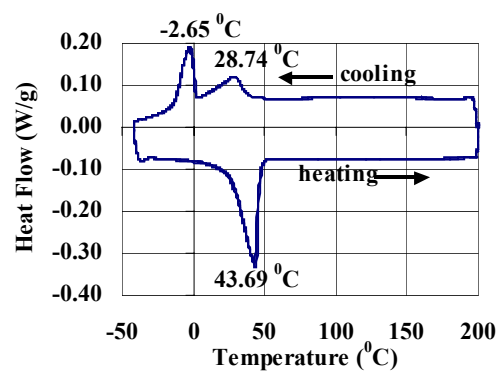
(b)



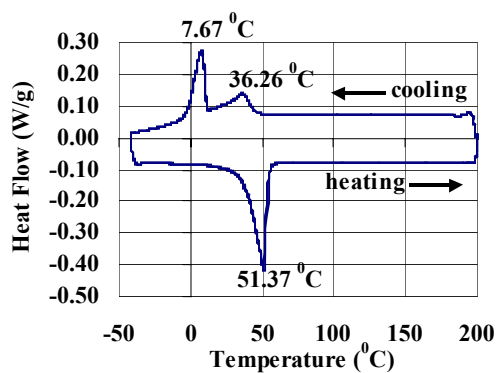
(c)



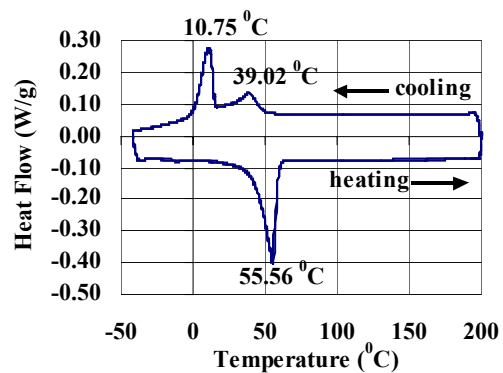
(d)



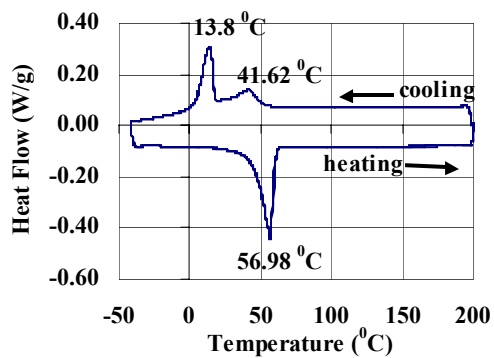
(e)



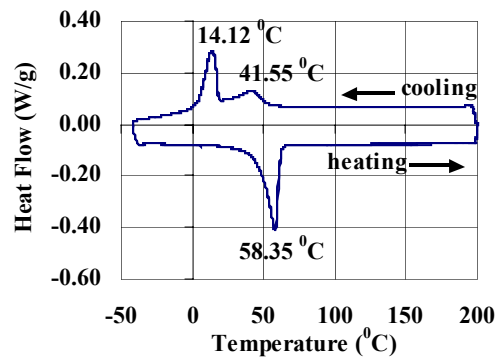
(f)



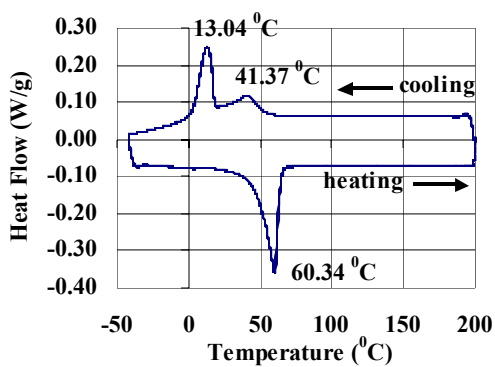
(g)



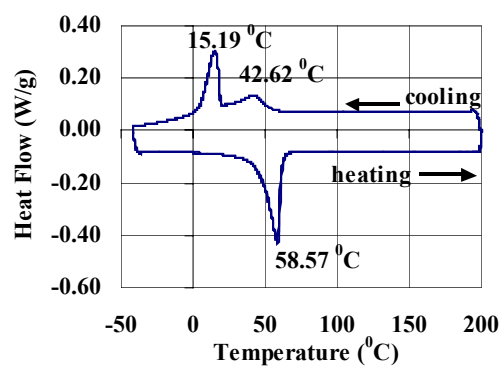
(h)



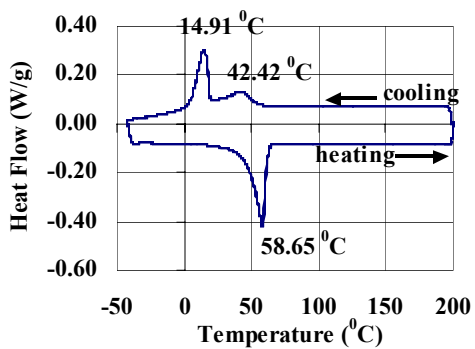
(i)



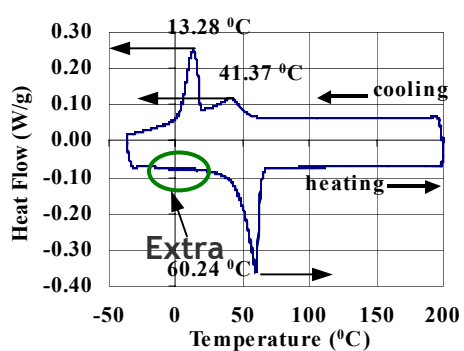
(j)



(k)



(l)



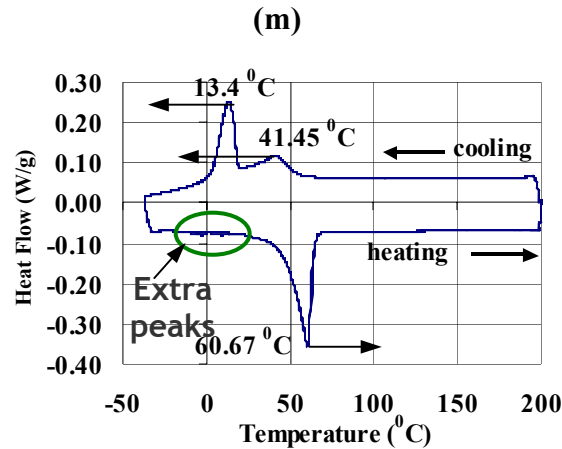


Figure 4.2: DSC thermograms obtained under different heat treatment conditions (annealing temperatures) –

- (a) as-is raw (pre-alloyed) NITINOL powder used for fabricating the samples;
- (b) Sample#1: $T=820$ °C, time = 1 hour, room temperature (t.) water quenched;
- (c) Sample#2: $T=500$ °C, time – 1 hour, room t. water quenched;
- (d) Sample#2: $T=450$ °C, time – 1 hour 30 min., room t. water quenched;
- (e) Sample#2: $T=424$ °C, time – 1 hour 30 min., room t. water quenched;
- (f) Sample#2: $T=408$ °C, time – 1 hour 30 min., room t. water quenched;
- (g) Sample#2: $T=396$ °C, time – 1 hour 30 min., room t. water quenched;
- (h) Sample#2: $T=358$ °C, time – 1 hour 30 min., room t. water quenched;
- (i) Sample#2: $T=331$ °C, time – 1 hour 30 min., room t. water quenched;
- (j) Sample#2: $T=309$ °C, time – 1 hour 30 min., room t. water quenched;
- (k) Sample#2: $T=282$ °C, time – 1 hour 30 min., room t. water quenched;
- (l) Sample#2: $T=282$ °C, time – 1 hour 30 min., no quenching;
- (m) Sample#2: $T=424$ °C, time – 1 hour 30 min., no quenching.

All thermograms show three heating and cooling cycles. The mass of NiTi Sample #1 was 65 mg and of Sample #2 – 66.47 mg. The DSC of the raw “as-is” NITINOL powder used in the sample fabrication is given in Fig. 4.2a.

4.2.1 Effect of thermal treatment on TTRs with the use of quenching

Sample #1 was solid-solution treated at different temperatures (above 630 °C). One of the corresponding thermograms (shown in Fig. 4.2b) shows very insignificant peaks, during the DSC heating cycle, at -14°C and -9°C . The heating cycle was performed in the maximal available measuring range of the particular DSC apparatus used. A further increase in the annealing temperature slightly increased the corresponding temperatures (TTRs) (to -3°C and $+2^{\circ}\text{C}$, not shown here) at which the two respective peaks occurred, but the magnitudes of the peaks remained insignificant.

Sample #2 was precipitation hardened at lower annealing temperatures than Sample #1. The resulting thermogram of Sample #2 (Fig. 4.2c) shows significantly larger magnitudes of the heat flux peaks at -10.35°C (cooling DSC cycle) and 6.26°C (heating DSC cycle) than the peaks in Sample #1. The two peaks correspond to the martensite and reverse martensite phase transformations in the material. This evidence supports the statement suggested by Bram, et al. (2002), that the phase transformations in the SMA material are mediated by precipitation (Ni_4Ti_3) growth. The so-far obtained TTRs were lower than room temperature. In order to increase the TTRs (shift the TTR peaks to the right of the DSC thermograms), the annealing temperature of Sample #2 was decreased and set to 450°C (Fig. 4.2d). Then, the annealing temperature was gradually decreased from 450°C to 282°C and Sample #2 was annealed at selected temperature level (annealing point) in this range. The corresponding shifts in the phase transformation temperatures were observed. The TTRs were measured after each annealing point. The TTRs very closely approached the desired room temperature level values (see Fig. 4.2d to Fig. 4.2k).

The variation of the TTRs versus the corresponding annealing temperatures is shown in Fig. 4.3. A, R, and M correspond to temperature levels at which the heat fluxes were measured by DSC during the reverse martensite, R-phase and martensite phase transformations, respectively. Figure 4.3 contains three curves corresponding to the TTRs of the three phase transformations. The curves were built based on the experimental points approximated using MatLab's curve fitting toolbox. A quadratic polynomial was used to fit the eight experimental points. It can be seen, that the lower the annealing temperature the higher the TTRs for all three phase transformations. Such behavior was found in the annealing temperature range from 282 to 500 °C. Beyond the annealing temperature of 500 °C the TTRs did not exist. Below the annealing temperature of 360 °C the TTRs decreased.

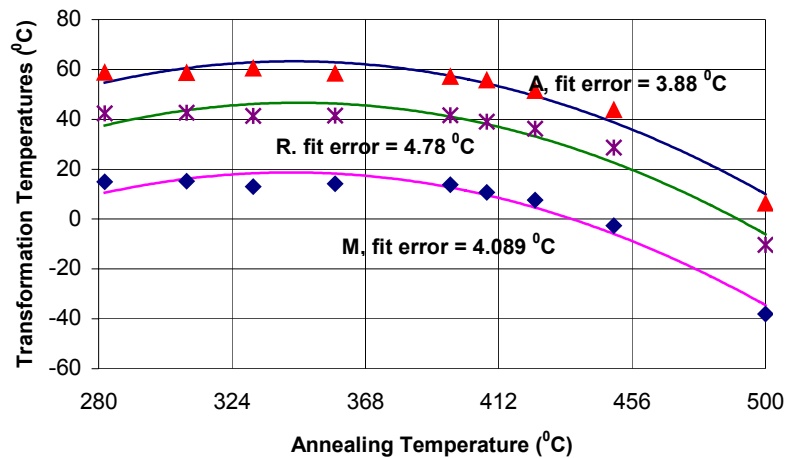


Figure 4.3: Cumulative annealing curves: TTRs versus annealing temperatures (T_m , T_a and T_r are the martensite, reverse martensite (austenite) and R- phase transformation temperatures).

As indicated before, Bram et al. (2002) have used HIP and MIM processes in order to fabricate SMA samples using: 1) a mixture of raw Ni and Ti powders and 2) a pre-alloyed NITINOL powder, respectively. A comparative analysis shows that the samples manufactured by

DMD exhibit much more pronounced and completely uniform heat flux peaks (Fig. 4.2c to 4.2k) than those achieved by the HIP and MIM processes (Bram et al., 2002). This is an indication of the high quality and homogeneity (Ni, Ti distribution) of the material fabricated by DMD. The successful achievement of the TTR peaks in Sample #2 proves that the DMD process is an efficient rapid prototyping (RP) method for fabricating high quality SMA based structures. It also shows that precipitation growth is one of the most important factors in achieving the necessary phase transformation properties used in shape memory effect driven motion. The heat flux peaks observed during three heating/cooling cycles in each separate DSC run (see thermograms), exhibit very little shift with respect to each other within that particular run, implying no or very little degradation of the phase transformation properties.

To approach the room temperature levels even closer, the TTRs can be further fine-tuned by modifying the thermal treatment and NiTi composition (including point defects introduced by quenching, and contamination with oxygen and carbon). These two factors were named by Ren and Otsuka (2000) to be the key answers to the strong dependence of the martensite phase transformation temperatures on composition. Also, according to Otsuka and Ren (1999) and other references on NiTi alloys, the TTRs linearly decrease in the SMA (NiTi) alloys with an increase of Ni content starting at 50 at.% (equivalent to 55wt.%) and up, with Ti balance.

4.2.2 Effect of thermal treatment on TTRs without the use of quenching

In order to study the effect of quenching on the TTRs, Sample #2 was heat treated under the same conditions as shown in Fig. 4.2k and Fig. 4.2l, but no water quenching was applied to

the sample. The sample was naturally cooled down inside the oven. The DSC results are shown in Fig. 4.2l and Fig. 4.2m. Comparison with the data from Fig. 4.2k shows that T_m and T_r decreased by almost 1.5 °C from 14.91 °C and 42.42 °C (quenched sample, Fig. 4.2k) to 13.28 °C and 41.37 °C (non-quenched sample, Fig. 4.2l) correspondingly.

The temperature T_a increased by 1.5 °C from 58.65 °C (quenched sample, Fig. 4.2k) to 60.24 °C (non-quenched sample, Fig. 4.2l). Comparison between Fig. 4.2e (quenched sample) and Fig. 4.2m (non-quenched sample) shows the same behavior – decrease in T_r , T_m and an increase in T_a . The aim of removing quenching was to increase all TTRs above room temperature, but the opposite effect occurred with T_m and T_r . In addition, the quality of the non-quenched material, namely, its homogeneity, became worse – new redundant small peaks appeared during the heating cycle (Figs. 4.2l, 4.2m). Because the removal of quenching tends to decrease T_m and T_r , thus moving them farther from the room temperature, quenching should be retained in the heat treatment procedure of the SMA material. Other possible factors influencing the TTRs are the oxygen and carbon contamination to be studied later.

4.3 Energy dispersive spectrum (EDS) analysis

In order to assess oxygen and carbon contamination levels in the fabricated NiTi sample and their influence on the TTR, an EDS analysis was conducted using a Hitachi S-3500N variable-pressure SEM equipped with an EDS detector. The sample, previously used for the DSC analysis, was further polished (final polishing was done by 0.05 μm microcloth). The resulting x-ray spectrum of the sample surface is shown in Fig. 4.4. It does not show any apparent

contamination with oxygen or carbon. The EDS equipment cannot determine contamination lower than 0.1 wt. %, so one can assume that if contamination took place it had to be at a lower level.

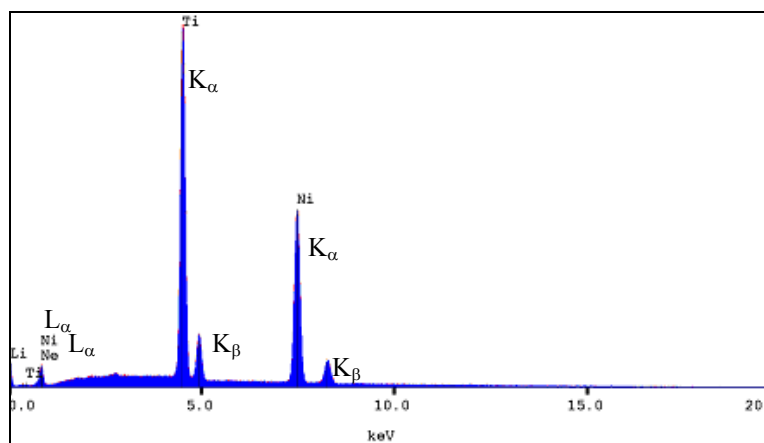


Figure 4.4: EDS spectrum of the manufactured NiTi sample.

4.4 X-ray diffraction (XRD) analysis

X-ray Diffraction (XRD) analysis was done on the 850 °C annealed raw sample (Fig. 4.1a) using a SCINTAG x-ray powder diffractometer. The raw XRD data are shown in Fig. 4.5.

The XRD data show the distribution of phases in the annealed NiTi material. The XRD data are unfiltered, and therefore show the superimposed background signal on top of the meaningful peak signals. The results are similar to the SMA (NiTi) XRD data from Mizar et al. (2000) or SMA neutron diffraction data from Lukas et al., 2001. The material contains austenite, martensite, and TiNi₃ precipitates. The existence of the precipitates undermines the presence of

the R-phase in the material, which is advantageous for having the Two Way Shape Memory Effect (TWSME).

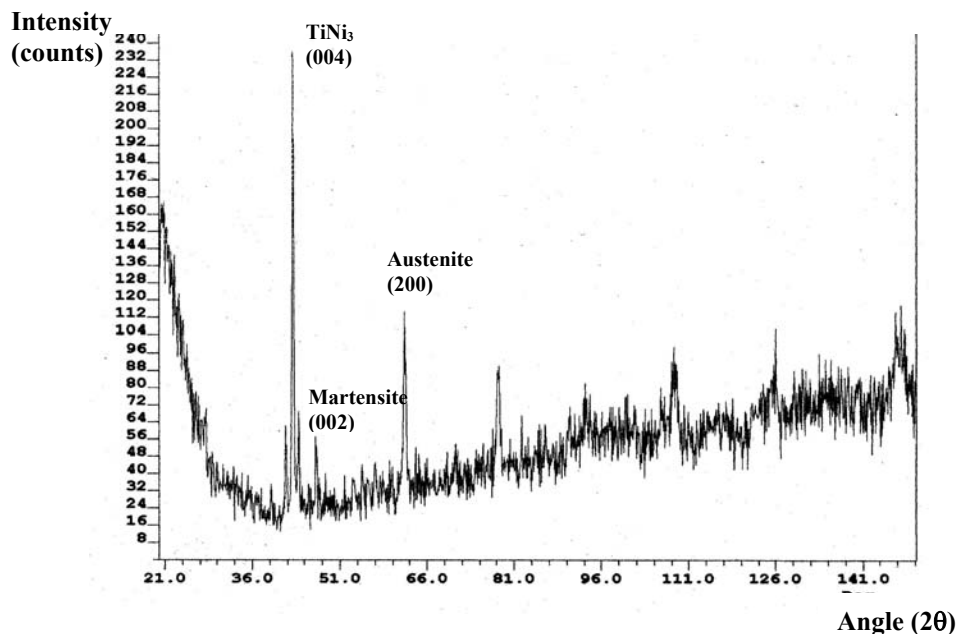


Figure 4.5: XRD raw data of the cylinder annealed at 850 °C.

4.5 Secondary ion mass spectroscopy (SIMS) analysis

The contamination level can also be estimated by doing SIMS (ToF-SIMS, PHI TRIFT III, Physical Electronics), which is more sensitive than EDS. SIMS allows conducting a chemical composition analysis of a material at a certain depth in the sample.

Two NiTi samples were analyzed by means of SIMS: the manufactured NITINOL Sample #1 and a commercially available NITINOL sample (purchased from Special Metals Corporation with a known chemical composition, i.e., with a known level of impurities) both under no stress conditions. The commercially available NITINOL sample was used as a standard

sample to compare the level of contamination with our manufactured sample. The SIMS depth profiling data (in the positive ion mode, used for identification of metals and oxides in a material) for the standard and for the manufactured samples are shown in Fig. 4.6a and in Fig. 4.6b respectively. The material depth, along which the profiles (chemical compositions) of all the chemical elements were built, was about 940 - 970 nm. Ion-milling (the removal of layers of the material) was done at approximately 0.18 nm/sec – “ion-milling feed”. The material was removed layer by layer. Mass spectroscopy was performed after a layer of the material was removed. The spectroscopy analysis lasted 300 s in each layer. The ion-milling window size was about 100nm × 100nm.

The data in Fig. 4.6 show that there is some contamination with O, C, TiO, K, and Na that changes with depth. Ni is less reactive with oxygen than Ti, hence oxides are mostly formed with Ti. All the contamination data are qualitative, but it is possible to estimate the level of contamination in our manufactured sample by comparing the corresponding SIMS data from both samples (Fig. 4.6a and Fig. 4.6b), since the quantitative chemical composition of the commercially available sample is known.

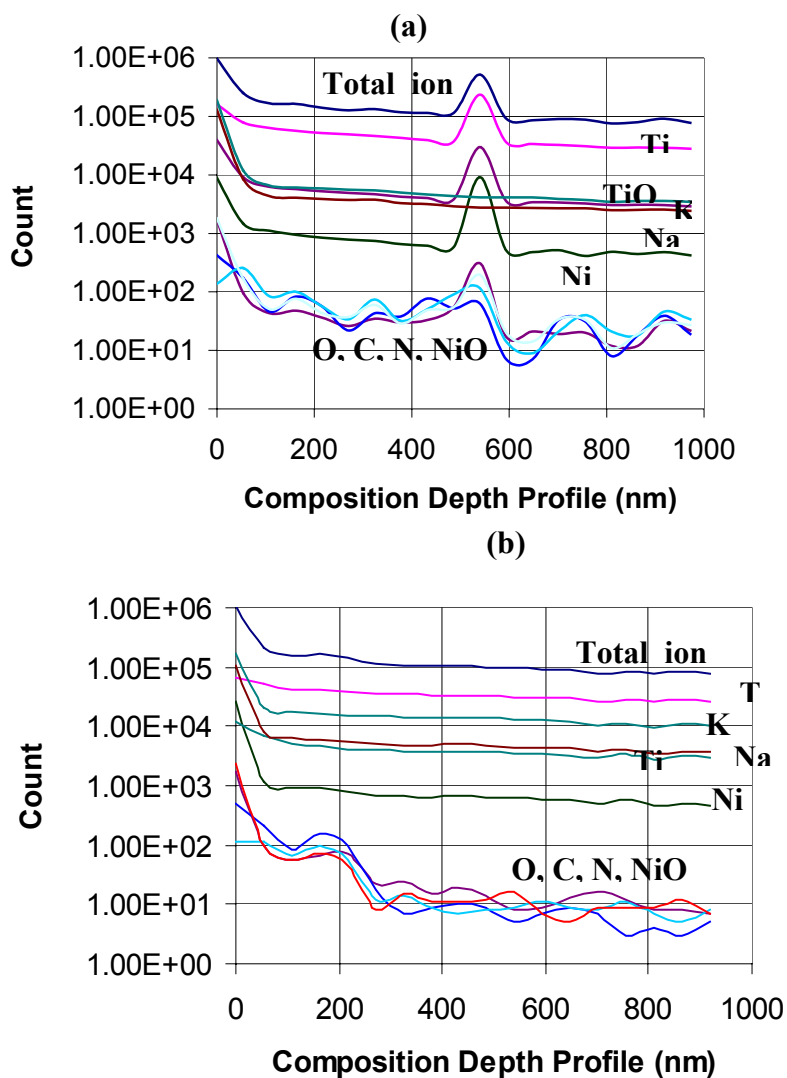


Figure 4.6: SIMS depth profiles: (a) commercially available (standard) NITINOL sample; (b) NiTi sample fabricated by means of DMD.

According to the manufacturer, the commercially available NITINOL sample, contains 185 ppm of oxygen, 310 ppm of carbon and less than 0.01wt.% of Na and other contaminants. The reference value for the maximal allowable amount of oxygen in SMAs is about 1000-2000 ppm. The complete information on the chemistry of the commercially available UDIMET

NITINOL material (in the form of a metal strip) was provided by Special Metals Corporation and is given in Table 4.1.

Table 4.1: Chemical analysis of UDIMET NITINOL material provided by Special Metals Corporation

Element	WGT%
Ni	55.49
Ti	Balance
C	310 ppm
O	185 ppm
Mn, Si, Cr, Co, Mo, W, Nb, Al	< 0.01
Zr, Cu, Ta, Hf, Ag, Pb, Bi, Ca	< 0.01
Mg, Sn, Cd, Zn, Sb, Sr, Na, As, Be	< 0.01
Ba, Fe	< 0.01
B	< 0.001

The comparative evaluation of the plots with spectra from both samples shows an almost identical or even smaller level of contamination in our, DMD manufactured sample. Therefore, the impurities can be excluded from the list of the factors that noticeably affect the TTRs in the NiTi sample, fabricated by DMD.

Our experimental studies allow us to conclude that:

- 1) It is important to have a protective anti-oxidation atmosphere (e.g., Ar gas) due to the high affinity of Ti to oxygen during the melting process of NiTi powder.

- 2) It is important to keep the level of impurities at a low level in the material. The MIM and HIP processes do not satisfy this condition. For example, the addition of a binder and wax in the MIM process could worsen the quality of the material and its ability to undergo phase transformations.
- 3) It is important to have high quality pre-alloyed homogenized NiTi starting powder with the proper Ni content in it. Bram et al. (2002) homogenized the NiTi powder themselves from elementary Ni and Ti powders for further use in the HIP process. We obtained already pre-alloyed homogenized NiTi powder from the manufacturer and fabricated better quality material from it.
- 4) Post-thermal treatment of the manufactured samples has to be done in an oven with an Ar protective atmosphere due to the high oxidation propensity of Ti.

4.6 Concluding remarks

A comprehensive set of experimental tests on NiTi samples fabricated by DMD was conducted, namely: optical microscopy, SEM, DSC, EDS, and SIMS. The following conclusions can be drawn:

- The obtained results have confirmed the capability of the DMD process to fabricate high quality almost non-porous NiTi samples from NITINOL powder. The samples do not require any further cold work, sintering or filling with an additional material.
- The samples exhibit smooth and pronounced TTR peaks as measured by DSC. The TTR peaks are the prerequisite for the SME and are in the desired range of values.

- The experiments show that removing the quenching procedure tends to decrease some of the TTRs (T_m and T_r), and worsen the quality of the material, therefore, it is not desirable to omit quenching from the heat treatment procedure. It can also be concluded that quenching does affect the TTRs.
- EDS revealed no visible contamination with O, C and other contaminating elements; therefore, a more sensitive method to detect the contamination level in the material needs to be used.
- SIMS depth profile analysis has shown a contamination with oxygen (TiO), Na, and K. The evaluation of SIMS spectra shows that the level of contamination in the manufactured NiTi sample is almost the same or even smaller, in comparison to the standard NITINOL sample (with known chemistry), provided by the supplier. Therefore, the impurities, present in the fabricated material, do not noticeably affect the TTRs in the sample.

CHAPTER 5

5. Fabrication of the SMA spring actuators - functional parts of mMM

A conceptual study of the possibility of designing, developing and fabricating a monolithic micro/meso scale manipulators (mMMs) from SMA powders by means of the DMD will be undertaken in this chapter. The mMM's design will be based on the capabilities of the previously described DMD process to fabricate metallic parts from SMA (NiTi) powders. The NiTi parts will have to be non-porous, non-cracked, and with low levels of contamination. After a series of thermo-mechanical treatments, they will have to possess martensite phase transformation properties, which are the prerequisite for the SME driven motion.

The design of a functional part of the mMM – accordion spring type SME driven actuator, is shown in Fig. 5.1. The DMD apparatus was lent to us by Prof. Kovacevic at Southern Methodist University (SMU). Several NiTi parts were fabricated by the “layer-by-layer” deposition process using the DMD apparatus: accordion spring type actuators, round plates, and a rectangular block. After the deposition, wire-EDM was used to detach the parts from their substrates, and to post-machine them into their final shapes.

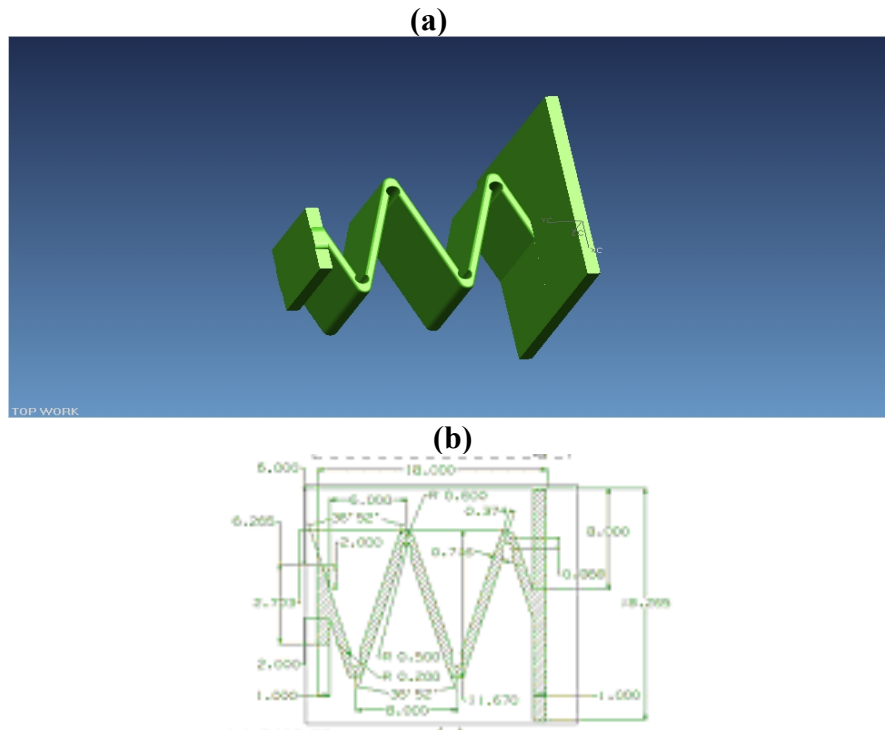


Figure 5.1: *Accordion spring (UNIGRAPHICS): (a) 3-D model, (b) 2-D drawing.*

The accordion spring type actuators were DMD fabricated based on the DMD process parameters for building bulk and thin wall structures, identified earlier in Chapter 3.

5.1 Fabrication of the SMA actuators by DMD using the DMD process parameters for building bulk structures

The DMD process parameters for building bulk structures from the SMA (NITINOL) powder were identified during one of our previous experimental studies (Table 3.1). For the current experimental investigations, the NITINOL powder was purchased from Special Metals

Corporation. The characteristics of the powder are given in Table 5.1. The powder was in the pre-alloyed condition.

Table 5.1: Chemical analysis of UDIMET NITINOL powder provided by Special Metals Corporation

Element	WGT%
Ni	55.49
Ti	Balance
C	310 ppm
O	185 ppm
Mn, Si, Cr, Co, Mo, W, Nb, Al	< 0.01
Zr, Cu, Ta, Hf, Ag, Pb, Bi, Ca	< 0.01
Mg, Sn, Cd, Zn, Sb, Sr, Na, As, Be	< 0.01
Ba, Fe	< 0.01
B	< 0.001

5.1.1 Fabrication of an accordion spring type actuator by DMD without further post-machining

A first attempt to manufacture several accordion spring type actuators by DMD without further post-machining was undertaken. The deposition parameters are given in Table 3.1 and in Figures 5.2 to 5.5. The actuators were fabricated through “layer-by-layer” deposition of NiTi powder using the CAD model shown in Fig. 5.1b. CNC G-code was generated from the model. The CNC machine’s table, a part of the DMD apparatus, was moving according to the generated

code during the deposition, melting and solidification processes. The deposition substrate used was a 3 mm thick NiTi metallic sheet in the “super-elastic” condition. Several accordion spring actuators were deposited. Three of the deposited springs are discussed below. A regular digital camera and an optical microscope equipped with a high resolution CCD camera were used in order to acquire and analyze the images of the fabricated parts.

Each spring was deposited using different sets of the DMD process parameters, namely, the laser power and Ar flow rate, in order to assess the effect of the parameters on the structure’s quality. Springs (1), (2) and (3) are shown in Fig. 5.2.

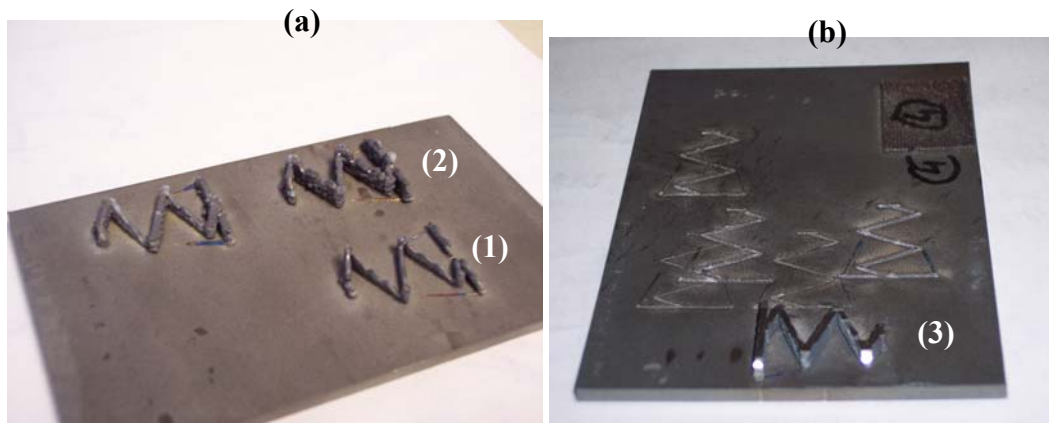


Figure 5.2: Digital camera images of the accordion springs, fabricated by DMD from NiTi powder on NiTi substrate with: (a) Ar flow rate 4.4...17.5 l/min and laser power 230...300 W, (b) Ar flow rate 17.5 l/min and laser power 300...350 W .

The detailed view of accordion spring (1) from Fig. 5.2a is shown in Fig. 5.3. The defects of the fabricated spring, visible in Fig. 5.3, are the corner build-ups and lack of material. Both types of defects are the result of the relatively low magnitudes of the Ar flow rate - at 4.4 l/min, and of the low laser power - at 250...300 W.

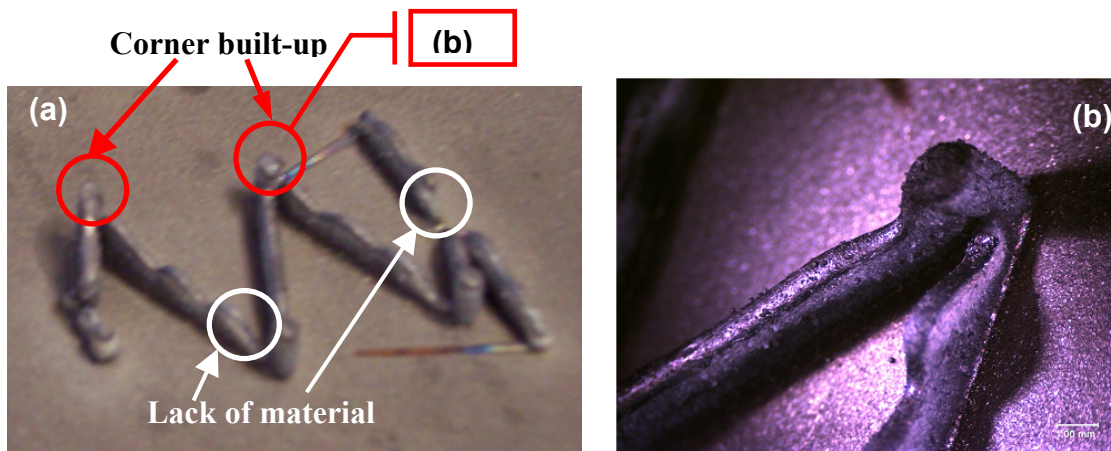


Figure 5.3: Detailed view of accordion spring (1) (DMD parameters: Ar flow rate 4.4 l/min, and laser power 230...250 W): (a) digital camera image, (b) optical microscope image – enlarged view of a corner of the spring from (a).

The detailed view of accordion spring (2) is shown in Fig. 5.4. Spring (2) was DMD fabricated using an Ar flow rate of 17.5 l/min, which was 4 times higher than in the case of spring (1). The laser power was increased as well, and was equal to 300 W. As a result of the increase of the magnitudes of both DMD parameters, the defects (corner build-ups and lack of material) in accordion spring (2) became less pronounced, although the spring's walls were still not smooth.

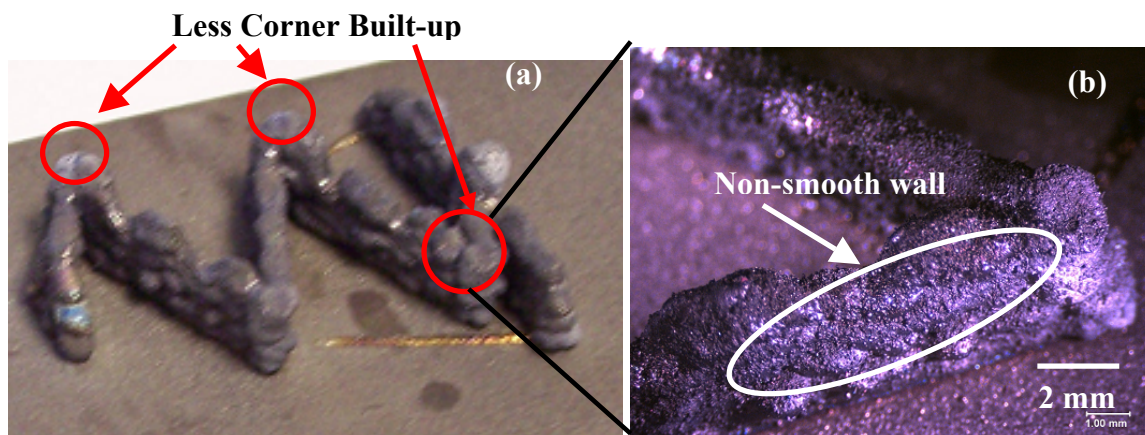


Figure 5.4: Detailed view of accordion spring (2) (DMD parameters: Ar flow rate 17.5 l/min, and laser power 300 W): (a) digital camera image, (b) optical microscope image – enlarged view of a corner of the spring from (a).

The detailed view of spring (3) is shown in Fig. 5.5. Spring (3) was fabricated at a magnitude of the laser power, set to 350-400 W. This is why spring (3) exhibits fewer defects in comparison to the previous two springs - smoother walls, and a more complete geometry.

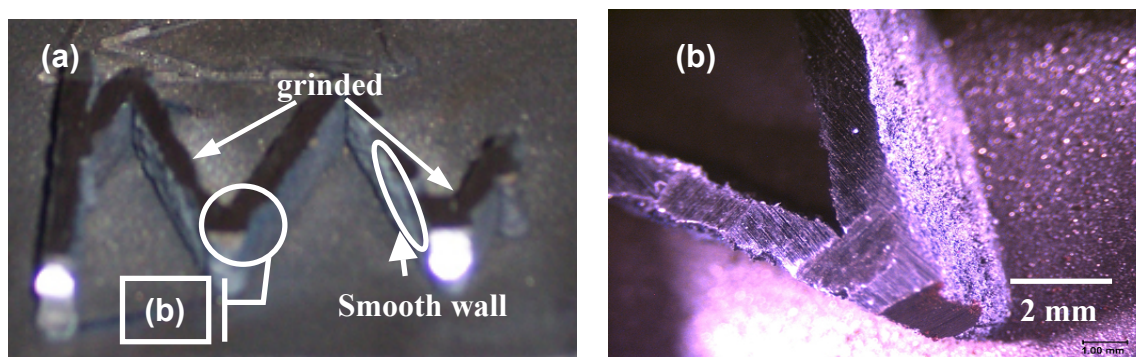


Figure 5.5: Detailed view of accordion spring (3) (DMD parameters: Ar flow rate 17.5 l/min, and laser power 350 W...400 W): (a) digital camera image, (b) optical microscope image – enlarged view of a corner of the spring from (a).

It is advantageous to compare the quality of the DMD fabricated parts from NiTi powder and from regular metallic powder that is usually used in DMD. For this purpose tool steel

powder (Crucible CPM 3V) was chosen. An accordion spring (4) was DMD manufactured from tool steel powder on a thin sheet tool steel substrate. Spring (4) is shown in Fig. 5.6. The height of the spring equals 12 mm. Spring (4) obviously has a better quality – better surface finish, no corner build-ups, and a complete geometry. This can be attributed to the fact that NITINOL has an about two times larger heat capacity and a 1.5 smaller heat conductance than tool steel: $C_p(\text{NITINOL}) = 920 \text{ J/kg}\cdot^\circ\text{C}$, $\lambda(\text{NITINOL}) = 18 \text{ W/m}\cdot^\circ\text{C}$ (Brinson et al., 1996), and $C_p(\text{any tool steel}) = 460\dots480 \text{ J/kg}\cdot^\circ\text{C}$, $\lambda(\text{tool steel Crucible CPM 3V}) = 24.2 \text{ W/m}\cdot^\circ\text{C}$ (Crucible Specialty Metals). Therefore, NITINOL powder, processed by the laser, melts at a faster rate and solidifies at a slower rate than tool steel powder, since more heat accumulates in the part during the DMD process. Or, in other words, there exists a limiting deposition layer thickness (Van't Land, 2005) – a maximal achievable height of the deposited parts for the given heat sink conditions after which the melt does not solidify and stays in the melted condition during the deposition process. The “limiting layer thickness” was discussed earlier in Section 3.3. Based on the materials' properties, the maximal achievable height for the NITINOL parts is lower than that for tool steel parts for the given heat sink conditions as seen from Fig. 5.5 (NITINOL) and Fig. 5.6 (tool steel).

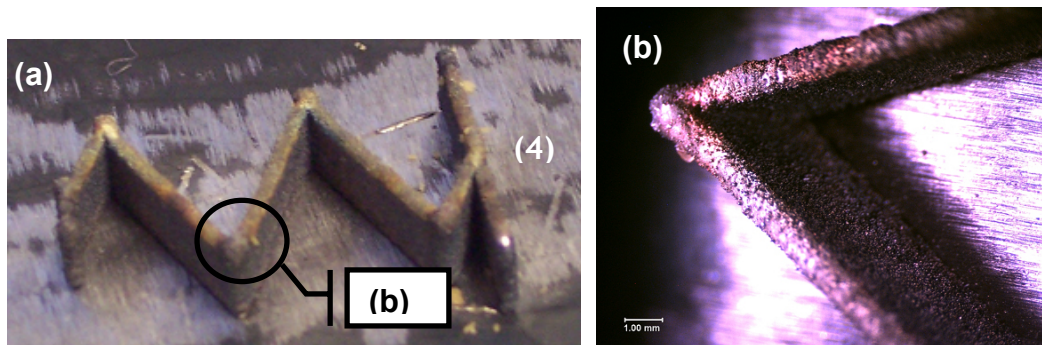


Figure 5.6: *Accordion spring (4) fabricated by DMD from tool steel Crucible CPM 3V powder: (a) digital camera image; (b) optical microscope image – enlarged view of (a).*

The volume of the material solidified (non-remelted) during the deposition process can be roughly estimated from the heat balance equations. This volume presents the non-porous material of the fabricated part. The volume of the solidified (non-porous) material, processed by DMD for NITINOL, is at least 3 times lower than the volume of the solidified material for tool steel. This observation will be verified further, during the analysis of the NITINOL rectangular block fabricated by DMD.

5.1.2 Fabrication of an accordion spring type actuator by DMD with further post-machining using wire electro-discharge machining (EDM)

The second attempt, aimed at the fabrication of the SMA accordion spring type actuator, was undertaken using DMD process parameters identified for the fabrication of bulk structures as in the previous case. A bulk rectangular ingot was manufactured by DMD from NITINOL powder and post-machined by wire-EDM into the final shape of the actuator.

The fabricated ingot is shown in Fig. 5.7. The ingot consisted of about 20 layers of NITINOL powder deposited, molten and solidified on a 3 mm thick NiTi substrate. Each layer was approximately 0.5 mm thick. The deposition was done in 4 runs with stops between them. About 5 deposition layers were manufactured during each run. The stops between the depositions of the consecutive layers within a run were about 15 sec. The stops between the consecutive runs, when no deposition took place, were about 2-3 min. The stops were used in order to cool the solidified part of the block part, even though an additional copper cold plate – a heat

exchanger, was used for cooling purposes. The heat exchanger was placed beneath the deposition substrate.

Side running cracks, tending to delaminate the structure, were observed in the block in Fig. 5.7. The ingot was cut off from the NiTi substrate and side-milled to remove the cracked regions. Afterwards, the sample was wire-EDM machined into the final shape of the accordion spring actuator as shown in Fig. 5.8.

From the observations of the machining process, it is clear, that the visible large side cracks in Fig. 5.7 do not propagate across the length and the width of the block. Most of the side cracks disappeared after side-milling and were not present in the body of the accordion spring.

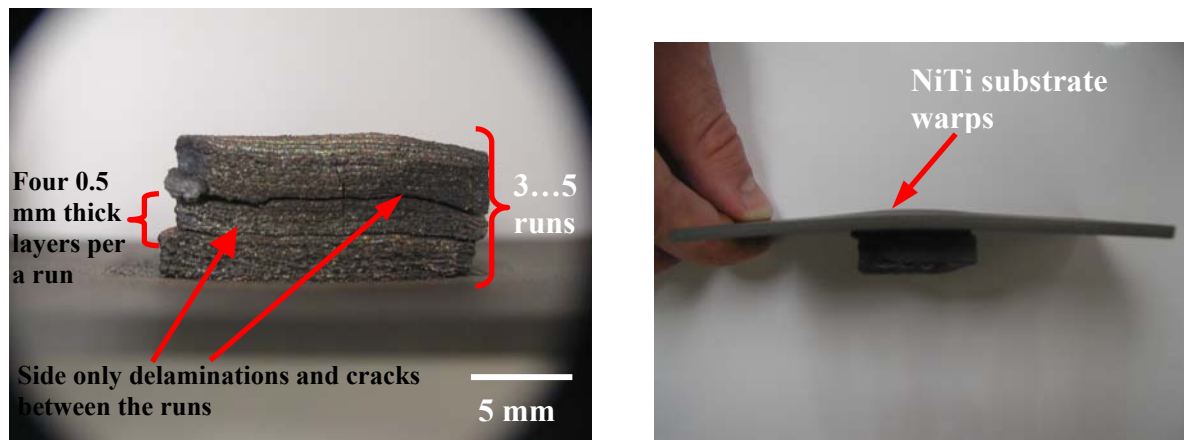


Figure 5.7: Digital camera image of the block part fabricated by DMD from NITINOL powder on NiTi substrate (Ar flow rate = 17.5 l/min, laser power = 350...400 W).



Figure 5.8: *Digital camera image of the NITINOL accordion spring.*

The close-up image of one of the side-views of the spring is shown in Fig. 5.9. Observations of Fig. 5.9 show, that there are two distinct regions that divide the spring into two halves along its height: a non-porous zone in the bottom half, and a highly porous, cracked zone in the upper half. The bottom half is about 2 mm high, the top (porous) half is about 8 mm high. The size of the pores in the top half ranges from 0.01 mm^2 to 0.03 mm^2 with the surface porosity estimated to be equal 6%. Visual observation shows that the porosity of the bottom half of the spring is $\sim 0\%$. The cracks in the top half of the spring were measured and their length ranged from 1 to 6 mm. All the geometrical measurements were done using the software that serves the data acquisition CCD camera of the optical microscope.

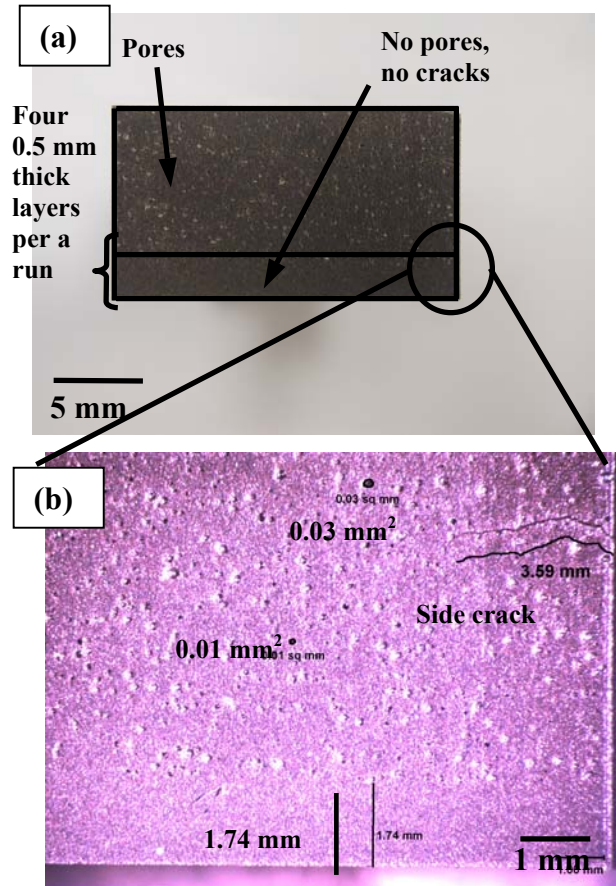


Figure 5.9: Spring: (a) digital camera image of a side view of the spring, (b) optical microscope micrograph of a zoomed region of the spring (Fig. 5.8).

The porosity in the spring structure appears due to the fact that the material stops solidifying and starts re-melting at the “limiting layer thickness” (maximal achievable height) as was discussed earlier in Chapter 3. Melt boils cause the generation of pores during further solidification. Re-melting occurs due to insufficient heat removal from the part during the DMD process. The DMD-EDM fabricated spring was cut by wire EDM into two halves along its height to separate the two zones (Fig. 5.10 a): 1.74 mm high non-porous half and 7.86 mm high-porous half (Fig. 5.10 c). The separation was done in order to study the influence of porosity on the SME thermo-mechanical treatment, which is to be done on both halves of the accordion spring later on. It is anticipated that the non-porous part of the spring will possess a much more

pronounced SME than the porous one. The ultimate goal will be to have a spring that has a 12 mm height without porosity.

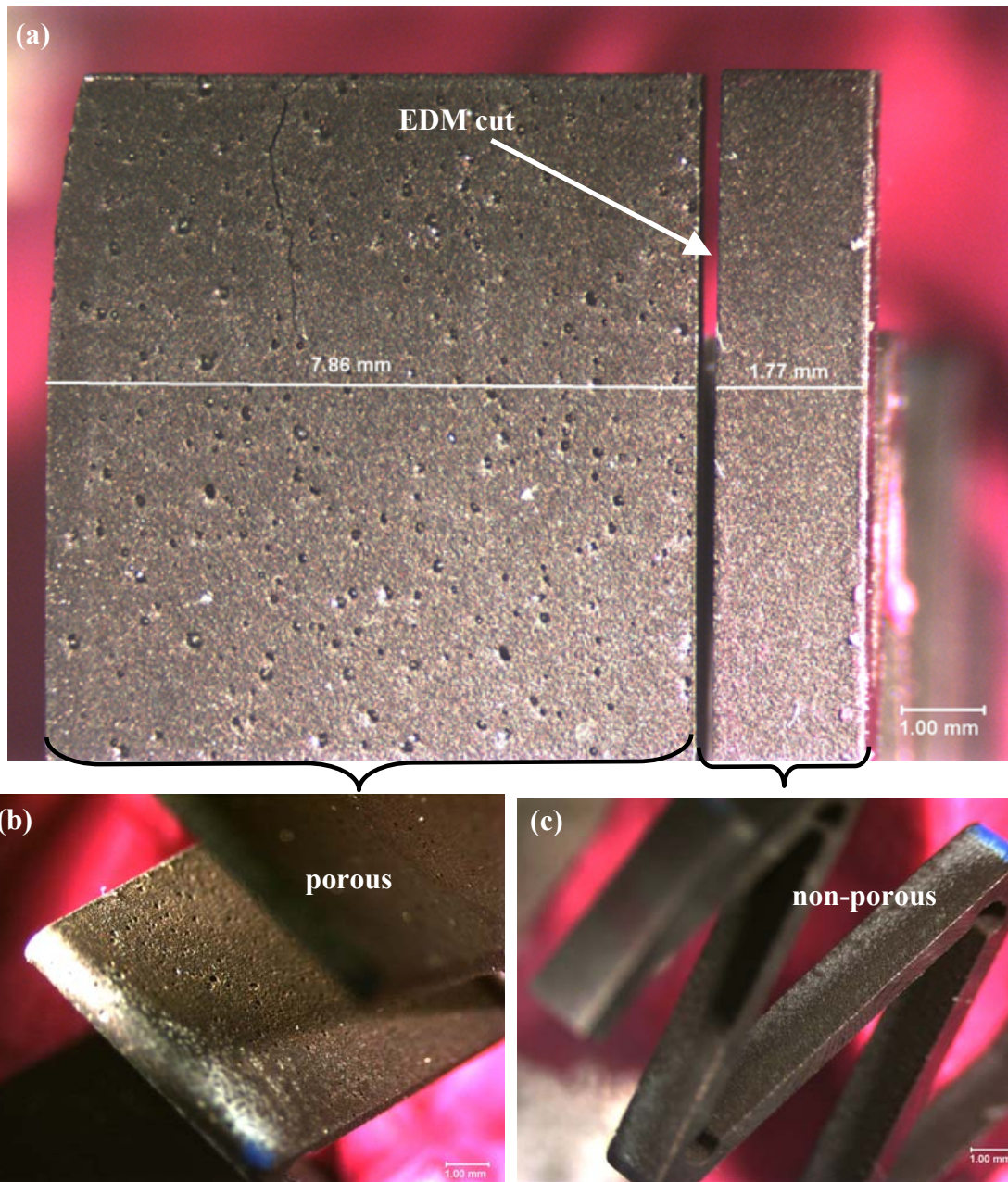


Figure 5.10: Optical microscope micrographs of: (a) SMA spring EDM cut into two halves: (b) porous and (c) non-porous.

5.1.3 One-way (OW) shape memory effect (SME) “training” of the accordion spring

The accordion spring fabricated from NITINOL powder by the DMD-EDM process can work as an actuator provided that the OWSME or Two-Way (TW) SME are imposed on the spring during a thermo-mechanical treatment (“training”). In the current study, the accordion spring actuator, shown in Fig. 5.8, was “trained” to exhibit the OWSME. The OWSME will provide its linear movement. Later on, the TWSME will be used to impose the clamping movement on the grippers of the mMM.

The SME occurs due to the temperature-induced martensite phase transformation that takes place in the accordion spring actuator upon its heating/cooling. The martensite phase transformation is characterized by the TTRs. The procedure of achieving the TTRs in the material (NITINOL), fabricated and processed by DMD, was identified in Chapter 4. According to this procedure, the non-porous accordion spring (shown in Fig. 5.10c) was annealed for 1.5 h in a vertical oven in an Ar atmosphere at 800 °C, at which the solid solution and homogenization of the material occur in NiTi according to the NiTi phase diagram. Afterwards, the spring was quenched in room temperature water. Secondly, the spring was compressed (constrained) with a force F as shown in Fig. 5.11a, annealed in the vertical oven in the Ar atmosphere for 1 h at 423 °C, at which NiTi precipitation hardening occurs and again quenched in room temperature water to form an unstable (monoclinic) twinned martensite structure. These particular parameters for annealing (temperature levels and time intervals) were chosen based on the previously obtained annealing curve in Chapter 4 (Fig. 4.4) to achieve the desired TTRs, as close as possible to room temperature. According to the annealing curve, one can achieve the austenite phase transformation start temperature $A_s = 45$ °C in the NiTi material by means of annealing the

material at the annealing temperature of 423 °C during the second step of the “training”.

After annealing was done, the corresponding DSC measurements were conducted in order to identify all 4 phase transformation temperatures in the material. The DSC thermogram is shown in Fig. 5.11c, where $A_s = 70$ °C, $A_f = 84$ °C, $M_f = 38$ °C, $M_s = 51$ °C. The difference between the targeted A_s (45 °C) and the achieved measured A_s (70 °C) occurs due to the fact that the annealing curve (Fig. 4.4) was obtained for the material with a Ni content in the NiTi slightly different from the one used in the experimental studies in the current chapter. The difference in the Ni content leads to the shift of the annealing curve temperatures.

Testing of the SME was done as follows. The spring was manually pre-stretched to its original length (non-compressed length) to achieve the de-twinned martensite structure in the material. Afterwards the pre-stretching force was removed and the spring stayed in the pre-stretched position. The stretched spring was heated above the austenite finish temperature A_f and recovered its original non-prestretched shape, thus achieving the desirable linear actuation movement. The heating was accomplished by placing the spring on the surface of a hot plate located under an optical microscope equipped with a CCD camera. The camera captured the *in-situ* recovery movement of the spring during heating.

The overall length of the “as-is” SME “trained” accordion spring was 11.47 mm as shown in Fig. 5.11a. After stretching (Fig. 5.11b) the spring in the X-direction by 4 mm and heating it above its A_f temperature (Fig. 5.11c), the spring recovers its original shape as depicted in Fig. 5.11a. Therefore, the linear motion provided by the spring due to the recovery effect was about 4 mm. By increasing the pre-stretched length it is possible to increase the linear recovery motion of the spring. The response time of the actuator - the time it took to completely

recover the shape of the spring upon heating - was about 20 s. This time depends on the magnitude of the heat flux applied to the spring actuator.

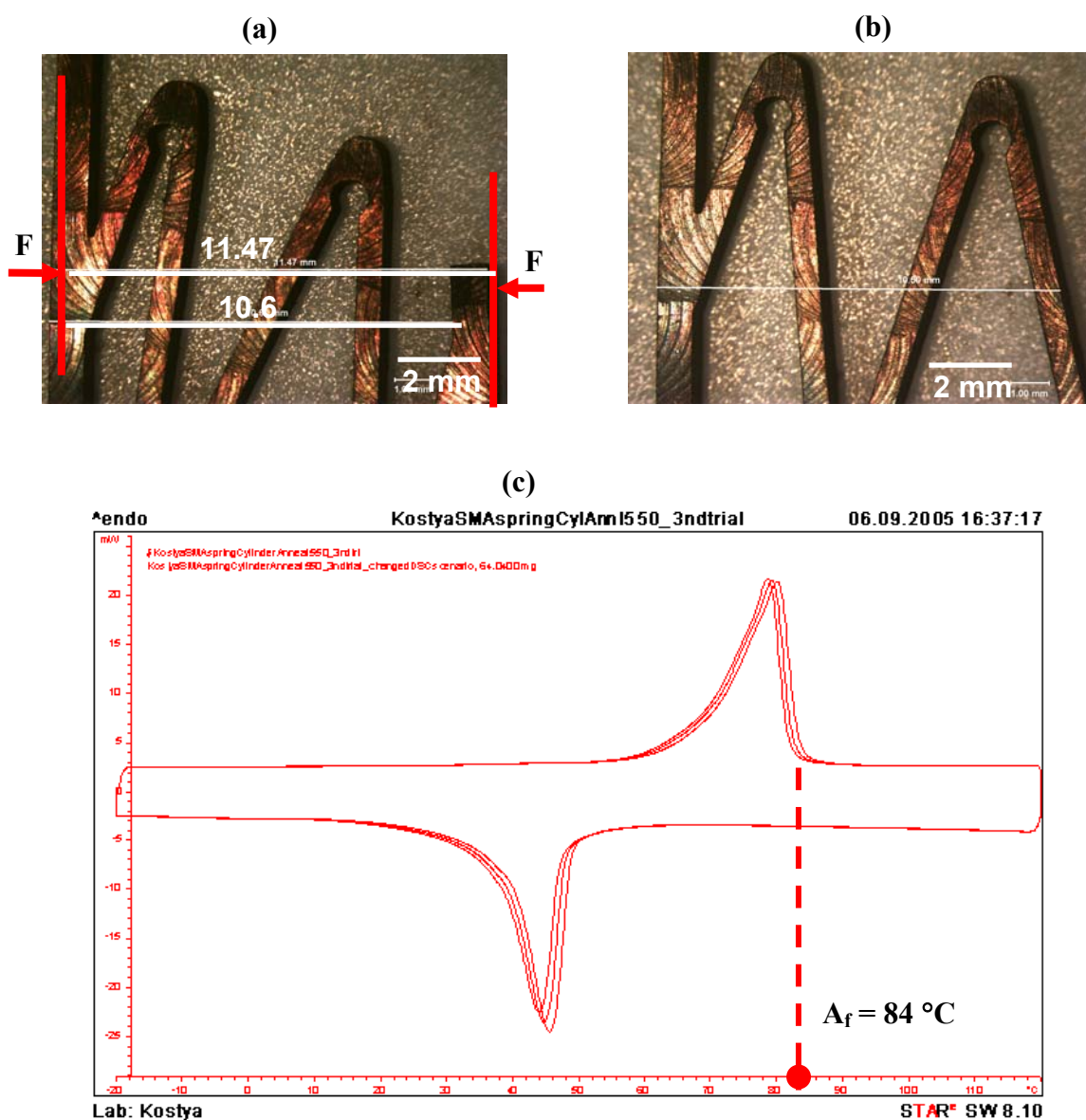


Figure 5.11: SME "trained" accordion spring: (a) optical microscope micrograph of the spring after "training"; (b) optical microscope micrograph of the pre-stretched spring (c) DSC thermogram of the spring material.

5.2 Fabrication of SMA actuators by DMD using the DMD process parameters for building thin-wall structures

The SMA accordion springs, described in section 5.1.1, were fabricated by DMD, using the deposition parameters for building bulk structures. As a result of the deposition, the SMA springs did not possess satisfactory surface finish and quality of the material. Chapter 3 described the experimental investigations using the full factorial experimental design aimed at the identification of DMD parameters for depositing thin-wall structures from NiTi powder. Several vertical thin walls were deposited on a 3-mm thick NiTi substrates as described in Chapter 3. Based on these experimental investigations and the corresponding statistical analysis, a set of parameters for DMD of thin-wall structures was selected and given in Table 5.2.

Table 5.2: *DMD parameters for fabrication of thin-wall structures*

Laser power	200 W
Beam spot size	Not more than 1 mm
Traverse speed (scan speed)	5 mm/s
Z-incremental (layer thickness)	0.381 mm
Shielding gas	Ar, at 5.899 l/min
Carrier gas	Ar, @ ΔP (pressure difference) of 13.79 kPa
Flow rate of powder (set point)	5.78 g/min
Layer thickness	0.2 mm

Four (4) SMA accordion springs were deposited on a 3 mm thick NiTi substrate using the DMD parameters given in Table 5.2. The springs are shown in Fig. 5.12.

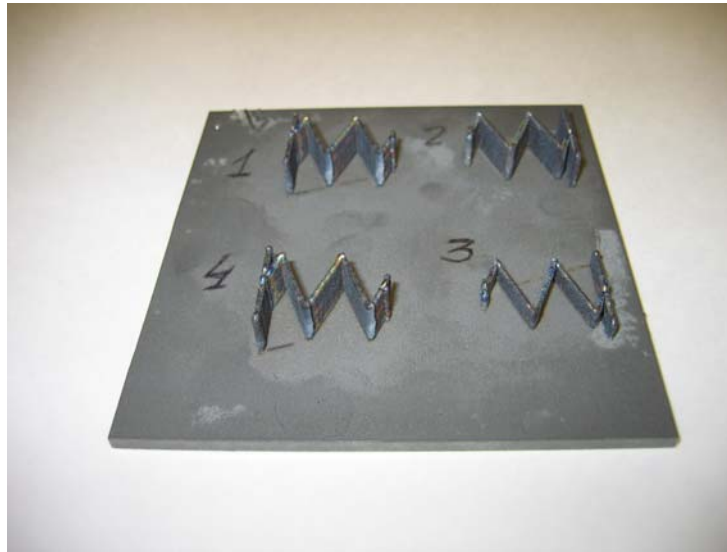


Figure 5.12: *Digital camera image of NiTi accordion springs deposited on NiTi substrate, using DMD process parameters for building thin wall structures.*

It is obvious, that there are no apparent material defects encountered in comparison to the same type of structures shown earlier in Fig. 5.2, i.e., no or very insignificant corner build-ups, no lack of material and a much smoother surface finish (Fig. 5.12). An enlarged image of the “as-is” deposited SMA spring (4), not detached from the NiTi substrate, is shown in Fig. 5.13.

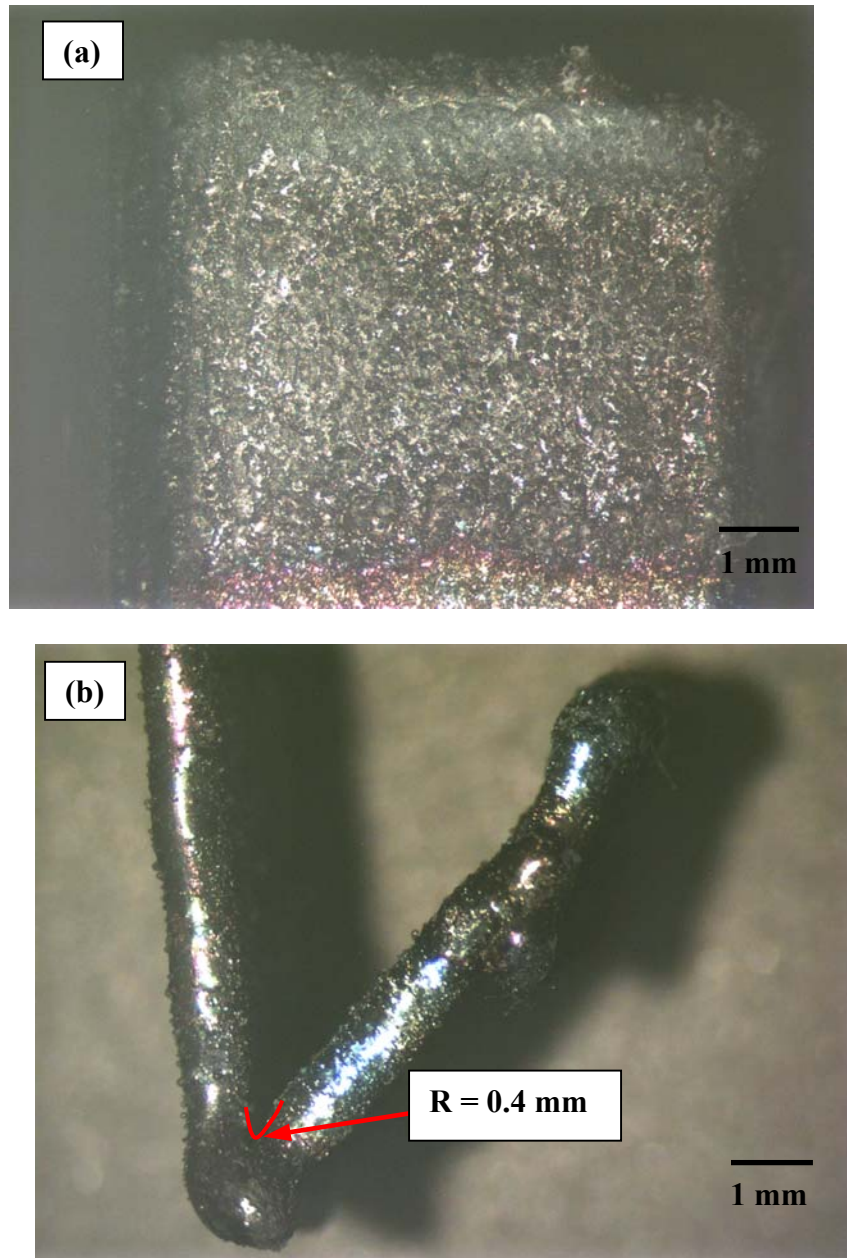


Figure 5.13: *Optical microscope micrographs of the as-is NiTi accordion spring (4), not detached from its substrate: (a) side view, (b) top view.*

It is seen from Fig. 5.13 b, that the smallest feature, the available DMD apparatus was capable of achieving during the fabrication process, was the radius of the corners of the spring. The radius was approximately equal to 0.4 mm.

After the deposition, spring (4) was detached from the NiTi substrate by wire-EDM. The spring was polished and its surface was investigated under an optical microscope (Fig. 5.14).

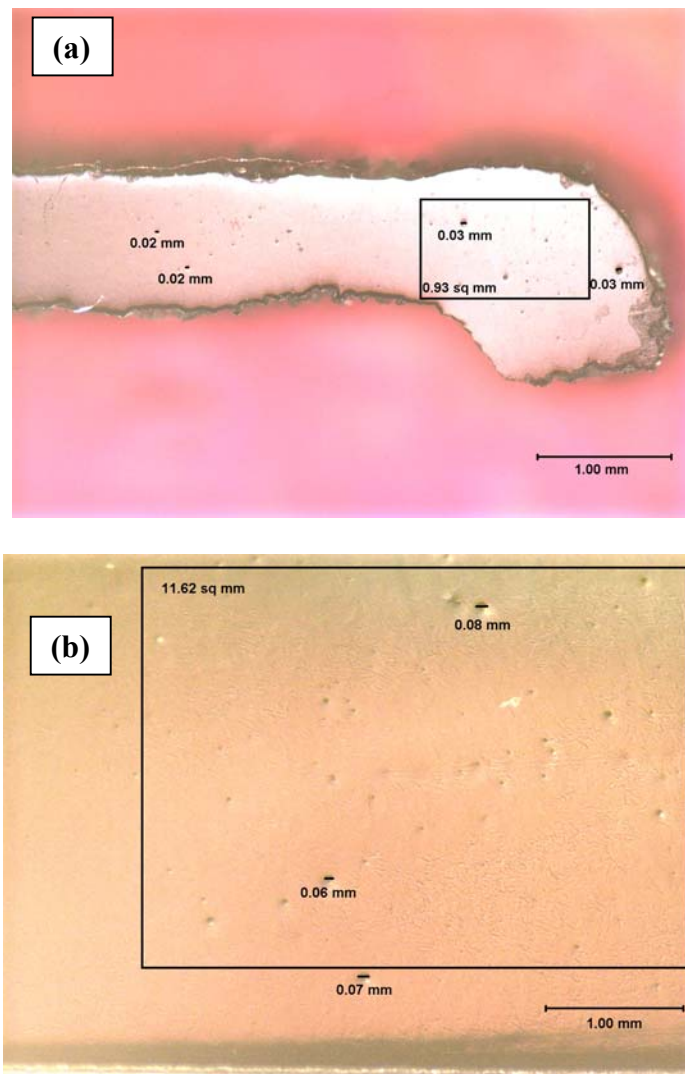


Figure 5.14: *Optical microscope micrographs of the NiTi accordion spring (4), detached from its substrate and polished: (a) top view, (b) side view.*

The amount of porosity in the fabricated spring (4) was estimated from the optical microscope images in Fig. 5.14 a and b and is equal to 1.5% and 1.3 % respectively. The porosity was identified as the ratio of the porous and non-porous areas in the images.

For SME “training” purposes springs (1) and (2) were detached from the substrate by wire-EDM as well. SME “training” of one of the 4 springs was done according to the SME “training” procedure described in Section 5.1.3, thus completing the process of building an accordion spring type actuator. The corresponding DSC thermogram of the material of the SME “trained” spring is shown in Fig. 5.15.

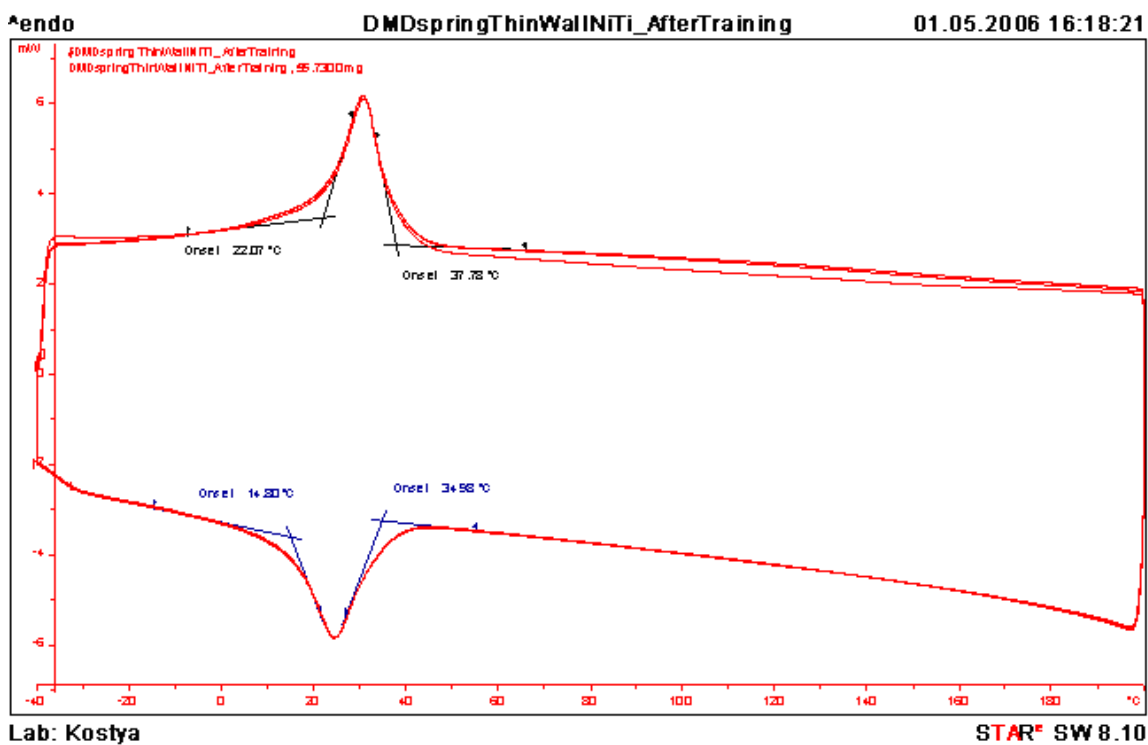


Figure 5.15: DSC thermogram of an SME trained thin wall actuator.

The thermogram (Fig. 5.15) shows a much smaller hysteresis in the TTRs in comparison to the TTRs in Fig. 5.11 - smaller difference in the start and finish temperatures of martensite and austenite phase transformations, namely, $A_s = 37\text{ °C}$, $A_f = 22\text{ °C}$, $M_s = 14\text{ °C}$, $M_f = 34\text{ °C}$. Figure 5.15 shows that the heat flux peaks are obviously pronounced and smooth, which is an indicator of the homogeneity of the material. One of the possible explanations of the decrease in the hysteresis is a change of the Ni content and of the amount of the porosity in the material that

affects the TTRs as was discussed earlier in Chapter 4. In general, the ultimate goal of the SME “training” is to achieve the absence of hysteresis in the TTRs, which is advantageous from the standpoint of the motion control aspects of the SMA actuators.

5.3 Concluding remarks

The results obtained from the experiments with DMD of NiTi powder, show that intermetallics such as NiTi can be used in DMD fabrication of monolithic functional structures, i.e., of the accordion spring actuators that require minimal post-machining. Several SMA actuators were fabricated by DMD.

The springs that were DMD fabricated using the DMD parameters for building bulk structures require a significant amount of post-machining – milling and wire-EDM. Those springs which were DMD fabricated using the DMD parameters for building thin wall structures require a much lower amount of post-machining. The DMD parameters such as laser power, powder flow rate and Ar flow rate need to be varied depending on the type of the fabricated part: bulk- or thin-wall structure. The DMD parameters affect the characteristics of the manufactured material including its porosity, amount of cracks, surface finish and others. An SMA spring actuator was thermo-mechanically “trained” in order to impart the SME in it. The TTRs achieved in the material of this actuator show significant hysteresis. The SME “trained” spring was capable of developing a 4 mm linear motion upon its heating above A_f .

The second actuator, built by using the DMD process for the deposition of thin-wall structures was SME “trained” as well and showed a much lower hysteresis. The decrease in the

hysteresis might be explained by the fact that the second “trained” spring actuator was DMD fabricated using the DMD parameters for building thin wall parts, while the first spring was DMD fabricated using the DMD parameters for building bulk structures. This implies that the parts, manufactured using DMD parameters for building thin-wall structures, have a lower amount of defects in the SMA material, that are known to alter the phase transformation properties, namely the TTR (see Chapter 4).

CHAPTER 6

6. “Self-sensing” property of SMA actuators - resolution, sensitivity and dynamics

The successful implementation of the SME in the SMA accordion spring actuator, described earlier in Section 5.1.3, poses a challenging problem from its motion control standpoint. SMA actuators can be considered as non-linear dynamic systems due to the fact that the phase transformations in SMAs exhibit a certain degree of hysteresis. Since the phase transformation properties drive the SME-induced motion of the actuators, it is advantageous to use these properties for control purposes, thus avoiding extra sensors, increasing robustness and minimizing the working space occupied by the actuators.

SMAs change their crystallographic structure and shape when they undergo phase transformations. Their electrical resistance changes as well. This property allows the use of the electrical resistance change in determining the location of an SMA-based structure in space without separate motion sensors. In this Chapter this “self-sensing” concept will be explored in SMA wires. The SMA wires will be heated/cooled by applying/removing electrical current (resistive heating) to/from them. The resistance change (voltage drop change) across the SMA wire, temperature of the SMA wire and the corresponding displacements of the SMA wire will be measured and analyzed.

Thus, the major goal of this Chapter is to study the possibility of developing SMA-based sensors. This study will be based on the analysis of the relationships between the resistance

change, temperature change and displacement of the SMA wires. The types of the analyzes that will be used in this study are correlation analysis, sensitivity analysis and system identification.

6.1 Control of “self-sensing” actuators

A schematic of a motion control system that uses an SMA sensor is shown in Figure 6.1, where the SMA sensor is also an integral part of the plant that produces the displacement D . Therefore, the analysis of the operation of the SMA sensor itself, in connection with the motion of the SMA structure, constituting the sensor, will be undertaken below.

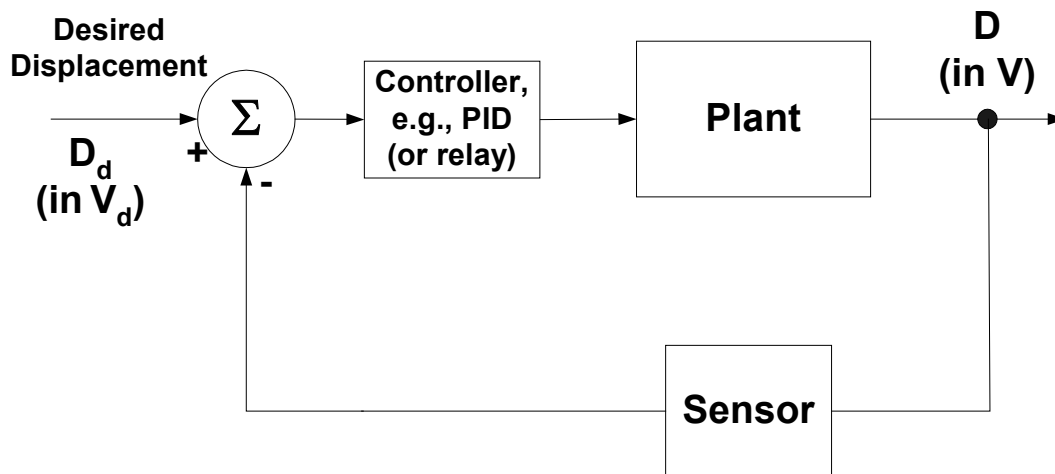


Figure 6.1: *Schematic of SMA-based sensing*

The schematic in Fig. 6.1 shows that the plant-actuator generates a motion when a voltage is applied, thus heating the plant. The resistive heating of the plant creates the SME driven motion. The heating also changes the plant’s properties, namely the electrical resistivity of the material (SMA) of the plant. Therefore, the plant can also operate as a “sensor” of the generated motion,

by correlating the property change with the motion (displacement of the plant). The “sensing” behavior of the SMA actuator will be referred to in this work as the “self-sensing” principle and will be used in the development of the mMM control system. The possibility of this concept to be used for the motion control of the mMM will be explored in this Chapter.

6.1.1 The “self-sensing” principle

The “self-sensing” principle is described as follows. The SMA structure is pre-deformed by an external force (e.g., by a bias spring) at room temperature at which the SMA material is in its martensite state. In case of the SMA wire, the pre-deformation is imposed by stretching the wire to its maximal length. Electric current is applied to the pre-deformed SMA structure, thus heating it above its A_s temperature and causing its displacements due to the SME based recovery motion, during which the SMA material converts to the austenite state. During this motion the electrical resistance of the structure changes and the change in the corresponding voltage drop is measured using the 4-point method. Figure 6.2 shows the principle of “self-sensing” in which a electrical current is passed between the two outer points, thus heating the structure and causing the phase transformation. The voltage is measured between the two inner points. The voltage drop can then be converted to change in electrical resistance and correlated to the SMA structure’s displacements.

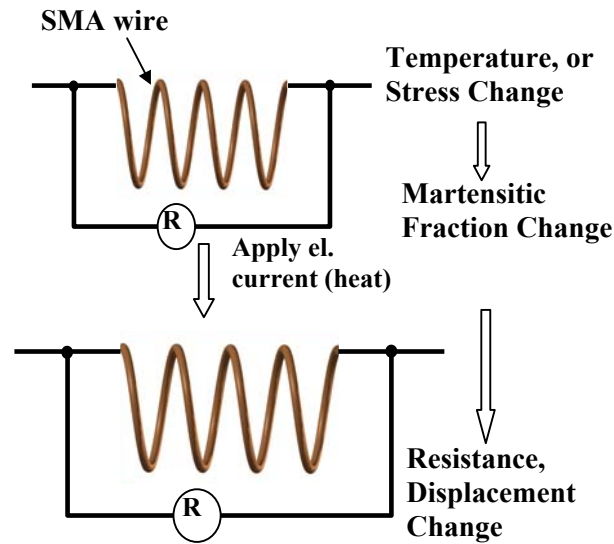


Figure 6.2: Principle of the integral sensing (“self-sensing”) system.

During the martensite-austenite transformation the electrical resistance of the SMA structure changes. This change is related to the recovery motion and provides the information about the location of the SMA structure, thus serving as a motion sensor.

6.1.2 mMM actuation

During the resistive heating of the mMM, electrical current is applied directly through the mMM’s structure, namely through the accordion springs, thus making them move in the X-Y directions due to the SME. The distribution of the electric currents in the mMM under different electrical (heating) loads is further analyzed.

The linear stage, that provides the X-Y motion of the mMM, consists of 3 elements (Fig. 1.1), i.e., four accordion springs, the center point and the base. The accordion springs are

attached to the base and connected between each other through the center point. The accordion springs are in the annealed condition, and, therefore, have a lower electrical resistance than the non-annealed center point and the base. There exist several possible scenarios of heating the accordion springs, e.g.: (a) application of electrical current to only one of the springs at a time; and (b) application of electrical current to several springs simultaneously. During Scenario (a) only the spring that is under the electrical current serves as the actuator, while the other (non-heated) springs serve as bias springs. During Scenario (b) more than one spring may serve as the actuator.

In this chapter, for simplicity, Scenario (a) will be analyzed. Therefore, the electric current will be considered to be applied to only one, out of the four, accordion springs at a time. The rest of the mMM's structure must be under no electric current to prevent it from heating. Since the mMM represents a monolithic metallic structure, there exists a possibility of having extra parasitic electric currents besides the actuation electric current, that heats the accordion spring.

The mMM structure can be treated as an electric circuit whose elements serve as their own corresponding electrical resistances. Figure 6.3a shows all possible electrical connections between the elements, thus composing the electrical circuit in Fig. 6.3b.

The electrical resistances in the circuit can be subdivided into two types (Fig. 6.3): constant electrical resistances denoted by “ r ” and variable electrical resistances denoted by “ R ”.

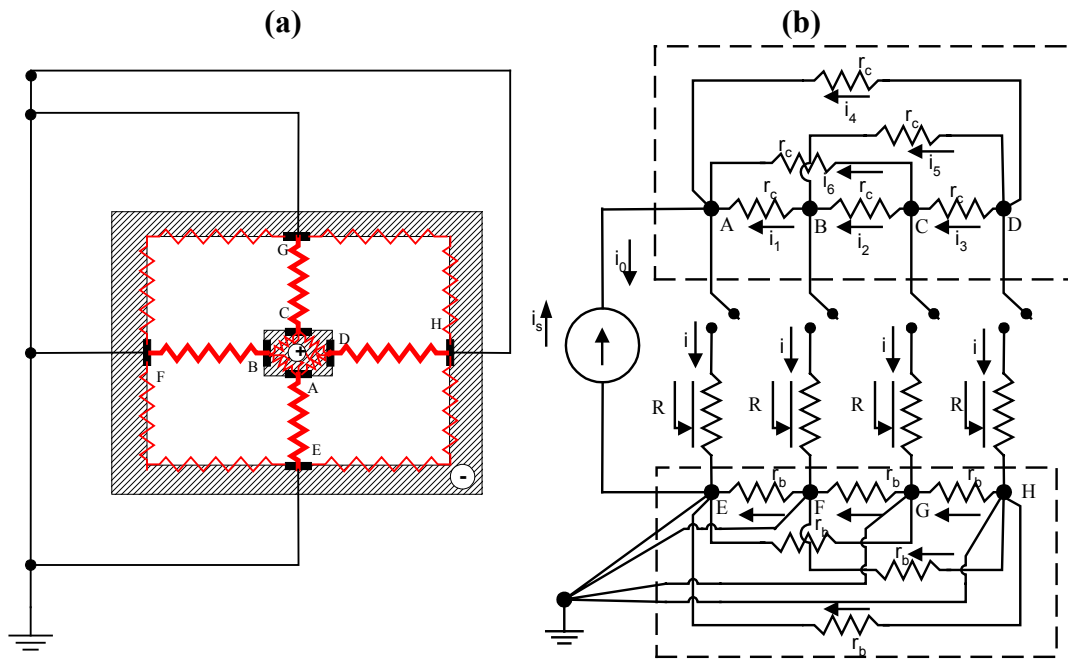


Figure 6.3: *mMM linear stage: (a) electrical layout; (b) electrical circuit diagram.*

The annealing of the springs imposes on them the property of undergoing a phase transformation when cooled or heated. Therefore, the springs will exhibit variable electrical resistances, alternating between the austenite phase resistance when hot and the martensite phase resistance when cold. This is why, the four accordion springs are represented by variable resistances (pots) “R”. The electrical connections between the adjacent springs and the center point are treated as constant resistances and are denoted by “ r_c ”. The electrical connections between the adjacent springs and the base are treated as constant resistances, and shown as “ r_b ” in Fig. 6.3 b. Possible parasitic currents will flow through the electrical connections denoted as “ r_c ” or “ r_b ”. There are 6 possible connections “ r_c ” and 6 corresponding parasitic currents $i_1 \dots i_6$ going through those electrical connections.

Electric circuit analysis was performed to estimate the distribution (direction) and magnitude of all the possible parasitic electric currents that could exist in the linear stage. In Fig. 6.3b the points, denoted by A, B, C, D, E, F, G, and H are the connection points (electrical nodes) between different electrical resistances (or physical elements represented by their own electrical resistances). Relays # 1, 2, 3, 4 are used to turn on/off the electrical current in the corresponding accordion springs. When a constant electrical current “ i_s ” is applied to the circuit and Relay j is closed ($j = 1, 2, 3, 4$) in Fig. 6.3 b, it creates a corresponding electrical current “ i ” through that spring. The other three relays stay open (no electrical current is flowing through the springs) preventing the corresponding three springs from resistive heating.

The distribution and magnitudes of the electrical currents in the equivalent electrical circuit can be formulated according to Kirhgoff’s laws. The electrical nodes were identified as follows: A, B, C, D – non-referenced nodes with unknown voltages U_A, U_B, U_C, U_D , and nodes E, F, G, H – referenced (ground) nodes with known voltages $U_E = U_F = U_G = U_H = 0$.

It was assumed, that during one heating cycle only one relay (e.g., Relay #1) is closed, while the other three relays stay open, therefore, $U_A = U_B = U_C = U_D$.

The other assumptions and notations used in the analysis are:

- resistivity of the annealed accordion springs is 5 to 6 times lower than the resistivity of the non-annealed base and center point, $\rho_r \cong (5 \text{ to } 6)\rho_R$ - resistivity of SMA;
- the magnitude of the constant source of the electrical current $i_0 = -i_s$.

The corresponding Kirhgoff’s law equations written for each electrical node are as follows:

Node A:	$-i_0 - i + i_6 + i_1 + i_4 = 0$
Node B:	$-i_1 + i_2 + i_5 = 0$
Node C:	$-i_2 + i_3 - i_6 = 0$
Node D:	$-i_4 + i_3 - i_5 = 0$
R:	$i = (U_A - 0)/R$
r_c, i₁:	$i_1 = (U_B - U_A)/R = 0$
r_c, i₂:	$i_2 = (U_C - U_B)/R = 0$
r_c, i₃:	$i_3 = (U_D - U_C)/R = 0$
r_c, i₄:	$i_4 = (U_D - U_A)/R = 0$
r_c, i₅:	$i_5 = (U_D - U_B)/R = 0$
r_c, i₆:	$i_6 = (U_C - U_A)/R = 0$

By solving the above system of equations one obtains $i = -i_0 = i_s$. All other electrical currents (parasitic electrical currents $i_1 \dots i_6$) are equal to zero (see equations for nodes A, B, C, and D above). In order to reach the desired level of the phase transformation temperatures in the SMAs (NiTi) and based on the geometry and mass of the accordion springs, the desired value of i_s ranges between 1...10A (depends on the level of the TTR in the SMA). This electrical current will provide the necessary heat flux needed to actuate the spring.

The electrical circuit analysis shows that there are no parasitic electrical currents (all possible currents are equal to zero) in the electric circuit diagram (Fig. 6.3b) and, therefore, it does not matter if the base and center point are electrically conductive or not (since no parasitic electrical currents exist). In the case, when more than one relay is closed, there will be no

parasitic electrical currents either, provided that each accordion spring is actuated by a common current source as shown in Fig. 6.3b. It is also clear, that the 4-point method, described above, is a suitable method for measuring the resistance change and hence the motion of the mMM.

6.1.3 Working ranges of the sensor

The SMA “self-sensing” sensor can be used both as a linear and a non-linear response sensor. The SMA sensor exhibits a linear response (linear relationship between resistance and displacement) when the SMA material experiences an incomplete phase transformation, which can be explained by using any DSC thermogram. The heat flux peaks in the thermogram in Fig. 6.4 show the non-linear behavior of the phase transformation (change of the slope of the thermogram curve through the points A, B and C). If the transformation is incomplete, for example, less than half of the peak through points A and B, then the heat flux is a linear function of the temperature in that region.

The incomplete transformation (section between points A and B in Fig. 6.4) produces small range displacements in comparison to the complete transformation. Therefore, during the incomplete transformation the SMA sensor can be used as a motion sensor with linear characteristics for measuring small displacements. In our studies, small displacements of the SMA wire are considered displacements that are less than 1 mm.

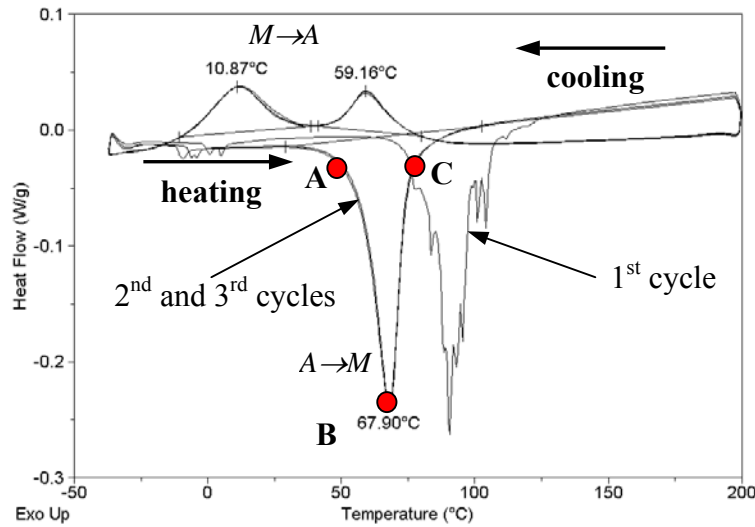


Figure 6.4: DSC thermogram of the SMA wire.

The SMA sensor exhibits non-linear response characteristics during the complete phase transformation cycle (points A-B-C in Fig. 6.4), following the same logic as described above, namely, the dependence of the motion of the SMA structure on the voltage drop in the SMA due to phase transformation is a non-linear function to be determined later. Therefore, the sensor can be used as a motion sensor with non-linear characteristics for measuring large displacements. The following corresponding experimental studies will be aimed at the investigation of the characteristics of the sensor used for both small and large displacement measurements.

6.2 Experimental setup and experimental procedure

An SMA wire was used in the “self-sensing” principle studies. A wire was chosen because the wire can be represented by a simple spring and damping elements and, therefore, can be easily analyzed. The “self-sensing” principle will be studied here according to the following procedure. An SMA wire will be stretched at room temperature and heated by applying an

electrical current through the wire. Heating will cause contraction due to the SME and, therefore, the wire will operate as an actuator. The electrical resistance change in the wire will be monitored by measuring the corresponding voltage drop change. The wire temperature change and the contraction displacement of the wire will be measured as well. The description of the experimental setup and procedures for testing the “self-sensing” concept in the SMA wire based actuator follows.

6.2.1 Experimental set-up

The evaluation of the principle of integral sensing (“self-sensing”) is verified by a setup constructed to monitor the position of the end-point movement of a commercially available SMA wire (TEFLON insulated FLEXINOL wire obtained from Dynalloy, Inc) due to its temperature change. The FLEXINOL wire has a diameter of 0.254 mm (0.01 inches) and a length of 228.6 mm (9 inches). The TTRs in the FLEXINOL wire were measured, and the results are shown in the DSC thermogram in Fig. 6.4. Three heating/cooling cycles were undertaken in the DSC measurements. The first heating cycle of the DSC measurements shows that the phase transformation from martensite to austenite ($M \rightarrow A$) occurs at higher temperature levels in comparison to the second and third cycles that overlap between each other. This happens due to the existence of residual stresses in the “as-is” SMA wire.

The experimental setup consists of the SMA wire, an air-bearing linear stage, measurement system and data acquisition system (DAQ) and LabView software to record all the measured signals.

The schematic of the experimental setup is shown in Fig. 6.5. The air-bearing stage has a zero coefficient of friction and as such it is an ideal device to test the SMA wire actuator's performance.

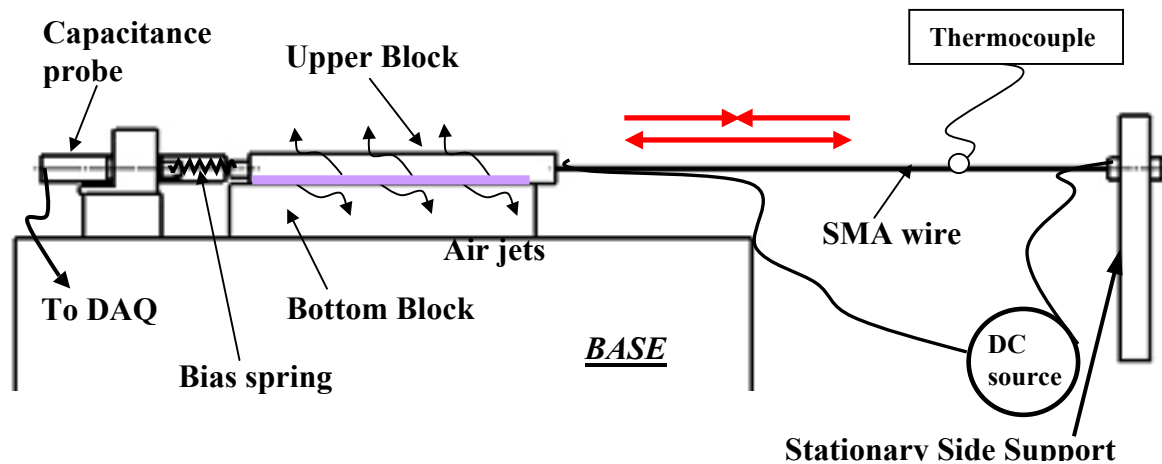


Figure 6.5: *The SMA wire based linear stage.*

The air-bearing linear stage includes an air bearing that provides the axial movement of the Upper Block with respect to the Bottom Block as depicted in Fig. 6.5. One of the ends of the SMA wire is connected to the Upper Block while the other end is connected to the stationary Side Support, which is, in its turn, connected to the bias spring in series. The displacement of the SMA wire is measured by measuring the movement of the Upper Block by a capacitance probe (ASP-20-CTA). A DC source (Tektronix PS 280) is connected to the SMA wire to supply a DC voltage V_0 to it. Upon the application of the voltage the SMA wire shrinks and moves the Upper Block. The displacements of the block, measured by the capacitance probe, are recorded by a

data acquisition card DAQ (CIO-DAS08/Jr-AO, ± 5 V full scale range, 0.0024 V resolution).

The electrical schematic of the setup is given in Fig. 6.6.

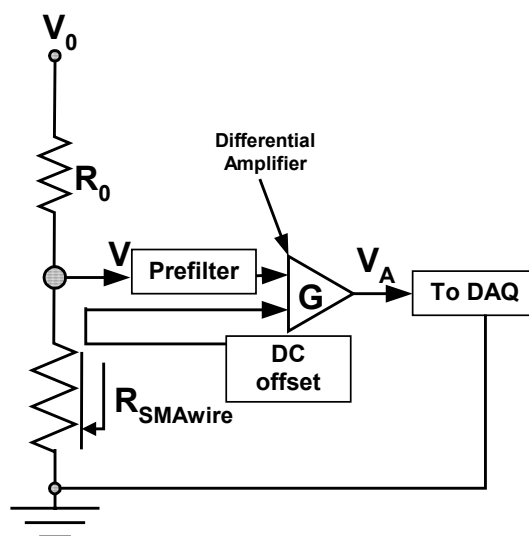


Figure 6.6: *Electrical schematic.*

During the heating process the reference voltage V is amplified using a differential amplifier and the amplified voltage V_A is recorded by the DAQ. The DC offset of the amplifier is powered by a DC power supply BK Precision 1610 (30 V, 1 (0.5) A). The DC offset is used in order to maintain the measured amplified voltage within the full scale (FS) of the DAQ, i.e., within ± 5 V.

V_A indicates the amount of the resistance change in the SMA wire upon its heating. The SMA wire temperature is measured by a K-type thermocouple (“Omega Engineering”, dia. < 0.01 inch.) attached to the wire. The thermocouple was used in conjunction with a calibrated digital readout from “Omega Engineering”. The temperature was recorded by the DAQ.

The MTI capacitance probe signal was amplified by an MTI amplification system (ACCUMEASURE-1000). The probe was calibrated to measure displacements in its linear range

from 0 to 1 mm. This calibration (see calibration curve #1 in Fig. 6.7a) can be used for measurements of small displacements. In order to measure large displacements, the probe was additionally calibrated in its linear and non-linear range from 0 to 15 mm (see calibration curve #2 in Fig. 6.7b). Depending on the particular experiment (large or small displacement measuring range), either the calibration curve #1 or #2 was used during the data acquisition process. The conversion was done based on the calibration equations (shown in Fig. 6.7a and b) in the LabView program, that was created and used to acquire the signals from the capacitance probe, the thermocouple, and the reference and amplified voltages in all the experiments.

In addition, the amplified probe signal and the amplified voltage signal V_A were filtered by two Wavetek 852 analog low pass filters.

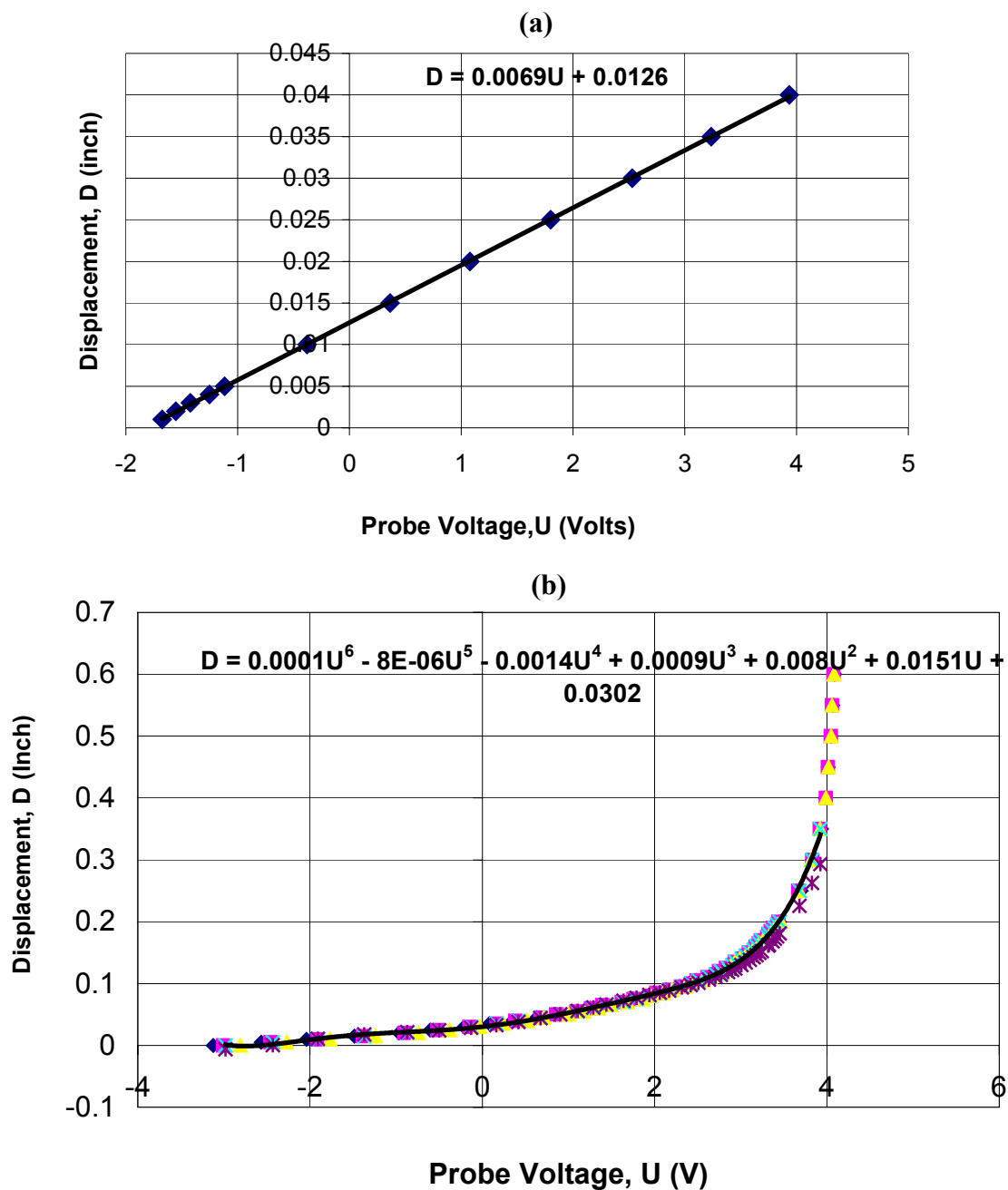


Figure 6.7: Calibration curves: (a) #1 (for small displacement) and (b) #2 (for large displacements).

6.2.2 Experimental procedure

The experiments were performed under controlled strain recovery conditions. Controlled strain recovery is defined as SME driven displacements restricted by an externally applied stress. For example, a bias spring is connected to one end of the SMA wire while the other end is being fixed as shown in Fig. 6.8. While recovering its shape during the heating process, the wire will have to overcome the force imposed by the spring.

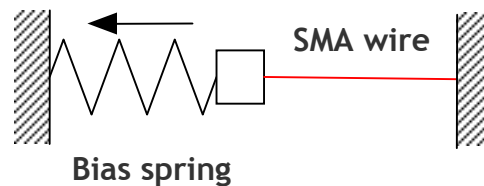


Figure 6.8: *Controlled recovery schematics.*

The experimental procedure followed in all the experimental series was the following:

- (a) depending on the task the SMA wire was either pre-stretched or non pre-stretched at room temperature,
- (b) the initial voltage V_0 (Fig. 6.6) of the DC source was set to the desired value,
- (c) the voltage V_0 (the thermal load) was applied to the SMA wire in a step-like way. The corresponding SMA wire displacement D , voltage V_A (Fig. 6.6) and temperature T responses versus time were measured by the DAQ and recorded into a text file using the LabView software. The voltage V_0 was varied between 4 and 5 volts. The resistance R_0 in the voltage divider circuit was about 2Ω .

The step responses of the thermally insulated and thermally non-insulated SMA wires due to the thermal load were studied. Fifty seven (57) controlled strain recovery experiments

were conducted. Controlled strain recovery most closely resembles the working conditions of an actuator because of the way the bias spring and the SMA wire are connected together. Of the 57 experiments, 37 experiments were conducted with the SMA wire without and 20 with thermal insulation. The thermal insulation was provided by cotton wool wrapped around the wire. All the experiments differed in the magnitudes of the SMA wire pre-strain, amplification gain G and applied voltages V_0 . Pre-stretched length was measured by a ruler with respect to the initial non-stretched length L_0 of the wire.

The reason for using the insulation was the fact that the air-bearing was generating turbulent air jets (Fig. 6.5) that affected the temperature of the SMA wire by creating a forced convection environment around it. In this case, the temperature of the wire was not stable and the temperature fluctuation range was up to 10 °C with respect to the SMA wire's average temperature. The temperature fluctuations created fluctuations in the displacement of the SMA wire due to the on-going phase transformations caused by rapid cooling and heating. As it will be shown, both fluctuations in temperature T and displacement D , were pronounced and qualitatively similar to each other.

Since the capacitance probe's measuring capability was limited to the probe's maximal linear measuring range from 0 to 1mm, the probe was shifted manually every time the SMA wire displacement D exceeded the maximal range.

The DC offset of the differential amplifier (Fig. 6.6) was also adjusted every time when the measured voltage V_A was out of the DAQ's FS range.

6.3 Experiments with small displacement range sensing

Experimental results were obtained according to the experimental procedure described in the section 6.2.2 for small range displacements. An example of the typical results is given and analyzed below.

6.3.1 Step response of the thermally non-insulated SMA wire actuator

A typical set of step response results consisted of measurements of the wire's displacement, D , the corresponding amplified reference voltage change, V_A , and the temperature change, T . The results from one of the experiments are depicted in Fig. 6.9 a, b, c. The controlled strain recovery test in Fig. 6.9 was conducted with the non-prestrained non-insulated SMA wire heated at room temperature heat sink conditions. The bias spring was attached to the Upper Block (Fig. 6.5). The initial tension provided by the spring through the block to the wire was small and was used only to straighten the wire without pre-straining it.

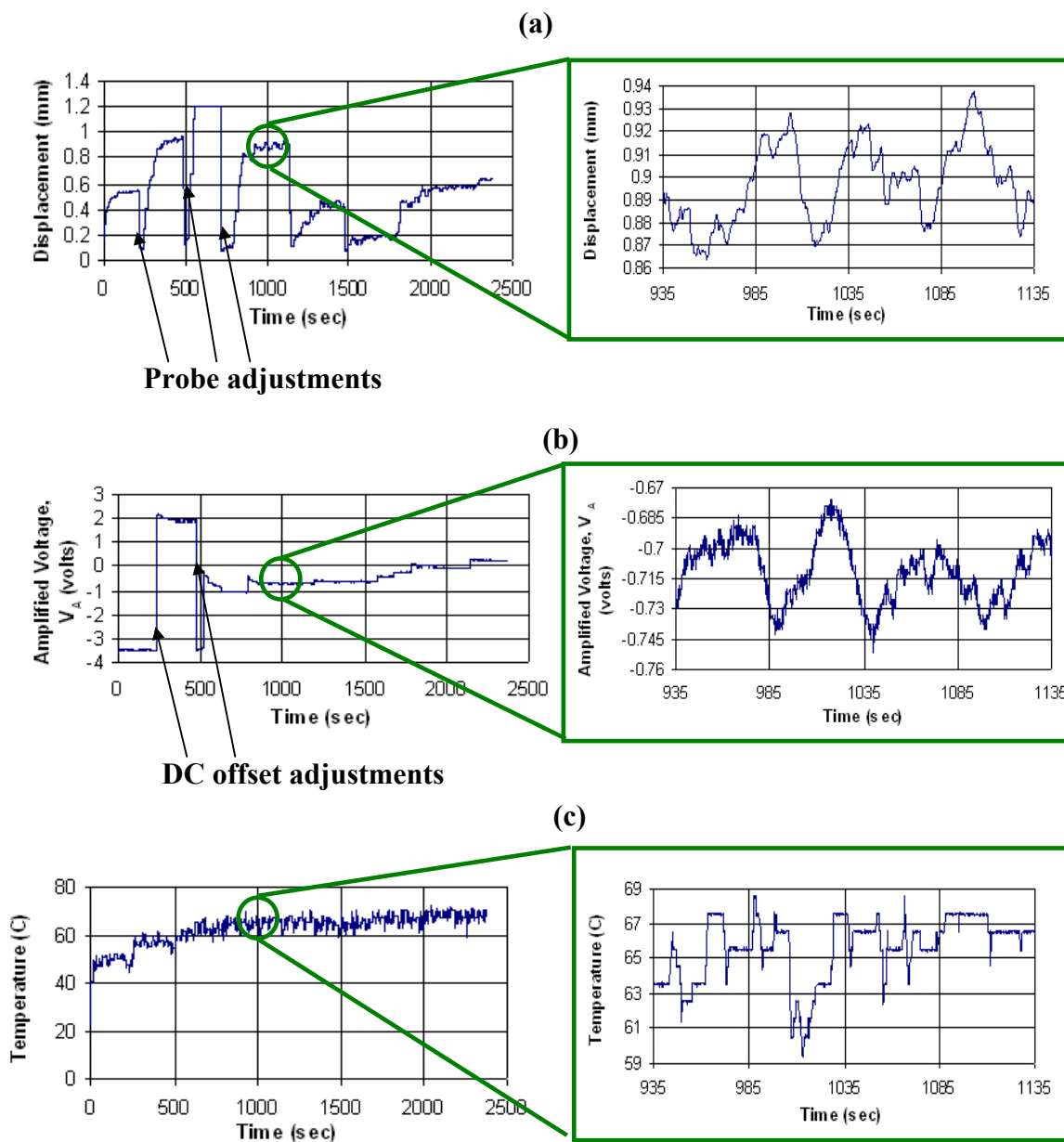


Figure 6.9: Controlled strain recovery of the non-prestrained SMA wire: (a) SMA wire displacement, D , (b) amplified reference voltage, V_A , (c) SMA wire temperature, T .

The DC offset adjustments (according to the experimental procedure above) are clearly visible in Figures 6.9 a and b and are characterized by the discontinuities in the plots. The general trends of the experimental results show that when the temperatures and the

displacements of the SMA wire increase, the electrical resistance (or the voltage V_A) decreases correspondingly. Due to the presence of forced convection (from the air-bearings) that resulted in fluctuations of the temperature T , the step response of the SMA wire represented by the displacement D and voltage V_A signals, did not stabilize at the end of the response transients. One can notice the corresponding instabilities from the corresponding zoomed parts in Figures 6.9 a, b, and c. Furthermore, the analysis of the response shows, that the fluctuations of the magnitudes of the displacements, D , are directly proportional to temperature fluctuations, T . In contrast, V_A fluctuations are inversely proportional to the temperature, T , fluctuations with some time delay. The time delay is largely related to the thermal inertia of the wire.

6.3.2 Step response of the thermally insulated SMA wire actuator

In order to remove the fluctuations from the signals D , V_A and T , the SMA wire was thermally insulated. Cotton wool was wrapped around the wire. The results from one of the corresponding controlled strain recovery tests are shown in Fig. 6.10. The wire was given an initial pre-strain of 2.77 %.

The major goal of these experiments was to achieve micron level displacements of the SMA wire actuator.

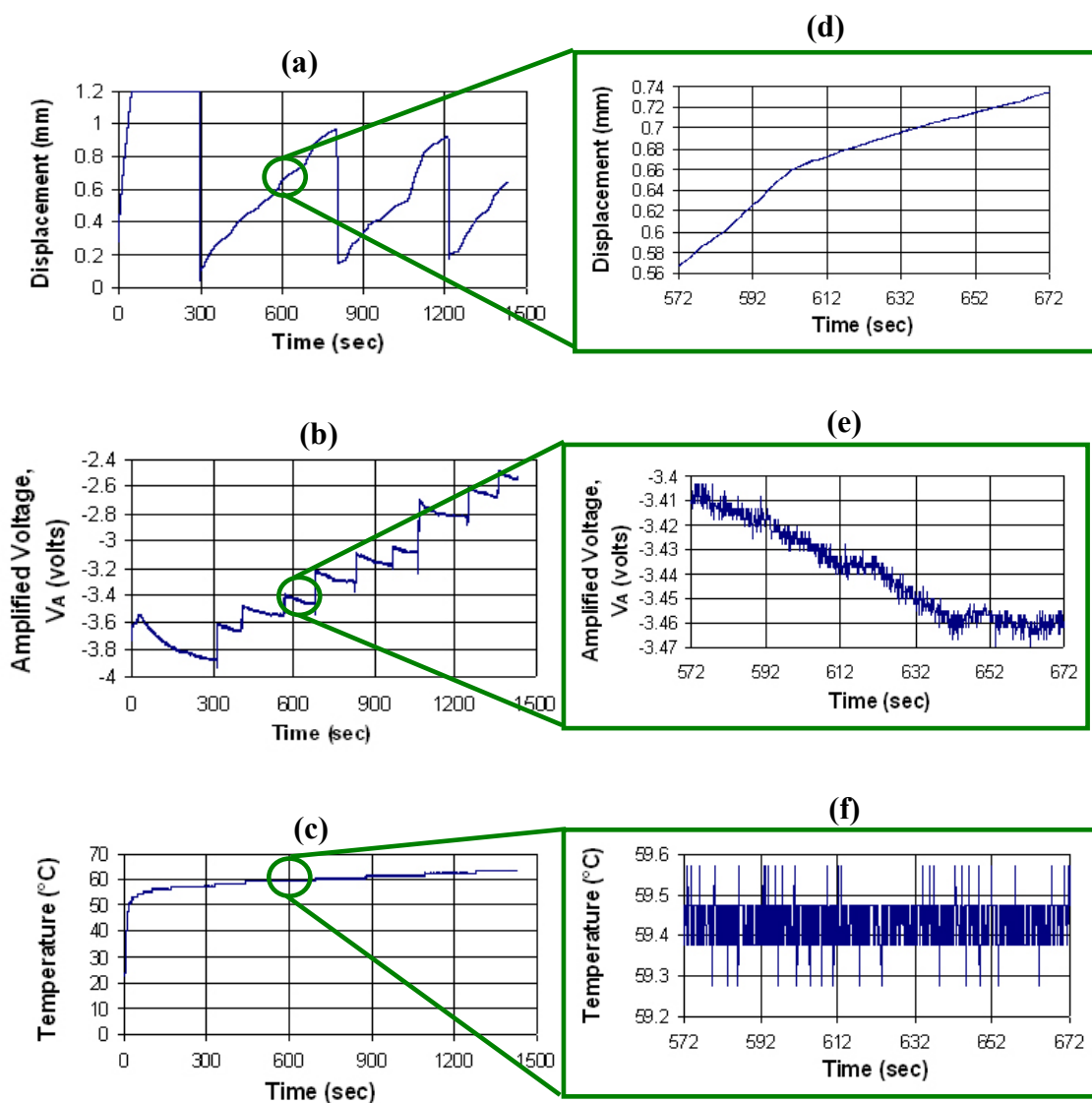


Figure 6.10: *Controlled strain recovery of the initially pre-strained (2.77% strain) thermally insulated SMA wire: (a) SMA wire displacement, D , (b) amplified reference voltage, V_A , (c) SMA wire temperature, T , (d) zoom of (a), (e) zoom of (b), zoom of (c).*

As it was shown in the previously described experiments, with an increase in the wire's contracting displacement upon heating (Fig. 6.10 d), the wire's electrical resistance decreases

(Fig. 6.10 e). The average displacement step was about $200\ \mu\text{m}$ (Fig. 6.10a). It is seen that such a small contraction of the wire occurs almost isothermally (Fig. 6.10f).

The presence of thermal insulation has significantly improved the quality of the SMA wire's response, but has also slowed it down. The improvement manifests itself in the absence of fluctuations in the measured displacement (Fig. 6.10a) and temperature (Fig. 6.10c) in comparison to the same quantities in the experiments with thermally non-insulated wire (e.g., in Fig. 6.9).

6.3.3 Correlation analysis

It is important to identify the correlation between the voltage, V_A , and the displacement, D , since the measured voltage V_A , most truthfully reflects the load history of the wire (its thermal and stress states), which can be used for motion control purposes of the SMA wire actuator by using the corresponding electrical resistance change (due to the measured voltage) in the wire as a feedback signal.

The analysis can be done on the signals subject to periodic change. Therefore, the analysis is done using the experiments with the thermally non-insulated SMA wire, where the absence of the thermal insulation allows the periodic change in the temperature (above its A_s level) of the wire due to the change of the heat sink conditions around the wire (see Fig. 6.9a). The wire gets periodically heated and cooled, and therefore, it produces periodic contracting and expanding displacements and voltage drops, which serve as the input to the correlation analysis.

Based on similar experimental studies by other researchers [Lee et al., 2001; Tohyama et al., 2001], it is assumed, that the measured voltage is proportional to the electrical resistance of the wire, which is, in turn, proportional to the martensite phase fraction change during the heating/cooling process. A portion of the value of the electrical resistance change, which is due to the geometrical change of the wire during its contraction or expansion, is neglected in this study due to its small magnitude. For example, a change in the length of the SMA wire of 200 μm yields a change in its resistance $\Delta R = 0.0039 \mu\text{Ohm}$ (here, the austenite resistivity = 1 $\mu\Omega\text{m}$). In order to determine the correlation between T, D, and V_A signals, three corresponding correlation coefficients were calculated using the MatLAB “corrcoeff” function. The results are shown in Fig. 6.11. The “corrcoeff” function computes Pearson’s correlation coefficient between any two signals (variables). The advantage of using Pearson’s correlation is that it removes the noise and the mean from the signals. In addition, it is possible to approximately define the time constant of the actuator’s response by evaluating the correlation function for different time lags between any of the two signals as shown in Fig. 6.11a. A total of 263 subrecords of 1200 experimental points each (window size) were used in the calculations of the coefficients. The experimental points are the values of the measured signals, acquired during the tests.

An important factor that characterizes the quality of the correlation coefficient is the homoscedasticity or homogeneity of the degree of variation of one of the variables with respect to the other one. As shown in Fig. 6.11b, the measured displacement D almost uniformly varies with the change of the amplified voltage V_A , meaning that the correlation coefficient gives a uniform estimation of the displacement change, D, with respect to the voltage change V_A .

Several experiments with different levels of pre-strain in the SMA wire were conducted. The correlation coefficients between temperature and displacement, R_{TD} , temperature and voltage, R_{TV} , voltage and displacement, R_{VD} , were calculated for each experimental set of the measured signals. The coefficients show how the relation between the signals changes in terms of linearity when the initial pre-strain of the SMA wire changes. For a comparison, some of the correlation coefficients are shown in Table 6.1.

Table 6.1: *Correlation coefficients*

Pre-strain, %	R_{DV}	R_{TD}	R_{TV}
	Time Lag, sec	Time Lag, sec	Time Lag, sec
0	-0.97 1.024	0.9 -4.1	-0.93 -4.29
0.69	-0.59 0.96	0.89 -0.58	-0.54 -2.11
0.347	-0.48 1.67	0.87 -0.9	-0.41 5.25
4.16	-0.74 5.5	0.81 1.41	-0.47 6.91

The results of the calculation of the correlation coefficients for the experiments with the thermally non-insulated wire with an initial pre-strain equal to 0% are shown in Fig. 6.11. Figure 6.10a shows that all three correlation coefficients are close to unity at around the zero seconds time lag: $R_{DV} = -0.9661$ at time lag = 1.024 sec, $R_{TD} = 0.8999$ at time lag = -4.096 sec, and $R_{TV} = -0.929$ at time lag = -4.288 sec.

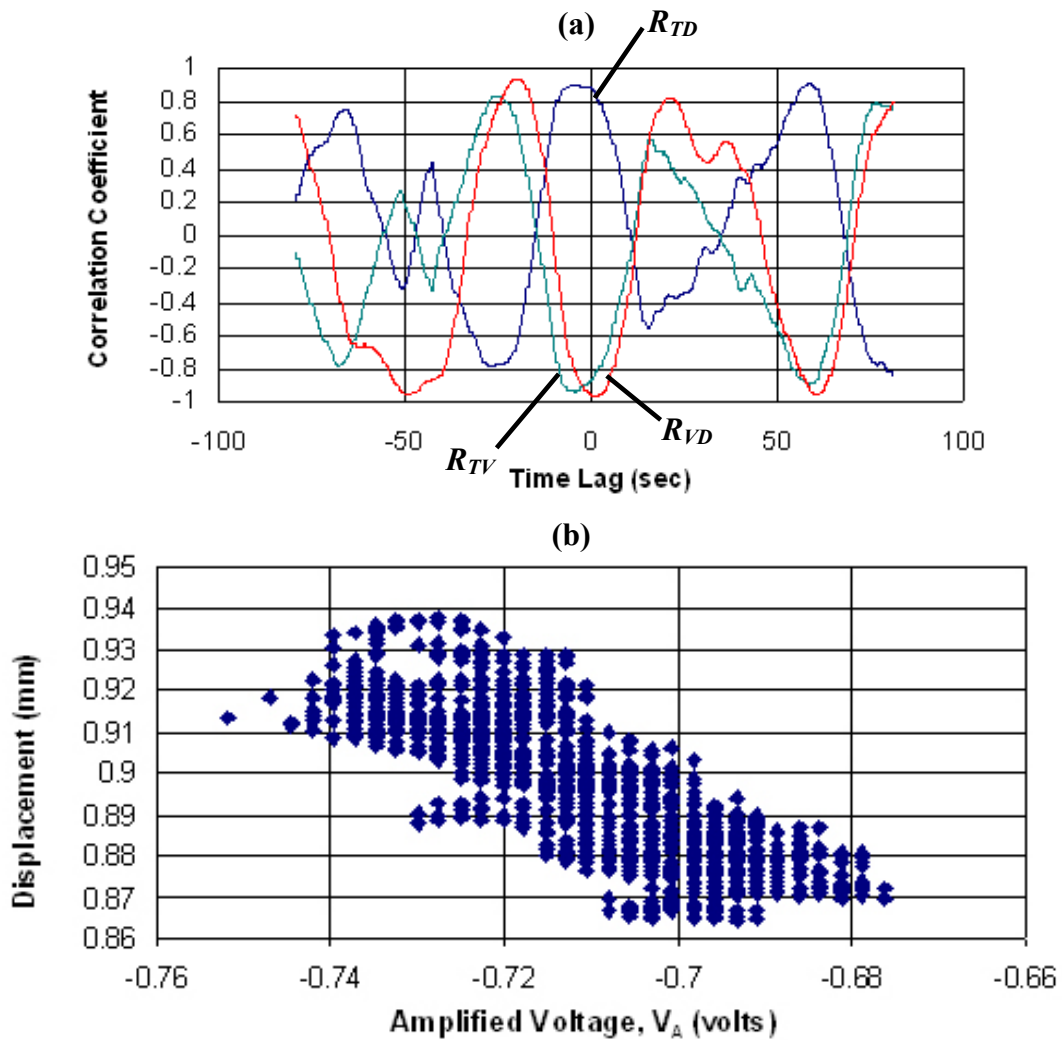


Figure 6.11: Statistical analysis: (a) correlation coefficients between: temperature and displacement, R_{TD} , temperature and voltage, R_{TV} , voltage and displacement, R_{VD} ; (b) homoscedasticity test.

The correlation coefficients between T , V_A , and D for a controlled strain recovery test with a small initial pre-strain of 0.69 % show lower correlation coefficient values than the ones previously calculated for the case with a pre-strain of 0 % (Fig. 6.11a), namely: $R_{TD} = 0.8828$ at time lag = -0.576 sec, $R_{TV} = -0.5386$ at time lag = -2.112 sec, and $R_{DV} = -0.5873$ at time lag = 0.96 sec. There are two reasons for this behavior. First, the martensite phase transformation

process shows its non-linear behavior, represented by a non-linear dependence of the values of the heat flux versus the corresponding temperatures (TTRs) at which those heat fluxes were measured (see the corresponding non-linear peaks in the DSC thermogram in Fig. 6.4). Points A, B, and C in the thermogram show the start (point A), the middle part (point B), and the end (point C) of the phase transformation, where the change of the slopes occur.

The amount of heat (level of heat flux) released/consumed during the phase transformations is proportional to the speed of the transformations. The speed of the transformation is characterized by the slope of the peak as it was explained earlier. Since in the experiment with a 0.69% pre-strain level, the working temperatures of the SMA wire, T , were lower than in the experiment with a 0% pre-strain level (Fig. 6.9c), therefore, the speed of the phase transformations was lower according to the DSC thermogram, where the beginning of the peak (Fig. 6.4) has a lower slope at lower temperatures. Secondly, the pre-strain of the wire adds an additional internal stress that results in a shift of the TTRs to the right in the DSC thermogram (Fig. 6.4), thus even more decreasing the sensitivity of the SMA wire to the phase transformation.

The correlation coefficients between T , V_A , and D for a controlled strain recovery test with yet a smaller initial pre-strain of 0.347 % give: $R_{TD} = 0.8607$ at time lag = -0.896 sec, $R_{TV} = -0.4131$ at time lag = 5.248 sec, and $R_{DV} = -0.4759$ at time lag = 1.664 sec. They are lower for the same reason as before – the experiments were conducted at a relatively low temperature, T , and the wire was given a non-zero initial pre-strain.

Another controlled strain recovery test was conducted for the 4.16% initially pre-strained non-insulated SMA wire. The corresponding correlation coefficients between T , V_A , and D are: $R_{TD} = 0.8144$ at time lag = 1.408 sec, $R_{TV} = -0.4691$ at time lag = 6.912 sec, and $R_{DV} = -0.7383$

at time lag = 5.504 sec. In spite of the high working temperatures, T , these correlation coefficients were still lower than the correlation coefficients shown in the case with 0.69 % initially pre-strained wire. This occurs, because the increase in the initial pre-strain (pre-stress) of the wire shifts TTR peaks to the right in a DSC thermogram. It means, that the peaks occur at the higher transformation temperatures, while the working temperatures of the wire remain at the same level.

Cumulative results, presenting the correlation coefficients as functions of pre-strain and temperature from different experiments, are shown in Fig. 6.12 a and b correspondingly.

It can be concluded that at the beginning and at the end of the phase transformation the correlation between the electrical resistance (voltage drop) and the displacement, D , becomes almost linear, resulting in correlation coefficients nearly equal to -1 (Fig. 6.12b). This can be explained by the fact, that the speed of the phase transformation changes slowly at the beginning and at the end of the transformation as seen from the corresponding regions of the peaks in the DSC thermogram (Fig. 6.4). A smaller initial pre-strain leads to a correlation coefficient equal to 1 as well (Fig. 6.12a). Therefore, the correlation between the displacements of the SMA wire actuator and the voltage drop changes in the SMA wire can be described by a linear equation under low working loads (low pre-strains).

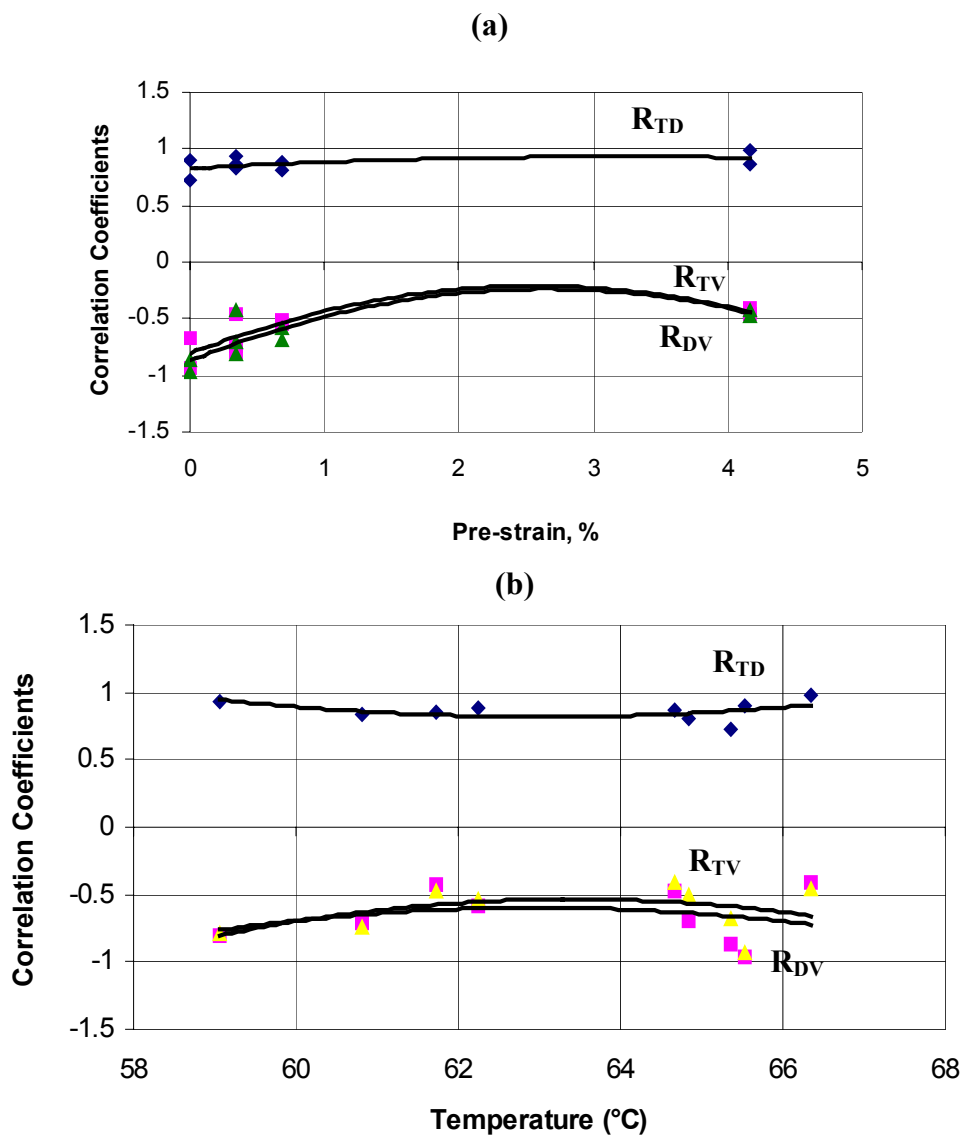


Figure 6.12: Cumulative correlation coefficients data: (a) as a function of pre-strain, (b) as a function of temperature.

6.3.4 Sensitivity analysis

In a practical application of an SMA wire actuator, the dependence of the voltage V_A on the displacement D will be used to control the motion and position of the actuator. Therefore, it

is necessary to analyze the resolution and sensitivity of the “self-sensing” methodology that uses the V_A signal in order to predict the displacement D . The analysis of the resolution and sensitivity is based on the experimental data (V_A and D signals) from the experiments with the controlled strain recovery of the thermally insulated SMA wire, since the insulation provides stable signals (measured voltage and displacement), rather than the non-insulated wire as described in the previous section. Therefore, the experiments with the thermally insulated wire give more precise sensitivity estimates.

Here, sensitivity is defined as the capability of the SMA wire setup to sense the change in the displacement through the corresponding resistance (voltage V_A) change. In other words, the sensitivity represents the slope of the displacement versus voltage curve (e.g., Fig. 6.13 a, b). The resolution, in turn, can be defined as the smallest displacement the “self-sensing” method can measure based on the resolution of the given DAQ and the performance (phase transformation properties) of the SMA wire.

In order to show the difference between small range displacement and large range displacement responses of the wire, the corresponding constrained recovery experiments are described further.

As an example of the data reduction for the resolution and the sensitivity analysis, the experiment described in Section 6.3.2 will be analyzed. Figure 6.13 shows the measured signals – voltage V_A and displacement D – taken from the step responses from Fig. 6.10. V_A and D were taken from two step responses at 330 sec and 413 sec (see Fig. 6.13 a and b) from the plots in Fig. 6.10. It is seen from the linear regression shown in Fig. 6.13 b, that the step response of the SMA wire actuator with the maximal displacement step equal to 200 μm is characterized by a sensitivity equal to 2.8 $\mu\text{m}/\text{mV}$, being the slope of the regression. Therefore, the corresponding

resolution of the “self-sensing” method, based on the given DAQ resolution (12 bits), is

$$2.8\mu\text{m}/\text{mV} * 2.4\text{mV} = 6.7\mu\text{m}.$$

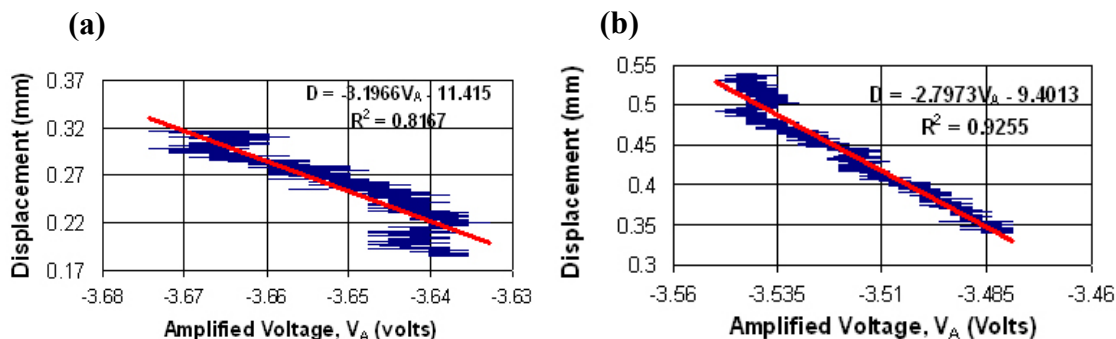


Figure 6.13: *Displacement, D , vs. amplified voltage, V_A (from Fig.6.8): (a) step response at 330...399 sec, with the maximal displacement step (displacement range) $131\ \mu\text{m}$, (b) step response at 413...553 sec, with the maximal displacement step (displacement range) $200\ \mu\text{m}$*

The above-described experiments were accomplished using the capacitance probe calibrated for measuring small displacements, between 0 and 1 mm (see the calibration curve #1 in Fig. 6.7a).

Both, the sensitivity and resolution values were calculated for all the steps in all the small displacement range experiments (see the corresponding Table D.1 in Appendix D). They are plotted as functions of the magnitudes of the maximal displacements measured during each of the step responses. Both functions characterize the performance of the “self-sensing” method and are depicted in Fig. 6.14. Figures 6.14 a, b show that the values of the resolution and of the sensitivity decrease with the increase of the maximal displacement value (displacement range). The minimal displacement equals to $17\ \mu\text{m}$ and can be measured with a resolution of $1.7\ \mu\text{m}$. In turn, the maximal displacement equals to $360\ \mu\text{m}$ and can be measured with an $8\ \mu\text{m}$ resolution (based on the current DAQ sensitivity and the performance of the SMA wire). The resolution of

the “self-sensing” method in the current study is a joint characteristic of the experimental setup sensitivity and the DAQ resolution.

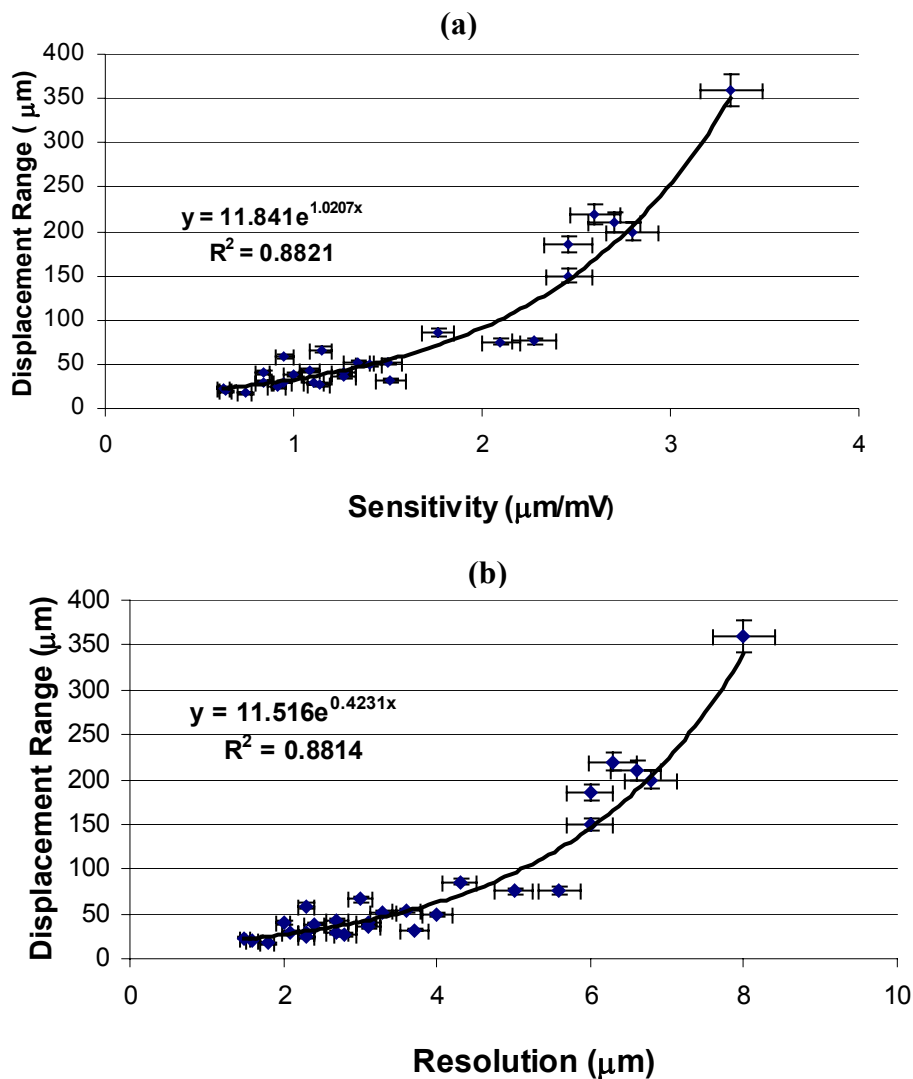


Figure 6.14: Characteristics of the “self-sensing” method: (a) sensitivity and (b) resolution versus displacement ranges.

Provided that the working conditions do not change, it can be shown by Fig. 6.13 and by the correlation analysis, that the relation between the measured displacement and measured voltage can be described by a linear dependence (linear regression as shown in Fig. 6.13) for small range displacements (less than 1 mm) produced under the following working conditions:

low working loads, stable heat sink conditions, and equal input heat loads. Therefore, it is advantageous to use the measured voltage as a sensor, or a feedback signal to control the motion of the SMA wire.

Although, Fig. 6.14 shows, that the slope of this regression changes due to the change in the magnitude of the measured displacements (under different heat loads or working conditions), hence the SMA wire system can be described as a system with varying properties under varying working conditions, which can be analyzed by the system identification.

6.3.5 Identification of the dynamics of motion of the SMA wire

The visual inspection of the experimental data from both the thermally non-insulated and thermally insulated SMA wire controlled strain recovery tests suggests that the performance of the SMA wire based setup could be described approximately by a first or a second order dynamic system. System identification will be used to determine whether the actuator's dynamics can be described or approximated by a linear time invariant system.

The system's transfer functions were identified for each step response experiment using MatLAB. The system identification conditions are summarized in Table 6.2. The sampling frequency of the data acquisition was 0.05 sec.

The step response experimental data were taken from the experiments described earlier. The time plots of the experimental input (voltage) and output (displacement) data for the thermally non-insulated SMA wire are shown in Fig. 6.15 a, b. The time plots of the

experimental input and output data for the thermally insulated SMA wire are shown in Fig.

6.16 a, b.

The output variation parameter in Table 6.2 describes the goodness of fit reproduced by a model output, e.g., by an ARX (1,1,1) model output, obtained by using the toolbox “ident” in the MatLAB environment based on the measured experimental data. The goodness of fit is the best (gives the minimal variation between the model that approximate the experimental data and the experimental data) if the output variation is equal to unity – therefore, the mean of the model output (approximation model) is equal to the mean of the measured output (experimental data).

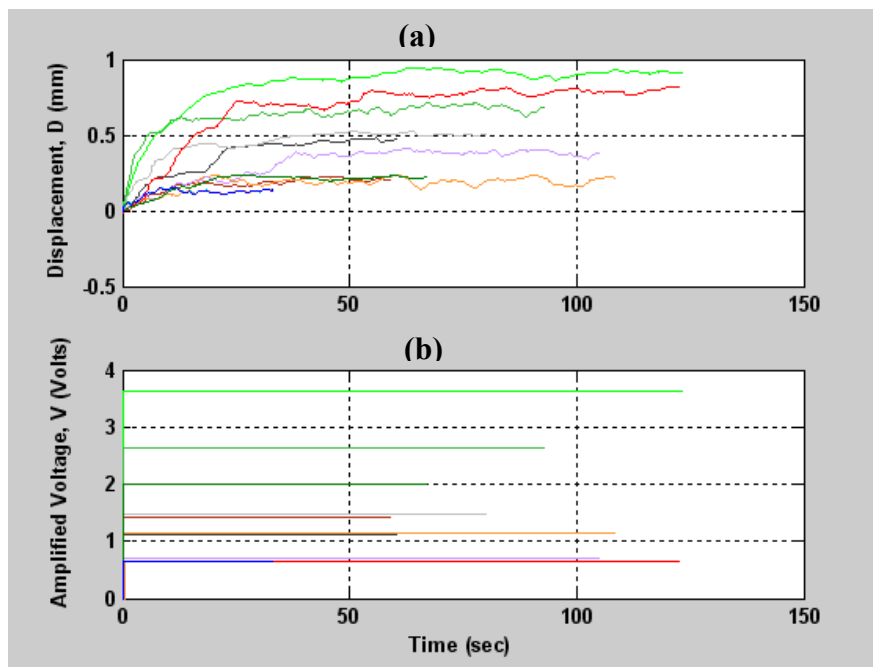


Figure 6.15: *Input and output data for the SMA wire step response with no thermal insulation: (a) output - displacement, (b) input - voltage.*

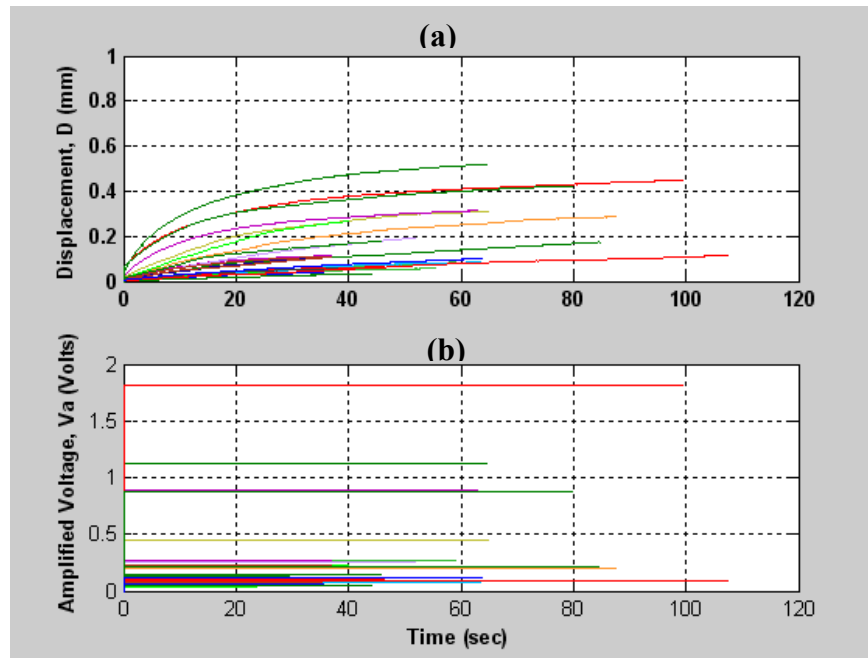


Figure 6.16: *Input and output data for the SMA wire step response with thermal insulation: (a) output - displacement, (b) input - voltage.*

Table 6.2: *Identification conditions and criteria*

Experimental conditions	Model order	Sampling interval, sec	Output variation (between experimental and fitted data)
SMA wire without thermal insulation	ARX (1, 1, 1)	0.05	≥ 0.8
SMA wire with thermal insulation	ARX (2, 1, 1)	0.05	≥ 0.8

The identified frequency response data corresponding to Fig. 6.15 (thermally non-insulated SMA wire) are shown in Fig. 6.17. The simplest parametric model structure,

ARX(1,1,1), was chosen to derive all the transfer functions for each curve using MatLAB.

The criterion for the choice of the model was the maximal value of the output variation between the experimental data and the model data (e.g., Fig. 6.19).

Since all the responses (and, therefore, transfer functions) are very similar to each other - only some of them are shown in Fig. 6.19. For example, a transfer function corresponding to a model whose response is shown in Fig. 6.16a is given as:

$$\frac{0.001899}{z - 0.9912} \quad (6.1a)$$

In the transfer function (6.1a), the pole equals to 0.9912, which is close to the unit circle, thus resulting in a system close to an unstable condition. By decreasing the sampling frequency a more stable system model (root farther away from the unit circle) can be obtained. For example, re-sampling the experimental data with a lower than the original 0.05 s sampling frequency of 1.25 s and 2.5 s, gives transfer functions with more stable roots as shown by the corresponding equations 6.1b and 6.1c:

$$\frac{0.07876}{z - 0.9352} \quad (6.1b)$$

and

$$\frac{0.1664}{z - 0.8613} \quad (6.1c)$$

The frequency response data corresponding to Fig. 6.16 (experiments with thermally insulated SMA wire) are shown in Fig. 6.18. All the transfer functions for each curve were derived using an ARX (2,1,1) model. Some of the model outputs are shown in Fig. 6.20. For example, a transfer function corresponding to a model whose response is shown in Fig. 6.20a can be derived as follows:

$$\frac{0.001708z}{z^2 - 0.6047z - 0.3939} \quad (6.2)$$

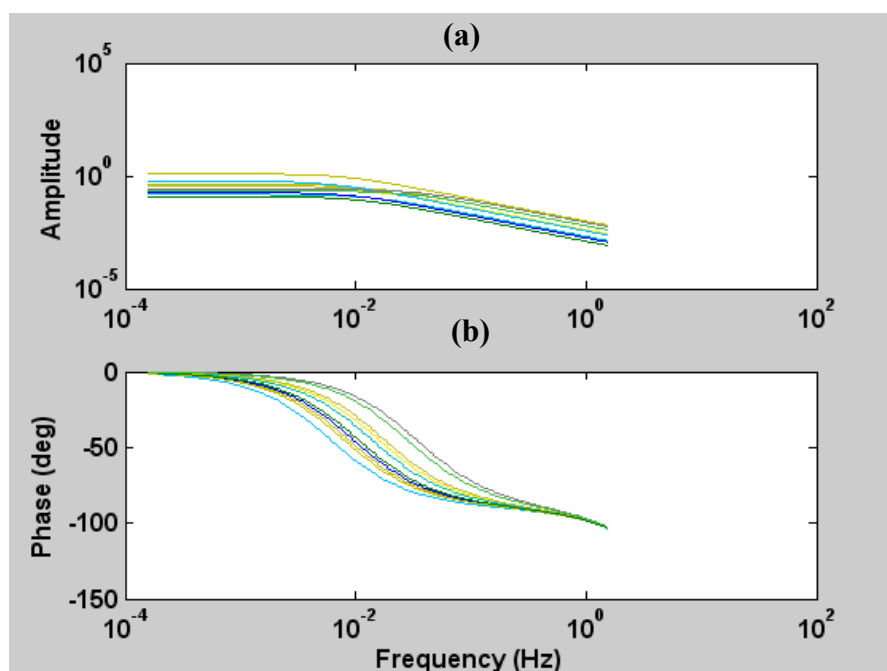


Figure 6.17: Frequency response data for the SMA wire step response with no thermal insulation: (a) amplitude, (b) phase.

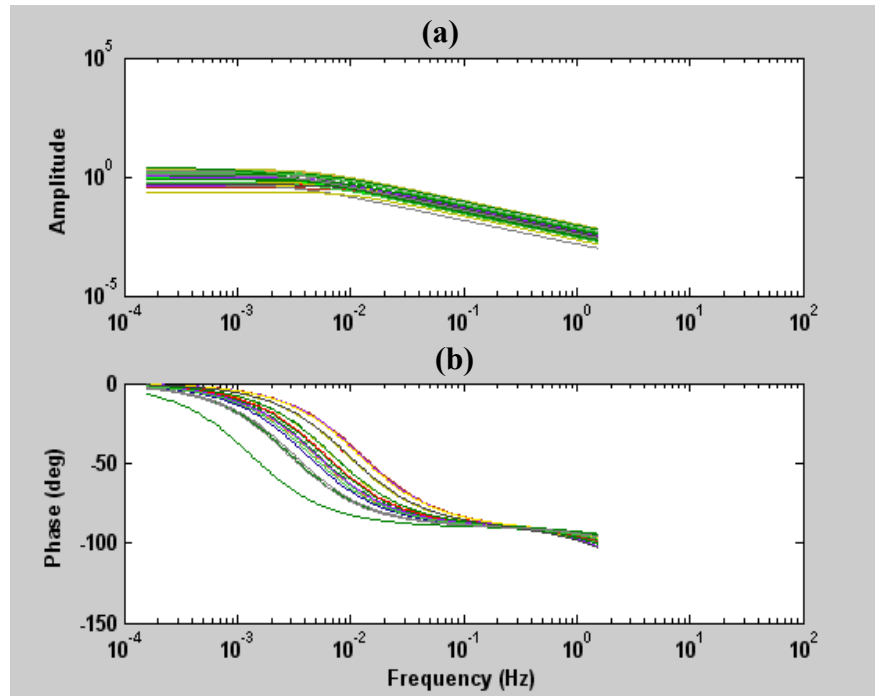


Figure 6.18: Frequency response data for the SMA wire step response with thermal insulation: (a) amplitude, (b) phase.

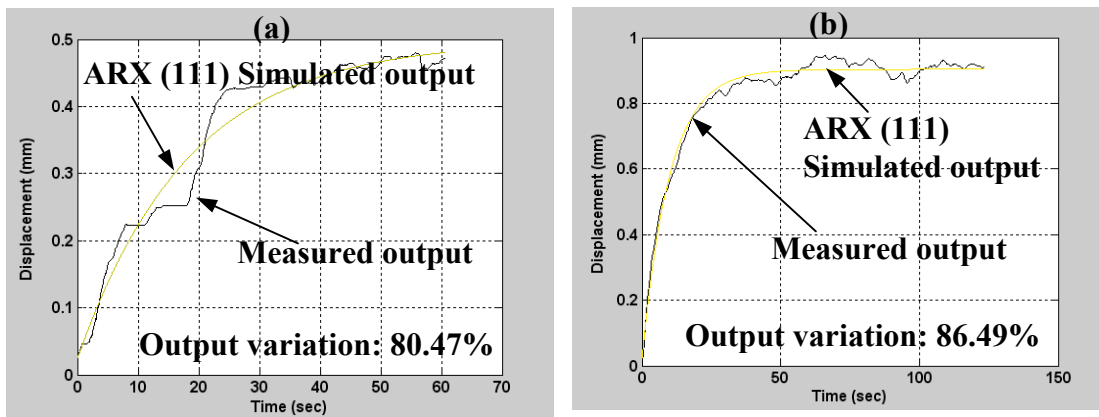


Figure 6.19: Measured and simulated output of the thermally non-insulated SMA wire: (a) Exp. 27, (b) Exp. 32.

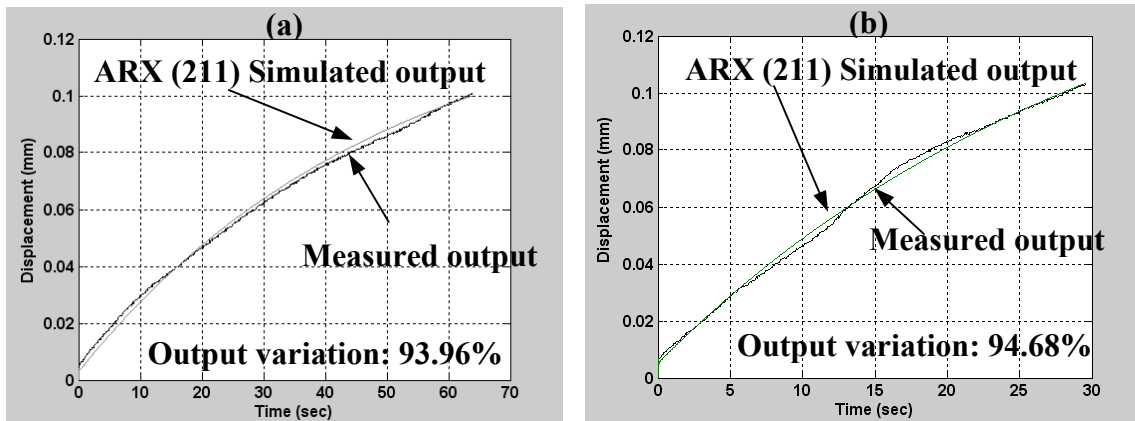


Figure 6.20: Measured and simulated output of the thermally insulated SMA wire: (a) Exp. 45, (b) Exp. 41.

F-test statistics of the data from 6 experiments with the thermally non-insulated wire yield an F-ratio of $F=0.9454$, while the standard value is equal to $F_{0.95, 6, \infty} = 2.21$ (with a significance level of 0.05 from the statistics tables). F-test statistics of the data from 6 experiments with thermally insulated wire give $F=1.3549$, while the standard value is equal to $F_{0.95, 6, \infty} = 2.21$. Therefore, it can be concluded that the null-hypothesis cannot be rejected at the 0.05 significance level and that all the experimental samples (e.g., Fig. 6.19 and 6.20) are from the same population having normal distribution and may have the same means, therefore the model is valid.

The transfer functions for all the frequency response curves (Fig. 6.17 and Fig. 6.18) resemble equations (6.1) and (6.2) correspondingly. Based on all ARX (1,1,1) models, that simulate the step responses of the experiments with the thermally non-insulated wire, it is possible to compute an average time constant $\tau = 14.9$ sec and an average gain of 0.319. For the thermally insulated wire (ARX(2,1,1) model) the average natural frequency is $\omega_n = 0.0387$ rad/sec, the average damping ratio equals 1, the average rise time is $t_r = 46.51$ sec, and the

average gain is 0.957. The transfer functions, derived for all experiments, are given in Appendix E. The DSC thermogram in Fig. 6.4 shows that the phase transformation is a temperature sensitive phenomenon. The dependence of the magnitudes of the frequency response curves versus the average temperatures (average temperature in each step response time interval) at which the data (displacements and voltages) for those curves were recorded are shown in Fig. 6.21a for the thermally non-insulated wire and Fig. 6.21b for the thermally insulated wire.

The analysis of both plots, at the same temperature levels, shows that the gains of the frequency response curves for the experiments with the non-insulated wires (Fig. 6.21a) increase with temperature increase. Similar behavior can be noticed in the case with thermally insulated wire (Fig. 6.21b). In this case the gains increase with temperature increase up to a certain temperature level after which they decrease. Such behavior is consistent with the DSC thermogram in Fig. 6.4, which shows that the heat flux peak intensity of the austenite phase transformation increases with temperature increase. Point A in Fig. 6.4 characterizes low sensitivity of the material to austenite phase transformation (and, therefore, to the shape memory effect driven motion).

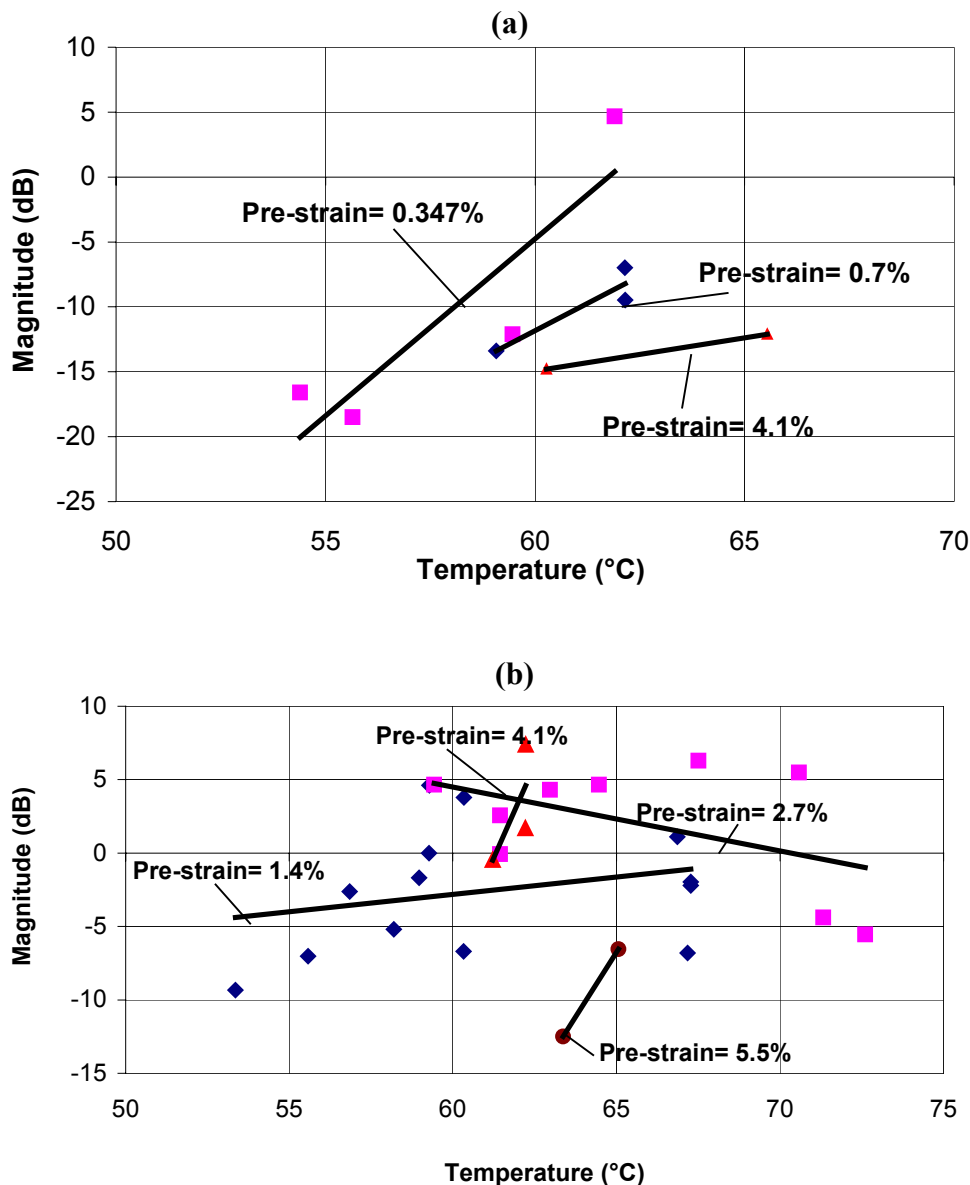


Figure 6.21: *Magnitudes versus average temperatures: (a) frequency response of the thermally non- insulated SMA wire and (b) frequency response of the thermally insulated SMA wire.*

When the peak reaches its maximum at point B (Fig. 6.4), the sensitivity of the SMA material is at its maximum as well, implying the fastest response of the phase transformation (and strain change) due to the heat input. The sensitivity decreases at point C on the peak. The scatter of the data points in Fig. 6.21 can be explained by the different pre-strain levels in some of the

experiments. Linear regressions were chosen to fit the experimental points in Fig. 6.21.

Linear regressions were used due to the lack of a sufficient number of experimental points needed for a non-linear fit. These plots in Fig. 6.21 allow one to conclude that the thermally insulated wire develops a more pronounced response in terms of the magnitudes of the displacements developed at the same temperature levels as compared to the experiments with the thermally non-insulated wire.

Figure 6.21a shows that in the case of thermally non-insulated SMA wire the larger the initial pre-strain the smaller the amplitude of the step response. Similar behavior holds for the thermally insulated SMA wire (Fig. 6.21b), although the behavior is not completely consistent.

Experimental observations also suggest that larger initial pre-strains give smoother responses in terms of smaller displacement fluctuations for the thermally non-insulated wire. The time constant for the non-insulated wire is three times lower than the rise time of the insulated wire. Therefore, the non-insulated SMA wire contracts faster than the thermally insulated SMA wire.

The faster contraction of the non-insulated SMA, compared to the thermally insulated SMA wire, can be explained using the diagram in Fig. 6.22 and the energy conservation law with the assumption that the wire is characterized by an average temperature T :

$$\frac{dT}{dt} = \frac{q_{in}^1 - q_{out}^1 + q_{in}^2}{C_p M}. \quad (6.3)$$

where:

T – average temperature of the SMA wire, °C;

t - time, sec;

$q_{in}^1, q_{in}^2, q_{out}^1$ - input and output heat fluxes affecting the wire thermal state, W;

C_p – heat capacitance of the SMA, J/kg;

M – mass of the SMA wire, kg.

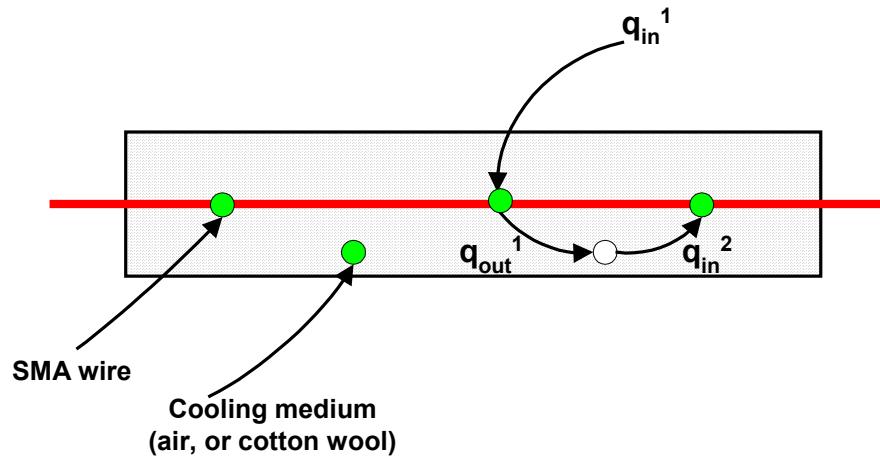


Figure 6.22: SMA wire heat balance diagram.

Figure 6.22 shows that due to the higher heat capacitance of air (in case of the wire without thermal insulation) in comparison to the heat capacitance of the cotton wool (in case of the wire with thermal insulation), the wire gets higher heat fluxes due to the additional q_{in}^2 heat flux from the boundary layer of air surrounding the SMA wire. Therefore, the heating rate (degrees of temperature per second) of the non-insulated SMA wire is higher than the heating rate for the insulated wire. As a result, the non-insulated SMA wire contracts faster or has a lower time constant. It can be also concluded, that:

- larger magnitudes of the step input signals (large magnitudes of the applied voltages) give faster displacement responses due to the larger heating rates, and therefore, larger

sensitivity to the phase transformation (larger displacement of the wire due to the shape memory effect);

- equal magnitudes of the input voltages, applied at different temperatures, give different magnitudes of the displacements. Therefore, it can be concluded, that the SMA wire actuator is a non-linear system. This was explained by the DSC thermogram (Fig. 6.4), that showed, that depending on the SMA temperature there were regions with a larger phase transformation sensitivity (point B in Fig. 6.4).

6.3.6 Analysis of the feasibility of the “self-sensing” principle for small displacements

The experimental studies of the performance of the actuator with the SMA wire were conducted in order to assess the feasibility of the “self-sensing” principle to be used in the motion control of the actuator. The concept is feasible if its application allows meeting the actuator’s technical specifications, namely, the resolution and sensitivity of the actuator.

It is planned to use the actuator in space-limited applications, e.g., microfactories, requiring displacement resolutions equal to several microns. In the current studies, the actuator’s minimal achievable resolution was less than 2 μm (Fig. 6.14b) and its sensitivity – less than 1 $\mu\text{m}/\text{mV}$ (Fig. 6.14a). Hence, the “self-sensing” concept can be considered feasible in terms of resolution and sensitivity parameters. Generally, sensitivity and resolution tend to exponentially increase (Fig. 6.14) with the increase of the wire’s displacement step.

6.4 Experiments with large scale displacement sensing

A series of experiments for measuring large displacements of the SMA wire, between 0 and 12 mm, was also conducted, using the capacitance probe calibrated for large displacement measurements (see calibration curve #2 in Fig. 6.6 b).

The experimental procedure and the experimental apparatus used in the current experiments were analogous to the ones used for small-scale displacements. The SMA wire was pre-stretched and a heat load was applied to it by applying an electrical current through the wire. The resistive heating of the wire generated the SME contraction of the wire. The large-scale displacement experiments differed from the small-scale displacement experiments due to the larger heat loads applied to the SMA wire, and consequently larger displacements.

An example of displacement-voltage dependence from one such experiment is shown in Fig. 6.23. It is seen, that the dependence is non-linear, compared to the small range displacements shown in Fig. 6.13. This can be explained by the fact that, the phase transformation in SMAs is a non-linear process as shown in the thermogram (see the non-linear heat flux peaks) in Fig. 6.4, where point A shows the change in the slope, and therefore, the non-linearity of the phase transformation process. As a consequence, the larger the amount of heat flux applied to the SMA wire (larger displacements), the greater the non-linearity of the heat flux peaks in the thermogram, and, therefore, in the corresponding displacement-voltage curves.

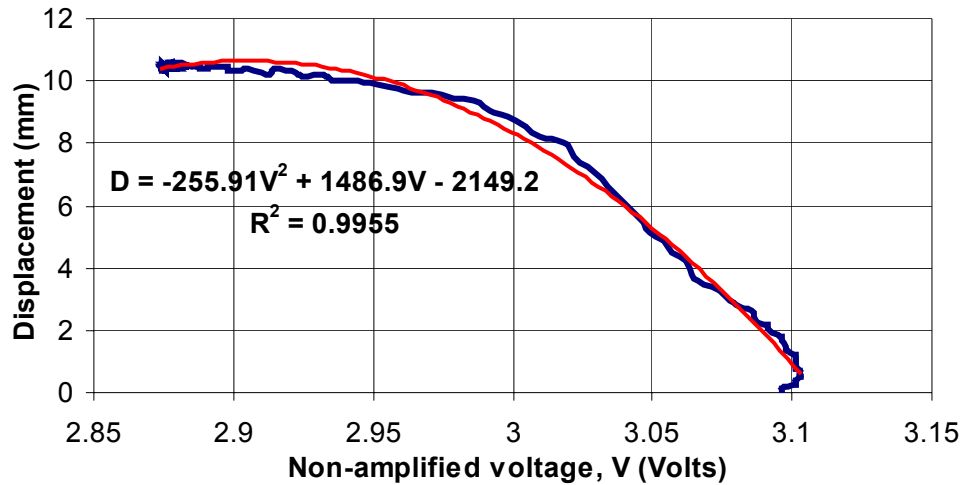


Figure 6.23: *Step response from a large displacement experiment*

In spite of the fact that the dependence in Fig.6.23 is non-linear, SMAs can still be used in sensing of large-scale displacements by considering the calibration curve #2 in Fig.6.6b for the same working conditions (load and temperature levels). If the working conditions change, then the dependence between input and output of the sensor must be described in a more complex way, for example, by using neural network logic (e.g., as in Lee et al., 2001). Therefore, the schematic in Fig.6.1 will have to be adjusted according to the non-linear logic of the sensor. If neural networks are used in the logic then the “sensor” block will contain the corresponding correlation between the produced motion of the plant and the output voltage of the sensor. The neural networks will account for the working conditions change by means of the corresponding correlation.

6.5 Conclusions

The following conclusions can be drawn, based on the above experimental investigations:

1) The SMA sensor shows different characteristics when used for measurements in small and large displacement ranges. In the small displacement range its behavior is linear (only under the same working conditions), while in the large displacements range its behavior is non-linear due to the non-linearity of the phase transformation process.

2) The linearity between the voltage and the displacement in the small displacement range can be justified only for the same working conditions of the SMA wire (pre-strain, working temperature, heat sink).

3) The resolution and the sensitivity of the “self-sensing” method decreases with the increase of the magnitudes of the maximal displacements during each step response, which shows that the actuator system changes its properties when the working conditions change. For example, equal magnitudes of the input voltages, applied at different temperatures, produce different displacements, proving that the SMA wire actuator is a non-linear system under varying working conditions.

4) The non-insulated SMA wire contracts faster or it has a lower time constant, which is explained by the boundary layer concept. Larger applied input voltages give faster displacement responses due to the larger heating rates, and therefore, faster phase transformation.

5) The present studies show that high actuation temperatures and low working loads are preferable from the point of view of control of motion of the SMA wire based actuator,

since these working conditions give almost linear correlation between the measured voltages and displacements.

6) It is known, that the response of the SMA material is a loading path dependent process (Bekker and Brinson, 1998; He et al., 2006), consequently, the current research results apply only to experimental conditions during which the SMA actuator is heated from its fully detwinned (oriented) martensite state. Therefore, it does not account for the influence from other phases in the material (R-phase, twinned martensite) and from the micro-structure of the material (grain orientation, etc.) on the electrical resistance, that introduce a non-linearity into the relationship between the resistance and displacement. That is why the presented results on the “self-sensing” technique developed in this research are limited to such conditions only. To account for SMA material behavior under general cyclic thermal and stress loading further investigations are warranted.

7) In general, SMAs can be used as linear sensors of motion in small-scale displacement sensing applications provided that the working conditions during the loading of the SMAs stay at the same level (low loads, high working temperatures). SMAs can be also used as non-linear sensors of motion in large scale displacement sensing, but the changing properties of such sensors require the use of a more complex way of representation of the sensor’s output based on the input signals and changing working conditions, for example, by using neuron networks (e.g., in Lee et al., 2000).

CHAPTER 7

7. A new mathematical model of the kinetics of the austenite phase transformation in NiTi SMAs and its experimental verification

Difficulties with the motion control of SMA actuators were discussed earlier in Chapter 6. They show that SMA-based actuators can be considered as non-linear systems that change their properties if the working conditions change: the load, initial stress (pre-strain), temperature and phase state, and heat sink conditions. Conventional system identification procedure was used in the modeling of the dynamic response of the SMA wire based actuator. The experimental results from step response experiments with the SMA wire actuator were fit into polynomial functions, allowing one to mathematically model the actuators' dynamic response.

In light of the above-described observations, it would, however, be advantageous to develop a motion law and a motion control law that are based on the fundamental properties of SMAs, because it would uniquely identify the system's state and its response would be easily predictable. The motion law based on the fundamental properties could simplify the conventional identification procedure (used in Chapter 6) by drastically decreasing the number of multiple experimental investigations performed during the system identification of SME driven actuators for different working conditions. Simplification would become possible due to the fact, that only one unique set of experiments should have to be performed to identify the dynamic response of the SMA actuator system using one set of working conditions (initial pre-strain, stress, heat load

and heat sink conditions). Afterwards, the identified system could be used to model the system dynamics at different sets of working conditions, thus eliminating the needs for additional experiments.

Temperature-induced phase transformation is the fundamental property of SMAs that drives the shape memory effect, and, therefore, the motion of the SMA actuator. A goal of this chapter is the development of a new mathematical model of the kinetics of the austenite phase transformation in NiTi alloys. The model will be applicable to the needs of this particular application - mMM. The model will be limited by the fact, that it will describe the phase transformation of the SMA material under a heating loading path only. It will be also be assumed that the initial state of the SMA material is fully detwinned (oriented) martensite that converts to pure austenite during the temperature-induced transformation, without any other possible phases of the material (R-phase, twinned martensite). The micro-structural changes (grain re-orientation, etc.) that take place in the material during the temperature-induced transformation will not be taken into account in this model, thus making it applicable only to the current application, where the corresponding non-linearity between the austenite phase fraction and applied temperature during the phase transformation process is not considered.

The model of the kinetics of the austenite phase transformation will be used in the description and implementation of a mathematical model of motion of the SMA actuator. The latter model will be, afterwards, used in the development of the motion control law of the actuator.

7.1 Overview of existing phenomenological models of phase transformation kinetics in SMAs

According to Bekker and Brinson (1997) four basic phenomenological models of phase transformation kinetics in SMAs can be distinguished:

- 1) **Group 1:** 1-D and 2-D models that are based on the Landau/Landau-Ginzburg free energy formulation in the description of the phase transformation process in SMAs at the microscopic level (several interatomic distances).
- 2) **Group 2:** 1-D models that are based on the linear momentum conservation equation with a non-monotone N-shape stress-strain function for description of the phase transformation process in SMAs at the meso/macro level.
- 3) **Group 3:** 0-D and 1-D models that are based on uniaxial constitutive energy and momentum conservation laws with the material's phase fraction as an internal variable in the description of the phase transformation process in SMAs at the macro level.
- 4) **Group 4:** 3-D and 1-D models that are based on different types of phase mixture theory written in terms of free energy in the description of the phase transformation process in SMAs at the meso/macro level.

A key controversial situation that exists at the present is related to the 3-D modeling of SMA behavior. Existing 3-D models are not really robust and need to be "tuned" for a particular material and design every time they are used.

In this study the focus will be on the third group of models, that represent 0-D (or “lumped parameter”) models based on uniaxial constitutive stress-strain laws. So far, several robust and reliable 1-D SMA mathematical models were developed. From the practical point of view, phenomenological models were used to solve engineering problems involving SMAs. The models use fitted experimental data and are not capable of capturing in detail the underlying thermo-mechanical behavior of the SMA.

The classical phenomenological models developed by Tanaka and Nagaki (1982), Brinson (1993), Liang and Rogers (1990) and Lagoudas (2001) describe the SMA behavior by means of constitutive laws (relations between temperature, stress, strain and phase composition in the material). They use a phase transformation function that uses the austenite-martensite phase transformation fraction as an internal variable in the equations describing the corresponding constitutive laws. The advanced version of this type of models was developed by Brinson (1993), where instead of one internal variable, martensite phase fraction, two internal variables have been introduced – de-twinned and twinned martensite phase fractions.

The phase transformation functions in the above mentioned models represent semi-empirical dependences of the phase transformation fraction (either martensite or austenite) on temperature and stress. There exist several different types of the phase transformation functions in the literature, e.g.: algebraic (Bekker and Brinson, 1998), exponential (Bekker and Brinson, 1998; Ikuta et al., 1991; Liang, 1990), tangential (Sittner et al., 2000), and cosine (Bekker and Brinson, 1998; Liang, 1990). These trigonometric functions were found to best fit the phase transformation fraction evolution in SMAs based on experimental data, since those functions can be easily parameterized to resemble the phase transformation function behavior. They have to be manually tuned to properly describe the phase transformation process. Therefore, there is a need

to develop a phase transformation function that would not be based on analytical fitting, and therefore be more reliable and robust. This might be possible by the use of generalized energy conservation laws, as it will be described in the next section.

7.2 Problem statement

A mathematical model describing the kinetics of the temperature-induced austenite (reverse martensite) phase transformation processes that take place in SMAs during heating is presented. The model is based on two energy balance equations formulated in the framework of control volume theory. The theory implies that a solid body is discretized into elementary control volumes, described by the energy balance equations. The model is formulated for a general stress and thermal state in the solid body and allows the computation of the austenite phase fraction evolution in it.

In the current study the theoretical work will focus on the modeling of the austenite phase fraction propagation in the SMA solid body using a subdivision of the body into thermal "nodes" (control volumes, finite elements). A so-called 0-D problem for SMA will be formulated in this Chapter. The 0-D model will be based on the lumped parameter approach (Grigoriev et al., 1999; Incropera and Dewitt, 2002; Kaviany, 2002) where the object is divided into several "nodes" described by the corresponding energy conservation law equations. The "nodes" are connected to each other by "heat conductors" - equivalent to the corresponding heat conductance and convective heat transfer equations, thus closing the system of equations. This is a rather robust

and simple schematic that allows one to cast a solid body into a 0-D problem, as shown in

Fig. 7.1 for an SMA wire.

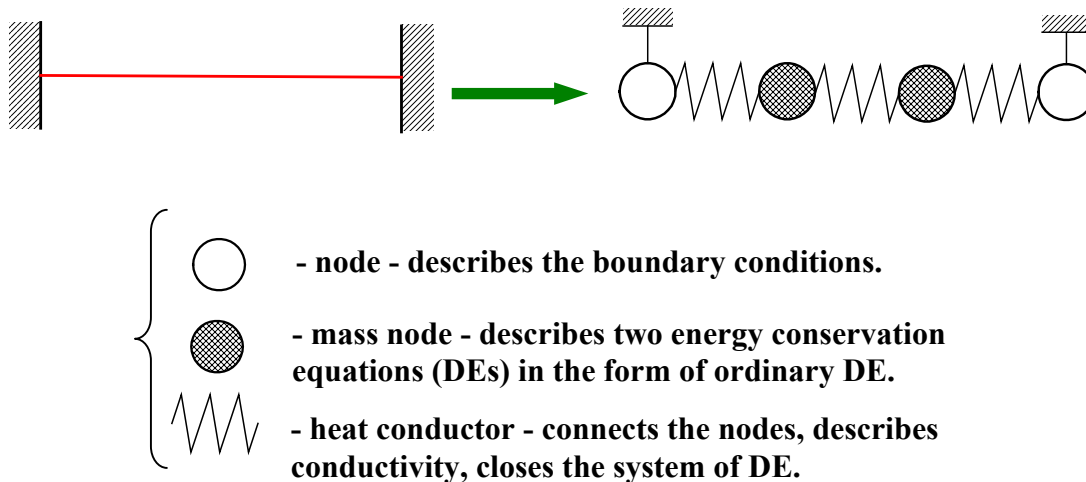


Figure 7.1: Nodalized representation of an SMA wire.

7.3 Constitutive energy conservation equations for SMAs

Traditionally, any 3-D structure can be represented by 3-D elementary control volumes or finite elements, e.g., 8-node bricks, as shown in Fig. 7.2. The temperature, T , characterizes the temperature distribution in the brick. In the current derivation, a 0-D control volume (thermal node) will be used (Fig. 7.3a) in order to simplify the problem.

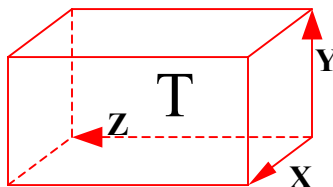


Figure 7.2: 3-D control volume.

Conventionally, 0-D problems (Grigoriev, 1999; Kaviany, 2002) that describe heat transfer in a solid body deal with so-called “thermal nodes” that are different from the “control volumes” (finite elements). The difference is in their visual representation only, as shown in Fig. 7.3 a and b, where \dot{q}_{in} and \dot{q}_{out} represent the input and output heat fluxes across the boundary of a control volume and a thermal node, and T – is the temperature of the control volume (or thermal node). 1-D to 3-D problems cannot be represented by “thermal nodes” since they do not reflect the geometrical distribution of the state variables (e.g., temperatures) inside the node.

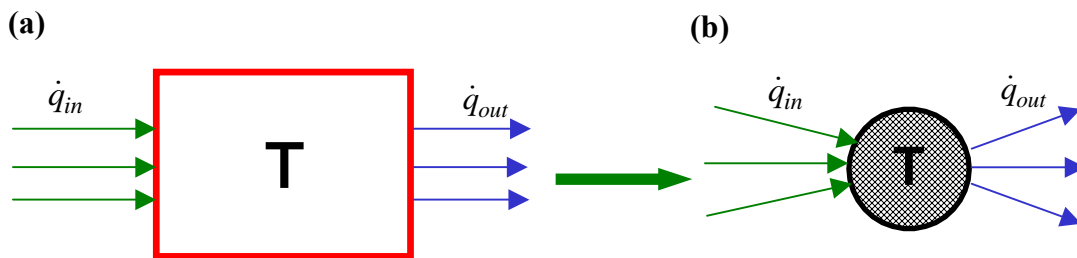


Figure 7.3: Discrete representation of continua by (a) 0-D control volume and (b) its equivalent thermal node.

In order to model the temperature-induced phase transformation in SMAs, it is assumed that heat is applied to the solid body made from SMAs that are in the martensite phase state. Two differently formulated energy balance equations can be written for the thermal node with a mass M_n .

The first formulation of an energy balance equation describes the temperature distribution in the solid body (7.1) (Grigoriev et al., 1999):

$$\frac{dT}{dt} = \frac{\sum \dot{Q}}{C_p M_n} \quad (7.1)$$

The second formulation represents a new energy balance equation describing the austenite fraction evolution in the solid body (7.2):

$$\frac{dM_A}{dt} = \frac{\sum \dot{Q} - \dot{q}_l}{r_A \xi_A} \quad (7.2)$$

where: T - temperature in a thermal node, °C,

C_p - heat capacity, J/(kg°C),

$\sum \dot{Q}$ - sum of the \dot{q}_{in} input and \dot{q}_{out} output heat fluxes, across the boundary of the thermal node, J/s,

M_n - mass of the thermal node, kg,

M_A - mass of austenite in the thermal node, kg,

ξ_A - austenite fraction in the thermal node,

r_A - latent heat of austenite transformation, J/kg,

\dot{q}_l - heat flux needed to conduct the austenite transformation, J/s.

The mass M_n represents an infinitely small mass of the solid body in question. Equation (7.2) that describes the austenite fraction generation in the solid body has been introduced in its present form for the first time in modeling of phase (austenite) transformation kinetics in SMAs. It describes the austenite fraction generation under the assumption that the heat flux, needed to transform martensite to austenite is proportional to the latent heat of the phase transformation, magnitude of the austenite phase fraction and the mass of the material already transformed into austenite.

Equations 7.1 and 7.2 do not consider the influence of the boundary layer of the media surrounding the solid body (see Fig. 6.20 in Section 6.6) and will have to be accounted for accordingly in future work. The boundary layer concept states, that the temperature distribution in the solid body is affected by the temperature of the boundary layer of the media surrounding the solid body. The boundary layer concept affects the dynamics of the heating process only.

Knowing that the austenite phase fraction can be defined as the following ratio (Liang, 1990):

$$\xi_A = \frac{M_A}{M_n}, \quad (7.3)$$

and, assuming that:

$$M_n = const, \quad (7.4)$$

Eq. (7.1) can be re-written, considering Eqs. (7.3) and (7.4), as:

$$\frac{d\xi_A}{dt} = \frac{\sum \dot{Q} - \dot{q}_l}{r_A \xi_A M_n}. \quad (7.5)$$

The integration of Eqs. (7.1) and (7.5) gives correspondingly:

$$\left\{ \begin{array}{l} T = \frac{\sum \dot{Q}}{C_p M_n} t + const1, \\ \frac{\xi_A^2}{2} = \frac{\sum \dot{Q} - \dot{q}_l}{r_A M_n} t + const2. \end{array} \right. \quad (7.6)$$

$$\left\{ \begin{array}{l} T = \frac{\sum \dot{Q}}{C_p M_n} t + const1, \\ \frac{\xi_A^2}{2} = \frac{\sum \dot{Q} - \dot{q}_l}{r_A M_n} t + const2. \end{array} \right. \quad (7.7)$$

The integration constants in Eqs. (7.6) and (7.7) are defined by assuming that at the beginning of the austenite phase transformation process ($t = 0$) the austenite phase transformation fraction is equal to zero ($\xi_A = 0$). Therefore: $const1 = A_s$ and $const2 = 0$.

Finally, after substituting both integration constants into the system of Eqs. (7.6) and (7.7), the analytical form of both equations can be expressed as:

$$\left\{ \begin{array}{l} T = \frac{\sum \dot{Q}}{C_p M_n} t + A_s, \\ \frac{\xi_A^2}{2} = \frac{\sum \dot{Q} - \dot{q}_l}{r_A M_n} t. \end{array} \right. \quad (7.8)$$

$$\left\{ \begin{array}{l} T = \frac{\sum \dot{Q}}{C_p M_n} t + A_s, \\ \frac{\xi_A^2}{2} = \frac{\sum \dot{Q} - \dot{q}_l}{r_A M_n} t. \end{array} \right. \quad (7.9)$$

After rearranging Eqs. (7.8) and (7.9) into a single equation, the expression for the austenite phase fraction in the solid body can be written as follows:

$$\xi_A = \sqrt{\frac{2(\sum \dot{Q} - \dot{q}_l) C_p}{r_A \sum \dot{Q}} (T - A_s)} \quad (7.10)$$

In general, \dot{q}_l and A_s are not constants and are dependent on the current stress state in the solid body. The influence of the stress state can be accounted for in the expression for $\sum \dot{Q}$ according

to the fundamental energy conservation equation for uniaxial deformations from thermomechanics (Liang and Rogers, 1992; Labudovic, 2003), where $\sum \dot{Q}$ contains a stress dependent component, $\sigma \cdot \dot{\epsilon}$ (σ - stress, $\dot{\epsilon}$ - strain rate).

7.4 Austenite phase transformation function

The expression for the austenite phase fraction – the austenite phase transformation function - given by Eq. (7.10), can be further simplified for several particular cases, namely, for stress-independent and stress-dependent conditions in the SMAs. Both cases are given below.

7.4.1 Stress independent formulation of the austenite phase transformation function

For the stress-independent conditions, Eq. 7.10 is nearly insensitive to the magnitude of \dot{q}_l , which is at the level of several milliwatts according to the DSC thermograms (see the thermograms in Chapters 4, 5 and 6, for example, up to 20 mW in Fig. 5.11), while the magnitude of $\sum \dot{Q}$ is at the level of up to several watts (depending on a particular application, for examples up to 10 watts for the SMA wire). Therefore, it can be said, that the magnitude of \dot{q}_l is less than 1% of the magnitude of $\sum \dot{Q}$, and for the stress-independent conditions one can assume:

$$\dot{q}_l = 0,$$

and

$$A_S = A_{S0} = \text{const},$$

$$C_p = \text{const},$$

$$r_A = r_M = \text{const},$$

where: A_{S0} - is the austenite phase transformation start temperature for the stress-independent condition. Substituting all the above values into Eq. (7.10), the austenite phase transformation function, ξ_A , becomes:

$$\xi_A = \sqrt{\frac{2C_p}{r_A}(T - A_{S0})} \quad (7.11)$$

The analysis of Eq. 7.11 shows that the austenite fraction in the stress-independent solid body in the current representation is not dependent on mass M_n of the initially discretized control volume and on the heat balance in the control volume.

The standard physical properties of NITINOL are used in order to validate Eq. 7.11. It is assumed, that when the temperature of the solid body is equal to the austenite finish temperature, $T = A_F$, then the austenite fraction $\xi_A = 1$. The properties of SMA NITINOL are listed in Table 7.1:

Table 7.1: *Physical properties of NITINOL (Brinson et al., 1996; Liang and Rogers, 1992)*

NITINOL properties
austenite start temperature, $A_s = 34.5 \text{ }^\circ\text{C}$
austenite finish temperature, $A_f = 49 \text{ }^\circ\text{C}$
specific heat, $C_p = 920 \text{ J/(kg}^\circ\text{K)}$
latent heat of phase transformation, $r_M = r_A = 24171, \text{ J/kg (at } 40 \text{ }^\circ\text{C)}$

The austenite fraction evolution, computed according to Eq. 7.11, is shown in Fig. 7.4. The computed austenite fraction varies with varying SMA temperature T , that is the only variable in the equation (7.11). It is assumed that Eq. 7.11 does not depend on the discretization as it was formulated based on Eq. 7.10, where the discretization of the 0-D model vanishes during the derivation of Eq. 7.10.

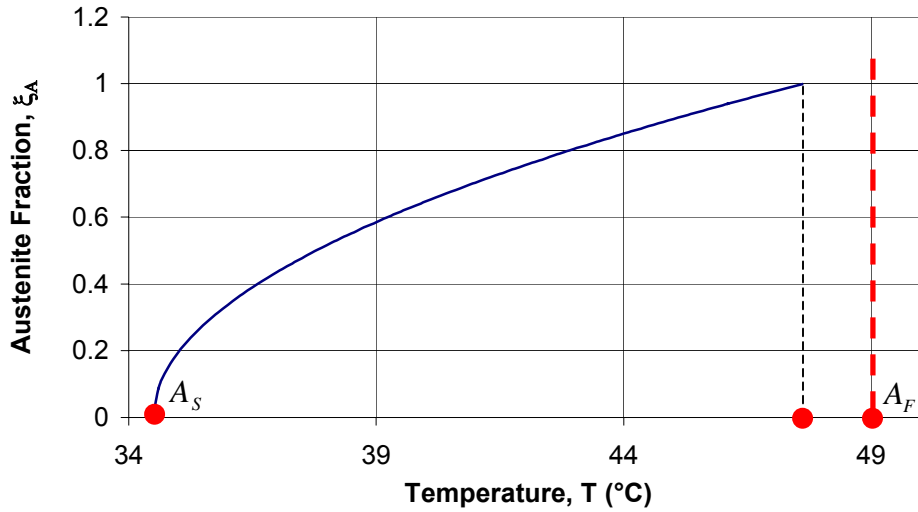


Figure 7.4: Austenite fraction evolution vs. temperature in NITINOL alloy for stress-independent conditions.

According to Fig. 7.4, Eq. (7.11) gives $A_F = 47.6$ °C when $\xi_A = 1$. The experimentally obtained tabulated value of $A_F = 49$ °C, when $\xi_A = 1$ (Table 7.1). Better (closer to the tabulated) values for A_F can be obtained by using the non-simplified version of the austenite fraction function in Eq. (7.10), which gives $A_F = 48.7$ °C, but the ambiguity in defining the value \dot{q}_l in it makes it difficult to ascertain its validity. For example, \dot{q}_l can be formulated as:

$$\dot{q}_l = r_m M_n V / L, \quad (7.12)$$

or

$$\dot{q}_l = r_m M_n / t \quad (7.13)$$

where: V - speed of the phase transformation, m/s,
 L - characteristic dimension of the idealized element (thermal node), m,
 t - time of the phase transformation process, s.

Therefore, in order to account for \dot{q}_l in Eq. 7.11 one needs to experimentally validate Eqs. (7.12) or (7.13). Though, the variation in \dot{q}_l can be neglected, since its magnitude constitutes approximately 1% of the total heat flux as it was mentioned earlier.

7.4.2 Stress dependent formulation of the austenite phase transformation function

Equation (7.11) for the stress-independent austenite phase transformation function can be rewritten for the general stress-dependent conditions by substituting the stress-dependent austenite start temperature A_s^σ in place of the stress-independent temperature A_s into Eq. (7.11):

$$\xi_A = \sqrt{\frac{2C_p}{r_A}(T - A_s^\sigma)} \quad (7.14)$$

The main assumption in Eq. (7.14) for the stress-dependent conditions is the same as the one for Eq. (7.11) for the stress-independent conditions, namely that:

$$\dot{q}_l = 0.$$

An expression for A_s^σ according to Liang and Rogers, 1992 is:

$$A_s^\sigma = A_{s0} + \frac{\sigma}{C_A} \quad (7.15)$$

where: σ - is the applied external (or internal residual) stress, Pa,

C_A - is the transformation constant that indicates the influence of the stress on the phase transformation temperatures, Pa/°C.

Therefore, substituting the expression for A_s^σ (from Eq. (7.15)) into the expression for the phase transformation function (Eq. (7.14)), the austenite stress-dependent phase transformation function becomes:

$$\xi_A = \sqrt{\frac{2C_p}{r_A} \left(T - A_{s0} - \frac{\sigma}{C_A} \right)} \quad (7.16)$$

The evaluation of Eq. 7.16 for different stress levels is shown in Fig. 7.5.

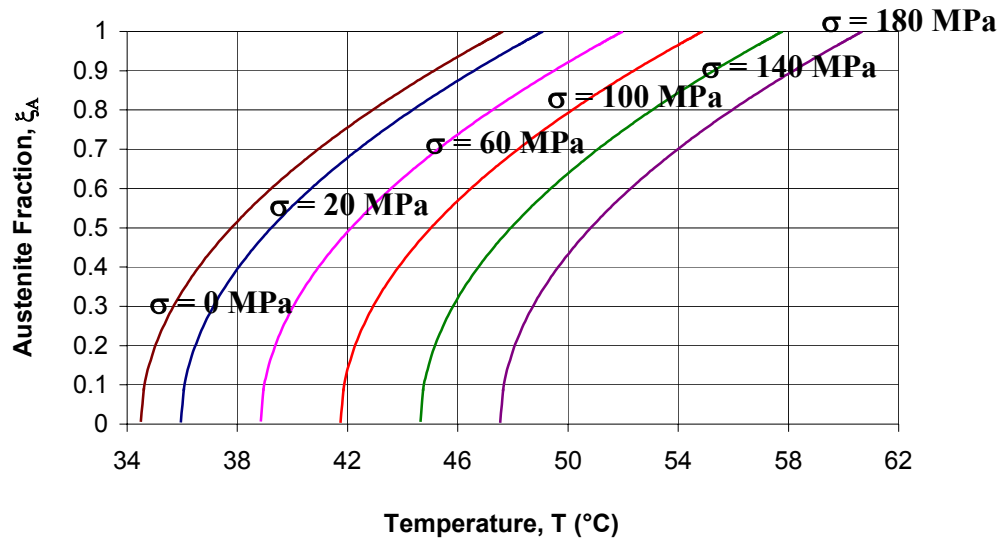


Figure 7.5: Austenite fraction evolution vs. temperature in NITINOL alloy for stress-dependent conditions.

7.4.3 Comparison of the suggested transformation function to a conventional existing transformation function.

It is advantageous to compare the results from the suggested phase transformation function and the already existing phase transformation functions. A widely used formula for the stress-dependent martensite phase transformation function is given, for example, by Brinson (1993) and reads as:

$$\xi_{M \cos} = \frac{\xi_{M0}}{2} \left\{ \cos \left[a_A \left(T - A_s - \frac{\sigma}{C_A} \right) \right] + 1 \right\}, \quad (7.17)$$

where

ξ_{M0} - initial value of the martensite fraction (here $\xi_{M0} = 1$),

Knowing that,
$$\xi_{A \cos} = 1 - \xi_{M \cos} \quad (7.18)$$

and that:
$$a_A = \frac{\pi}{A_F - A_S},$$

one can compute and plot the austenite transformation functions. The comparison of the results computed from Eqs (7.16) and (7.18) is shown in Fig. 7.6:

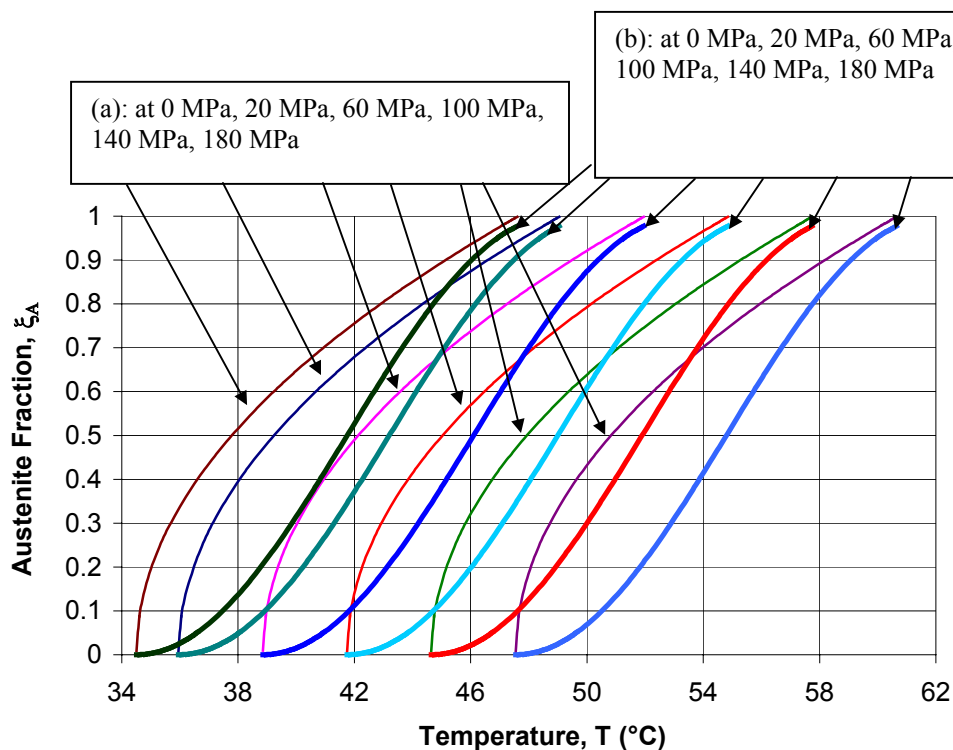


Figure 7.6: Austenite fraction evolution vs. temperature in NITINOL alloy for stress-dependent conditions: (a) from equation 7.16, (b) from equation 7.18.

The comparison between the two different austenite phase transformation functions shows, that at an intermediate point of the austenite phase transformation process, taken for example, at the zero stress level (0 MPa) and at an SMA temperature of $T = 38 \text{ }^\circ\text{C}$, our suggested Eq. (7.16) gives a magnitude of $\xi_A = 0.516$, while the conventionally used Eq. (7.18) computes a $\xi_{A\cos} = 0.137$ value. Therefore, the difference in the values of ξ_A for the given stress and temperature conditions is significant, i.e., 500%. On the other hand, at the end of the phase transformation process for the current stress level (0 MPa) and an SMA temperature of $T = 49 \text{ }^\circ\text{C}$, the difference between Eqs. (7.16) and (7.18) becomes insignificant and both equations approach $\xi_A = 1$ simultaneously.

Summarizing the above derivations, one can say that the suggested expression for the austenite transformation function ξ_A from Eq. (7.16) gives an up to a 5 times higher estimate of ξ_A at intermediate points of the austenite phase transformation process, than the conventional expression for ξ_A from Eq. (7.18) does. In the sequel, an experimental verification of both the suggested and of the conventional mathematical models will be undertaken.

7.5 Experimental verification of the mathematical model of the stress-independent austenite phase transformation.

The mathematical model of the stress-independent austenite phase transformation described by Eq. (7.11) is validated in this Section. The validation is based on a series of experimental investigations of the step (displacement) response of a commercially available

SMA wire, subjected to heat loads. The SMA wire is a TEFLON insulated FLEXINOL wire obtained from Dynalloy, Inc. The “as-is” wire was purchased already in a pre-stretched condition, such that the wire would contract after heat is applied to it. To perform multiple contractions, the wire would have to be pre-stretched again by an external bias force.

The experiments were conducted as follows. The SMA wire was connected to the air-bearing linear stage to be able to measure the displacements of the wire (Fig. 7.7). External load (stress) was not initially applied to the wire. Afterwards, the wire was heated by passing an electrical current through it, thus making the wire contract. One of the ends of the SMA wire was attached to the moving part of the air-bearing stage (Fig. 7.7) while the other end was permanently fixed. Upon contraction, the wire’s displacements and temperatures were recorded by a data acquisition system, equipped with a DAQ and operated by the LabVIEW software. In place of the capacitance probe (Section 6.3), a linear variable differential transformer (LVDT) was used to record the displacements of the wire during its contraction. The core of the LVDT was attached to the moving part of the air-bearing stage in parallel with the SMA wire. A thermocouple was attached to the SMA wire to measure the temperature of the TEFLON insulated wire.

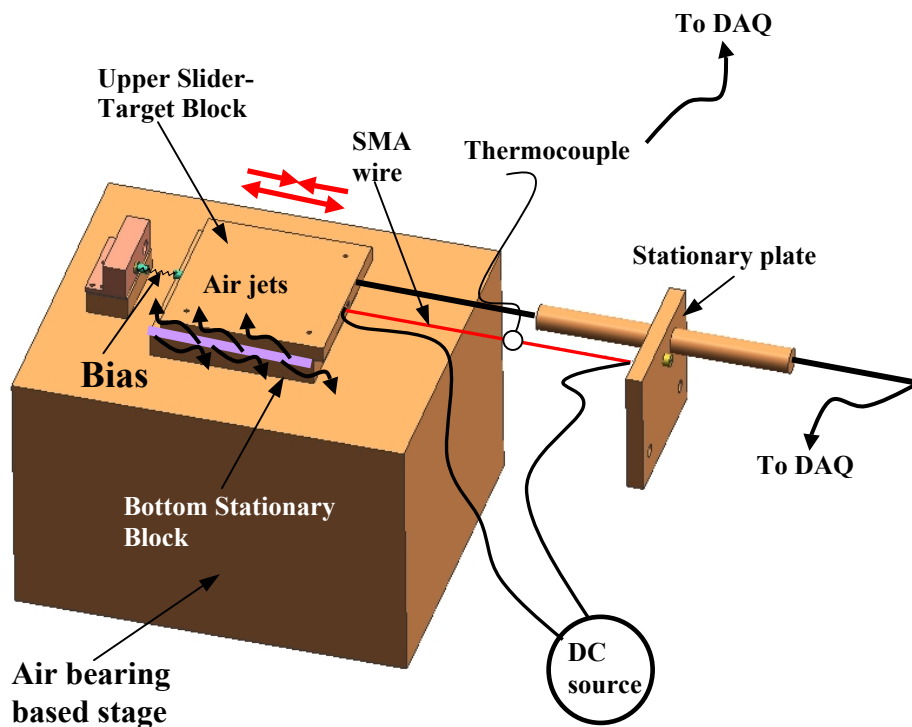


Figure 7.7: *FLEXINOL* wire, attached to the air-bearing linear stage.

The experimental procedure (heating/cooling cycles) was almost the same as the experimental procedure described in Chapter 6. The difference was in the way the SMA wire's contraction displacement was measured: here an LVDT was used, instead of the capacitance probe. One of the experimental data sets from a SMA wire step response experiment is shown in Fig. 7.8. The wire was heated by applying electrical current through it. Each step in the displacement of the SMA wire in Fig. 7.8a corresponds to a step in the applied voltage (current). The corresponding temperatures are depicted in the plot in Fig. 7.8 b.

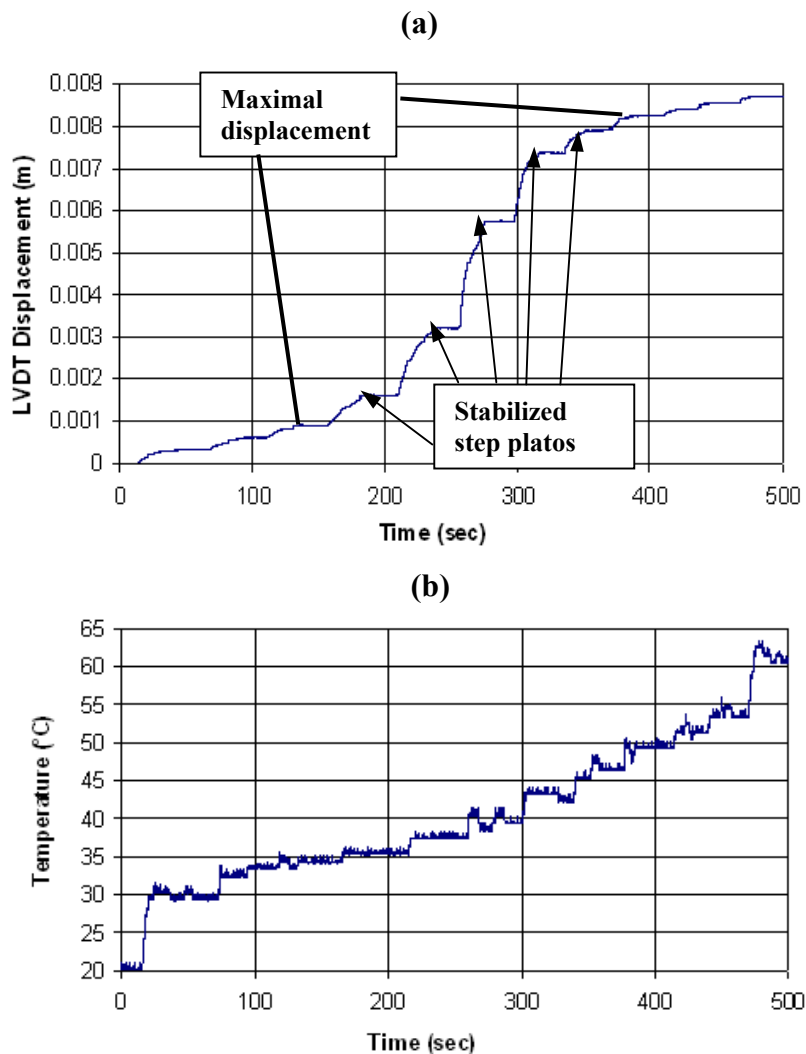


Figure 7.8: *Experimental data from SMA wire heating cycle: (a) SMA wire displacement, (b) SMA wire temperature.*

The displacements from five experimental data-sets (additionally shown in Appendix F) were converted into the austenite phase fraction values and plotted versus the corresponding temperatures in Fig. 7.9. The theoretical values of the austenite phase fraction, obtained from our suggested model and from the conventionally used model, were also plotted in Fig. 7.9 as curve

(1) and curve (2) relatively. They were taken from the plot in Fig. 7.6 for the zero-stress case, where no initial external stress was applied to the wire.

The conversion of the SMA wire displacement values (Fig. 7.8a) into the austenite phase fraction values was done by means of normalization of the maximal magnitude of every displacement step. The maximal magnitude of each step is the magnitude of the displacement at the end of its transient. The maximal magnitudes of each step (shown in Fig. 7.8) were divided by the magnitude of the overall maximal final displacement developed by the wire at the end of the experiment. They were plotted in curve (3) in Fig. 7.9.

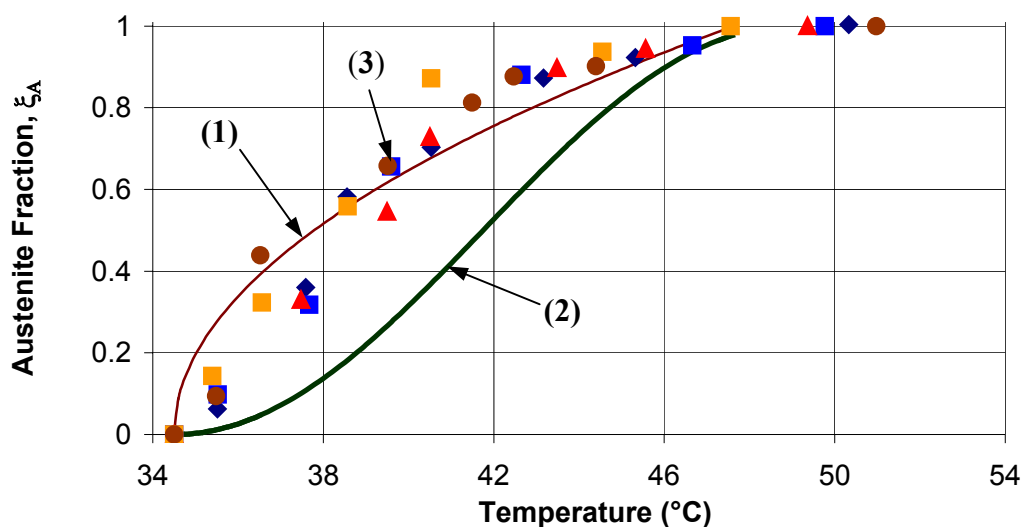


Figure 7.9: Austenite phase fraction vs. temperature in NiTi alloy under zero-stress conditions: (1) from the suggested equation (7.11), (2) from equation (7.18), (3) from experimental data in the plot in Figure 7.8 and Appendix F.

The three (3) curves plotted in Fig. 7.9 can be analyzed as follows. The experimental curve (3) shows a good agreement with the data obtained from our mathematical model

represented by Eq. 7.11 and plotted as curve (1) in Fig. 7.9. The best agreement between the theoretical and experimental values in curves (1) and (3) can be found in the region, with the austenite fraction values between $\xi_A = 0.15$ to 1. In this region, the conventional formula (Eq. 7.18, curve (2)) gives the largest error (difference from the experimental data equal to almost 500%), while the maximal error of our proposed model is approximately 15%.

Both formulas give equally good prediction of the austenite fraction for $\xi_A < 0.15$ and $\xi_A > 0.9$.

7.6 Concluding remarks

A mathematical model, describing the kinetics of the austenite phase transformation in an SMA wire, was proposed. The final result represents an analytical expression for the austenite phase transformation function. The function computes the values of the austenite phase transformation fraction in SMAs under different stress and temperature conditions for the general case. The suggested model shows good agreement with experimental results for the stress-independent formulation. The proposed mathematical model suggests that the computation of the austenite phase transformation fraction is not dependent on the discretization of a solid body into the elementary control volumes or thermal nodes and uses physical parameters that are known.

CHAPTER 8

8. Mathematical model of the motion of SMA actuators based on the new model of the kinetics of the phase transformation in SMAs

A new model, describing the kinetics of the austenite phase transformation in SMAs, was developed in Chapter 7. It was based on fundamental energy conservation equations and the physical properties of SMAs. The model presents a precise quantitative tool for the prediction of SME driven motions, and as such, it can be used to model the motion and dynamic response of SMA based mMMs.

The current Chapter describes the application of the suggested mathematical model of the austenite phase transformation in modeling the motion of SMA wire-based actuators for control purposes based on a model of motion of a “human muscle” (Wu et al., 1990). The model of motion of a “muscle” is used here due to its “agonist-antagonist” layout, similar to the layout of the experimental setup with the SMA wire opposed by a bias spring, connected to the X-Y linear stage, described in Chapter 6, and due to the fact that it is also based on the fundamental conservation equations of momentum, written for the “agonist-antagonist” actuator. The “muscle” motion model will be a part of the SMA wire-based actuator motion model, proposed in this Chapter, due to the similar dynamics behavior of the “muscle” and of the actuator. The earlier developed model of the kinetics of the austenite phase transformation will complete the proposed model of motion of the actuator. In combination, both models will form a

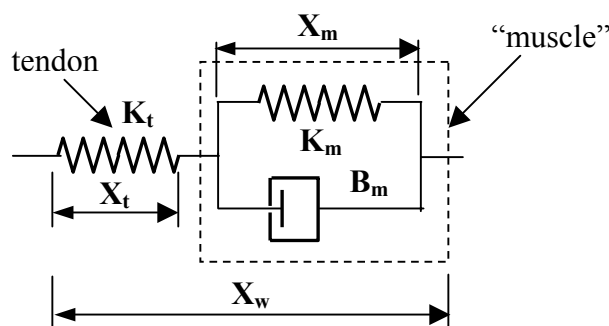
computational tool for the prediction of the motion of SMA actuators with non-linear dynamic characteristics.

8.1 Description of the model of motion of a “muscle” after Wu et al., 1990

A “muscle” motion model was developed by Wu et al. (1990). The model is represented in the form of a closed loop control system. The system is aimed at simulating the human muscle-reflex mechanism. The authors have verified the model by means of an experimental setup (Miller, 1984). The setup has allowed the study of the step and ramp disturbance responses of the human muscle, subject to an external payload, by measuring the human wrist’s flexion and extension in the horizontal plane. A natural wrist flexion-extension motion was provided by an arrangement of an arm brace such that a subject’s forearm was supported in the horizontal plane, while the subject was seated in a manner allowing the upper arm to be approximately perpendicular to the forearm (Wu et al., 1990). The subjects’ wrist held a handle attached to a mechanical stimulus generator. The generator produced payloads acting on the wrist. The corresponding reaction force from the wrist was measured by strain gauges located on the handle.

The experimental investigations have shown that the human muscle-reflex mechanism had non-linear dynamic properties which were similar to the non-linear dynamics of SMA wire actuators, explored in Chapter 6. Therefore, it was decided to explore the utility of the “muscle” model in conjunction with the developed phase transformation kinetics model in modeling and motion control of the SMA actuator.

The “muscle” model schematics is shown in Fig. 8.1. The “muscle” model is described by an “agonist-antagonist” actuator model, where the human tendon is connected to the human muscle in series. The tendon is represented by a spring with stiffness K_t . The “muscle” is represented by a spring with stiffness K_m and a non-linear damper with damping constant B_m , located in parallel to K_m .

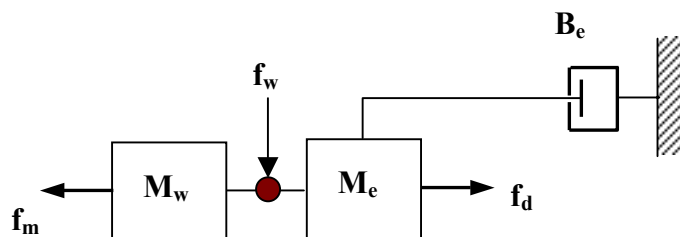


X_t – displacement of tendon, m ; X_m – displacement of “muscle”, m ; X_w – total displacement, m ; K_t – stiffness of tendon, N/m ; K_m – stiffness of muscle, N/m ; B_m – non-linear damping constant of muscle, $N \cdot (s/m)^{1/5}$.

Figure 8.1: “Muscle” motion model (Wu et al., 1990).

The equivalent schematic of the experimental setup is shown in Fig. 8.2. It shows the distribution of the applied and reaction forces in the “load-muscle-wrist” system, assuming that the “muscle” model is represented by the model shown in Fig. 8.1. The disturbance force f_d , being the reaction to a payload on the “load-muscle-wrist” system in Fig. 8.2, is applied to the human wrist such that it causes a reaction force at the wrist, f_w , and creates the corresponding reaction force of the muscle, f_m , which is further measured with strain gauges. The mass element, M_e , and the damping element characterized by the linear damping constant B_e are used in the experimental setup to model the payload on the wrist and to provide additional stability for the

whole system of the “load-muscle-wrist” setup. The total displacement of the wrist, X_w , is measured as well. The tendon is not shown in Fig. 8.2.



f_d – applied disturbance force, N; f_w – measured wrist force, N; f_m – reaction force of the muscle, N; M_w – mass of the wrist, kg; M_e – mass of payload, kg; B_e – damping constant from the device for stability consideration, N·s/m.

Figure 8.2: Equivalent schematic of the experimental setup of the “load-muscle-wrist” system (Wu et al., 1990).

The reaction of the muscle to a disturbance force applied to the wrist is described by the simulation block diagram shown in Fig. 8.3. The diagram schematically represents a mathematical model for studying step disturbances (from f_d) to the “load-muscle-wrist” system. The block includes the “muscle” motion model, according to Wu et al., 1990, shown in Fig. 8.1.

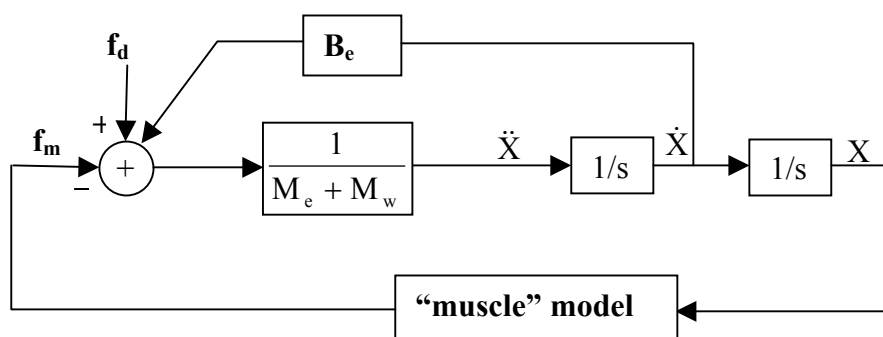


Figure 8.3: Simulation block for studying step disturbances to the “load-muscle-wrist” (Wu et al., 1990).

The feedback control system in Fig. 8.3 can be described by the following system of equations of motion, according to Wu et al., 1990:

$$\left. \begin{aligned} f_d - B_e \dot{X}_w - (M_e + M_w) \ddot{X}_w &= K_t (X_w - X_m), \\ f_m = f_t &= K_t (X_w - X_m) = K_m X_m + B_m \dot{X}_m^{1/5}, \\ f_w &= M_w \ddot{X}_w + K_t (X_w - X_m). \end{aligned} \right\} \quad (8.1)$$

A sample displacement simulation output (taken from Wu et. al., 1990) of the “load-muscle-wrist” model in response to a force step input, f_d , is shown in Fig. 8.4. Due to the non-linear damping term $B_m \dot{X}_m^{1/5}$ in Eq. (8.1), the output displacement, X_m , can be divided into two regions (Fig. 8.4): (a) a region that shows the fast displacement response evolution at the beginning of the time interval and (b) a region that shows a very slow displacement response evolution and stabilization at the end of the overall time interval.

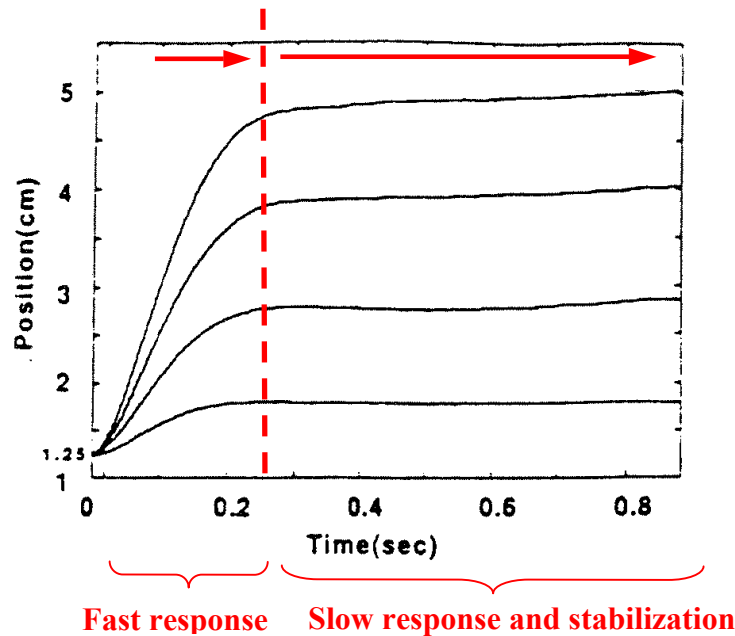


Figure 8.4: Displacement-time plot from the output of the step response simulations obtained from the “load-muscle-wrist” simulation model (Wu et al., 1990).

8.2 Formulation of the model of motion of the SMA actuator

The model of motion of the SMA actuator will be based on the new model of phase transformation kinetics in SMAs and the existing model of motion of the human muscle described in the previous section.

The dynamics of the response of the SMA wire actuator is shown Fig. 8.5. The displacement-time plot in Fig. 8.5 was taken from the step response data from one of our experiments with the thermally insulated SMA wire (similar to the displacement-time plot in Fig. 6.8a in Chapter 6, therefore, not shown in that chapter). This response shows a qualitatively very similar behavior to the response of the “load-muscle-wrist”, depicted by the plots in Fig. 8.4.

Namely, there is a fast response at the beginning of the time interval, and a very slow response and stabilization at the end in both Fig. 8.4 and Fig. 8.5.

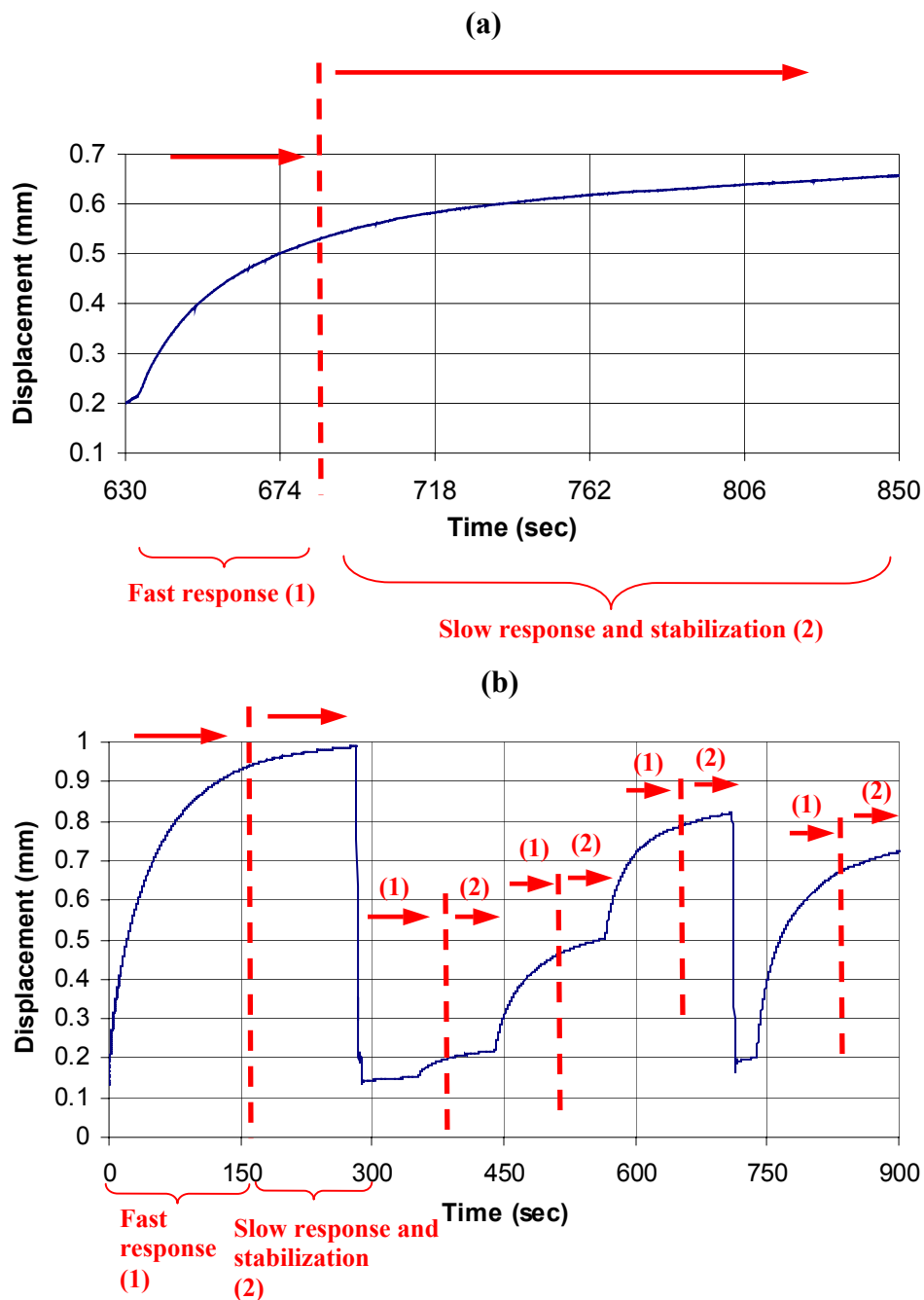
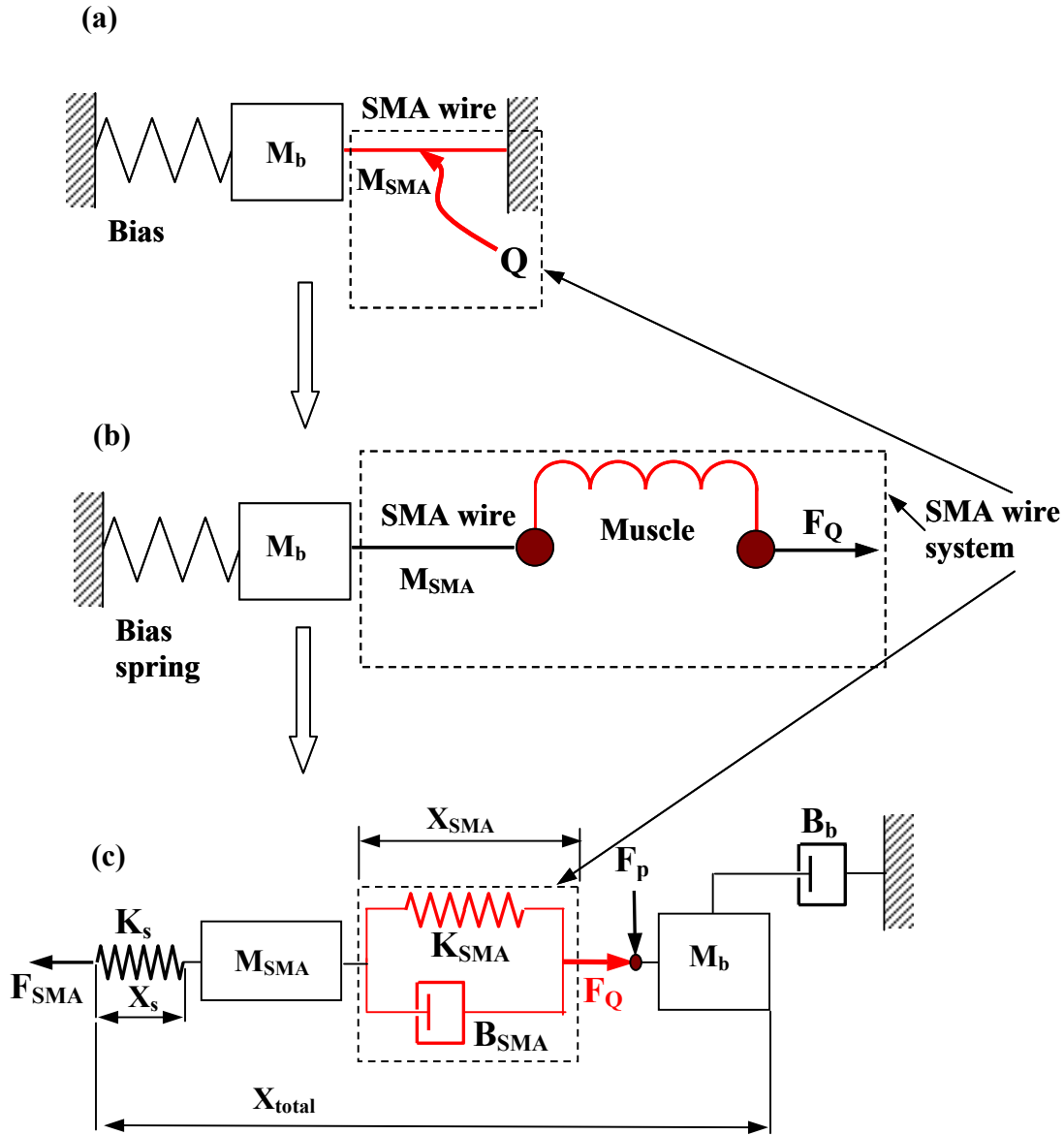


Figure 8.5: Experimental results from thermally insulated SMA wire step responses: (a) initial pre-strain = 5.55%, initial voltage ≈ 3 V, initial electric current ≈ 0.5 A, (b) (initial pre-strain = 1.38%, initial voltage ≈ 2.9 V, initial electric current ≈ 0.4 A)

Given the obvious similarities in Fig. 8.4 and Fig. 8.5, the “load-muscle-wrist” model was chosen as a basis for formulating the model of the SMA wire actuator. The “load-muscle-wrist” model was adapted such that it simulates the controlled strain recovery conditions present in the air-bearing based experimental setup with the SMA wire described in Chapter 6 and also the two opposing accordion springs of the mMM in the X- and Y-directions. The disturbance force in the adapted model is, in turn, simulated by the new austenite phase transformation function formulated in Chapter 7.

The adaptation procedure and the resulting model schematic are shown in Fig. 8.6. Figure 8.6a represents a simplified layout of the physical setup of the SMA wire actuator operating under controlled strain recovery conditions. The layout schematically depicts the bias spring, connected to the middle block of the air-bearing stage from one end and the SMA wire connected to the block from the other end. In general, the controlled strain recovery conditions for the SMA wire can be also used to represent a particular case of the controlled strain recovery conditions for the SMA spring with corresponding values of the stiffness and damping coefficients. Figure 8.6b shows, that the SMA wire is substituted by its equivalent representation for the purposes of modeling. The equivalent representation of the SMA wire requires three adaptations: (1) a regular wire with mass M_{SMA} , (2) a “muscle”, presenting the non-linear dynamics of the SMA wire response, and (3) a disturbance force F_Q , presenting the austenite phase transformation in the SMA wire. The “muscle” is modeled using the model suggested by Wu et al., 1990, while the force, F_Q , is modeled using the suggested austenite phase transformation function, ξ_A , given by Eq. (7.11). The final schematics of the equivalent mathematical model of the SMA wire actuator is shown in Fig. 8.6c.



F_{SMA} – reaction force of the SMA wire, N; F_Q – applied (recovery) force to the SMA wire, N; F_p – payload force, N; X_{SMA} – displacement of the SMA wire, m; X_{total} – total displacement of the SMA wire system, m; X_s – displacement of the bias spring, m; K_s – stiffness of the bias spring, N/m; K_{SMA} – stiffness of the SMA wire, N/m; B_{SMA} – non-linear damping constant of the SMA wire, $N \cdot (s/m)^{1/5}$; B_b – damping constant of the payload system (with pulling device), N·s/m; M_b – mass of the payload system, kg; M_{SMA} – mass of the SMA wire, kg; Q – heat flux applied to the SMA wire, W; F_Q – force developed in the SMA wire, based on the magnitude of the applied heat flux Q and the new phase transformation function, N.

Figure 8.6: Equivalent schematics of the mathematical model of the SMA wire actuator: (a) simplified schematics of the SMA wire actuator, (b) adapted schematics (c) final equivalent mathematical model of the SMA actuator.

The effect of the inertia of the air-bearing linear stage, used in the SMA wire experimental setup (Chapter 6), is modeled by the mass element, M_b , and damping coefficient, B_b , in Fig. 8.6c.

Using the above-described system of equations of motion, Eqs. (8.1), whose elements are taken from the schematics in Fig. 8.6c, the system of equations, describing the motion of the SMA wire actuator can be written analogously as:

$$\left. \begin{aligned} F_Q - B_b \dot{X}_{total} - (M_b + M_{SMA}) \ddot{X}_{SMA} &= K_s (X_{total} - X_{SMA}), \\ F_{SMA} = F_s = K_s (X_{total} - X_{SMA}) &= K_{SMA} X_{SMA} + B_{SMA} \dot{X}_{SMA}^{1/5}, \\ F_p = M_{SMA} \ddot{X}_{total} + K_s (X_{total} - X_{SMA}). \end{aligned} \right\} \quad (8.2)$$

where K_{SMA} is the stiffness of the SMA wire, N/m.

The derivation of the expression for the disturbance force, F_Q is based on the following approach under consideration of a number of assumptions and limitations:

- 1) The known approach for modeling of the stress-strain relation during the phase transformation in the SMA alloys (used, for example, by Brinson, 1993) can be used. In this approach, the force is considered to be proportional to the transformation stiffness of the SMA actuator (wire or spring) K_{SMA} , austenite fraction ξ_A , and maximal recovery displacement X_{SMA}^{\max} . Therefore, F_Q can be computed as follows:

$$F_Q = K_{SMA} \xi_A X_{SMA}^{\max} \quad (8.3)$$

where: K_{SMA} is the transformation stiffness of the SMA wire, N/m; X_{SMA}^{\max} is the maximal recovery displacement (or transformation displacement), m. This displacement is a maximally achievable displacement and is defined later. Eq. (8.3) is a convenient way of representation of the shape memory effect driven recovery force F_Q . This is an artificial way of representing F_Q , since in this form, the equation states that the force is developed due to the change in the effective stiffness of the material, while the stiffnesses of the austenite and martensite phases are almost equal. This approach of representation of the recovery force is a simplification of a more elaborate form of the driving force of the shape memory effect driven motion, which is based on the diffusionless phase transformation from detwinned martensite to austenite phase during heating (Liu and Xie, 2003; Wu et al., 2003). Our approach does not account for the micro-structural changes in the material during the shape memory effect recovery process (such as grain re-orientation, etc.) and therefore, cannot be used to model the SME driven motion during complex loading, where the micro-structural changes introduce non-linearity in the relation between the transformation strain and the driving force.

- 2) The rule of mixtures, generally used in thermodynamics for modeling the properties of a two-phase media, is applied for the modeling of the SMA properties of the wire material, namely the transformation stiffness of the wire as follows:

$$K_{SMA} = K_A \xi_A + K_M (1 - \xi_A) \quad (8.4)$$

In Eq (8.4) K_A and K_M represent the stiffness of the wire corresponding to the two phases, i.e., the austenite and martensite phases. The stiffness of the wire is given by:

$$K_A = E_A A / L_{wire} \quad (8.5a)$$

and

$$K_M = E_M A / L_{wire} \quad (8.5b)$$

for the austenite and martensite phases respectively. E_A represents the modulus of elasticity of the SMA in the austenite phase, N/m²; E_M is the modulus of elasticity of the SMA in the martensite phase, N/m²; A is the cross-sectional area of the SMA wire, m²; and L_{wire} - is the length of the SMA wire, m.

Equations (8.2) and (8.3) can now be combined into the following system of equations:

$$\left. \begin{aligned}
 F_Q - B_b \dot{X}_{total} - (M_b + M_{SMA}) \ddot{X}_{SMA} &= K_s (X_{total} - X_{SMA}), \\
 F_{SMA} = F_s &= K_s (X_{total} - X_{SMA}) = K_{SMA} X_{SMA} + B_{SMA} \dot{X}_{SMA}^{1/5}, \\
 F_p &= M_{SMA} \ddot{X}_{total} + K_s (X_{total} - X_{SMA}), \\
 F_Q &= K_{SMA} \xi_A X_{SMA}^{\max}.
 \end{aligned} \right\} \quad (8.6)$$

The system of equations, Eq. (8.6), represents the mathematical model of motion of the SMA wire actuator under the following assumptions and limitations:

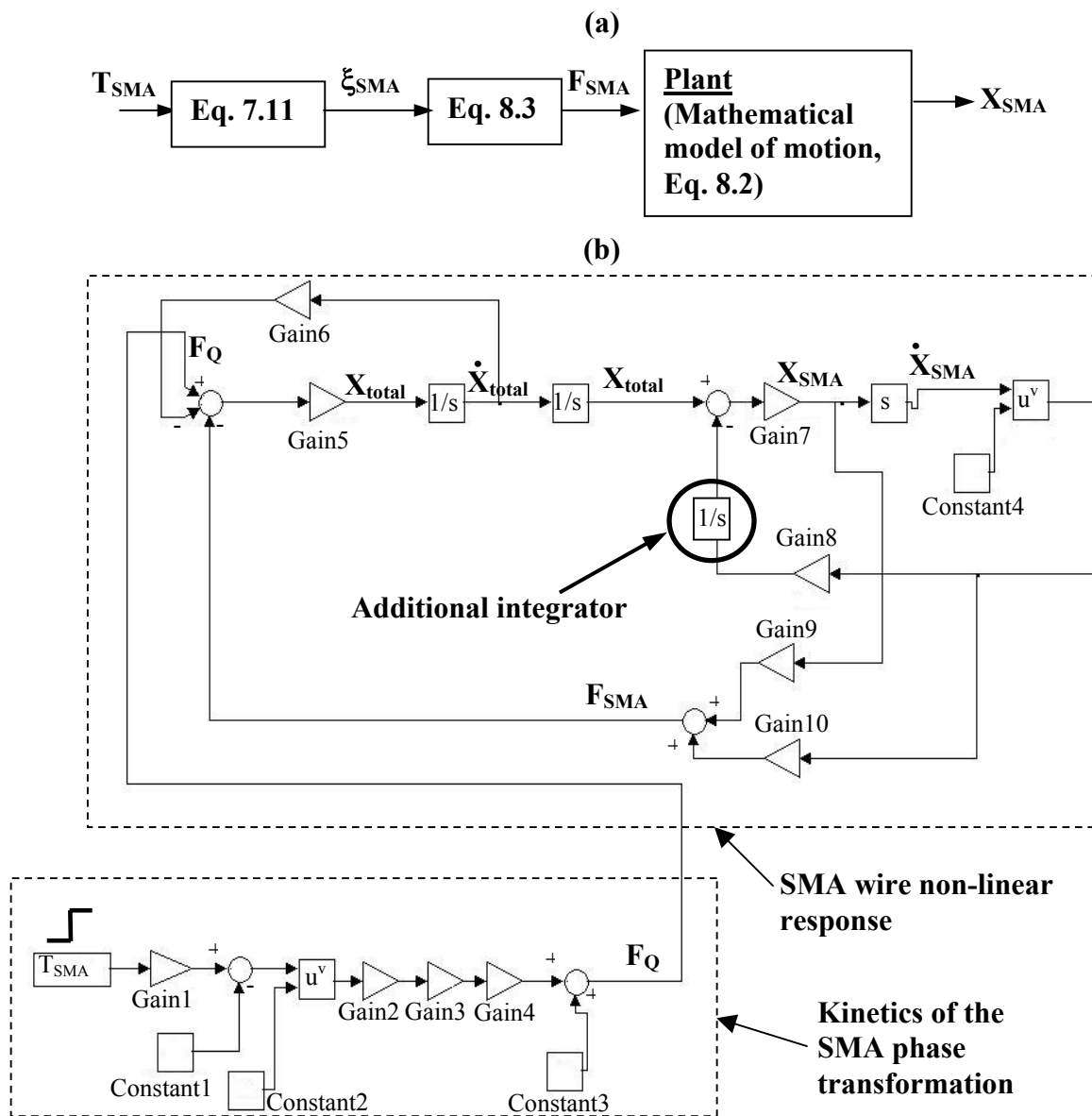
- 1) The SMA wire contracts uniaxially.
- 2) The SMA wire has negligibly small thermal inertia such that it is always in thermal equilibrium. Therefore, heat sink conditions have no effect on SMA wire dynamics.
- 3) Friction has no effect on SMA wire dynamics.
- 4) The austenite phase transformation occurs instantaneously upon temperature input in the wire. Therefore, the speed of the phase transformation has no effect on SMA wire dynamics.
- 5) The SMA wire actuator exhibits a non-linear damping property and a linear stiffness property.

8.3 Simulation model for the motion of the SMA wire actuator using “Simulink”

The of the system of equations, Eq. (8.6), was realized in a simulation block aimed at studying the step response of the SMA wire actuator due to an applied heat load Q. The block

diagram is shown in Fig. 8.7a. The diagram represents an open loop response schematic with the temperature as the input and displacement as the output. The simulation block is shown in Fig. 8.7b. It represents the mathematical model (equations (8.6)) of motion of the SMA wire actuator.

An additional integrator was added to the “Simulink” model for numerical stability purposes (see Fig. 8.7b). The integrator does not change the quantitative response of the system of equations (8.6). It stabilizes the integration of the differential equations of motion by adding a lag into the Gain8 path (similar to a sensor lag in a feedback path according to (Franklin et al., 2002)) in the “Simulink” block. The numerical instability in the Gain8 path is evoked by the existence of the rapidly changing derivative of the variable X_{SMA} due to the power term u^v (Fig. 8.7b), such that a steady state could not be achieved (solution would not converge) at the minimal possible integration step, available in the current “Simulink” environment.



(c)

Nomenclature:

$Gain1 = 2C_p/r_m$;
$Gain2 = EA$;
$Gain3 = A/L_{wire}$;
$Gain4 = \varepsilon_L L_{wire}$;
$Gain5 = 1/(M_b + M_{SMA})$;
$Gain6 = B_b$;
$Gain7 = 1/(K_{SMA}/K_s + 1)$;
$Gain8 = B_{SMA}/K_s$;
$Gain9 = K_{SMA}$;
$Gain10 = B_{SMA}$;
$Constant1 = 2C_p/r_m A_s$;
$Constant2 = 0.5$ (power of the equation (7.11));
$Constant3 = 0.00001$ (added for the purpose of numerical stability in the “Simulink” integration solver);
$Constant4 = 0.2$ (characterizes the non-linear behavior of the “muscle” system according to Wu et al., 1990).
M_{SMA} – mass of the wire, kg;
B_b – damping coefficient of the payload system, N·s/m;
K_m – stiffness of the wire in the martensite state, N/m;
K_t – stiffness of the bias spring, N/m;
B_{SMA} – damping coefficient of the wire actuator, N·s/m;
E_A – modulus of elasticity of the SMA material in the austenite state, N;
K_A – stiffness of the wire actuator in the austenite state, N/m;
ε_L – maximal recovery strain of the wire, m;
L_{wire} – length of the wire, m;
C_p – heat capacitance of the SMA material, J/(kgK);
r_m – latent heat of phase transformation, J/kg;
A_s – start temperature of austenite phase transformation, °C.

Figure 8.7: Block diagram (a), simulation block (b) for studying the step response of the SMA wire-based actuator, (c) nomenclature.

8.4 Verification of the suggested mathematical model of motion of the SMA wire actuator

The mathematical model of motion formulated above is verified in this section by using the experimental results from a step response experiment described in Chapter 6. The input parameters to the model are further defined and a comparative analysis is undertaken.

8.4.1 Definition of model parameters

The values of the input parameters to the model shown in Fig. 8.7 are given in Table 8.1. They were chosen based on the physical properties of the SMA material of the wire, geometry of the wire, and geometry of the experimental setup shown in Fig. 7.7. In the current computations, for simplicity purposes and based on the fact that the austenite stiffness differs from the martensite stiffness by approximately 3 times, it was assumed, that $K_{SMA} = K_A$ and $X_{SMA}^{\max} = \varepsilon_L L_{wire} = const$, where: ε_L - maximal transformation strain ($\varepsilon_L = 0.067$, from Brinson et al., 1996), L_{wire} - length of the SMA wire, m. The determination of B_{SMA} is described in the next section.

Table 8.1: Input parameters

Parameter	Value	Parameter	Value
C_p	920	M_{SMA}	7.52894e-5
r_m	24171	$K_{SMA} = K_A$	15516
E_A	70e9	K_s	706
E_M	26e9	K_m	5762.9
A	5.0669e-8	B_b	6000
L_{wire}	0.2286	B_{SMA}	0.00217
ε_L	0.067	A_s	34.5
M_b	2.16		

8.4.2 Determination of B_{SMA}

The procedure of estimation of the unknown damping coefficient B_{SMA} will be described in this section. The coefficient can be estimated from the experimental data of the step response experiments described earlier in Chapter 6 and/or based on the fundamental physical properties of the SMA material, SMA wire geometry and its working conditions. For this purpose, the system of equation of motion of the SMA (Eq. 8.6) will be used. The known parameters in the system of equations are the geometry of the wire, physical properties of the wire (including its stiffness and mass), the thermal load to the wire (input heat flux) that produces the recovery force of the wire, and the experimentally obtained displacement of the wire. It is also possible to use the known recovery conditions of the wire at its maximal recovery strain (ε_L) conditions –

which is a property of the wire as well (Table 8.1). The maximal recovery strain conditions occur when the wire is fully transformed to its austenite phase ($\xi_A = 1$) when heated to its A_s temperature level. The unknown parameter – the damping factor B_{SMA} is estimated by obtaining an analytical solution of the second equation in the system of equations of motion (Eq. 8.6) of the SMA wire actuator. The second equation represents the balance of forces between the bias spring (force F_s) and the SMA wire (force F_{SMA}) as follows:

$$F_{SMA} = F_s = K_s (X_{total} - X_{SMA}) = K_{SMA} X_{SMA} + B_{SMA} \dot{X}_{SMA}^{1/5}. \quad (8.7)$$

The reaction force F_{SMA} changes non-linearly. Equation (8.7) shows that the force can be represented by its linear and non-linear parts. Therefore, the linear part of the force is characterized by a constant stiffness coefficient K_{SMA} , which can be defined as the minimal (martensite) stiffness of the material K_M . The non-linear part of the force is characterized by a damping coefficient B_{SMA} . It is also possible to represent the reaction force of the SMA wire, F_{SMA} , as:

$$F_{SMA} = K_{SMA}^{eq} X_{SMA}, \quad (8.8)$$

where the non-linear behavior of the reaction force can be represented by an equivalent variable stiffness coefficient K_{SMA}^{eq} .

Equating expression (8.7) to (8.8), one obtains the following relation:

$$K_{SMA}^{eq} X_{SMA} = K_M X_{SMA} + B_{SMA} \dot{X}_{SMA}^{1/5}$$

or

$$(K_{SMA}^{eq} - K_M) X_{SMA} = B_{SMA} \dot{X}_{SMA}^{1/5} \quad (8.9)$$

Equation (8.9) can be re-written as:

$$\dot{X}_{SMA}^{1/5} = \frac{(K_{SMA}^{eq} - K_M) X_{SMA}}{B_{SMA}}$$

or

$$\dot{X}_{SMA} = \left(\frac{(K_{SMA}^{eq} - K_M) X_{SMA}}{B_{SMA}} \right)^5 \quad (8.10)$$

The differentiation of Eq. (8.10) yields:

$$\ddot{X}_{SMA} = 5 \left(\frac{(K_{SMA}^{eq} - K_M) X_{SMA}}{B_{SMA}} \right)^4 \left[\dot{X}_{SMA} \frac{(K_{SMA}^{eq} - K_M)}{B_{SMA}} \right] \quad (8.11)$$

Since the equivalent stiffness of the SMA wire K_{SMA}^{eq} changes non-linearly during phase transformation, Eq. 8.8 can also be re-written, using the force balance in Fig. 8.6c, as:

$$F_{SMA} = K_{SMA}^{eq} X_{SMA} = M_{SMA} \ddot{X}_{SMA}$$

or

$$X_{SMA} = M_{SMA} \ddot{X}_{SMA} / K_{SMA}^{eq} \quad (8.12)$$

Substituting X_{SMA} from Eq. (8.12) into equation (8.11) the following expression can be obtained:

$$\ddot{X}_{SMA} = 5 \left[\frac{M_{SMA} \ddot{X}_{SMA} (K_{SMA}^{eq} - K_M)}{K_{SMA}^{eq} B_{SMA}} \right]^4 \left\{ \dot{X}_{SMA} \frac{(K_{SMA}^{eq} - K_M)}{B_{SMA}} \right\} \quad (8.13)$$

Expression (8.13) can be simplified as:

$$1 = \underbrace{5 \left[\frac{M_{SMA} (K_{SMA}^{eq} - K_M)}{K_{SMA}^{eq} B_{SMA}} \right]^4 \left\{ \frac{(K_{SMA}^{eq} - K_M)}{B_{SMA}} \right\}}_A \dot{X}_{SMA} \ddot{X}_{SMA}^3$$

or

$$1 = A\dot{X}_{SMA} \ddot{X}_{SMA}^3 \quad (8.14)$$

Change of variables gives:

$$\dot{X}_{SMA} = Z, \quad \ddot{X}_{SMA} = \dot{Z}. \quad (8.15)$$

so that equation (8.14) becomes:

$$1 = AZ\dot{Z}^3 \quad (8.16)$$

or

$$Z^{1/3} \dot{Z} = (1/A)^{1/3}$$

and

$$Z^{1/3} dZ = dt(1/A)^{1/3} \quad (8.17)$$

Integration by parts of equation (8.17) gives:

$$Z = (4/3)^{3/4} A^{1/4} t^{3/4} + C_1. \quad (8.18)$$

The integration constant was determined to be $C_1 = 0$ based on the initial conditions given by $t = 0$ and $Z = 0$ (no initial motion).

Substituting Z from Eq. (8.15) into equation (8.18) yields:

$$\dot{X}_{SMA} = (4/3)^{3/4} A^{1/4} t^{3/4} \quad (8.19)$$

Integration of equation (8.19) gives:

$$X_{SMA} = \frac{(4/3)^{3/4}}{\underbrace{7/4}_N} A^{1/4} t^{7/4} + C_2$$

or

$$X_{SMA} = NA^{1/4} t^{7/4} + C_2 \quad (8.20)$$

The integration constant in equation (8.20) can be determined at $t = 0$ and $X_{SMA} = X_0$, as $C_2 = X_0$, where X_0 is the initial position (coordinate). Therefore, equation (8.20) reads as:

$$X_{SMA} = NA^{1/4} t^{7/4} + X_0 \quad (8.21)$$

Substituting the coefficients N and A, defined earlier, into equation (8.21), one can rewrite it as follows:

$$X_{SMA} = \frac{(4/3)^{3/4}}{7/4} \left(5 \left[\frac{M_{SMA}}{K_{SMA}^{eq}} \left(\frac{K_{SMA}^{eq} - K_M}{B_{SMA}} \right) \right]^4 \frac{K_{SMA}^{eq} - K_M}{B_{SMA}} \right)^{1/4} t^{7/4} + X_0$$

or

$$X_{SMA} = 1.06025 \frac{M_{SMA}}{K_{SMA}^{eq}} \left(\frac{K_{SMA}^{eq} - K_M}{B_{SMA}} \right)^{5/4} t^{7/4} + X_0. \quad (8.22)$$

The displacement of the SMA wire is defined as $D_{SMA} = X_{SMA} - X_0$ (where: $X_0 = 0$ at the initial position of the SMA wire). Therefore, the damping coefficient B_{SMA} can be found from Eq. (8.22) as follows:

$$B_{SMA} = \frac{K_{SMA}^{eq} - K_M}{\left[\frac{1}{1.06025} D_{SMA} \frac{K_{SMA}^{eq}}{M_{SMA}} \frac{1}{t^{7/4}} \right]^{4/5}}. \quad (8.23)$$

Equation (8.23) can be evaluated by using the maximal SME driven recovery conditions of the SMA wire obtained in two different ways: (a) from experimental step response data, or (b)

from a theoretical estimates based on the properties of the wire. The damping constant, B_{SMA} , can be computed for an actuator with any active element (SMA wire or SMA spring).

(a) Experimentally based evaluation. In case of the experimentally based evaluation – measured displacement, D_{SMA} , versus time, t , from a step response experiment, similar to the tests from Chapter 6 can be used. For example, the maximal measured displacement ($D_{SMA} = D_{max}$) and the corresponding time at which it was measured is substituted into Eq. 8.23. In the case of the maximal recovery, when the SMA wire is completely transformed into austenite, the austenite fraction $\xi_{SMA} = \xi_A = 1$ and the stiffness $K_{SMA}^{eq} = K_A = 15516$ N/m (Table 8.1). Therefore, all the input parameters for the evaluation of Eq. (8.23) are known: K_{SMA}^{eq} , K_M , M_{SMA} , D_{SMA} and t . For example, in case of a step response of the thermally non-insulated SMA wire, initially pre-stretched to its elongation $D_{SMA} = D_{max} = 7$ mm at room temperature and recovered its original (non-prestretched) length upon heating at $t = 17$ sec and temperature $T_{SMA} = 48.4$ °C, the damping ratio $B_{SMA} = 6.38$.

(b) Theoretically based evaluation. In this case, the ideal (theoretical) estimate of the maximal SME driven recovery ($D_{SMA} = D_{max}$) of the SMA wire, when the wire is completely transformed to its austenite state is used. The following are the sample (theoretical) parameters used to estimate the damping coefficient ($B_{SMA} = 0.00217$) given in Table 8.1: input heat flux $\dot{q} = 10$ W, $t = 0.089$ sec, $T_{SMA} = 47.34$ °C (computed at $t = 0.089$ sec, $\dot{q} = 10$ W, $C_p = 920$ J/(kg°C), and $M_{SMA} = 7.52894e-5$ kg from Table 8.1), $K_M = 5762.9$ N/m (Table 8.1), $K_{SMA}^{eq} = K_A = 15516$ N/m (Table 8.1), $D_{SMA} = D_{max} = \varepsilon_L L_{wire} = 0.0153$ m (Table 8.1).

The differences in the estimates between the experimental and theoretical data are mostly due to the differences in the heating times of the SMA wires, 17 sec and 0.089 sec respectively, that take the wire to develop the SME driven motion and transform to its austenite state.

8.4.3 Comparative analysis of experimental and simulation results

The simulation results and the experimental verification of the step response of the mathematical model of motion of the SMA actuator (Fig. 8.7) will be discussed next.

Numerical simulations of the step response of the SMA wire actuator using the suggested motion model (Fig. 8.7) were conducted using the solver in “Simulink/MatLAB” based on the parameters of the model given in Table 8.1. A stepped temperature function was the input load to the model of motion – parameter T_{SMA} in the schematic in Figure 8.7. The calculated displacement function is the output of the model of motion – parameter X_{SMA} in the schematics in Fig. 8.7.

The experimental verification of the model of motion was undertaken as described in Chapter 7. Experimental data from the step response experiments (experimental data set Exp. #21) with the SMA wire based actuator (Chapter 7) were used to validate the suggested model of motion. The comparison of the experimental and numerical simulations of the step response of the SMA wire actuator is shown in Fig. 8.8. Figure 8.8a shows the model input data corresponding to the actual SMA wire temperature, T_{SMA} , measured during one of the step response experiments with the SMA wire (from Chapter 7). For computational purposes, the experimental temperature, T_{SMA} , was averaged to remove the oscillations as shown in Fig. 8.8a.

Afterwards, the averaged T_{SMA} was shifted by $-0.96\text{ }^{\circ}\text{C}$ such that its initial value started at the level of $A_s = 34.5\text{ }^{\circ}\text{C}$ which is a physical property of the SMA wire (Table 7.1). The averaged and scaled T_{SMA} was used as the input to the mathematical model. Figure 8.8b contains two curves: (1) the displacement of the SMA wire, being the output data of the numerical simulations, and (2) the displacement of the SMA wire obtained from the experiment with the SMA wire (taken from Chapter 7).

Each step in the temperature T_{SMA} in Fig. 8.8a corresponds to a step in the displacements of the SMA wire in Fig. 8.8b. There is an excellent agreement between the displacement plots obtained from the numerically simulated SMA wire response and the displacement plot obtained from the experimentally measured SMA wire response (Fig. 8.8b). The beginning of the numerical simulation of motion of the SMA wire (see “output of the numerical model” in Fig. 8.8b) starts from the A_s temperature (see “input to the numerical model in Fig. 8.8a), while the beginning of the experimentally measured motion of the SMA wire (see “experimental data” in Fig. 8.8b) starts from a lower temperature, than the A_s temperature level (see “experimental data” in Fig. 8.8a). The same holds for the end of the motion (simulated and measured) of the SMA wire, characterized by the end of the austenite transformation at the A_f temperature level. This fact is due to the common practice of identifying the TTRs (A_s and A_f) to be at the cross-section points of the tangents at the beginning and at the end of the DSC picks (see, for example, DSC in Fig. 4.2).

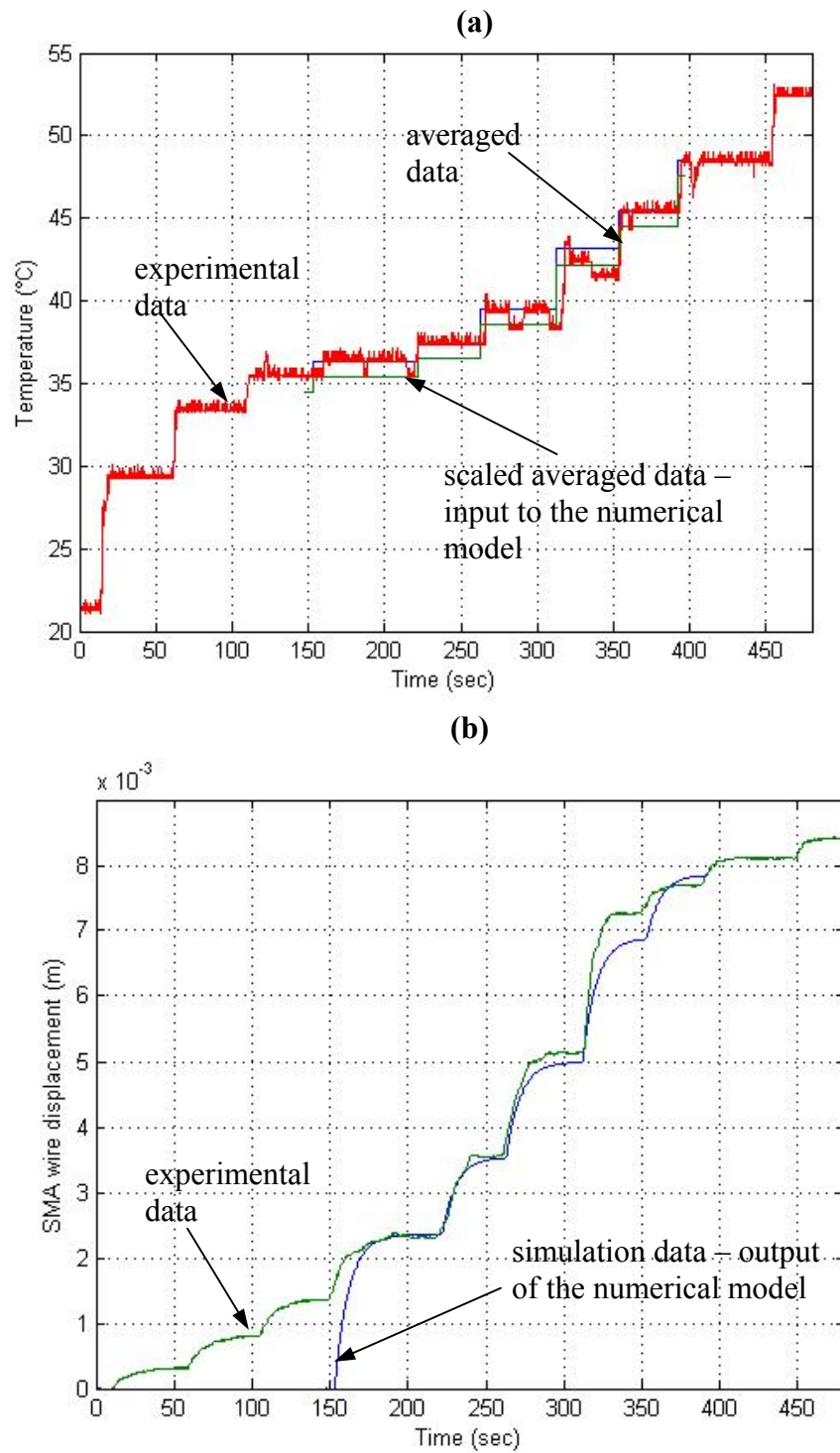


Figure 8.8: Comparison of the experimental data and simulations: (a) temperature T_{SMA} of the SMA wire, (b) displacement of the SMA wire.

While, practically, the beginning of the phase transformation is always at a lower temperature level than the assumed A_s , and, similarly, the end of the phase transformation is always at a higher temperature level than the assumed A_f . This is why, the beginning points of the simulated and measured motion of the SMA wire are different, and the end points are different as well. This deviation can possibly be eliminated by assuming that the transformation follows the non-linear profile of a thermogram. Although in common practice the transformation is assumed to follow the triangular profile defined by the intersection of the tangents to the DSC diagram.

The validity of the suggested model of the SMA actuator can be justified by the fact, that the input parameters to the “Simulink” model were the physical properties of the SMA wire (TTRs, heat capacitance, latent heat of phase transformation of NiTi) and the experimentally measured temperature T_{SMA} of the SMA wire.

Another similar computational example is shown in Fig. 8.9. Experimental data set #23 was used in the verification of the mathematical model in Fig. 8.9. Again, as in the case of Fig. 8.8, the results of the numerical simulations and the experimental tests show a good agreement.

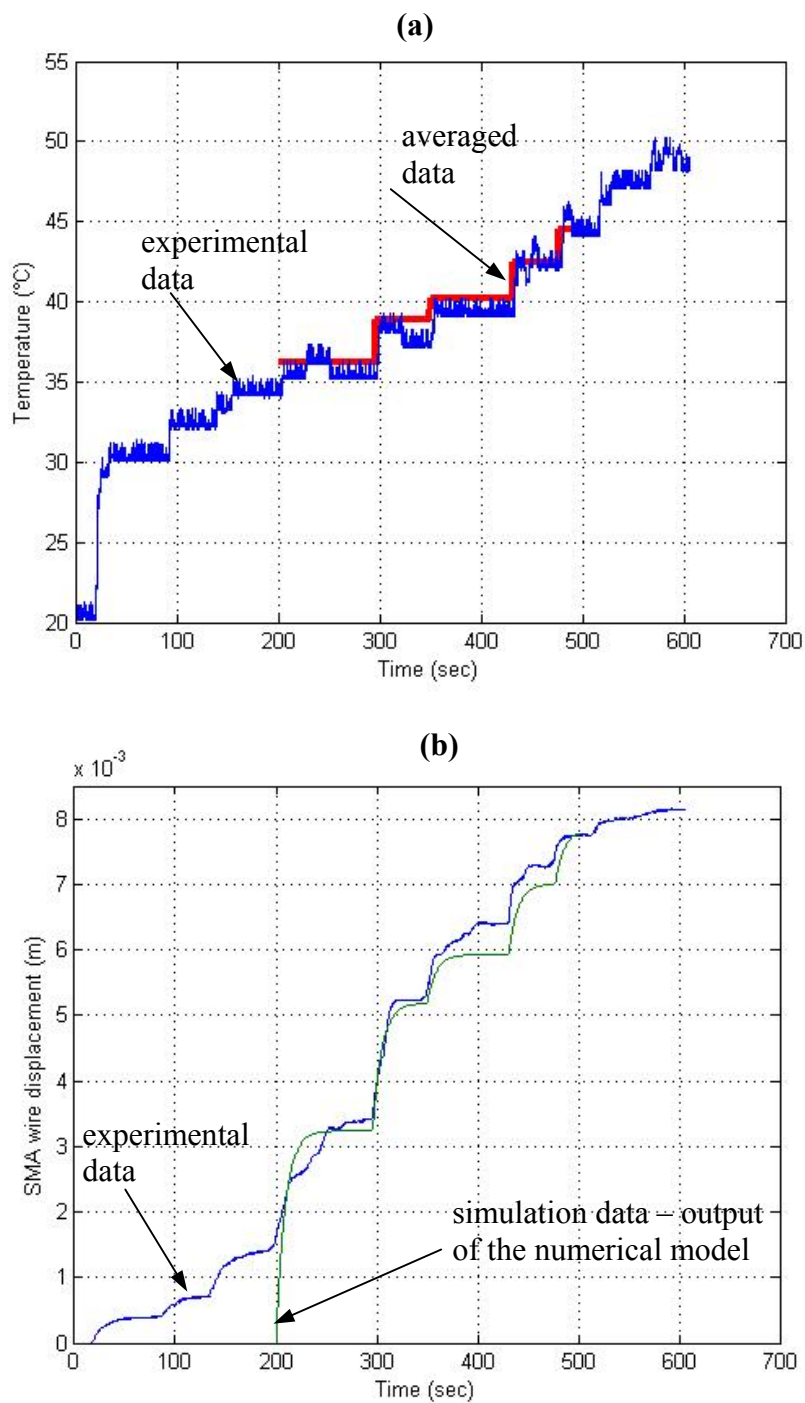


Figure 8.9: Comparison of experimental data and the corresponding simulations: (a) temperature T_{SMA} of the SMA wire, (b) displacement of the SMA wire.

8.5 Concluding remarks

A new, mathematical model of the SMA wire actuator was developed. The model is aimed at simulating the motion of SMA actuators. The model consists of the newly developed model for the kinetics of the phase transformation in SMAs and of the existing “muscle” motion model, describing the motion of a human muscle. The model was experimentally verified and agrees well with experimental data. The model of motion of the SMA wire actuator will be used as the “plant” model in the development for the model of motion control of the actuator.

CHAPTER 9

9. Experimental prototype of a linear stage of the mMM - SMA spring actuator

The overall goals of this Chapter is to design, manufacture and test an experimental prototype of an SMA actuator (a 1-DOF linear stage) that constitutes a part of the mMM using the experimental and computational techniques developed and described in the previous chapters of this dissertation.

First, methods will be sought to improve the material characteristics to be able to better control the linear stage (positioning accuracy, speed of response). The material improvement will be done by modifying the annealing procedure of the SMA actuator, which was previously developed. It is advantageous to anneal only selected parts of the mMM, e.g., only the accordion springs – one or both. This will ensure that the rest of the structure will not be able to undergo phase transformation when heated and, therefore, will not interfere with the motion of the actuator (mechanically or electrically). Therefore, the so-called Selective Laser Annealing (SLA) procedure will be developed.

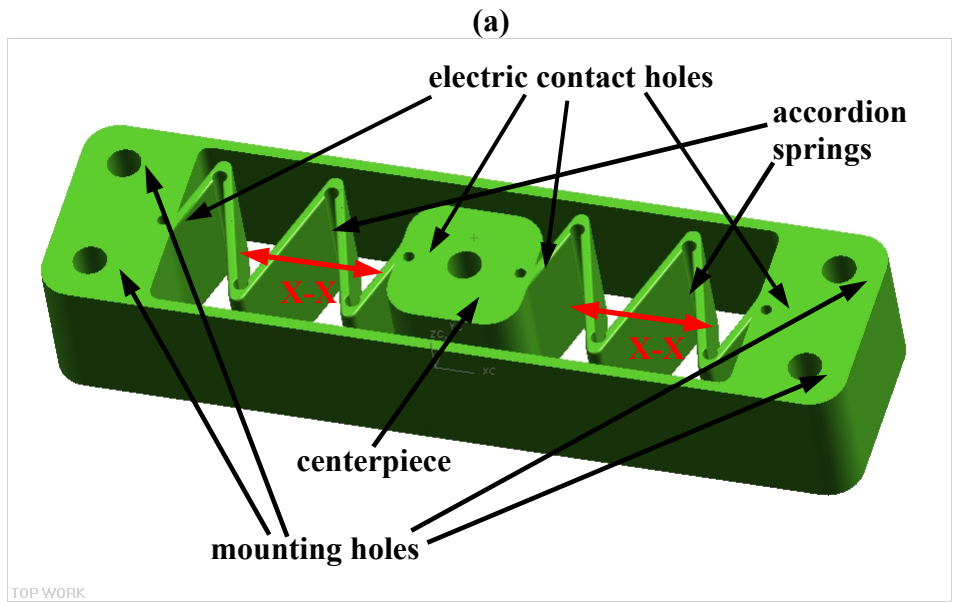
Second, the step response due to the input heat load to the active springs of the SLA treated linear stage will be investigated.

Third, a mathematical model of motion of the SMA spring-based actuator – the mMM linear stage, will be developed based on the previously described model of motion of the SMA wire actuator.

9.1 Design of the linear stage

The 1-DOF mMM prototype represents a part of the 2-DOF linear stage described in Chapter 1 and depicted in Fig. 1.2 a. It is a 1-DOF device that can develop a 5 to 10 mm linear movement, controlled with a precision of several microns. The device is shown in Fig. 9.1. It consists of two accordion springs, connected to each other in series through a centerpiece in the agonistic-antagonistic manner. Both accordion springs can function either as a pair of actuators (active spring – active spring) or as a pair consisting of a bias spring and actuator (passive spring – active spring) providing linear X-X movements of the centerpiece. The contraction/expansion movements of the active springs are made possible by the heat driven shape memory effect (exhibited by an active spring). In this chapter the layout consisting of an active and a bias spring will be used.

In order to accomplish a bi-directional motion, the bias spring will have to be annealed as well and be heated, serving as a second active spring, connected in series with the first one. In this chapter, the one-directional motion will be tested, therefore, only one of the springs will be selectively annealed.



(b)

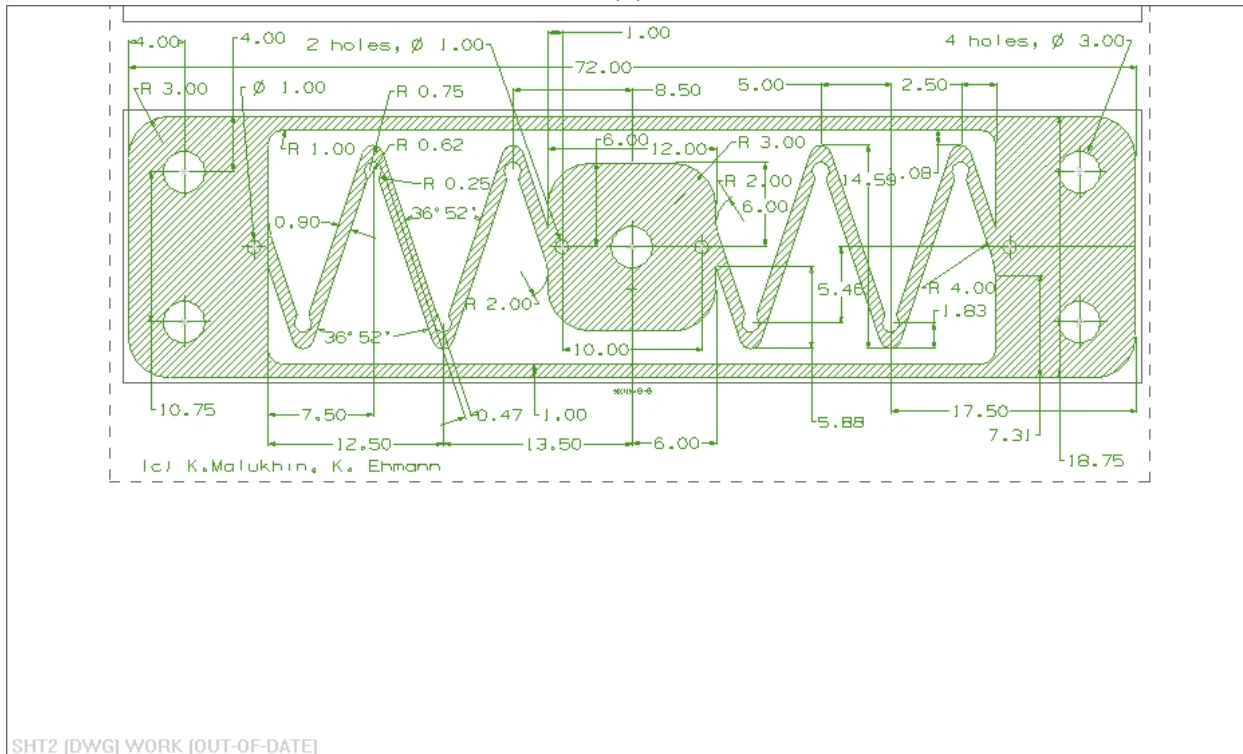


Figure 9.1: UNIGRAPHICS drawing of the mMM linear stage: (a) 3-D view, (b) 2-D view.

The SME “training” of the stage can be done using the heat treatment procedure that was developed and described in Chapter 4. The SME “trained” spring can be actuated such that

when, for instance, heat is applied to the right hand-side spring the spring will contract, while the non-heated left hand-side spring expands acting as a bias spring, and vice-versa. Heat can be applied by resistive heating when the electrical current is applied directly to the spring body, thus heating it. The electrical current is applied according to the procedure developed in Chapter 6 (see Fig. 6.1). The electrical schematic of the simplified 1DOF stage mMM prototype with two accordion springs is shown in Fig. 9.2.

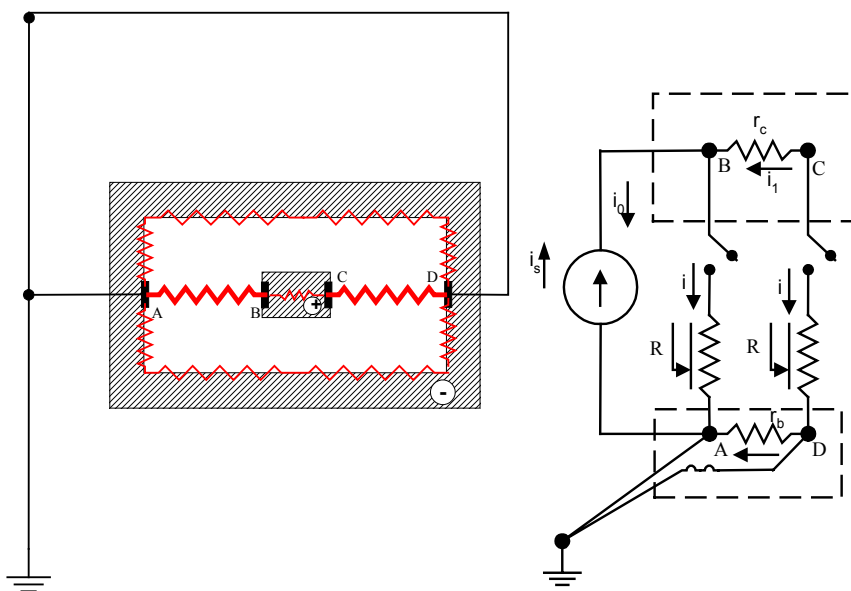


Figure 9.2: 1-DOF mMM linear stage: (a) electrical schematic; (b) electrical circuit diagram.

The NiTi linear stage with two springs was fabricated as a single monolithic part by wire-electrical discharge machining (wire-EDM) from a commercially available NiTi alloy, that was purchased from the NDC company.

9.2 Characterization of the material of the linear stage

Commercially available NiTi material, purchased in a heat-treated condition, already had phase transformation properties imparted in it. The NiTi ingot was purchased in the form of an annealed 0.8” diameter NiTi cylindrical bar. The material characteristics provided by the NDC company for the bar are given in Table 9.1. The properties of the NiTi ingot material differ from the NiTi powder material used in the deposition experiments in Chapter 4 and from the NiTi wire material used for the development of the “self-sensing” concept in Chapter 6 due to the different Ni content and, therefore, possesses different TTRs.

Although the A_f temperature was given by the manufacturer (Table 9.1), additional DSC measurements of the phase transformation temperatures (TTRs) in the supplied NiTi material were conducted. The measured TTRs are shown in Fig. 9.3. As it can be seen from the DSC thermogram the measured TTRs differ from the TTRs (A_f only) provided by the supplier (see Table 9.1). The measured TTRs are: $M_s = 10.01$ °C, $M_f = 27.32$ °C, $A_s = 45.25$ °C, $A_f = 63.6$ °C.

Table 9.1: Material characteristics of the NiTi ingot provided by the NDC company

Material parameter	Value
Ni, wt%	55.4
Ti, wt%	Balance
O, wt%	0.03
H, wt%	0.001
Co, wt%	NM
Fe, wt%	NM
Cu, wt%	NM
C, wt%	0.0038
Cr, wt%	NM
Nb, wt%	NM
A_f of the “as-is” ingot, °C	76...83

Due to the fact, that the phase transformation properties in the “as-is” purchased material were not satisfactory (non-uniform peaks in the DSC thermogram in Fig. 9.3), the material was additionally heat-treated according to the procedure described in Chapter 4 to achieve smooth and uniform peaks and, therefore, a stable SME in the spring actuators (active springs) of the linear stage, that will be heat-treated following a similar procedure.

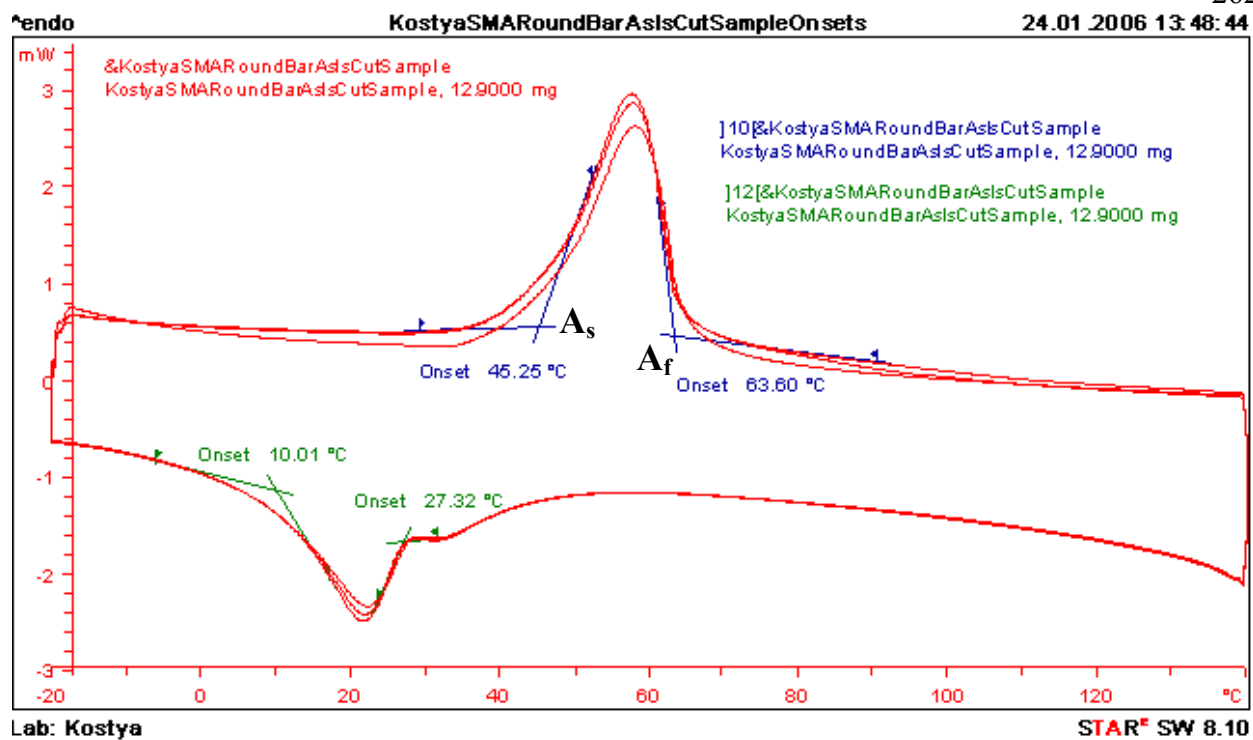


Figure 9.3: DSC measurements of the “as-is” raw NiTi ingot.

A sample of the purchased (raw) NiTi material was additionally heat-treated in an oven with an Ar protective atmosphere according to the procedure given in Chapter 4. The new TTRs were measured by DSC and shown in the corresponding DSC thermogram in Fig. 9.4.

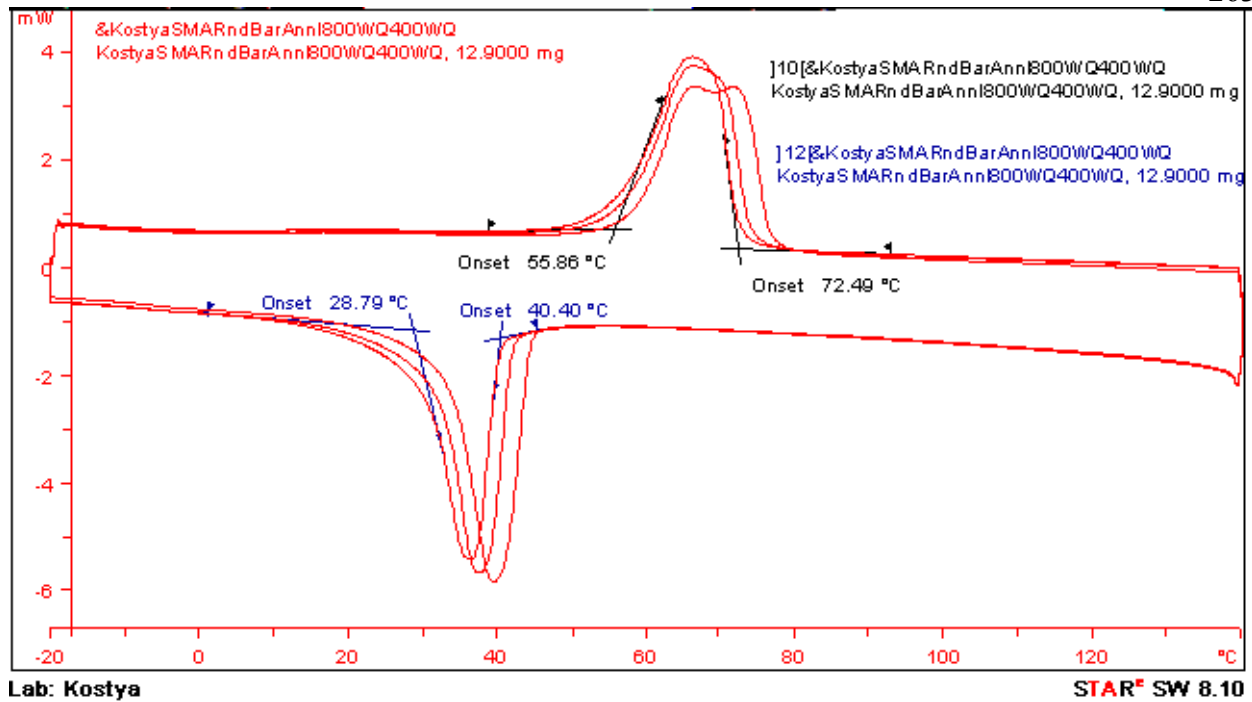


Figure 9.4: DSC of the thermally treated NiTi ingot.

The new TTRs are: $M_s = 28.79$ °C, $M_f = 40.40$ °C, $A_s = 55.86$ °C, $A_f = 72.49$ °C. Comparing Fig. 9.3 and Fig. 9.4, one can notice, that the thermal treatment improved the quality of the raw material. The material got homogenized and possesses more pronounced and uniform TTR peaks, which are advantageous for the purposes of mMM control due to its lower hysteresis. The new TTRs became higher than the TTRs in the non-treated NiTi material (the heat flux peaks were shifted to the right hand-side of the DSC thermogram). The new M_s and M_f temperatures increased up to above the room temperature level, thus simplifying the motion control procedure of the mMM.

9.3 Development of the selective laser annealing (SLA) technique

An oven with Ar atmosphere is not suitable for selective annealing. Therefore, it has been decided to explore the possibility of selective laser annealing (SLA) using a laser beam to heat only a selected area of the linear stage. As in the regular annealing procedure, SLA is followed by quenching of the object (a NiTi sample, or NiTi linear stage) in room temperature water. In the current study, depending on the way the object was held during the SLA procedure, it was either dropped into the vessel with water or water was poured onto it. The objective was to achieve the desired TTRs in the material to be above and as close as possible to room temperature levels. This can be accomplished by annealing the material in two steps as was determined and accomplished in Chapter 4: step 1 – annealing the material at a temperature level of 800 °C for 1 h and quenching it in room temperature water, and step 2 – annealing at a temperature level of 400 °C for 1 h and quenching in room temperature water. The level of annealing temperatures was determined using the annealing curve in Fig. 4.3, Chapter 4.

Two SLA processes to be described below were investigated.

Selective laser annealing #1 (SLA#1). In the first attempt, small samples (approximately 3 mm × 2 mm × 1 mm) of a commercially available NiTi material (purchased from NDC company) and of a DMD fabricated NiTi material (a piece of a NiTi vertical wall, DMD fabricated as described in Chapter 3) were used. The preliminary SLA procedure was developed by using conventional stationary laser equipment (courtesy to Prof. Ketterson, Department of Physics, Northwestern University, Evanston, IL). The SLA#1 procedure took place in open air. The experimental schematic of SLA#1 is shown in Fig. 9.5. A steel foil was used as a holder for the NiTi samples. The holder was placed horizontally with a sample inside it. A low power laser

beam was directed onto the surface of the sample through the opening at the tip of the holder, thus heating the sample to a certain annealing temperature level for the needed period of annealing time.

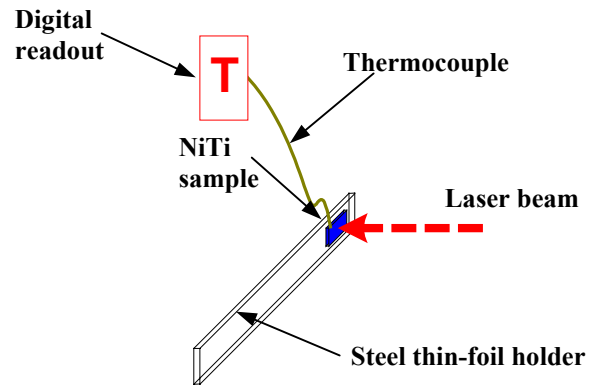


Figure 9.5: *Experimental setup for selective laser annealing #1.*

It was possible to modify the properties of the material (i.e., TTRs) during several experimental trials. The SLA#1 procedure was limited due to the limitation in the maximal laser power of 5 W and the maximal size of the diameter of the laser beam spot (less than 5 mm). It was also difficult to monitor the temperature of the heated sample with a K-type thermocouple connected to a hand-held digital readout that was used. The tip of the thermocouple was placed against the surface of the sample inside the steel holder, opposite to the surface heated by the laser beam (Fig. 9.6). The mechanical contact between the thermocouple and the sample surface was not sufficient to precisely estimate the temperature of the sample during the experiments.

Several experimental trials with different annealing temperature levels were conducted. Each annealing temperature level corresponded to a certain level of TTRs. The DSC thermograms of the heat-treated sample from the DMD fabricated material are shown in Fig. 9.6. The thermograms represent DSC curves of the sample before and after the SLA procedure. Due

to the limitation in the maximal laser power and maximal diameter of the laser beam spot, the achieved annealing temperatures (according to the DMD fabricated annealing curve identified in Fig. 4.3, Chapter 4) were limited as well. Therefore, it was not possible to achieve the desired TTR peaks to occur above room temperature levels as seen from Fig. 9.6. The DSC curves that correspond to trial #1 and trial #2 in Fig. 9.6 were obtained from the sample that was annealed at temperatures that were between 370 °C and 400 °C (according to the readings from the digital readout).

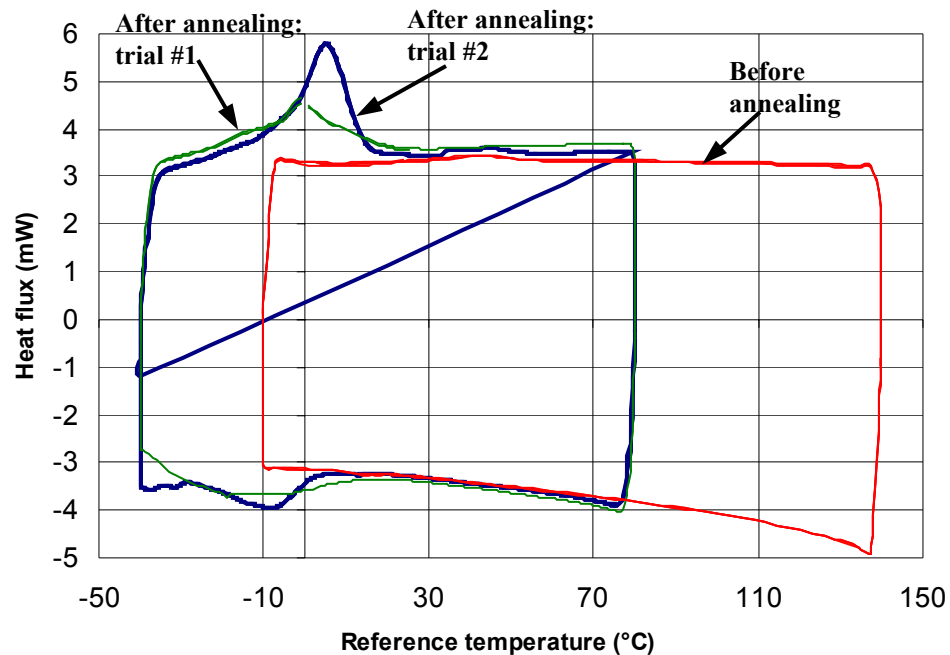


Figure 9.6: DSC thermograms: before and after selective laser annealing (SLA #1) of DMD fabricated material.

For comparison, the same NiTi sample was annealed in a vertical oven at different temperature levels. The oven had an Ar protective atmosphere and was equipped with a temperature control system (heater, cooler, thermocouple and a temperature controller). Each annealing step, using the oven, was followed by quenching the sample in room temperature

water. The DSC thermogram of a selectively laser annealed sample and the DSC thermograms of the oven annealed sample are shown in Fig. 9.7.

Figures 9.6 and 9.7 show that the TTRs in the SLA#1 treated material are lower than the TTRs in the oven treated material. For example, in the sample of DMD fabricated NiTi material treated by SLA#1 (trial #2, Fig. 9.6), the TTRs are $M_s = 3.98\text{ }^\circ\text{C}$, $M_f = -28.02\text{ }^\circ\text{C}$, $A_s = -4.23\text{ }^\circ\text{C}$, $A_f = 13.82\text{ }^\circ\text{C}$. While in the same sample heat treated inside the oven (trial #10, Fig. 9.7: annealing temperature = $307\text{ }^\circ\text{C}$, annealing time = 1h), the measured TTRs are $M_s = 21.76\text{ }^\circ\text{C}$, $M_f = 45.79\text{ }^\circ\text{C}$, $A_s = 27.77\text{ }^\circ\text{C}$, $A_f = 46.21\text{ }^\circ\text{C}$.

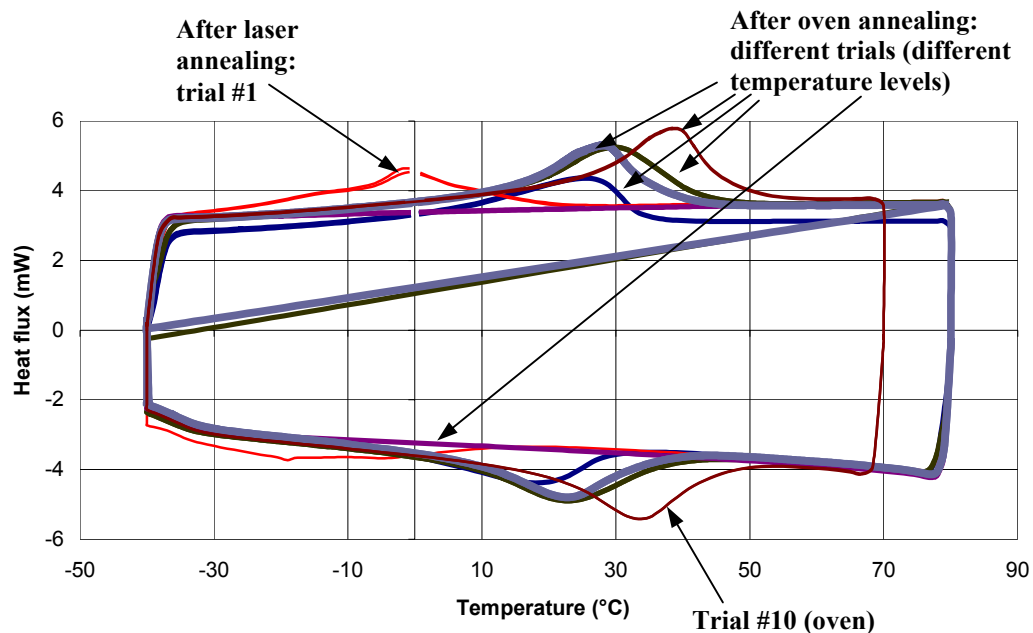


Figure 9.7: DSC thermograms: comparison of a laser annealed and oven annealed NiTi samples (DMD fabricated material).

Selective laser annealing #2 (SLA#2). In order to achieve the necessary temperature levels and be able to anneal larger objects, such as the accordion spring, a more powerful fiber-optics laser was used (courtesy of Prof. Pfefferkorn, Department of Mechanical Engineering,

University of Wisconsin-Madison). This laser equipment had a minimal power of 33 W. The effective diameter of the spot of the laser beam varied between 14 to 34 mm, such that the maximal possible area of the spring could be affected by the heat treatment and different annealing temperature levels could be achieved. The experimental layout of the SLA#2 setup is shown in Fig. 9.8a.

SLA#2 was done on two NiTi samples and the NiTi linear stage (Fig. 9.8). The samples were prepared from both the commercially available material and the DMD fabricated material (see Chapter 3). SLA#2 of the NiTi samples was conducted as follows: the sample was placed on the horizontally located substrate that served as a thermal insulator as shown in Fig. 9.8a. The laser fiber-optics cable was set such that the laser-beam was directed vertically onto the surface of the NiTi sample, thus heating it in open air. A K-type thermocouple with a digital readout was mechanically attached to the sample in order to measure its temperature during the annealing process.

SLA#2 of one of the spring actuators of the NiTi linear stage was done in a similar way. The portion of the linear stage with one of the accordion spring actuators was subject to the heat load from the laser beam. This actuator will be called “active” since it will be used to produce the SME driven motion. It was placed onto the thermally insulating substrate. The other portion of the stage with the second accordion spring was placed on a Cu-plate, covered with heat conductive paste. This spring will serve as a “bias” and it won’t be used to produce the SME driven motion. The Cu-plate served as a heat sink (Fig. 9.8b) to prevent that portion of the linear stage from excessive heating.

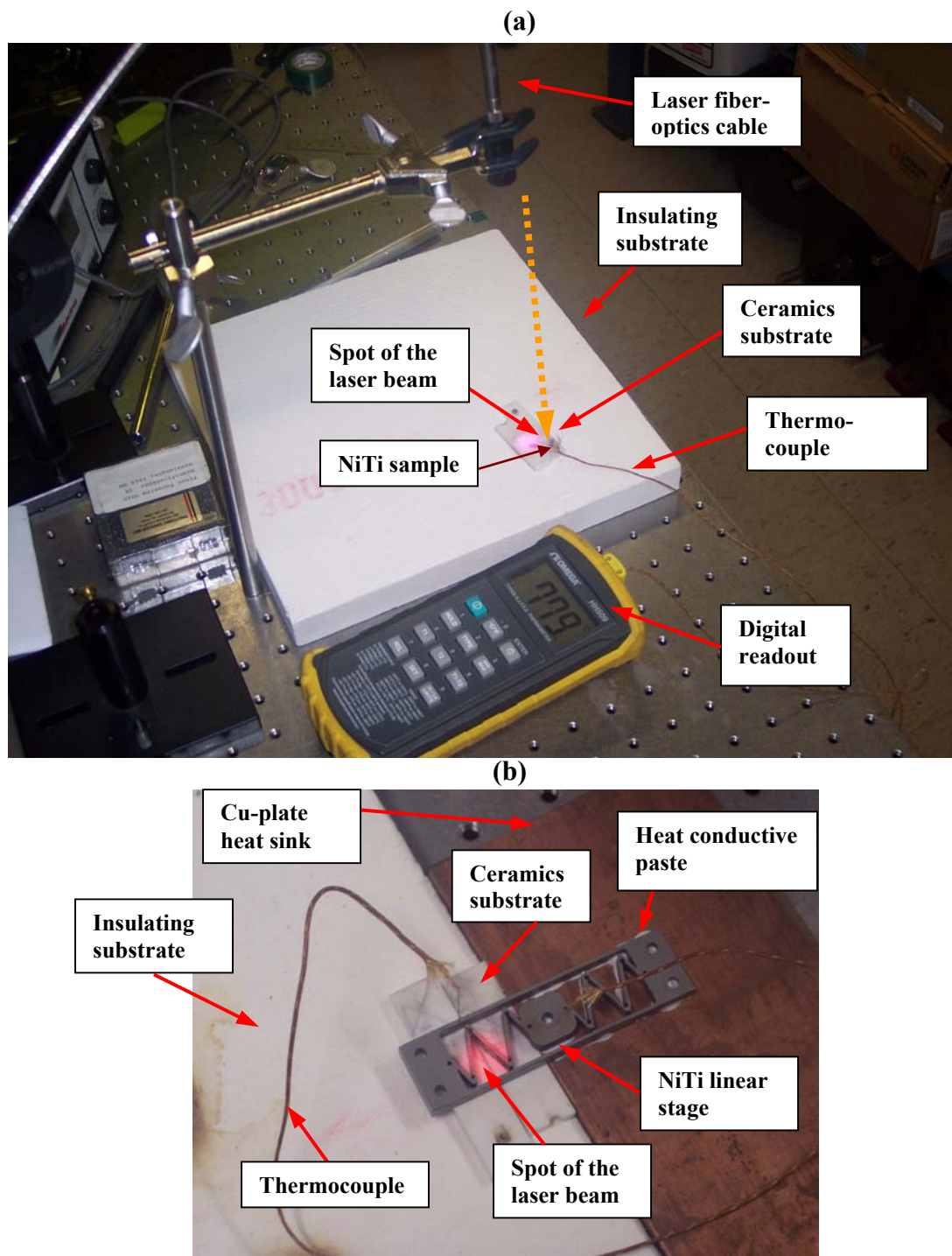


Figure 9.8: *Experimental layout of the method for selective laser annealing #2: (a) with NiTi sample, (b) with NiTi linear stage.*

The selective laser annealing process was conducted in open air on both samples and on the stage according to the procedure identified in Chapter 4. The laser power and the diameter of the laser beam spot were chosen such, that the targeted annealing temperatures of the thermally treated objects were around 800 °C and 400 °C to obtain the desired TTRs above and as close as possible to room temperature (see annealing curve in Chapter 4). Temperature measurements, conducted during the annealing procedure show that both samples were kept at temperatures 785 °C to 840 °C for 1 h (annealing step #1) and at \cong 450 °C for 1 h (annealing step #2). The samples were quenched in room temperature water at the end of each heat treatment. The rest of the linear stage was kept at a lower temperature level (between 25 °C to 41 °C) during annealing. This was possible due to the presence of the heat sink and due to the fact, that the NiTi alloy has a relatively low heat conductance and high heat capacitance in comparison, for example, to tool steel. The corresponding DSC thermograms from two NiTi samples are shown in Fig. 9.9.

Each DSC thermogram contains three heating/cooling curves (cycles). Generally, the DSC curves from all of the cycles, performed under the same conditions, coincide. Figure 9.9b shows a discrepancy of the DSC cycles in the measurements conducted on the commercially available material. This might be the result of mis-calibrated DSC equipment or of the presence of residual stresses in the material. As shown in the DSC thermograms, the TTRs in the DMD fabricated material are $M_s = 41.25$ °C, $M_f = -6.14$ °C, $A_s = -3.67$ °C, $A_f = 40.34$ °C (Fig. 9.9a), while the TTRs in the commercially available material are $M_s = 45.29$ °C, $M_f = 26.37$ °C, $A_s = 60.91$ °C, $A_f = 84.81$ °C (Fig. 9.9b).

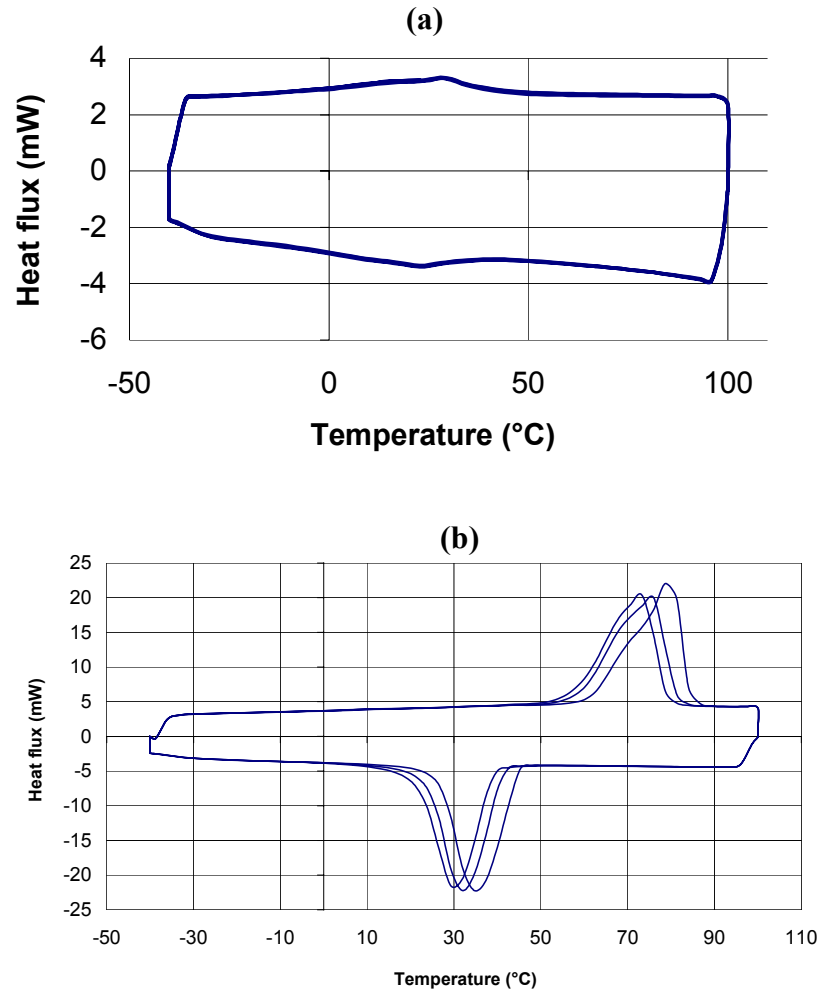


Figure 9.9: DSC thermograms of the NiTi samples after SLA #2: (a) DMD fabricated material, (b) commercially available material.

In conclusion it can be said that the developed selective laser annealing method (SLA#2) is capable of achieving the needed distribution of annealing temperatures during the annealing procedure in a complex NiTi part such as the linear stage. The method has allowed the achievement and maintenance, for a period of time (1 hour in each selective laser annealing step), of high annealing temperature levels (up to 800 °C) in a selected portion of the linear stage (the active spring actuator). This portion of the stage will exhibit the shape memory effect property. The rest of the stage (the bias spring, the center-piece and a portion of the frame) was

kept at a relatively low temperature level between 25 °C and 41 °C, which implies that the heat treatment did not affect this part of the stage.

9.4 Experimental investigation of the response of the 1DOF stage

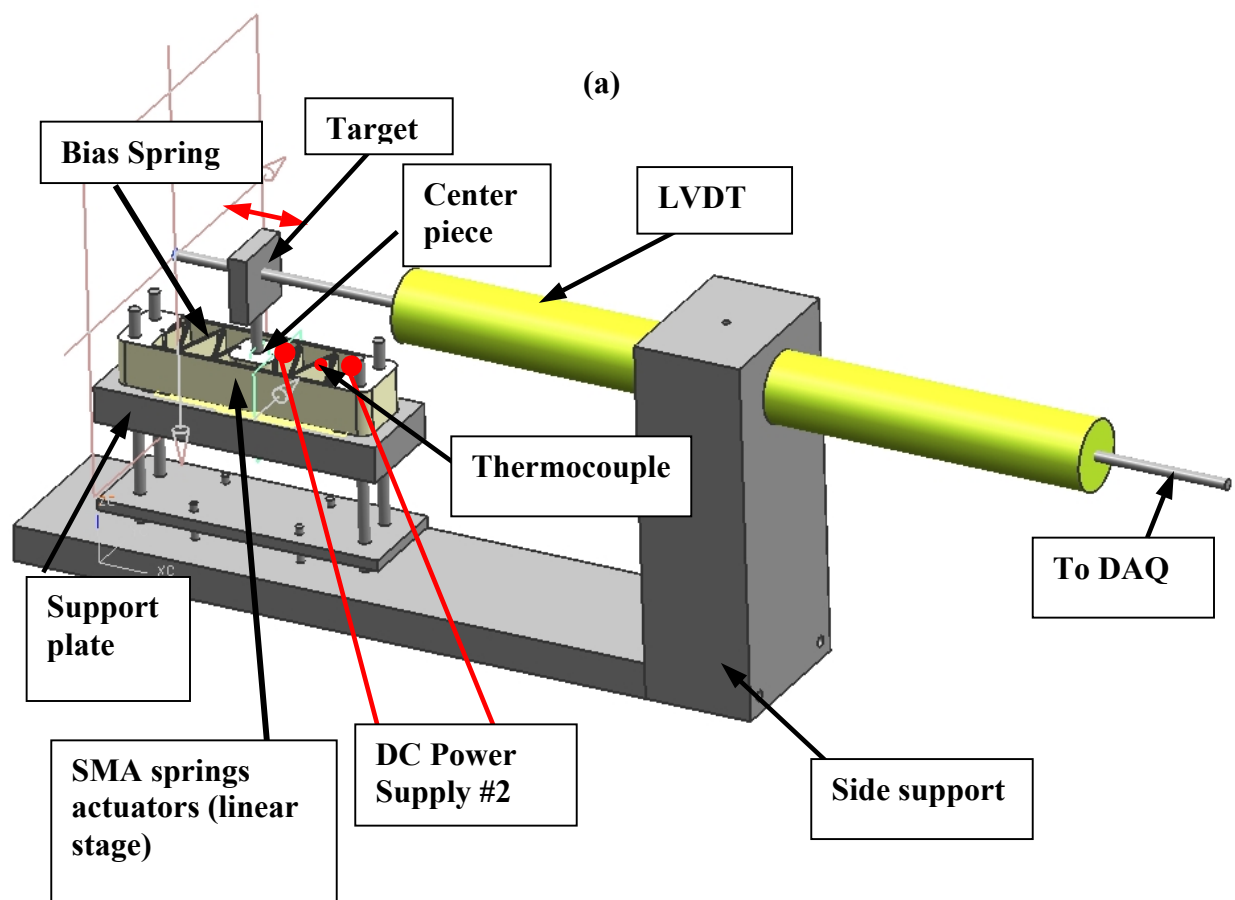
The goal of this section is to identify the dynamics of motion of the spring actuators of the linear stage by means of step response experiments, similar to those conducted with the SMA wire and described in Chapter 6. The stage used in the study had one of its springs selectively annealed as described above. The selectively annealed (active) spring will be pre-deformed (compressed) and heat (electric current) will be applied to it. The spring will produce OWSME driven motion (or one-directional motion) and recover its initial (non-deformed) shape, while the bias spring will be acting as a payload to the active spring.

9.4.1. Experimental setup

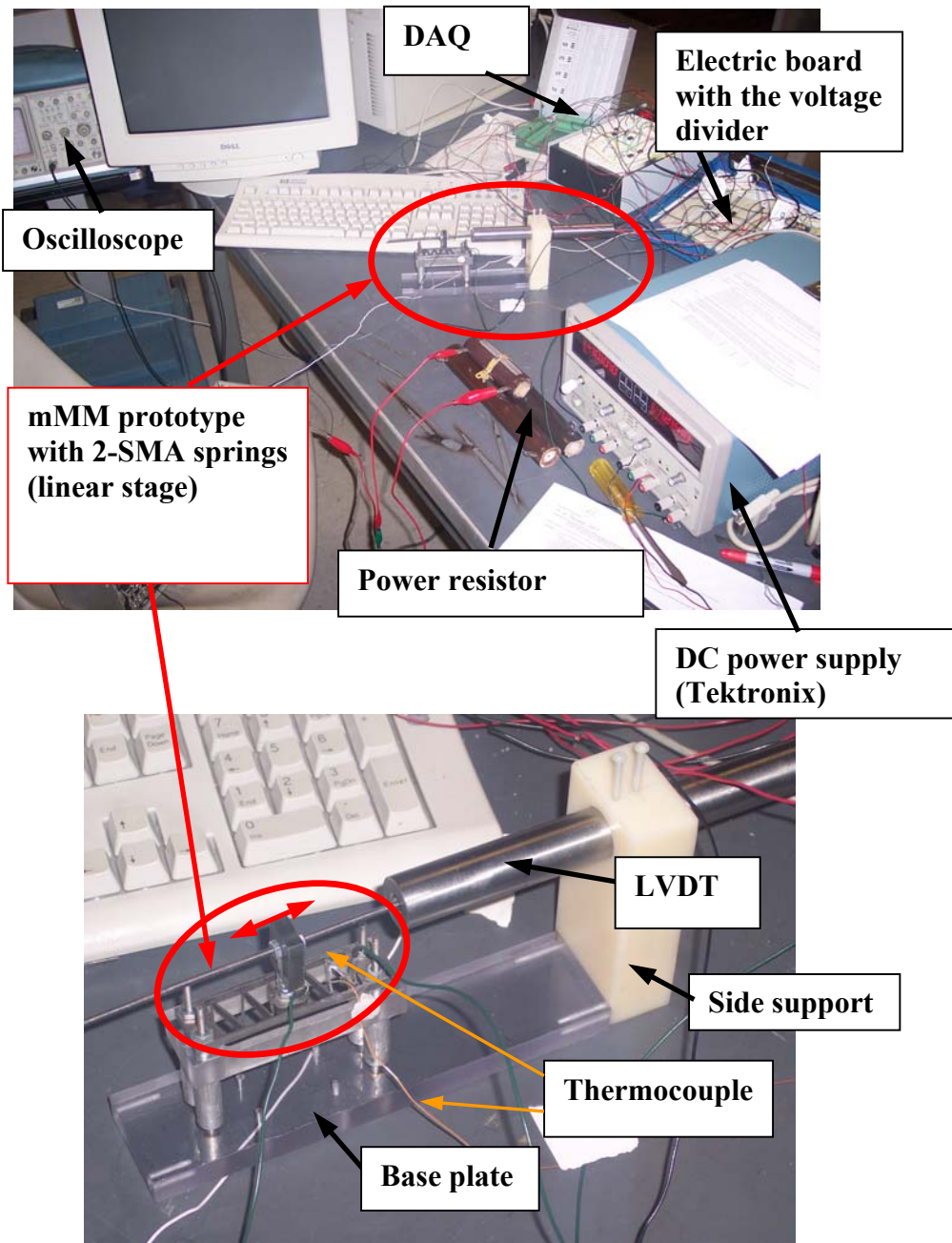
The experimental setup has been designed (see Fig. 9.10a) and built (see Fig. 9.10b) to measure the step response of the SMA accordion spring actuators of the linear stage. It does not use any kind of bearings (linear or air-bearings that were used previously with the SMA wires) as seen from the experimental setup in Fig. 9.10b.

The experimental setup includes the 1-DOF linear stage mounted on a support plate and the measurement system. The measurement system consists of an LVDT “Schaevitz”, a thermocouple with an adaptor, electric board with the voltage divider circuit (see Fig. 9.10c), a

new, different from the previously used, DC source (model 1745A, “BK Precision”, not shown in Fig. 9.10), a power supply (model Tektronix PS-280) and data acquisition system. The data acquisition system consists of a 12-bit DAQ (“National Instruments”, 6025E) controlled by a LabVIEW program, written to acquire and record the experimental data from the sensors. In these series of experiments the measured voltage drop across the SMA spring was not pre-filtered and not amplified as in the previously described experiments with the SMA wire.



(b)



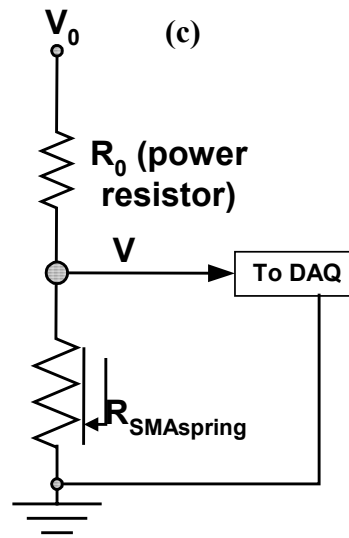


Figure 9.10: Linear stage: (a) UNIGRAPHICS NX3 drawing of the assembly of the 1-DOF linear stage, (b) digital camera photo of the experimental setup with the measurement system, (c) voltage divider circuit

9.4.2 Experimental procedure

A series of experiments was conducted with the linear stage, with one of the two spring actuators selectively laser annealed in open air. The step response behavior of the spring actuator subject to a heat load was investigated. The heat load was applied to the right-hand side accordion spring (Fig. 9.10b) by direct resistive heating. The DC source, that supplied the electric current to the spring, was connected to it as shown in Fig. 9.10 a. The maximal supplied electrical current was 10 A, the maximal applied voltage was 30 Volts.

The scenario of the step response experiments was similar to the one, described in Chapter 6 (Section 6.2.2). The active spring actuator was manually compressed and left in the deformed state. The compressed length was between 1 to 2 mm in different experiments.

Afterwards, the heat load \dot{Q} (in these series of the experiments – the maximal electrical current, 10A, and voltage, 0...30 Volts) was applied to the spring. Upon heating, the spring recovered its original un-compressed shape due to the shape memory effect. The linear recovery motion of the spring was recorded by the LVDT attached to the spring (Fig. 9.10 b) through the center-piece of the linear stage. The temperature of the spring was recorded by the K-type thermocouple glued to its surface. The voltage drops across the active spring were measured (based on the voltage divider circuit) and recorded as well. The data acquisition system was used to record the measured temperatures and the one-directional motion displacements of the SMA spring. During the step response experiments, the spring was given different levels of compression (pre-strain) that were recovered under different applied heat loads (the maximal electrical current and different voltage levels).

9.4.3 Experimental results

An example of a large displacement (more than 1 mm) step response of the heat-treated spring is shown in Fig. 9.11. The experiment was conducted according to the scenario described in the previous section. The temperature of the spring, the voltage drop across the spring, and the recovery displacement were measured and recorded. Another example of a small displacement (less than 1 mm) step response of the spring, that developed a small displacement, range is shown in Fig. 9.12.

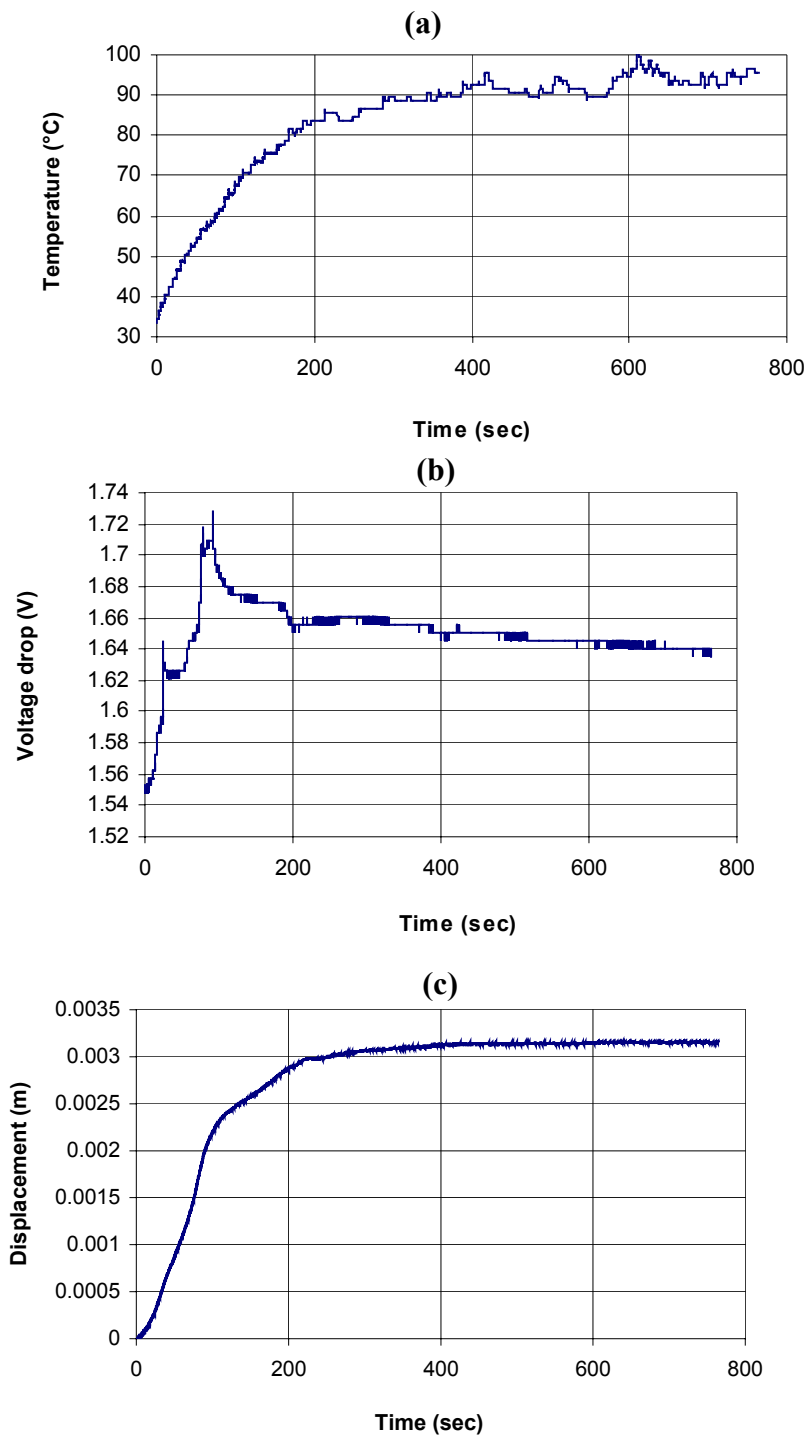


Figure 9.11: Step response of the linear stage with the heat-treated spring (large pre-strain $\approx 3\text{mm}$, electrical current $\approx 10\text{ A}$, voltage $\approx 30\text{V}$): (a) temperature input, (c) voltage drop across the spring, (c) displacement output.

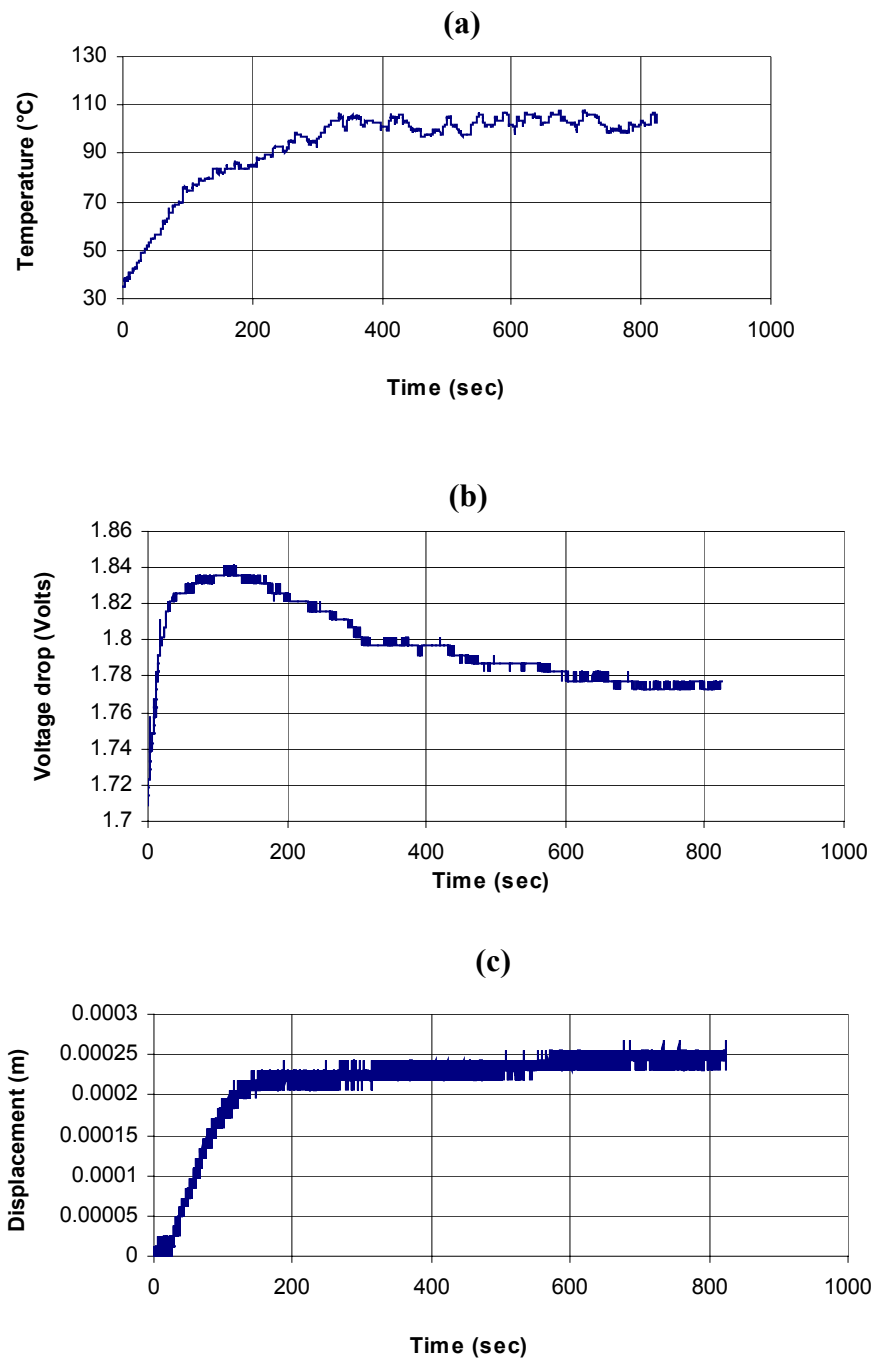


Figure 9.12: *Step response of the linear stage with the heat-treated spring (small pre-strain ≈ 0.25 mm, electrical current ≈ 10 A, voltage ≈ 30 V): (a) temperature input, (c) voltage drop across the spring, (c) displacement output.*

The experimental results show, that the step response of the SMA spring is similar to the step response of the SMA wire, described in the Chapter 6. But due to the fact that, the heat balance of the SMA wire stabilized faster then the one for the spring because of the wire's smaller mass and surface area the following additional analysis, that pertains only to the step response experiments with the spring, has been undertaken.

9.4.4 Analysis of the experiments

It is desirable, to correlate the heat load, consumed by the active spring in each experiment, with the corresponding displacement of the spring to be used in the verification of the mathematical model of motion of the spring. This was not done in the experiments with the SMA wire, because the wire had a smaller surface area and smaller mass, therefore, the heat balance was achieved faster and the measured temperature of the SMA wire was a satisfactory indicator of its performance used for the verification of the mathematical model of motion.

The actual applied heat load can be computed based on the measured temperature of the spring according to the heat balance equation written for a solid body (SMA spring in this case) as follows:

$$\dot{Q}_{\Delta T} = C_{NiTi} \cdot M_{spr} \cdot \frac{(T_{end} - T_{beg})}{\Delta t} \quad (9.1)$$

where:

C_{NiTi} – heat capacitance of NiTi, $C_{NiTi} = 920$ J/kg (Brinson et al., 1996);

M_{spr} – mass of the active spring, kg;

T_{beg} – temperature at the beginning of the application of the heat load step, °C;

T_{end} – temperature at the end of the application of the heat load step, °C;

Δt – time interval of a heat load step, sec.

It was assumed, that the spring reaches its thermal equilibrium instantaneously upon the application of the heat load. The heat load ($Q_{\Delta T}$) applied to the SMA spring can be calculated based on Eq. 9.1 using the experimentally measured temperature, T_{SMA} , of the SMA spring.

For a comparison to Eq. 9.1, the heat load can also be calculated based on the known applied electrical current, I , and voltage, U , according to the following formula, ($Q_{\Delta V}$):

$$\dot{Q}_{\Delta V} = I \cdot \Delta U = I \cdot (U_{beg} - U_{end}). \quad (9.2)$$

where:

I – electric current, applied in each heat load step, A;

ΔU – measured voltage drop across the active spring actuator, V.

U_{beg} – voltage at the beginning of the time interval during which measurements were acquired, V.

U_{end} – voltage at the end of the time interval during which measurements were acquired, V.

Twelve experimental points with different amounts of pre-strain of the SLA treated spring were processed using equations (9.1) and (9.2) and the cumulative data are shown in Fig.

9.13. Each point contains the measured step response data with the corresponding temperatures and voltage drops at the end of each step response. The temperatures are the inputs to equation (9.1) and the voltage drops are the inputs to equation (9.2). Figure 9.13 shows the dependence of the heat loads computed based on Eqs. 9.1 and 9.2 – $Q_{\Delta T}$ and $Q_{\Delta V}$ respectively, on the displacement of the SLA treated spring. Each point corresponds to a displacement step response of the spring to a heat load. For example, point A, shown in Fig. 9.13 and Fig. 9.14, was computed from equation 9.2 using the experimental results depicted in Fig. 9.11: the applied electrical current was $\approx 10A$, the voltage U_{beg} was taken at 90 sec (beginning of the time interval, when the austenite transformation starts) and the voltage U_{end} was taken at 300 sec (end of the interval, where the austenite transformation ends and the displacement is considered to be not changing). There are two distinguishing regions in Fig. 9.13. Region #1 corresponds to small displacements, up to 0.25 mm. Region #2 corresponds to the relatively large displacements, between 1 mm and 1.8 mm.

The small displacements in Region #1 in Fig. 9.13 were measured after no initial manual pre-strain. The recovery displacement in this case was possible due to the fact that the springs were permanently off-centered possibly due to the partial plastic deformation that appeared in the material of the springs after several cycles of pre-strain and subsequent recovery. The large displacements in Region #2 were measured after an initial pre-strain of the active spring was manually imposed. The absence of the intermediate points between Region #1 and Region #2 was due to the fact that a manual pre-strain of less than 1 mm was difficult to achieve as seen from Fig. 9.13, and, therefore, no experiments were done in that region. The dependence of the heat load versus the recovered displacement in Fig. 9.13 is non-linear. It is seen, that the heat

flux $Q_{\Delta V}$ has a higher value, than the heat flux $Q_{\Delta T}$, which can serve as a conservative estimate of the applied heat – upper and lower limits correspondingly.

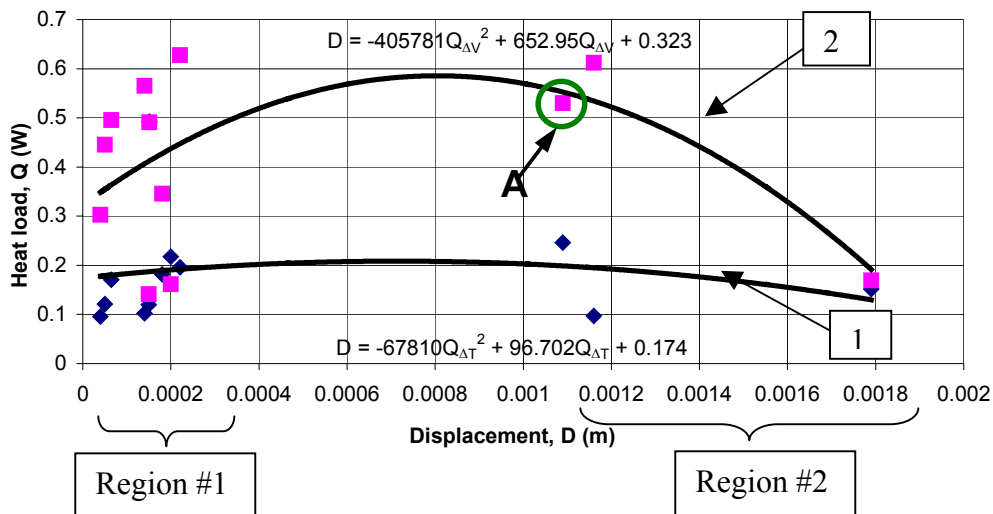


Figure 9.13: Cumulative data of the heat loads versus corresponding displacement of the SLA heat-treated spring (curve 1 from Eq. 9.1 and curve 2 from Eq. 9.2)

An auxiliary plot that shows how the values of the heat fluxes, computed based on both heat loads (Fig. 9.13), are related to each other is shown in Fig. 9.14.

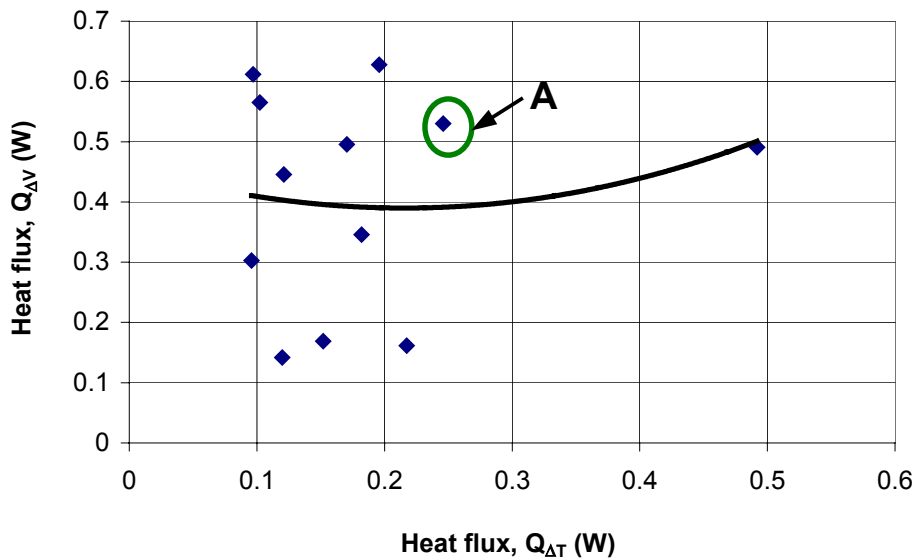


Figure 9.14: Dependence between the heat load values $Q_{\Delta V}$ and $Q_{\Delta T}$.

Ideally, the plot in Fig. 9.14 should have shown a straight-line behavior, which would correspond to coinciding values of $Q_{\Delta V}$ and $Q_{\Delta T}$. The possible reason for such a discrepancy in the values of the heat fluxes is due to the thermal inertia of the spring. The existence of the thermal inertia results in temperature levels that correspond to the lower heat fluxes, while the voltage drop levels, recorded in the same time interval as the temperatures were, correspond to the higher heat fluxes. In other words the formula for $Q_{\Delta V}$ overestimates the heat flux values, while the formula for underestimate the heat flux values.

9.5 Mathematical model of the 1DOF stage

The model of motion of the SMA spring actuator (Model #1 here) will be based on our phase transformation kinetics model and the “muscle” motion model as previously described for the case of modeling of the SMA wire-based actuator in Chapter 8.

9.5.1 Formulation of the mathematical model of motion

The mathematical model of the motion of the SMA spring-based actuator of the linear stage (Fig. 9.1) is based on the derived general mathematical model of motion of the SMA wire-based actuator (Eqs. 8.6), described in Section 8.2. The general model of motion of the “agonist-

antagonist” SMA accordion spring actuator is built in a similar way to the model of motion of the SMA wire actuator shown in Fig. 8.6.

The conceptual difference between the two models of motion is the substitution of the SMA spring element instead of the SMA wire element (see original model in Fig. 8.6). The model with the SMA spring actuator also has a different bias spring and a payload system, resulting only in different stiffness and damping coefficients of the elements of the model. Therefore, the system of equations of motion of the SMA spring actuator is equivalent to the system of equations of motion of the SMA wire actuator (see Eqs. 8.2) and will not be repeated in this section.

The stiffness coefficients corresponding to the accordion springs can be estimated using the FEM analysis package available in the UNIGRAPHICS/Structures software by modeling the force-controlled response of the springs. In the current study, the response was estimated for the springs in their austenite state. In the force-controlled experiments, an external force was applied to a spring in the X-X direction, and the corresponding displacement was computed. Therefore, the corresponding force-displacement curves can be generated, and the stiffnesses of the springs can be computed.

The damping coefficient of the model (B_{SMA}) can be estimated based on the procedure given in Section 8.4 (see Eq. 8.13). The solution can be applied to predict the damping coefficient (B_{SMA}) of the SMA spring actuator. The only differences in the determination of the damping coefficient for the SMA wire actuator and for the SMA spring actuator are the different values of the input parameters in Eq. 8.13: namely, different geometry and the mass of the active element (spring, in this case) and experimentally measured displacements in the corresponding

step response experiments. The simplified block diagram that represents the model of motion of the SMA spring actuator is similar to the one for the wire actuator and is shown in Fig. 8.7a.

For the spring, it is, however, necessary to evaluate the effect of the thermal inertia on the motion of the spring, because of its larger mass and complicated geometry in comparison to the wire. For this purpose, it is more convenient to have the desired (reference) displacements, D_r , of the accordion spring actuator to be the input to the mathematical model of motion in order to compare the reference displacement to the computed displacements of the actuator. Therefore, the temperature (T_{SMA}), in the model, has to be correlated to a corresponding input (reference) displacement. This can be done by establishing a correlation between the applied heat flux to the SMA spring actuator and the temperature T_{SMA} . The heat flux can be computed based on the known electrical current applied to the SMA actuator and the corresponding voltage drop, U , across the spring actuator.

The heat balance equation, written for a solid body (spring actuator), can be represented as follows (Grigoriev et al., 1999; Incropera and Dewitt, 2002; Kaviany, 2002):

$$\frac{\Delta T_{SMA}}{\Delta t} = \frac{\sum \dot{Q}}{C_p M_{SMA}} = \frac{\dot{Q}_{input} - \dot{Q}_{output}}{C_p M_{SMA}} = \frac{IU - \alpha F \Delta T_{SMA}}{C_p M_{SMA}}$$

or it can be re-written in terms of temperatures T_{SMA} as:

$$T_{SMA} = T_{room} + \frac{IU}{(C_p M_{SMA} / \Delta t + \alpha F)} \quad (9.3)$$

where: $\Delta T_{SMA} = T_{SMA} - T_{room}$;

T_{SMA} - temperature of the SMA spring, °C;

T_{room} - room temperature, °C;

I - electrical current, A;

U - voltage drop across the spring, V;
 α - convective heat transfer coefficient, $W/(m^2 \text{ } ^\circ\text{K})$;
 Δt - time interval, s;
 F - surface area of the spring actuator, m^2 ;
 C_p - heat capacitance of the SMA material, $J/(kg \text{ } ^\circ\text{K})$;
 T_{room} - room temperature, $^\circ\text{C}$.
 M_{SMA} - mass of the spring actuator, kg.

The last equation represents the heat balance in a solid body described by lumped parameters. It states, that the change in the heat flux at the solid body boundaries is proportional to the change of the temperature of the solid body.

The voltage drop, ΔU , across the spring actuator can be computed based on the experimental correlation between the voltage drop and the desired input displacement, D_r . The correlation can be obtained from experimental data from step response tests of the SMA spring actuator (similar to the one, described in the previous section), where the voltage drop and the displacement of the spring were measured and recorded in each step response test. The voltage drop (U) across the spring actuator versus time and the displacement ($D = D_r$) of the spring actuator versus time from the step response experiment shown in Fig. 9.12 in the interval from 10 sec to 130 sec were re-plotted as voltage versus displacement and shown in Fig. 9.15. The corresponding regression between the voltage and displacement is given in Fig. 9.15 as well. The spread of the experimental points in the beginning of the curve in Fig. 9.15 occurs due to the sampling noise during the measurement of small LVDT voltage output signal (see the Fig. 9.12c).

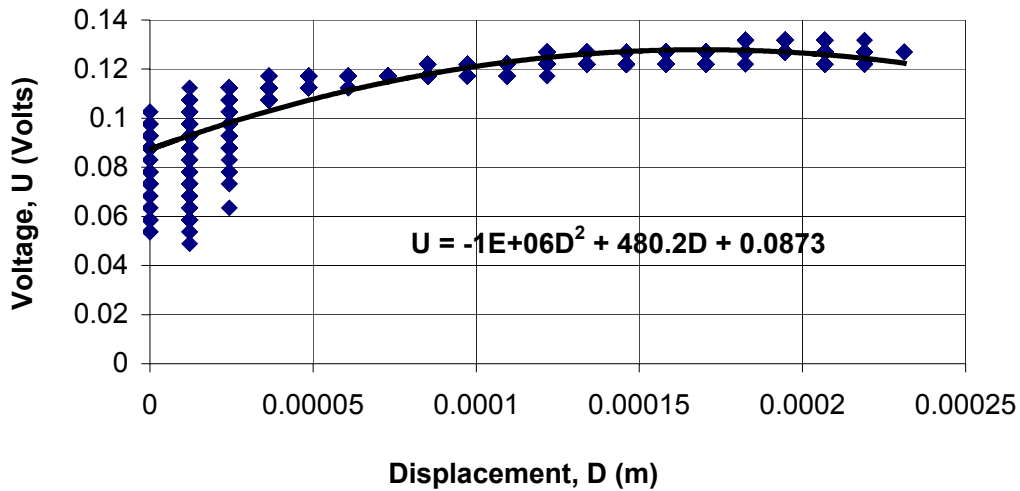


Figure 9.15: Voltage drop across the spring vs. the displacement of the spring

It is seen from Fig. 9.15, that the dependence between the experimentally measured voltage drop, U , across the spring and the spring displacement, D , of the spring can be represented by a non-linear regression (a second order polynomial) fitted to the experimental data points. The regression between the measured spring displacement, D , of the SMA spring actuator and the voltage drop, ΔU , across the spring is written as follows:

$$U = K_1 D^2 + K_2 D + K_3 \quad (9.4)$$

where: K_1 , K_2 , K_3 – coefficients of the polynomial (see Fig. 9.15).

An example of the coefficients K_1 , K_2 , and K_3 of the polynomial is shown in the regression in Fig. 9.15. They are used in the mathematical model of motion of the spring actuator

and in the simulation block of the model. In order to obtain a good agreement between the experimental and simulated results in terms of the minimal output variation between the model and the experiment, the coefficients in Fig. 9.15 should be changed for different working conditions of the spring actuator (input temperatures, pre-strains, heat sink conditions).

The schematics of the model of motion of the SMA wire (see Fig. 8.7a) can be modified by introducing Eqs. 9.3 and 9.4 into the model. This modification transforms the model of motion of the SMA wire into the model of motion of the spring, in which the input to the model of motion of the spring is the desired displacement, D_r (same as D in Fig. 9.15 and Eq. 9.4), as shown in Fig. 9.16. This modification is used only in the study of the spring motion due to the fact that the input heat load values (in the spring motion model) are preferable to the input temperatures (as in the SMA wire motion model), because the heat balance is more complicated in the case of the spring as compared to the case of the SMA wire in terms of the thermal inertia, geometry, and mass.

Figure 9.16 shows that the input (desired) displacement, D_r , is converted to the shape memory effect driven recovery force, F_Q , through a series of transformations. Finally, the force F_Q serves as the input to the model of motion (Eqs. 8.6) of the spring actuator that is used to compute the displacement of the spring under a payload. The output of the model of motion of the spring is the computed displacement of the spring, D_c as shown in Figure 9.16.

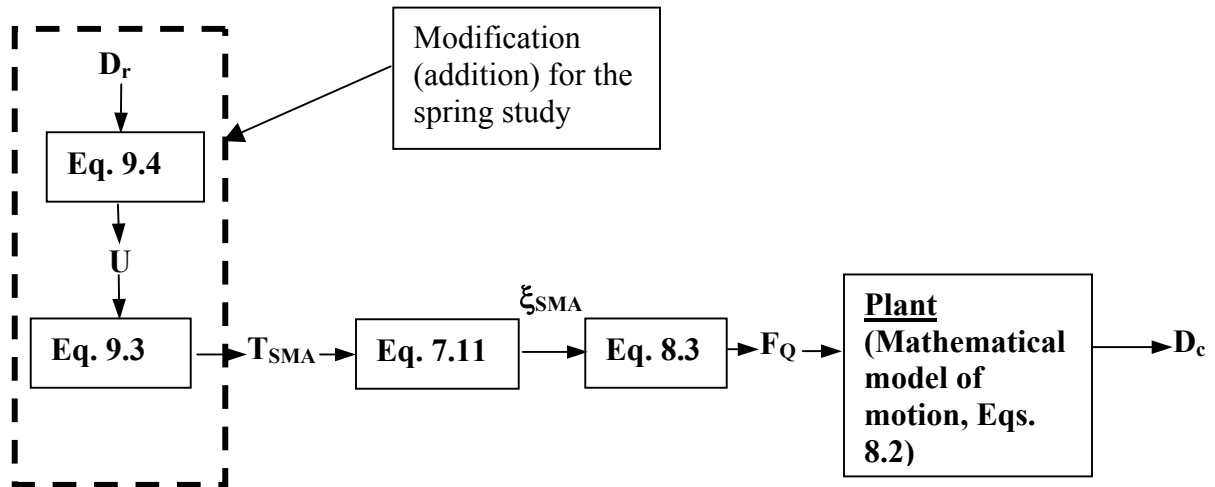
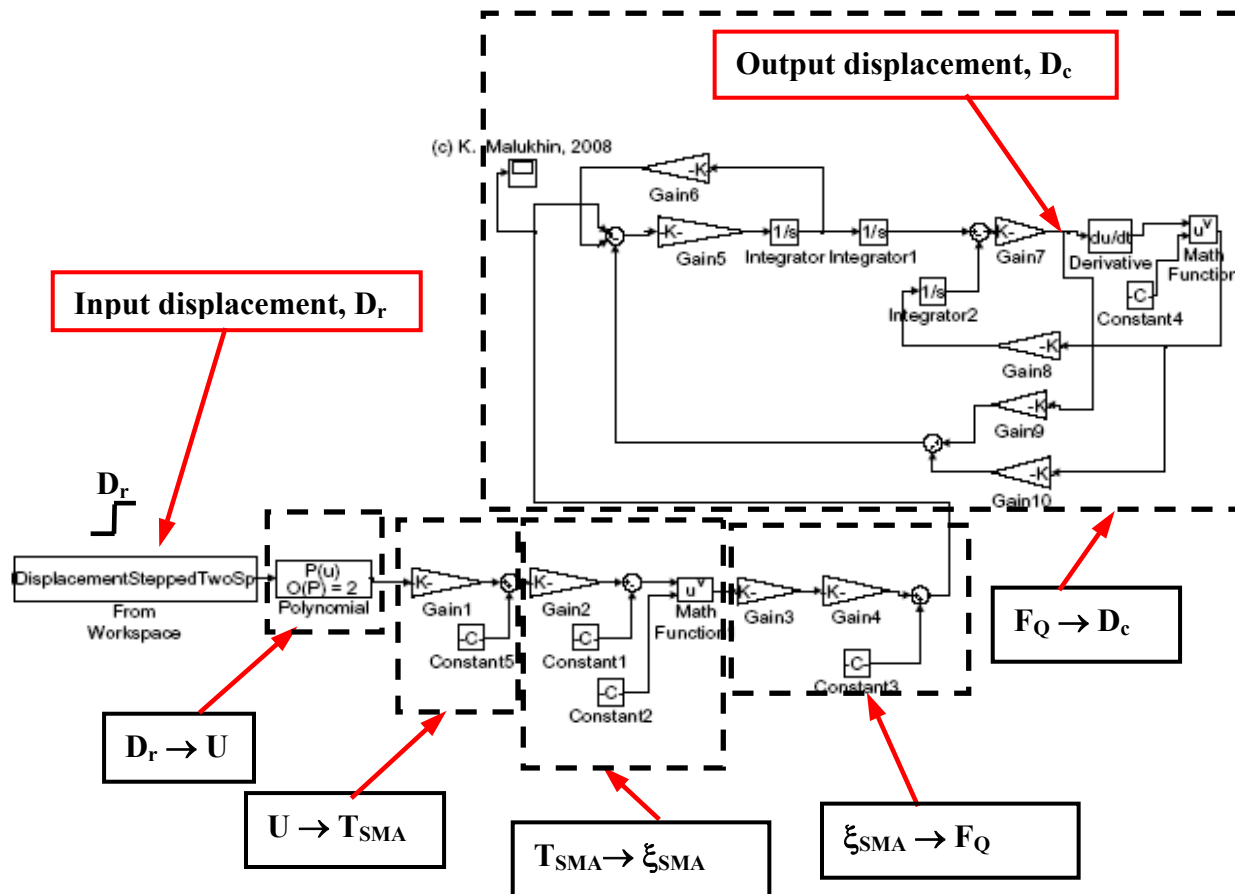


Figure 9.16: *The model of motion of the spring actuator*

The simulation block that corresponds to the model of motion (Fig. 9.16) of the spring actuator in a SIMULINK-based program is shown in Fig. 9.17. It differs from the analogous simulation block for the SMA wire actuator because of the different input: reference displacements (see Fig. 9.16), instead of the temperatures (see Fig. 8.7a).

This simulation block in Fig. 9.17a models the open loop step response of the actuator. The notation used in the simulation block is shown in Fig. 9.17 b. In the block, the displacement, D_r , is converted to the corresponding voltage drop, U , which is converted to the temperature, T_{SMA} . The temperature T_{SMA} serves as the input to the model of the kinetics of the austenite fraction evolution, ξ_A , that, in its turn, is used to compute the force F_Q - an input to the model of motion of the linear stage. The applied electrical current, I , in the model is assumed to be constant.

(a)



Nomenclature:

<i>polynomial</i> = $K_1 * D_r^2 + K_2 * D_r + K_3 = U$, (see Eq. 9.4);
<i>Dr</i> – reference displacement, m;
<i>Dc</i> – computed displacement, m;
<i>Gain1</i> = $I * \Delta t / (C_p * M_{SMA} * \Delta t + \alpha * F)$, (from Eq. 9.3);
<i>Gain2</i> = $2C_p / r_m$;
<i>Gain3</i> = K_A ;
<i>Gain4</i> = Δ_{Max} ;
<i>Gain5</i> = $1 / (M_b + M_{SMA})$;
<i>Gain6</i> = B_b ;
<i>Gain7</i> = $1 / (K_m / K_t + 1)$;
<i>Gain8</i> = B_m / K_t ;
<i>Gain9</i> = K_m ;
<i>Gain10</i> = B_m ;
<i>Constant1</i> = $2C_p / r_m A_s$;
<i>Constant2</i> = 0.5 (power of the equation (7.11));
<i>Constant3</i> = 0.00001 (added for the purpose of numerical stabilities in the “Simulink” integration solver);
<i>Constant4</i> = 0.2 (characterizes the non-linear behavior of the “muscle” system according to Wu et al., 1990);
<i>Constant5</i> = $T_{room} + 18.000$;
<i>M_b</i> – mass of the payload, kg;
<i>M_{SMA}</i> – mass of the spring actuator, kg;
<i>B_b</i> – damping coefficient of the payload system, N·s/m;
<i>K_m</i> – stiffness of the spring actuator in the martensite state, N/m;
<i>K_t</i> – stiffness of the bias spring, N/m;
<i>B_m</i> – damping coefficient of the spring actuator, N·s/m;
<i>K_A</i> – stiffness of the spring actuator in the austenite state, N/m;
<i>DeltaMax</i> – maximal linear displacement of the spring actuator, m;
<i>I</i> – electrical current, applied to the spring actuator, A; <i>I</i> = const;
<i>Δt</i> – time interval, s; <i>Δt</i> = const;
<i>α</i> – convective heat transfer coefficient, W/(m ² K);
<i>F</i> – surface area of the spring actuator, m ² ;
<i>C_p</i> – heat capacitance of the SMA material, J/(kgK);
<i>r_m</i> – latent heat of phase transformation, J/kg;
<i>A_s</i> – start temperature of austenite phase transformation, °C;
<i>T_{room}</i> – room temperature, °C.

Figure 9.17: The simulation block of the model of motion of the linear stage with the accordion spring actuator (a) and nomenclature (b)

9.5.2 Verification of the model

The mathematical model, shown in Fig. 9.16, presents the open loop model of motion of the spring actuator of the linear stage in which the heat applied to the active spring actuator (equivalent to a shape memory effect driven recovery force F_Q), results in a displacement of the spring.

Numerical simulations of the motion of the spring actuator of the linear stage were done in the "Simulink" environment using the model, shown in Fig. 9.16, and the simulation block in Fig. 9.17. The input parameters used in the simulations are given in Table 9.2 (equivalent to Table 8.1).

Table 9.2: *Properties of the SMA NiTi material*

Parameter	Value	Parameter	Value
C_p	920	M_{SMA}	1.25e-3
r_m	24171	$K_{SMA} = K_A$	10111
E_A	70e9	K_s	3389
E_M	26e9	K_m	3389
A	5.0669e-8	B_b	6
L_{wire}	0.2286	B_{SMA}	0.00217
ε_L	0.067	A_s	40
M_b	2.5e-3		

It is seen from Table 9.2 that the value of the heat capacitance in these simulations is almost 3 times lower (326 J/(kg°K)) than the value of the heat capacitance cited earlier (920

$J/(kg^{\circ}K)$) in Table 7.1. From the DSC measurements (e.g., see DSC thermogram in Fig. 5.15) the value of the heat capacitance changes during the phase transformation in NiTi, as the heat flux changes. It is assumed by many researchers, that the heat capacitance is constant (does not change with temperature) during the phase transformation process and is equal to its maximal value (e.g., $920 J/(kg^{\circ}K)$ for a given NiTi material), which is exhibited by the material in the middle of the phase transformation (e.g., see DSC thermogram in Fig. 5.15). Since at the end of the austenite phase transformation, the heat capacitance is at its minimal value (e.g., Fig. 5.15), we have assumed, that the heat capacitance is equal to this value during the numerical simulations (i.e., $326 J/(kg^{\circ}K)$ for the given NiTi material). In spite of this fact, the difference in the values of the heat capacitance does not affect significantly the results of the numerical simulations, partially, because the mathematical expression for the temperature, T_{SMA} (see Eq. 9.3 or see Gain 14 in Fig. 9.17) have the heat capacitance, C_p , in the denominator, while the mathematical expression for the austenite fraction, ξ_A (see Eq. 7.14, Chapter 7 or Gain 9 and Constant 1 in Fig. 9.17), have heat capacitance, C_p , in the numerators, thus decreasing the influence of the heat capacitance on the numerical results.

The results of one of the numerical simulations using the open loop model of motion are shown in Fig. 9.18. Figure 9.18a shows the input temperature, T_{SMA} , that represents the lumped parameter, which characterizes the SMA spring's temperature state. T_{SMA} is assumed to have the same value at each point of the spring based on the fact that the spring has a low mass, $M_{SMA} = 1.5$ gram. Therefore, it is assumed, that the thermal equilibrium in the spring actuator is achieved instantaneously when heat is applied. Another assumption in the mathematical model of motion is that the SMA material (NiTi) of the linear stage is initially in the de-twinned martensitic state,

and that upon heating the material instantaneously transforms into austenite. This assumption is based on the fact, that the temperature-induced phase transformation takes about $10^{-6} \dots 10^{-7}$ s.

Results of the step response of the open loop model of motion of the spring actuator show that heating of the pre-deformed (pre-compressed by 2 mm) SMA spring actuator by approximately 4 °C above its A_s temperature, makes the spring recover its initial length and contract by approximately 2 mm (Fig. 9.18e). The computed recovery force (according to Eq. 8.2) was: $F_Q \approx 7$ N (Fig. 9.18c). The reference displacement, D_r , and the computed output displacement, D_c , show excellent agreement based on the plots in Fig. 9.18c.

The difference between the minimal and the maximal input temperatures in the model is $\Delta T_{SMA} \approx 4$ °C. The minimal temperature corresponds to the beginning of the temperature-induced phase transformation in the SMA material and to the beginning of the motion of the SMA actuator. The maximal temperature corresponds to the finish of the temperature-induced phase transformation in the SMA material and to the end of the motion of the SMA actuator.

The input temperature range ($\Delta T_{SMA} \approx 4$ °C) in the numerical simulation is lower, than the one in the experimental investigations of the shape memory effect driven recovery motion of the active spring actuator of the linear stage, where the input temperature range was about $\Delta T_{SMA} \approx 20$ °C (see Fig. 9.11a , time interval 100...280 sec).

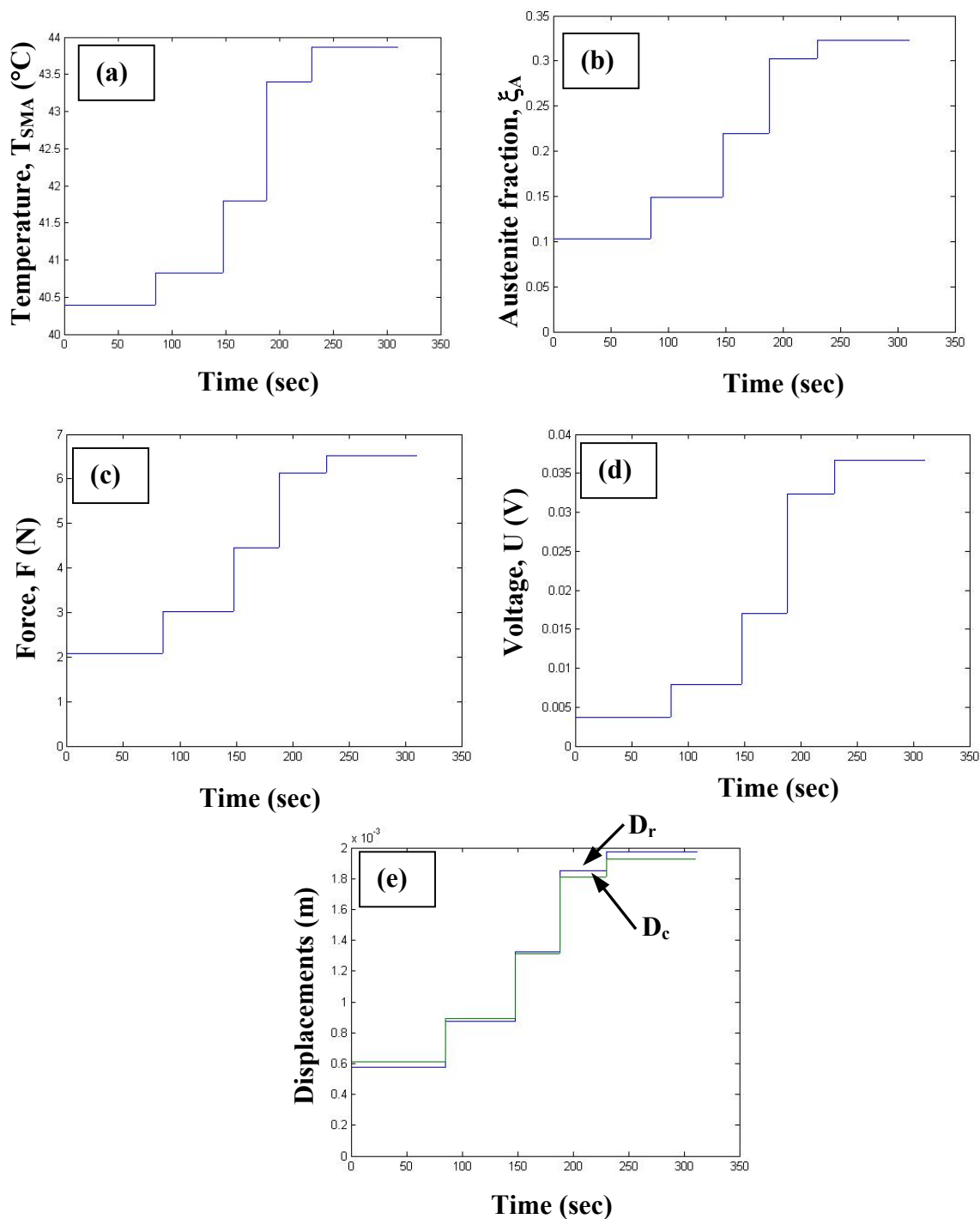


Figure 9.18: Result of the numerical simulations of the open loop response of the model of motion of the spring actuator: (a) temperature of the SMA spring, T_{SMA} ; (b) fraction of austenite, ξ_A ; (c) recovery force, F_Q ; (d) voltage drop across the spring, U ; (e) reference and computed displacements, D_r and D_c .

In the computations, the input temperature range, ΔT_{SMA} , is the difference between the A_s and A_f temperatures (see, for example, DSC in Fig. 9.3), where the temperature-induced phase transformation and, therefore, the shape memory effect driven linear recovery takes place. In spite of the difference between the theoretical and the experimental values of ΔT_{SMA} , both, the numerical simulations and the experimental investigations, resulted in the complete recovery of the spring. The reason for the discrepancy in the temperature ranges is the consequence of the simplified way in which the recovery force, F_Q (which represents the actual input parameter to the model of motion), is calculated in the current version of the mathematical model (according to Eq. 8.6). In the calculation of the recovery force, the maximal recovery length of the uniaxial displacement (X_{SMA}^{MAX} in Eq. 8.6) is a constant value, while in reality it has to vary depending on the value of the computed output displacement, D_c .

According to the experimental results from a sample step response of the spring actuator, the voltage drop measured across the spring during the time interval 100...280 sec (see Fig. 9.11b) was equal to $U \approx 50$ mV and the corresponding spring recovery length (displacement) was $D \approx 1$ mm (see Fig. 9.11c). Mathematical modeling of the spring recovery using the open loop motion model gives a satisfactory agreement with the experimental results: the total voltage drop (total of all the voltage drops in Fig. 9.18d) across the spring $U \approx 40$ mV and the total displacement of the spring, $D_c \approx 2$ mm (Fig. 9.18e). The discrepancy between the experimentally measured and computed voltage drops and displacements can be explained by the fact, that the maximal recovery length of the uniaxial displacement was constant as was discussed earlier in the text. In the future modifications of the mathematical model of the linear stage, the maximal

recovery length parameter X_{SMA}^{MAX} will vary, for example, by making it equal to the computed displacement, D_c , at each integration step in the Simulink model.

9.6 Concluding remarks

An experimental prototype of the linear stage of the mMM with the accordion spring actuators was designed and manufactured from a commercially available SMA NiTi alloy. The linear stage was used to develop an SLA procedure to impart the phase transformation properties in SMA structures only in selected regions only. Step response experiments with an SLA-treated spring actuator were conducted, described and analyzed. In these experiments the spring actuators developed a 2.5...3 mm shape memory effect driven motion during the constrained recovery of the pre-deformed shapes of the spring under a heat load. In future research a feedback controlled DC source will be used to be able to measure the full range of the displacements of the spring actuators.

An open loop model of motion of the spring actuator was developed. The model computes the shape memory effect driven displacement of the spring actuator subject to a heat input. The results of the model were compared to experimental results of the open loop motion of the spring actuator and a satisfactory agreement was found. A further modification of the open loop model will be done in future research. A closed loop controlled motion model of the spring actuator will be developed as well.

CHAPTER 10

10. A gripper for mMMs with a short range gripping motion range

The goal of this chapter is to design and manufacture an SMA gripper whose grasping (clamping) motion (Fig. 1.1) is based on the TWSME driven recovery motion. The gripper should be capable of clamping micro-tools of approximately 3 mm in diameter.

The gripper will be designed such, that when the temperature of the material of the gripper rises above its A_s level – the gripper will generate an expanding motion, while when the temperature of the material will drop below its M_s level – the gripper will generate a contracting (clamping) motion. The heating of the gripper can be done by an external heating element (a heater), while the cooling of the gripper can be done by natural convection at ambient temperature or by forced convection.

10.1 Conceptual design of the gripper

The goal of this section is to design a gripper with a small gripping motion that allows the clamping of micro-tools with an approximately 3 mm diameter. The TWSME driven gripping motion range will be 20...60 μm . Two alternative conceptual designs of the grippers - gripper #1 and gripper #2 - are shown in Figures 10.1 and 10.2 respectively.

Gripper #1 in Fig. 10.1 represents a gripping element with four clamping jaws. In this design the gripping element is a monolithic part (no assembly is required), made of NiTi SMA. The principle of work is based on the TWSME driven expanding/compressing motion of the clamping jaws of the gripper that would allow clamping of the tool inside it.

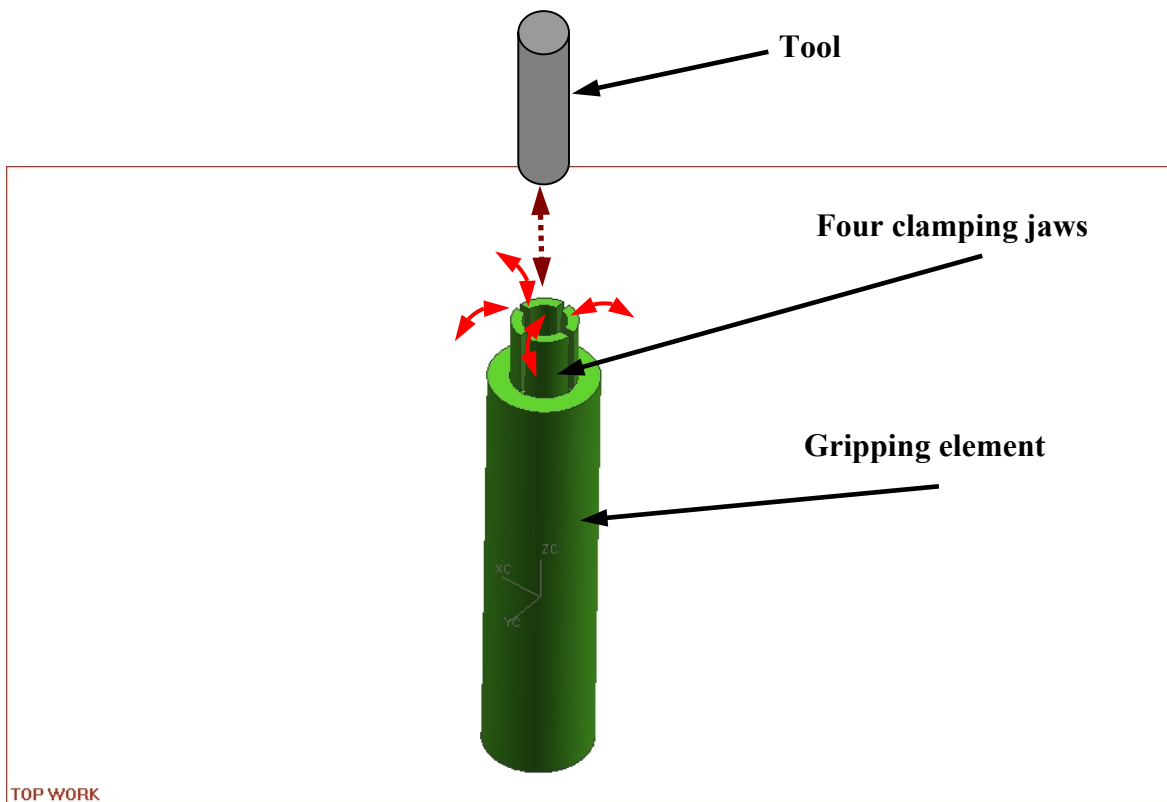


Figure 10.1: *Conceptual design of gripper #1 (UNIGRAPHICS).*

The tip of the gripper is thermo-mechanically treated to possess the TWSME. Afterwards, the TWSME “trained” gripper will operate as the gripping device, by heating and cooling its tip. The tip of the gripper, heated above its A_f temperature, will expand. When an object of interest (e.g., a tool) is inserted inside the open jaws of the tip, it will be cooled below the M_f temperature, thus creating a contracting motion and clamping the object inside the jaws.

Another gripping mechanism, gripper #2, is shown in Fig. 10.2. Gripper #2 consists of a two-part assembly: a steel gripping element with four clamping jaws and an SMA (NiTi) ring. The NiTi ring is thermo-mechanically treated to possess the TWSME. The TWSME “trained” ring is assembled on the steel gripping element to form the gripper and allow the assembled gripper to function as the gripping device.

The assembly of the gripper will be done by heating the ring above its A_f temperature, that must ensure that its internal diameter is larger than the outside diameter of the tip of the open steel gripping element so that, the tip of the steel gripping element can be inserted inside the ring. Afterwards, the ring will be cooled below its M_f temperature and, therefore, contract, thus making a “press” fit with the tip of the steel gripping element and creating the final assembly of the gripper. The jaws of the tip will be compressed in the assembled state.

The assembled gripper will operate as the gripping device by heating and cooling the tip of the gripper together with the ring. In this case, the NiTi ring, heated above its A_f temperature, will expand, thus allowing the compressed steel jaws to expand as well. When an object of interest (e.g., a tool) is inserted inside the open jaws, the tip of the gripper will be cooled below the M_f temperature, thus creating a contracting motion of the ring and clamping the object inside the jaws.

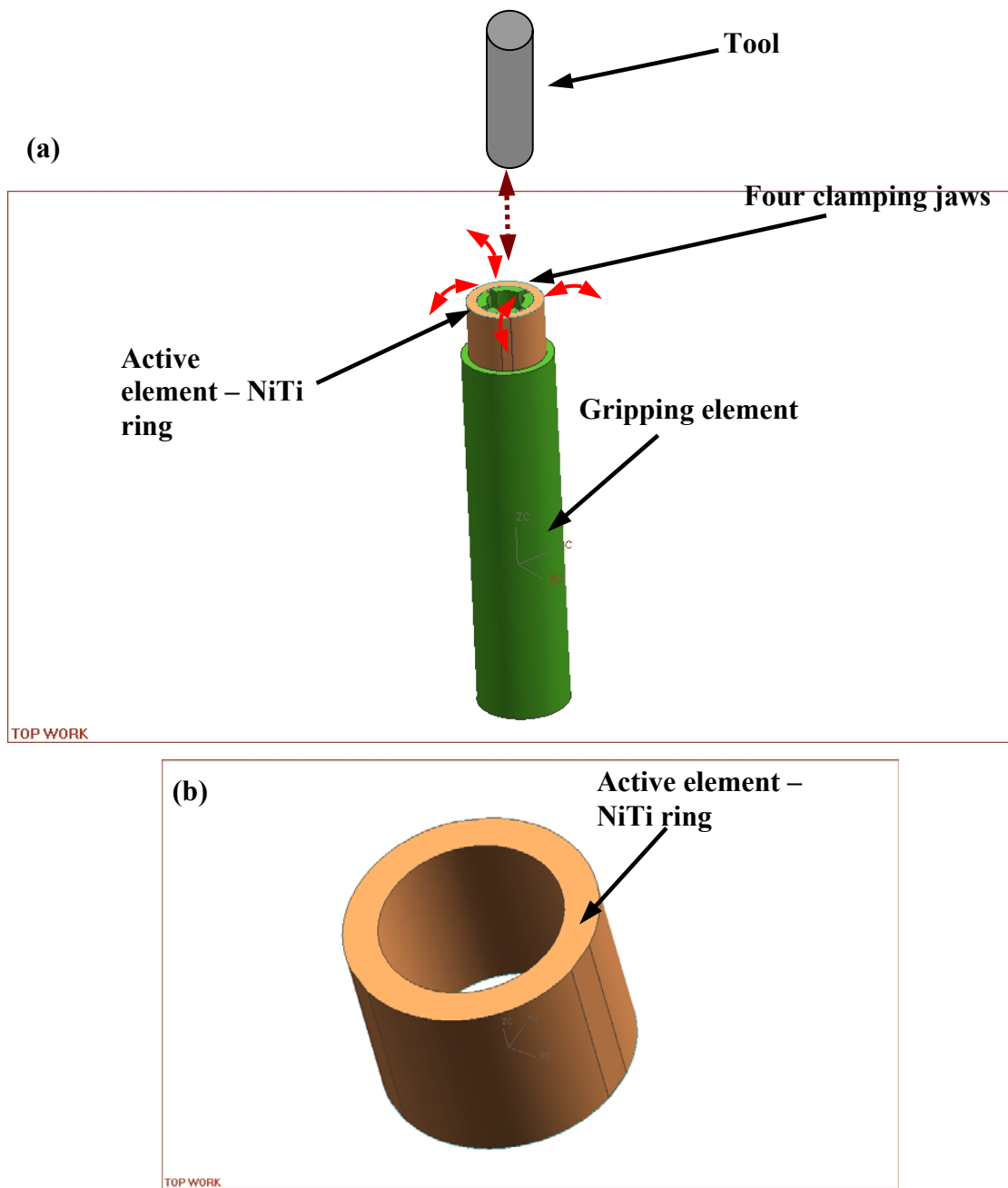
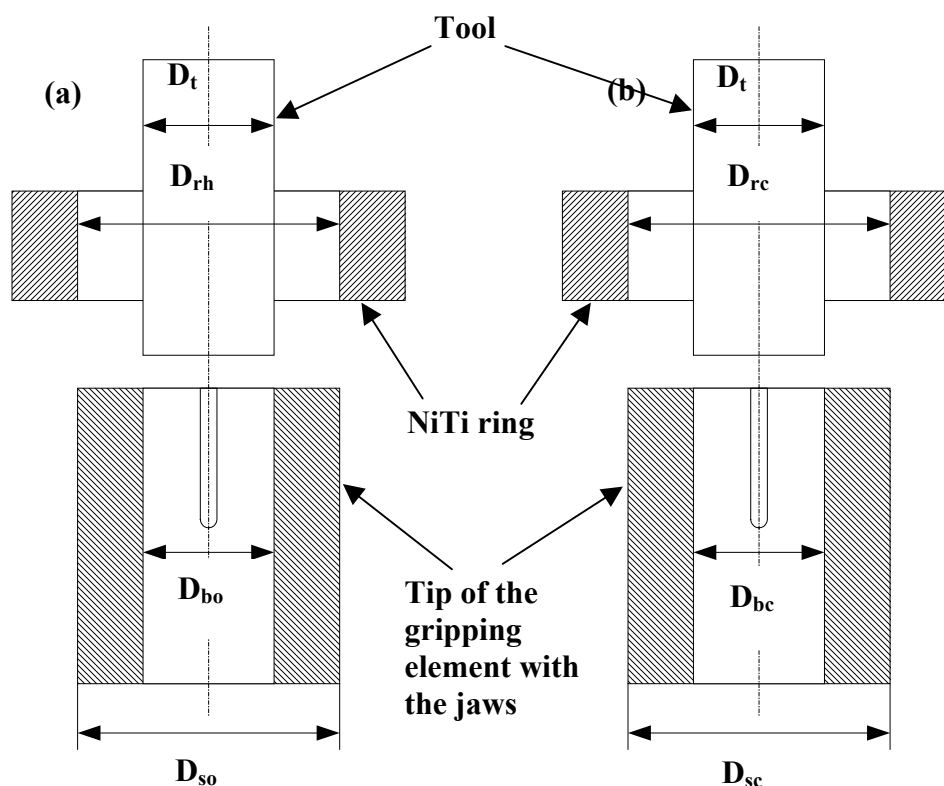


Figure 10.2: *Conceptual design of gripper #2 (UNIGRAPHICS): (a) assembly, (b) NiTi ring.*

10.2 Fabrication of the gripper

In this work, gripper #2 was built and tested, therefore, in the subsequent discussions it will be referred to as “gripper”. The fabrication of the gripper was done based on the analysis of the assembly dimensions (Fig. 10.3). The schematic in Fig. 10.3 allows the identification of the relations between the geometric parameters of the parts of the assembly (steel gripping element and NiTi ring) and of the tool in their heated (Fig. 10.3a) and cooled states (Fig. 10.3b).



where: D_{bo} – internal diameter of the gripping element in the open (“hot”) state, D_{bc} – internal diameter of the gripping element in the closed (“cold”) state, D_{so} – outside diameter of the gripping element in the open (“hot”) state, D_{sc} – outside diameter of the gripping element in the closed (“cold”) state, D_{rh} – internal diameter of the ring in the open (“hot”) state, D_{rc} – internal diameter of the ring in the closed (“cold”) state, D_t – tool diameter.

Figure 10.3: Schematic of the assembly of the NiTi ring and the steel spindle: (a) “hot” state, (b) “cold” state

The tolerances of the assembly depend on the tolerances of the tool, on the fabrication process that will be used to machine the parts of the assembly and on the range of the TWSME driven motion during the heating/cooling process. When the NiTi ring is heated above its A_f temperature (Fig. 10.3a), then - $D_{rh} > D_{so}$ with a minimal clearance of about $2 \mu\text{m}$, while $D_{bo} > D_t$ with the minimal clearance of $2 \dots 5 \mu\text{m}$. When the NiTi ring is cooled below the M_f temperature, then - $D_t \approx D_s$, $D_{rc} \approx D_{bc}$. The difference between the diameter D_{rc} and diameter D_{rh} must provide sufficient motion to clamp the tool and generate the desired gripping force (several N, see Table 1.1). Based on the above considerations, the final drawing of the gripper is shown in Fig. 10.4.

Several experimental prototypes of the steel gripping element and of the NiTi ring have been machined according to the drawing in Fig. 10.4. The steel gripping elements and the NiTi rings are shown in Fig. 10.5.

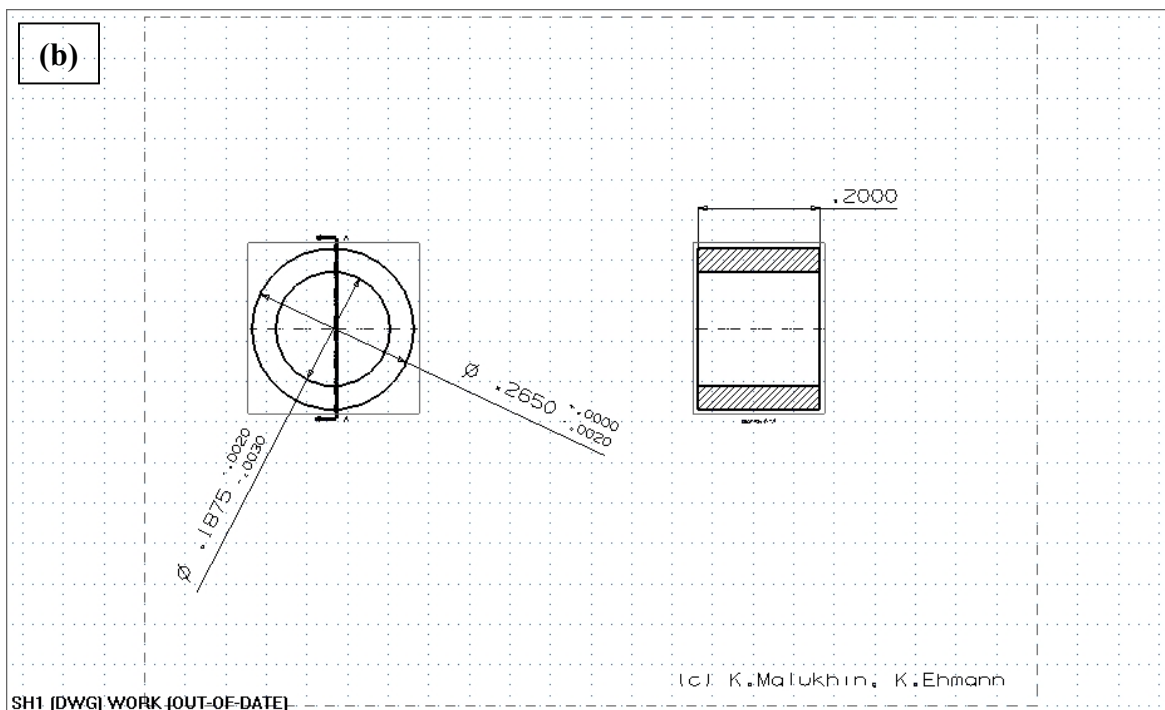
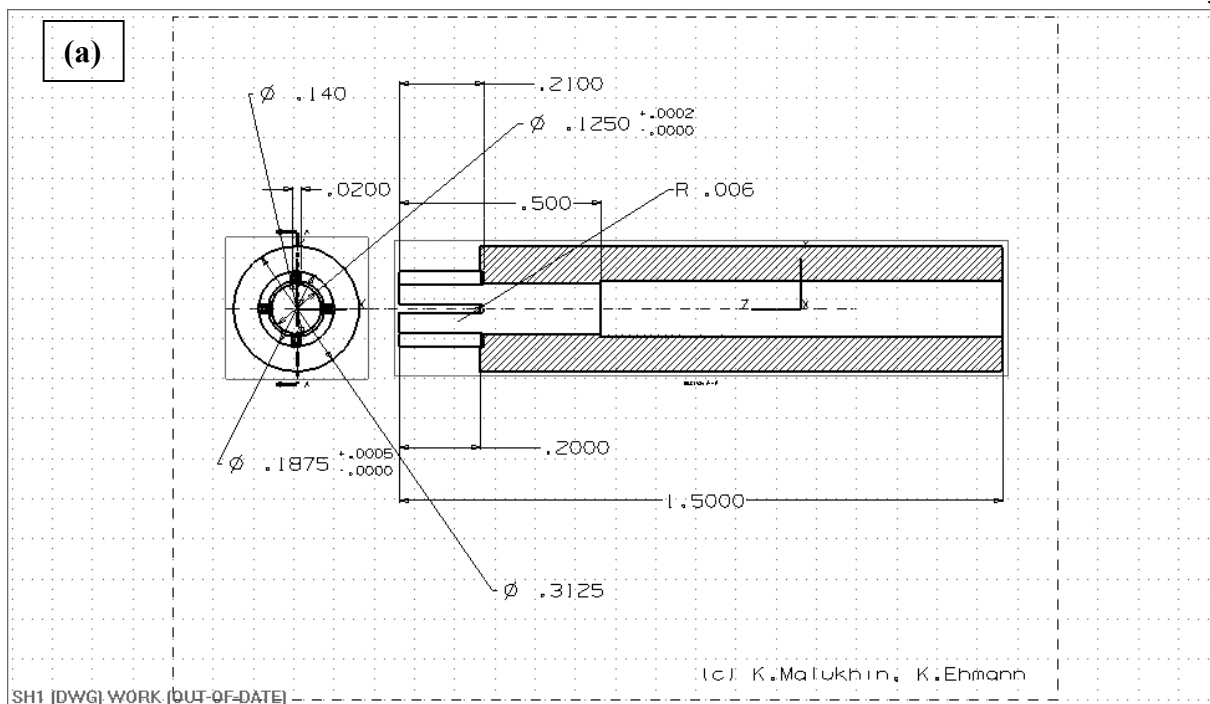


Figure 10.4: Drawing of gripper #2 (UNIGRAPHICS): (a) stainless steel gripping element, (b) NiTi ring.

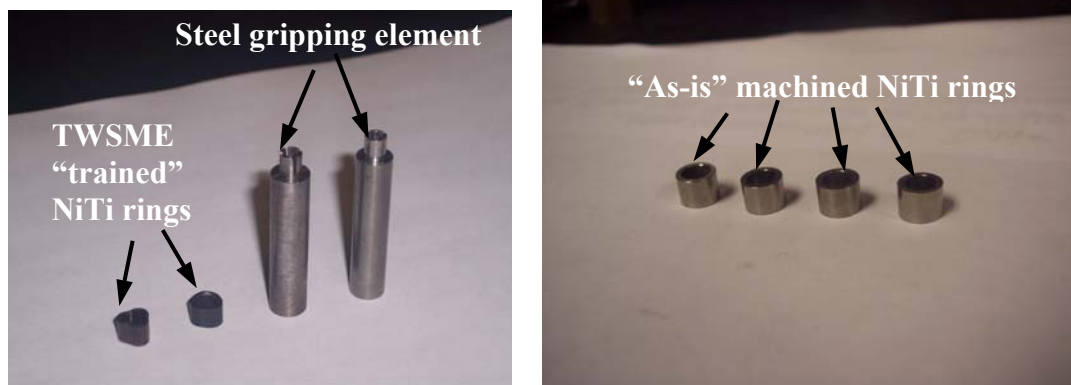


Figure 10.5: Prototypes of the gripping element and NiTi rings – parts of the gripper.

10.3 Development of the TWSME training procedure for the SMA ring

As described in Chapter 6 the TWSME has a smaller recovery range than the OWSME. The TWSME driven SMA structure can recover a uniaxial strain of 0.5 to 1%, while the OWSME driven structure can recover a uniaxial strain of 6 to 7%. There exist several ways of achieving the TWSME in NiTi structures (see Chapter 6). In this work we have explored the so-called “constrained aging” method, where a two-step thermo-mechanical treatment procedure of the NiTi rings is used to achieve the TWSME in them (Lei et al., 2000; Lind et al., 2000; Wu et al., 2000).

10.3.1 Step #1 of the TWSME training

The goal of the first step of the TWSME thermo-mechanical treatment is to initially achieve the OWSME in the SMA material. The procedure of OWSME “training” was described

in Chapter 4. Here, it was applied to the thermo-mechanical treatment of all of our NiTi rings. A NiTi ring, purchased from the UNILOCK company, was used in the early stages of the development of the TWSME treatment procedure and is shown in Fig. 10.6. The dimensions of these rings do not correspond to the drawing in Fig. 10.4.

The OWSME “training” was done in two stages as follows. Figure 10.6 shows the NiTi ring, constrained from its inside surface by press-fitting it on a mandrel, enforcing thereby the shape of the ring in its “open” position. During the first stage of the OWSME “training”, the constrained ring was annealed in a vertical oven with an Ar gas protective atmosphere at a temperature of 800 °C for 1 hour and quenched in room temperature water afterwards. This solid-solution treatment was done in order to homogenize the NiTi alloy according to its phase diagram. During the second stage of the OWSME “training”, the constrained NiTi ring was annealed in the same oven at a temperature of 400 °C for 1 hour and quenched in room temperature water afterwards. According to the NiTi alloy phase diagram, this temperature level corresponds to the precipitation-hardening region of the material and imposes the phase transformation property in it (see Chapter 4 for explanations).

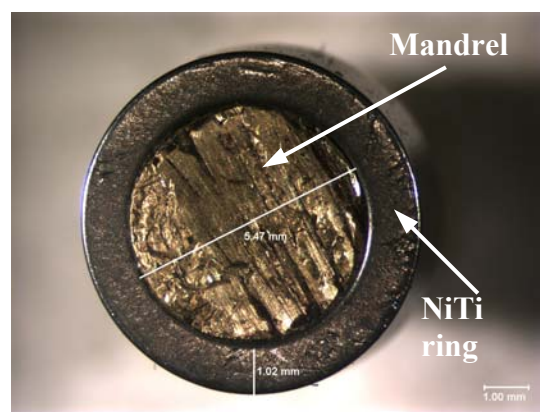


Figure 10.6: TWSME “training” of a NiTi ring – Step #1

10.3.2 Step #2 of the TWSME training

The second step of the TWSME “training” process is related to the development of partially plastically deformed zones in the material. The plastic energy, stored in the SMA structure creates a corresponding bias force (also - gripping force), when this energy is greater than the elastic energy of the rest of the material.

There are several ways to develop the partially plastically deformed zones in the SMA material, depending on the desired form of the plastically deformed zone. For example, by constraining the SMA ring inside a collet as shown in Fig. 10.7 and aging at room temperature for 24 hours. Since the gripping force of the SMA gripper is based on the second step of the TWSME “training” process it is advantageous to model the TWSME “training” of the SMA gripper to better estimate the value of the gripping force.

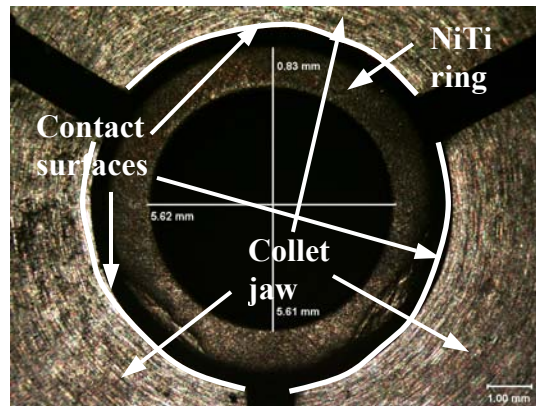
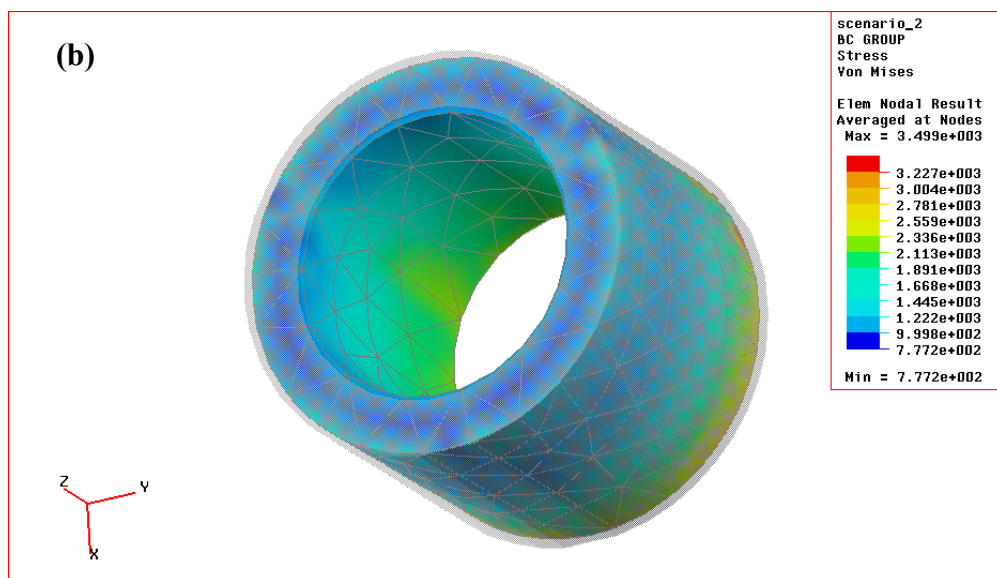
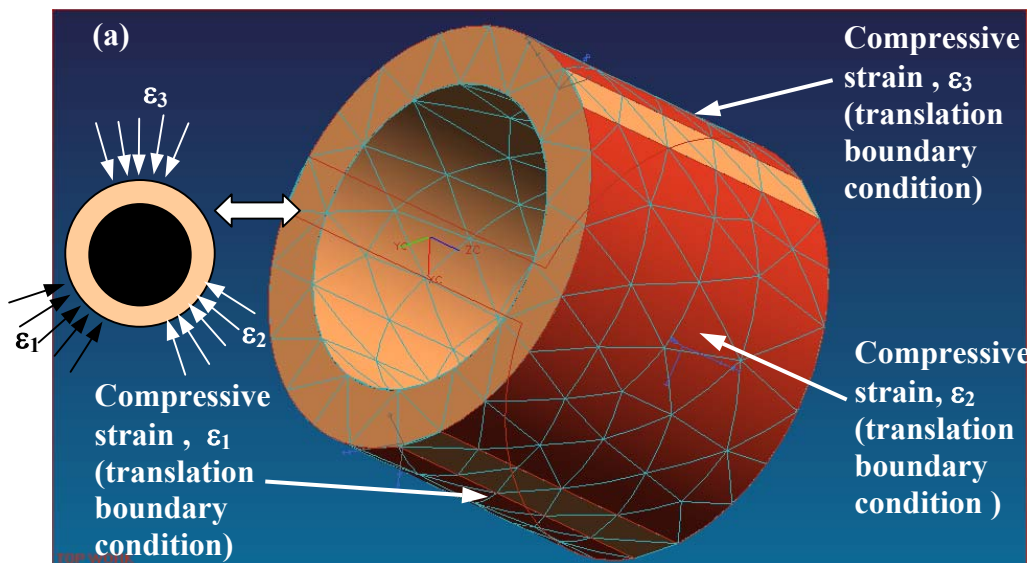


Figure 10.7: TWSME training of the NiTi ring – Step #2

10.3.2.1 FEM (UNIGRAPHICS) modeling of the NiTi ring

Strain-controlled numerical simulations were performed to estimate the amount of constraint in the SMA ring during step #2 of the process that will be necessary to develop a gripping force of several Newtons. The FEM computations were performed using the FEA package “Structures” of the “Unigraphics NX” environment. Only step #2 of the TWSME training when the ring is aged at room temperature and constrained on its outside surface, i.e., inside of a collet was simulated. The FEM simulation results are shown in Fig. 10.8. The goal of these simulations was to define the amount of the outside constraint in order to better control the TWSME driven expansion/contraction displacement of the ring when it is used in gripping. The boundary conditions (see Fig 10.8a) were the three radial compressing strains ($\varepsilon_1, \varepsilon_2, \varepsilon_3$) – effect of the three collet jaws – applied on the three contact surfaces (shown in red color in Fig. 10.8 a) of the ring to plastically deform it. The three contact surfaces correspond to the three jaws of the collet as shown in Fig. 10.7. By applying such a constraint to the ring/collet contact surfaces the ring becomes deformed to its minimal diameter as shown in Fig. 10.7. The deformation is not uniform and the deformed shape of the ring represents a conical structure. The FEM results show that during the strain controlled simulations after application of 10 to 15% of compressive uniaxial strain on the outside surface of the ring, as shown in Fig. 10.8, the final (compressed) shape of the ring is not cylindrical as in the beginning of the simulations. The final shape of the ring is conical (or tapered) as seen in Fig. 10.8 c, i.e., $D_1 > D_2$. This will affect the gripping capability of the ring and needs to be studied more thoroughly.



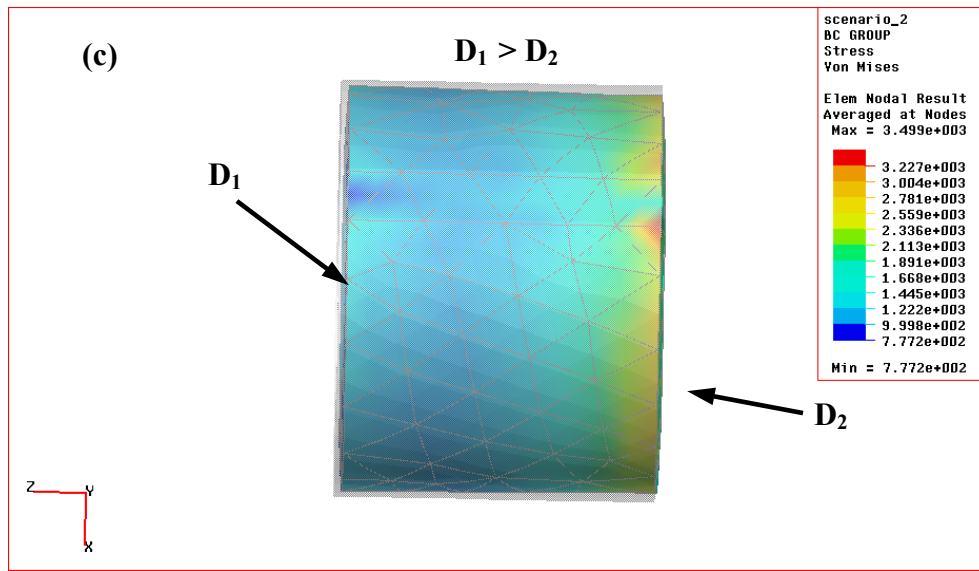
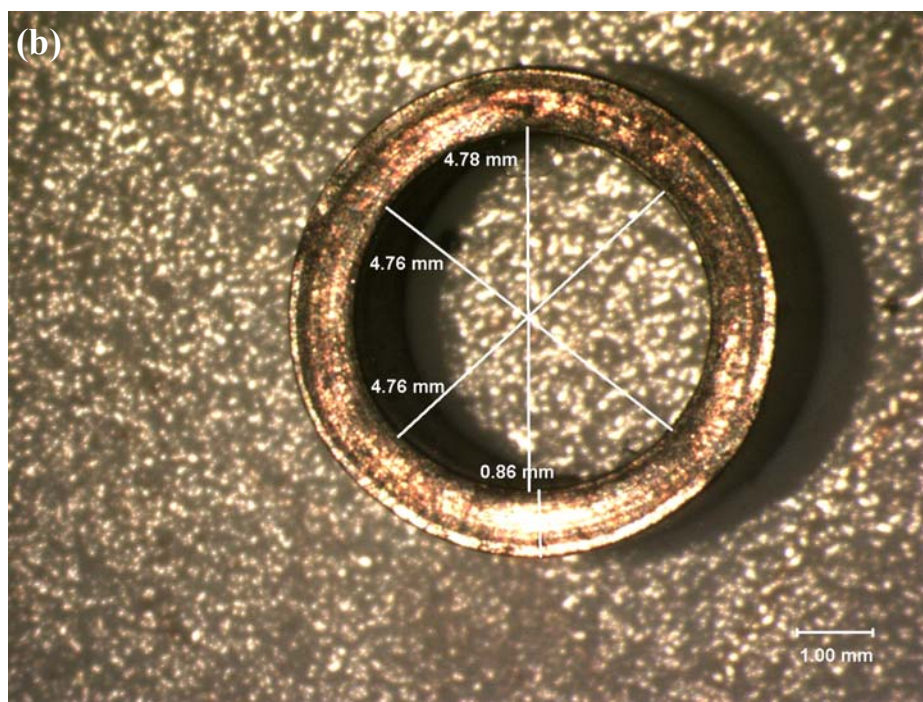
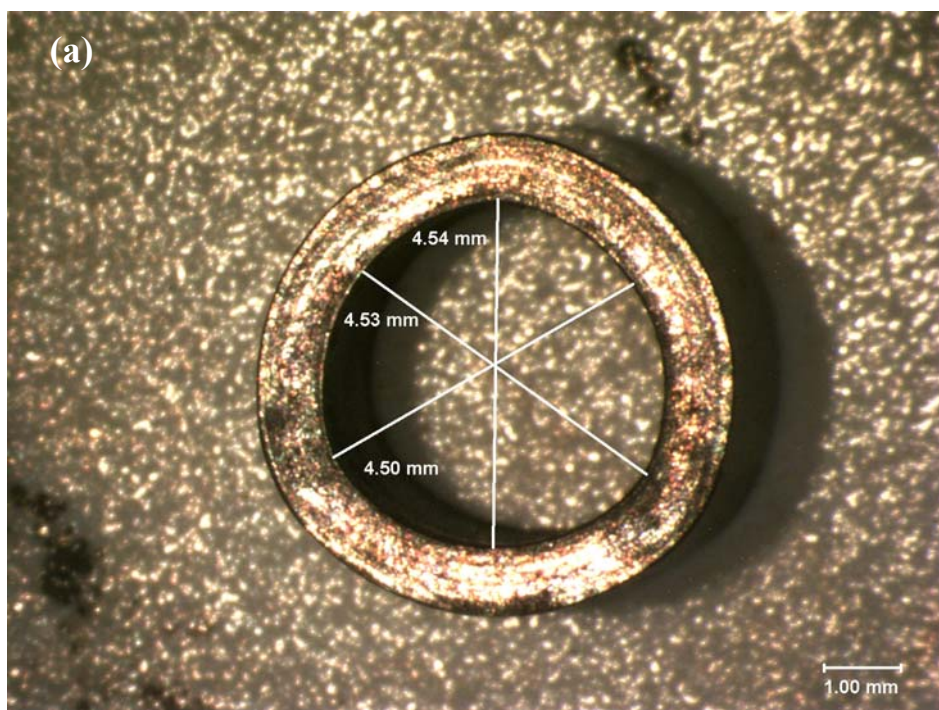


Figure 10.8: Finite element modeling of the SMA ring (UNIGRAPHICS): (a) model, (b) results – view 1, (b) results - view 2.

10.3.2.2 Experimental verification of step #2

Several NiTi rings were “trained” to impart the TWSME. One of the rings is shown in Fig. 10.9a. It can be seen that after the final step of the TWSME “training” procedure the ring has a non-round shape due to the compression from the collet. To test the TWSME, a hot plate was used. The ring was placed on the surface of the hot plate. The hot plate was placed under an optical microscope equipped with a CCD camera and image capturing software, such that the TWSME driven motion of the NiTi ring could be captured “in-situ”. Afterwards, several heating/cooling cycles were performed on the NiTi ring to investigate its expansion/contraction capability. One of the cycles is shown in Fig. 10.9. The ring was heated above its A_f temperature level (for the current NiTi material) as shown in Fig. 10.9b and consequently expanded. Then, the ring was cooled by natural convection and contracted as shown in Fig. 10.9c.



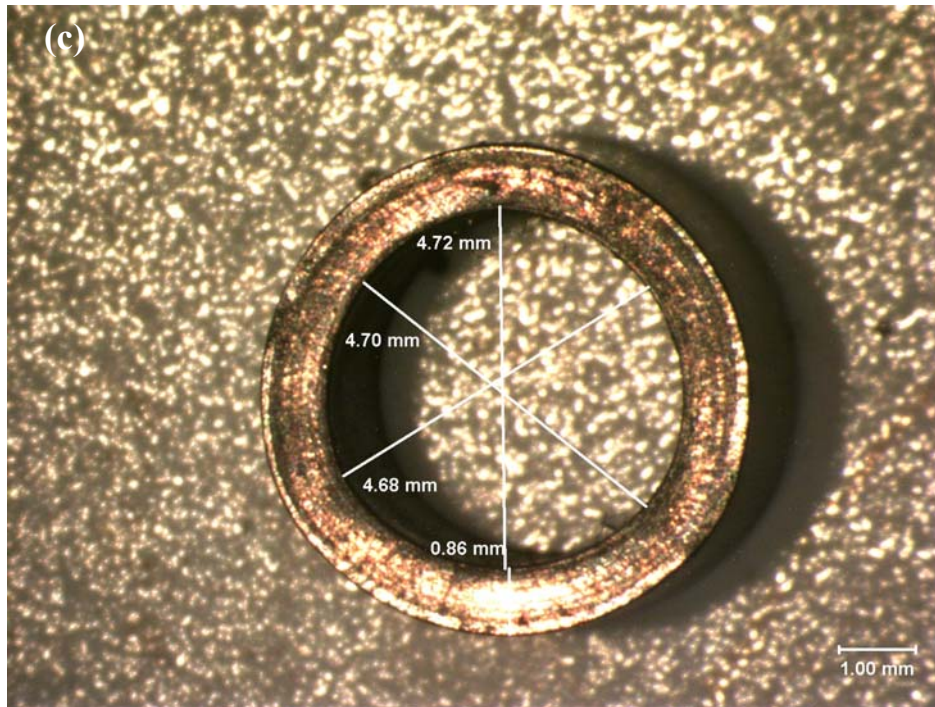


Figure 10.9: *Optical microscope images of the NiTi ring: (a) after the TWSME “training”, (b) heated, (c) cooled.*

In this particular case, the maximal difference between the internal diameters of the expanded (hot) and contacted (cold) ring was about $60\ \mu\text{m}$, which constitutes the TWSME driven gripping motion.

10.4 Experimental testing of the gripper

In order to experimentally test the gripping capability of the SMA gripper, the TWSME “trained” NiTi ring was assembled with the steel gripping element. The assembly was done as described earlier. The ring was heated on the hot plate above its A_f temperature. Then, the tip of the steel gripping element was inserted inside the expanded ring. Afterwards, the whole structure

was cooled by natural convection below the M_s temperature of the NiTi alloy. The NiTi ring contracted, thus, compressing the jaws of the tip and making a “press” fit with the steel gripping element as shown in Fig. 10.10. The assembled SMA gripper was tested by gripping a micro-milling tool, shown in Fig. 10.11.

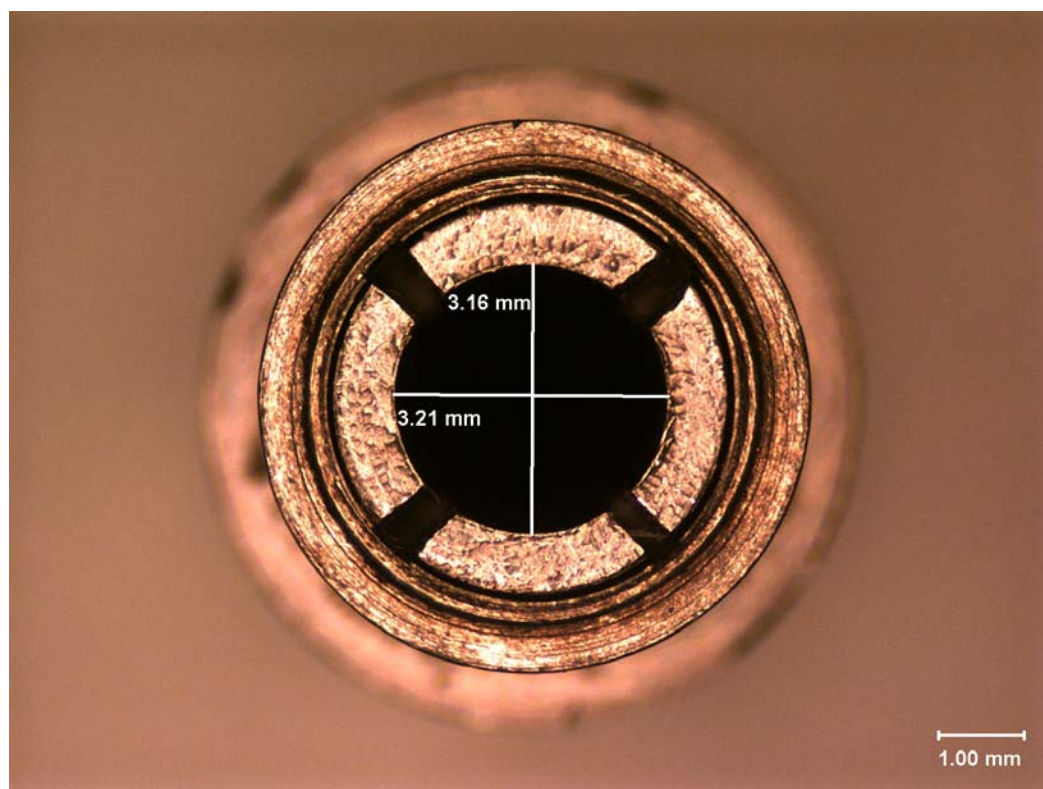


Figure 10.10: *Optical microscope image of the SMA gripper - assembly of the NiTi ring and steel gripping element*

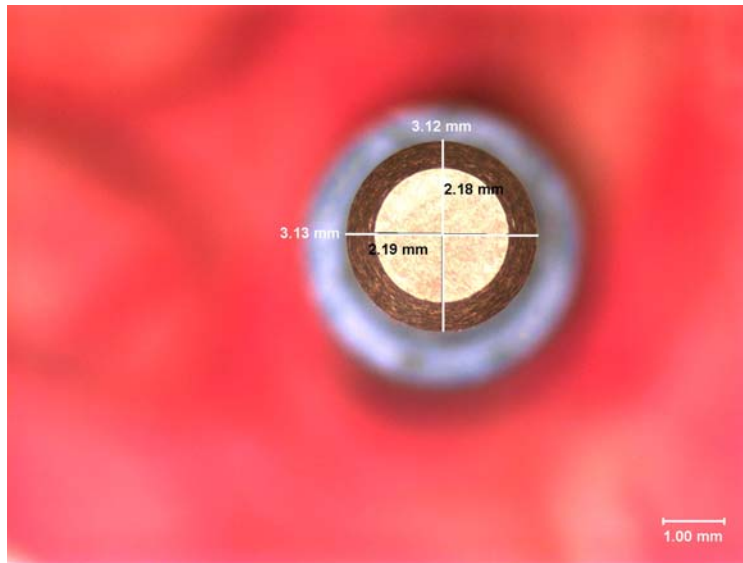


Figure 10.11: *Tool (micro-mill)*

The gripping procedure was as follows. The SMA gripper (Fig. 11.10) was placed vertically on the hot plate and heated above the A_f temperature of the SMA material of the ring. Afterwards, the tool was inserted inside the expanded grippers' jaws and the heat load was removed from the gripper. The jaws of the gripper, cooled below the M_s temperature of the SMA material, contracted, thus gripping the tool (Fig.10.11) inside it.

The gripping force of the SMA gripper was measured by a Kistler dynamometer, and acquired and recorded by the HP DAQ system. The gripper together with the clamped tool was vertically placed on the surface of the dynamometer. Afterwards, a payload (axial load) was applied to the tool. The maximal load at which the tool started slipping inside the gripper was considered to be the clamping force. Several clamping cycles were accomplished in order to estimate the variation of the clamping force of the material. During several clamping cycles the measured clamping forces were between 10 to 30 N. A typical plot of the experimental measurement of the clamping force is shown in Figure 10.12.

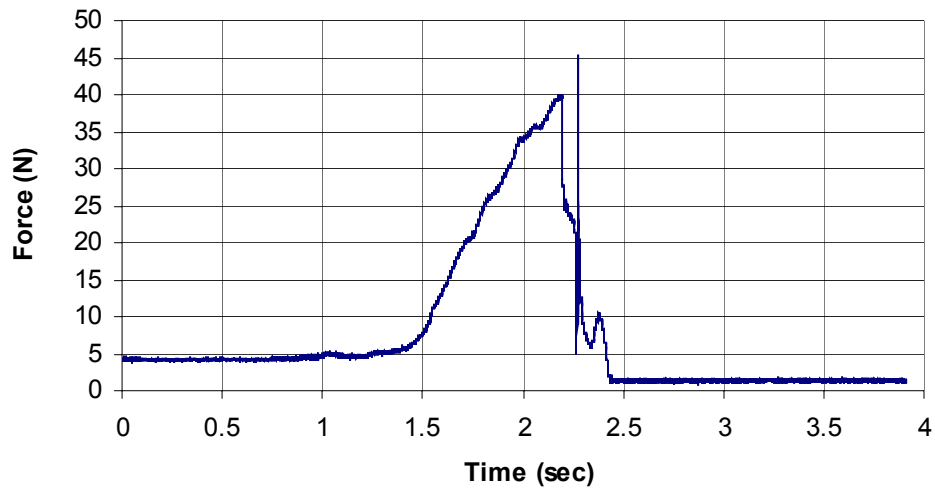


Figure 10.12: *Clamping force due to the TWSME*

10.5 Concluding remarks

An SMA gripper was designed, fabricated and tested. A TWSME “training” procedure was developed and applied to the SMA gripper. It was possible to achieve a TWSME driven clamping (gripping) force of tens of Newtons during gripping a micro-milling tool inside the gripper.

CHAPTER 11

11. Conclusions and future work

The conducted research represents an effort to combine leading edge rapid prototyping technologies and advanced materials to develop a functional micro/meso-scale SMA-based manipulator. The SMA manipulator is an advanced robot intended for the manipulation of micro/meso-scale objects through micron- and millimeter-scale motions.

11.1 Conclusions

The work completed in this dissertation allows the following conclusions to be drawn:

- (A) A technique for fabricating an mMM by a laser-assisted rapid prototyping process (DMD) from NiTi SMA powder was developed. The technique allows the fabrication of thin-wall and bulk structures from SMAs. The DMD parameters for the fabrication of bulk structures were also identified and several high quality (non-cracked, almost non-porous) bulk objects were fabricated. DMD parameters for fabrication of thin-wall structures were also identified. They were used to fabricate several high quality (non-cracked, almost non-porous) NiTi accordion spring actuators – parts of the linear stage of the mMM.

- (B) A new method for imparting phase transformation properties and achieving the OWSME in an SMA material manufactured by DMD was developed. OWSME “training” was used to impart the phase transformation properties in a DMD fabricated SMA material. A NiTi spring actuator, fabricated by DMD was processed using this technique. It exhibited the phase transformation properties and was able to generate several millimeters of motion due to the one-way shape memory effect. The OWSME “training” was used to modify and improve the phase transformation properties in a commercially available SMA NiTi material as well. The accordion spring actuator of the linear stage, fabricated from the commercially available material, heat treated by the developed method, was able to generate several millimeters of motion due to the OWSME.
- (C) A new technique – Selective Laser Annealing (SLA) – aimed at imparting phase transformation properties in selected areas of SMA structures was developed. One of the spring actuators of the wire-EDM fabricated linear stage was heat-treated using SLA in order to impart the phase transformation properties in the selected part of the stage.
- (D) A technique for achieving TWSME driven gripping motion in an SMA NiTi gripper structure was developed. The technique allows the achievement of a 30...60 μm clamping motion in a gripper. The TWSME driven gripper is capable of achieving a clamping force of 10...30 N.
- (E) An SMA wire actuator was built and used to study the step response behavior of SME driven actuators. A system identification of the thermally insulated

and non-insulated SMA wire actuator was undertaken. The thermally insulated SMA wire actuator was identified as a linear first order dynamic system. The thermally non-insulated SMA wire actuator was identified as a linear second order dynamic system.

- (F) A study of the feasibility of the control of motion of the SMA NiTi actuators at the micron/sub-micron displacement level was undertaken. A “self-sensing” concept was introduced. The “self-sensing” principle shows that the SMA actuators can be controlled with a sub-millimeter precision by using the fundamental properties of the SMA materials only and avoiding the use of external motion sensors. Experimental studies of the step response of the actuator shown that for the small range motion (0...1mm) the relation between the displacements of the SMA wire actuator and the voltage drop in the SMA wire can be described by a linear equation, while for the large range motion (more than 1mm) – the relation becomes non-linear due to the nature of the phase transformation as explained in the dissertation. The presented “self-sensing” technique does not account for the microstructural changes in the material (grain re-orientation, etc.) and for the presence of the different phases in the material (R-phase, twinned martensite) that introduce a non-linearity into the relationship between the electrical resistance of the material and recovery motion. Therefore, it does not account for different loading paths and cycling conditions.
- (G) A linear stage with two accordion spring actuators was designed and fabricated by the wire-EDM method from a commercially available NiTi

ingot. The step response of the accordion spring actuator of the linear stage with one of the springs that were selectively annealed, was studied. It was shown that the spring actuator is capable of generating a several millimeter recovery motion due to the SME.

- (H) A new mathematical model aimed at the evaluation of the evolution of the fraction of the austenite in the SMA material during the temperature-induced phase transformation was developed. The model represents a system of ordinary differential equations that describe the energy balance in the solid NiTi body in different mathematical formulations. The model resulted in an analytical expression that allows the prediction of the amount of the austenite fraction during the temperature-induced phase transformation in NiTi alloys under certain assumptions and limitations. The mathematical model of the kinetics of the austenite phase transformation was experimentally verified using an SMA NiTi wire. The experimental results show an excellent agreement with the mathematical model. The limitation of the model is that it does not account for the microstructural changes in the material and for the presence of different phases that introduce a non-linearity into the relationship between the austenite phase fraction and applied temperature.
- (I) A new mathematical model of motion of the SMA wire and spring based actuators, based on the developed model of the kinetics of phase transformation in SMAs and based on the existing model of motion of a “human muscle”, was suggested. The model was used in modeling the motion of SMA wire and spring actuators and will be applied to the motion control

model of the actuators in future research and needs to be verified experimentally.

11.2 Future work

Future research, as the continuation of the current achievements, should include:

- (A) The manufacture of the SMA mMM as initially proposed in the dissertation. The mMM will contain the accordion spring actuators and the gripper as a monolithic one-piece part requiring no assembly.
- (B) A further modification and advancement of the created DMD technique will be necessary. The technique must allow the creation of thin-wall structures with a better surface finish and the capability of building smaller size features, then those achieved in this study. In order to accomplish this task the following modifications to the fabrication process and equipment are needed:
 - (1) DMD equipment that can generate a higher power laser beam with a spot diameter as small as 200 – 300 μm . The size of the laser beam diameter determines the size of the smallest feature of the fabricated object. Ultimately, the size of the laser beam has to be small enough to be able to create smooth surfaces with a roughness R_a of about 1...2 μm . In this case, the laser beam will have to be ultimately about 1...2 μm in diameter as well. Otherwise, a way of polishing or post-processing the DMD fabricated objects has to be found.

- (2) Based on the analysis of the factorial design of the experiments, conducted in this study, heat sink conditions of the DMD process must be effectively controlled. Therefore, a heat exchanger that allows removal of large amounts of heat, present during the DMD process in the fabricated object, is required. One of the possibilities of increasing the effectiveness of the heat sink exchanger is the use of a two-phase flow heat exchanger.
 - (3) A method that provides an *in-situ* non-destructive inspection of the DMD quality and geometry of the fabricated parts is desirable as well. For example, this can be achieved by optics-based equipment (laser, infrared, etc.) or ultrasound-based methods. Feedback between the results of the *in-situ* measurements and the DMD process is desirable as well.
- (C) Different heating/cooling capabilities of the SMA actuators have to be explored. In this dissertation direct heating (by electrical current) was used in order to actuate the accordion spring actuators. Indirect heating could be more advantageous, since it would allow for a better control of the temperature of the actuators, for example, by means of thin film heaters attached or deposited onto the surface of the actuators. MEMS-based wireless heaters are another option.
- (D) The experimental verification of the model of motion of the SMA wire actuator has been accomplished. Therefore, one of the other major goals of the future initiatives is the development and verification of the mathematical

model of the motion control for the spring actuators, based on the model of motion proposed in this dissertation. The experimental verification should be based on the linear stage with two accordion spring actuators.

(E) The experimental setup for the further verification of both open and closed loop control models of motion should be modified as well. In the experimental setup the intent was to use the voltage drop in the SMA spring (when the spring is heated by applying an electrical current through it) as a feedback parameter. The second option is to use the signal from the LVDT as the feedback signal. In both cases, the experimental setup of the linear stage with the SMA spring actuator did not allow the control of the voltage drop programmatically, since the available DC source did not have an interface, compatible with the data acquisition system (DAQ PSI-6025E). The LVDT measured displacement of the spring actuator could not also be used as a feedback parameter for the same reasons, since the control voltage in both cases (voltage or displacement feedback) had to be adjusted during the data acquisition process according to the feedback signal based law. Therefore, the model of the closed loop controlled motion to be developed should be experimentally verified in the future work, when a programmable DC source will be available.

(F) The present model of the phase transformation kinetics is based on the following basic assumptions: (1) the initial state of the material is martensite, (2) the model describes only the martensite-austenite phase transformation, (3) the model derivation was based on 0-D elementary nodes. Therefore, an

improved model of the phase transformation kinetics should be developed to account for different initial conditions of the material and different thermal load scenarios. The model should account for the non-linearity introduced into the transformation function from different phases (R-phase, twinned martensite) and microstructures (differently oriented grains, etc.) present in the material and should be able to model the phase state of the material under different loading paths conditions (cooling, heating, cycling between the incompletely transformed material).

- (G) The future model should be able to describe the phase transformation process by using 3-D elementary nodes.
- (H) An advanced mathematical model of motion of the SMA spring actuator should be developed based on the mathematical models of motion derived in this dissertation and based on the phase transformation kinetics model described under (F) above. This model should also account for the non-linear behavior of the SMAs in the large-scale motion and should take into consideration the changing working conditions (heat sink, loading history). The model should use a modified expression for the shape memory effect driving force, where the microstructural changes in the material are taken into account (such as grain re-orientation, etc.), thus introducing a non-linearity between the transformation strain and stress into the expression.
- (I) The “self-sensing” principle should be expanded to account for the cycling experimental condition, where the material undergoes heating and cooling loading paths, a mixed phase state (austenite, R-phase, detwinned and

twinned martensite and, changes in the microstructure of the material.

Therefore, the non-linear relationship between the electrical resistivity of the material and recovery displacement should be obtained.

REFERENCES

- Bellouard, Y., Clavel, R., Sidler, T., Gotthardt, R., (2000). "Monolithic Shape Memory Alloys: a Smart Material for the Micro-Factory", 2nd International Workshop on Microfactories, Fribourg, Switzerland, October 9-10, Ed. FSRM, pp. 51 – 54.
- Bekker, A., Brinson, L.C., (1997). "Temperature-Induced Phase Transformation in a Shape Memory Alloy: Phase Diagram Based Kinetics Approach", *Journal of the Mechanics and Physics of Solids*, Vol. 45 (6), pp. 949 – 988.
- Bekker, A., Brinson, L.C., (1998). "Phase Diagram Based Description of the Hysteresis Behavior of Shape Memory Alloys", *Acta Materialia*, Vol. 46, pp. 3649 – 3665.
- Bellouard, Y., Suulzmann, A., Jacot, J., Clavel, R., (1997). "Design and Highly Accurate 3D Displacement Characterization of Monolithic SMA Micro-Gripper Using Computer Vision", *Proceedings of SPIE*, Vol. 3202, pp. 2 – 11.
- Bourell, D. L., Marcus, H.L., Barlow, J.W. and Beaman, J.J., (1992). "Selective Laser Sintering of Metals and Ceramics", *The International Journal of Powder Metallurgy*, Vol.28 (4), pp. 369 – 381.
- Bleuler, H., Clavel, R., Breguet, J.-M., Langen, H., Bellouard, Y., (2001). "Applications of Microrobotics and Microhandling", *RIKEN Review*, Vol. 36, pp. 26 – 28.
- Bram, M., Ahmad-Khanlou, A., Heckmann, A., Fuchs, B., Buchkremer, H.P., and Stover, D., (2002). "Powder Metallurgical Fabrication Processes for NiTi Shape Memory Alloy Parts", *Materials Science and Engineering*, Vol. A337, pp. 254 – 263.
- Brinson, L.C., (1993). "One-Dimensional Constitutive Behavior of Shape Memory Alloys: Thermomechanical Derivation with Non-Constant Material Functions and Redefined Martensite

Internal Variable”, *Journal of Intelligent Materials Systems and Structures*, Vol. 4 (2), pp. 229 – 242.

Brinson, L.C., Bekker, A., and Hwang, S., (1996). “Deformation of Shape Memory Alloys Due to Thermo-Induced Transformation,” *Journal of Intelligent Material Systems and Structures*, Vol. 7, pp. 97 – 107.

Chu, C.L., Chung, C.Y., Lin, P.H., Wang, S.D., (2003). “Fabrication of Porous NiTi Shape Memory Alloy for Hard Tissue Implants by Combustion Synthesis”, *Materials Science and Engineering*, Vol. A 366, pp. 114 – 119.

Cooper, A., (1999). “Fabrication of Ceramic Components using Mold Shape Deposition Manufacturing”, PhD Dissertation, Department of Mechanical Engineering, Stanford University, USA.

Cui Z.D., Man, H.C., Cheng, F.T., Yue, T.M., (2003). “Cavitation Erosion–Corrosion Characteristics of Laser Surface Modified NiTi Shape Memory Alloy”, *Surface and Coatings Technology*, Vol. 162, pp. 147 – 153.

Duerig, T., Pelton, A., Stockel, D., (1999), “An Overview of Nitinol Medical Applications”, *Materials Science and Engineering*, Vol. A 273–275, pp. 149 – 160.

Eggeler, G., Hornbogen, E., Yawny, A., Heckmann, A., Wagner, M., (2004). “Structural and Functional Fatigue of NiTi Shape Memory Alloys”, *Materials Science and Engineering*, Vol. A378, pp. 24 – 33.

Elahinia, M.H., (2001). “Nonlinear Control of a Shape Memory Alloy Actuated Manipulator”, Master Thesis, Mechanical Engineering Department of Villanova University, USA.

Fearon, E., Watkins, K.G., Sharp, M.C., (2004). "Increasing Laser Coupling Using Proactive Layer Height Control In Direct Laser Deposition", Proceedings of the Laser Assisted Net Shape Engineering 4, M. Geiger and A. Otto, (eds.), pp. 511 – 521.

Franklin, G.F., Powell, J.D., Emami-Naeini, A., (2002). "Feedback Control of Dynamic Systems", Prentice-Hall, Upper Saddle River: New Jersey, 910 p.

Fu, Y., Huang, W., Du, H., Huang, X., Tan, J., Gao, X., (2001). "Characterization of TiNi shape-Memory Alloy Thin Films for MEMS Applications", Surface Coatings and Technology, Vol. 145, pp. 107 – 112.

Furuya, Y., (2000). "Rapid-Solidified Metallic Actuator Materials Developed by Electromagnetic Nozzleless Melt Spinning Method", Material Research Society Symposium Proceedings, Vol. 604, pp. 109 – 116.

Gall, K., Maier, H.J., (2002). "Cyclic Deformation Mechanisms in Precipitated NiTi Shape Memory Alloys", Acta Materialia, Vol. 50, pp. 4643 – 4657.

Gall, K., Sehitoglu, H., Anderson, R., Karaman, I., Chumlyakov, Y. I., Kireeva, I. V., (2001). "On the Mechanical Behavior of Single Crystal NiTi Shape Memory Alloys and Related Polycrystalline Phenomenon", Materials Science and Engineering, Vol. A 317, pp. 85 – 92.

Griffith, M. L., Keicher, D. M., Atwood, C. L., Romero, J. A., Smugeresky, J. E., Harwell, L. D., Greene, D. L., (1996). "Free Form Fabrication of Metallic Components Using Laser Engineered Net Shaping (LENS®)", Proceedings of the Solid Freeform Fabrication Symposium, p. 125.

Grigoriev, Y.I., Cykhotsky, V.M., Sementsov, A.N., Prokhorov, Y.M., Gorbenko, G.A., Malukhin, C.A., (1999). "Two-Phase Central Thermal Control System (TPS) of International Space Station "ALPHA" Russian Segment", Thermal and Fluid Analysis Workshop (TFAWS-

98) Proceedings, NASA Lewis Research Center, Cleveland, Ohio, August 30 - September 3, 1998 USA, pp. 69 – 81.

He Z., Gall K.R., Brinson, L.C., (2006). “Use of Electrical Resistance Testing to Redefine the Transformation Kinetics and Phase Diagram for Shape-Memory Alloys”, *Metallurgical and Material Transactions A*, 37 A, pp. 579 – 587.

Hu, Y.P., Chen, C.W., Mukherjee, K., (1998). “Development of New Laser Cladding Process for Manufacturing Cutting and Stamping Dies”, *Journal of Materials Science*, 33, pp. 1287 – 1292.

Huang, W., (1998). “Shape Memory Alloys and Their Application to Actuators for Deployable Structures”, PhD Dissertation, Engineering Department, Cambridge University, England.

Ikuta, K., Tsukamoto, M., Hirose, S., (1988). “Shape Memory Alloy Servo Actuator System With Electric Resistance Feedback and Application for Active Endoscopes”, *Proceedings of the 1988 IEEE International Conference on Robotics and Automation*, Vol.1, pp. 427 – 430.

Ikuta, K., Tsukamoto, M., Hirose, S., (1991). “Mathematical Model and Experimental Verification of Shape Memory Alloy for Designing Micro Actuator”, *An Investigation of Micro Structures, Sensors, Actuators, Machines, and Robots*, NARA Proceedings, pp. 103-118.

Incropera, F.P., Dewitt D.P., (2002). “Fundamentals of Heat and Mass Transfer”, 5th ed. New York: Wiley, 981 p.

Irving, R., (1999). “Taking a Powder”. *Mechanical Engineering*, <http://www.memagazine.org/>.

Kalpakjian, S., and Schmid, S.R., (2006). “Manufacturing Engineering and Technology”, 5th ed., Pearson/Prentice Hall, Upper Saddle River: New Jersey, 1295 p.

Kathuria, Y.P., (1999). "3D Microstructuring by Selecting Laser Sintering/Micro-Cladding of Metallic Powder", Proceeding of SPIE – The International Society for Optical Engineering, Vol. 3822, pp. 103-109.

Kaviany, M., (2002). "Principles of Heat Transfer", New York: Wiley, 973 p.

Kennedy, D.K., Straub, F.K., Schetky, K McD., Chaudhry Z., (2000). "Development of a SMA Actuator for In-Flight Rotor Blade Tracking. Smart Structures and Materials 2000: Smart Structures and Integrated Systems", Norman M. Wereley, Ed., Proceedings of SPIE, Vol. 3985, pp. 62 – 79.

Kobryn, P.A., Moore E.H. and Semiatin, S.L., (2000). "The Effect of Laser Power and Traverse Speed on Microstructure, Porosity, and Build Height in Laser-Deposited Ti-6Al-4V", Scripta Materialia, Vol. 43, pp. 299 – 305.

Kohl, M., Krevet, B., Just, E., (2002). "SMA Microgripper System", Sensors and Actuators A, Vol. 97-98, pp. 646 – 652.

Kota, S., (2001). "Compliant Systems using Monolithic Mechanisms", Smart Material Bulletin: An International Newsletter, pp.7 – 10.

Kovacevic, R., (2005). <http://engr.smu.edu/rcam/rcamweb/index.htm>.

Kuribayashi, K., (2000). "Micro SMA Actuator and Motion Control", 2000 International Symposium on Micromechatronics and Human Science Proceedings, pp. 35 – 42.

Labudovic, M., Hu, D., Kovacevic, R., (2003). "A Three Dimensional Model for Direct Laser Metal Powder Deposition and Rapid Prototyping", Journal of Materials Science, Vol. 38, pp.35 – 49.

Lee, H.J., Lee, J.J., Kwon, D.S. and Yoon, Y.S., (2001). “Neural Network Based Control of SMA Actuator For The Active Catheter”, HWRS-ERC Proceedings, Vol. 2 (2), pp. 40 – 45.

Lei, K.-F., Yam, Y., (2000). “Modeling and Experimentation of a Positioning System of SMA wires”, Proceedings of the SPIE - The International Society for Optical Engineering, Vol. 3986, pp. 208 – 219.

Lewis, G. K., Schlienger, E., (2000). “Practical Considerations and Capabilities for Laser Assisted Direct Metal Deposition”, Materials and Design, Vol. 21 (4), pp. 417 – 423.

Liang, C., (1990). “The Constitutive Modeling of Shape Memory Alloys”, PhD Dissertation, Blacksburg, Virginia, USA.

Liang, C. and Rogers, C.A., (1990). “One-Dimensional Thermomechanical Constitutive Relations for Shape Memory Materials”, Journal of Intelligent Materials Systems and Structures, Vol. 1 (2), pp. 207 – 324.

Liang, C., Rogers, C.A., (1992). “A Multi-Dimensional Constitutive Model for Shape Memory Alloys”, Journal of Engineering Mathematics, Vol. 26, pp. 429 – 443.

Lind, R.J., Johnson, N., Doumanidis, C.C., (2000). “Active Deformable Sheets: Prototype Implementation, Modeling, and Control”, Proceedings of the SPIE - The International Society for Optical Engineering, Vol. 3985, pp. 572 – 582.

Liu, Y., Xie, Z., (2003), “TEM in situ study of the pre-strained NiTi shape memory alloy—driving force for shape recovery?”, Materials Science and Engineering, vol.A361, (1-2), pp. 185-190.

Mah, R., (1997). "Direct Light Fabrication", *Advanced Materials & Processes*, 151 (3), pp. 31 – 33.

Mazumder, J., Schiffer, A., Choi, J., (1999). "Direct Materials Deposition: Designed Macro and Microstructure", *Materials Research Innovations*, Vol. 3 (3), pp. 118 – 131.

Milewski, J.O., Lewis, G.K., Thoma, D.J., Keel, G.I., Nemec, R.B., Reinert, R.A., (1998). "Directed Light Fabrication of a Solid Metal Hemisphere Using 5-axis Powder Deposition", *Journal of Materials Processing Technology*, Vol. 75, pp. 167 – 172.

Miller, L.E., (1984). "Reflex Stiffness of the Human Wrist", M.S. Thesis, Department of Physiology, Northwestern University, Evanston, IL, USA.

Miyazaki, S., Otsuka, K., (1986). "Deformation and Transition Behavior Associated with the R-Phase in TiNi alloys", *Metallurgical Transactions A*, Vol. 17 A, pp. 53 – 63.

Mizar, S.P., Pech-Canul, M.I., Pryputniewicz, R.J., (2000). "Characterization of NiTi Materials Using a Novel ACES Methodology", *Material Research Society Symposium Proceedings*, Vol. 604, pp. 99 – 104.

Montgomery, D.C., (2001). "Design and Analysis of Experiments", John Wiley & Sons, Hoboken: New Jersey, 684 p.

Odonnchadha, B., Tansey, A., (2004). "A Note on Rapid Composite Tooling by Selective Laser Sintering", *Journal of Materials Processing Technology*, Vols. 153 – 154, pp. 28 – 34.

Otsuka, K., and Ren, X., (1999). "Recent Development in the Research of Shape Memory Alloys", *Intermetallics*, Vol. 7, pp. 511 – 528.

Otsuka, K., and Ren, X., (2002). "Factors Affecting the M_s Temperature And Its Control in Shape Memory Alloys", *Materials Science Forum*, Vol. 394 – 395, pp. 177 – 184.

Otsuka, K., and Wayman, C.M., (1998). "Shape Memory Materials", Cambridge University Press: New York, pp. 284.

Peirs, J., Reynaerts, D. and Brussel, H., (2001). "The 'True' Power of SMA Micro-Actuation", Proc. MME 2001 (Micromechanics Europe Workshop), pp. 217 – 220.

Perkins, J. and Hodgston, D., (1998). "The Two-Way Shape Memory Alloy Effect", Engineering Aspects of Shape Memory Alloys, Duerig T.W. et al., (eds.), Butterworth-Heinemann, pp. 195 – 206.

Petzoldt, F., Greul, M., Greulich, M., (1997). "Functional Components and Molds Produced by Laser Sintering", Advances in Powder Metallurgy & Particulate Materials – Proceedings of the 1997 International Conference on Powder Metallurgy & Particulate Materials, pp. 21-61 – 21-66.

Rajagopalan, S., Little, A.L., Bourke R., M. A. M., Vaidyanathan, R., (2005), "Elastic modulus of shape-memory NiTi from in situ neutron diffraction during macroscopic loading, instrumented indentation, and extensometry", Applied Physics Letters, 86, pp. 081901-1 - 081901-3.

Ren, X., and Otsuka, K., (2000). "Why Does the Martensitic Transformation Temperature Strongly Depend on Composition?", Materials Science Forum, Vol. 327-328, pp. 429 – 432.

Roch, I., Bidaud, P., Collard, D., Buchaillot, L., (2003). "Fabrication and Characterization of an SU-8 Gripper Actuated by a Shape Memory Alloy Thin Film", Journal of Micromechanics and Microengineering, Vol. 13, pp. 330 – 336.

Rocher, P., Medawar, L. El, Hornez, J.-C., Traisnel, M., Breme, J., Hildebrand, H.F., (2003). "Biocorrosion and Cytocompatibility Assessment of NiTi Shape Memory Alloys", Scripta Materialia, Vol. 50, pp. 255 – 260.

Ready, J. F. (ed.), (2001). "LIA Handbook of Laser Materials Processing", Magnolia Publishing, Orlando, FL: Laser Institute of America, 715 p.

Shestakov, N. I., and Shichkov A. N, (1984). "Heat Transfer from the Molten Pool to the Solid Phase in Continuous Casting", *Izvestiya Akademii Nauk SSSR, Metally*, Vol. 3, pp. 85 – 87.

Sittner, P., Stalmas, R., Tokuda, M., (2000). "An Algorithm for Prediction of the Hysteretic Responses of Shape Memory Alloys", *Smart Materials and Structures*, Vol. 9, pp. 452 – 465.

Smugersky, J.E., Keicher, D.M., Romero, J.A., Griffith, M.L. and Harwell, L.D., (1997). "Laser Engineered Net Shaping (LENS) Process: Optimization of Surface Finish and Microstructural Properties", *Advances in Powder Metallurgy and Particulate Materials*, Vol. 3, pp. 21.33 – 21.42.

Tanaka, K. and Nagaki, S., (1982). "A Thermomechanical Description of Materials with Internal Variables in the Process of Phase Transitions", *Ing. Arch.*, 51, pp. 287 – 299.

Tohyama, O., Maeda, S., Abe, K., Murayama, M., 2001. "Shape Memory Alloy Actuators and Their Reliability", *Proceedings of the SPIE - The International Society for Optical Engineering*, Vol. 4592, pp. 111 – 118.

Uchil, J., Ganesh, K. K., Mahesh K.K., (2002). "Simple Thermal Actuator Using R-phase Transformation of NITINOL", *Proceedings of the SPIE - The International Society for Optical Engineering*, Vol. 4701, pp. 435 – 442.

Van't Land, C.M., (2005). "Industrial Crystallization of Melts", Marcel Dekker: New York, 320 p.

Wessel, J. K., (2004). "Handbook of Advanced Materials: Enabling New Designs", J. Wiley, Hoboken: New Jersey, 645 p.

Williams, J. M., Adewunmi, A., Schek, R. M., Flanagan, C. L., (2005). “Bone Tissue Engineering Using Polycaprolactone Scaffolds Fabricated via Selective Laser Sintering”, *Biomaterials*, Vol. 26, pp. 4817 – 4827.

Wu, X.D., Fan, Y.Z., Wu, J.S., (2000). “A Study on the Variations of the Electrical Resistance for NiTi Shape Memory Alloy Wires During the Thermomechanical Loading”, *Materials & Design*, Vol. 21 (6), pp. 511 – 515.

Wu C.H., Houk J.C., Young K.-Y., Miller, L.E., (1990). “Nonlinear Damping of Limb Motion”, Winters J.M., and Woo S.L-Y. (eds.), *Multiple Muscle Systems: Biomechanics and Movement Organization*, Springer-Verlag, New York, 801 p.

Wu, X.D., Sun, G.J., Wu, J.S., (2003), “The nonlinear relationship between transformation strain and applied stress for nitinol”, *Materials Letters*, Vol. 57, pp. 1334–1338.

Wuttig, M., Quandt, E., Ludwig, A., Winzek, B., (1999). “Shape Memory and Magnetostrictive Materials for MEMS”, *Materials Science of Microelectromechanical Systems (MEMS) Devices*, pp. 145 – 151.

Yi, H.C., and Moore, J.J, (1988). “A Novel Technique for Producing NiTi Shape Memory Alloy Using the Thermal Explosion Mode of Combustion Synthesis”, *Scripta Metallurgica*, Vol. 22, pp. 1889 – 1892.

Zhang, H., Burdet, E., Hutmacher, D. W., Poo, A.-N., Bellouard, Y., Clavel, R., Sidler, T., (2002). “Robotic Micro-Assembly of Scaffold/Cell Constructs With a Shape Memory Alloy Gripper”, *Proceedings of 2002 IEEE International Conference on Robotics & Automation*, pp. 1483 – 1488.

www.azom.com

www.wtec.org

www.optomec.com/html/aerospace-ro.htm
www.ca.sandia.gov/.../content.php?cid=50
www.rpmandassociates.com/index_files/Page1557.htm
mfgshop.sandia.gov/1400_ext_LENS.htm
<http://www.huffmancorp.com/>
<http://www.lasercladding.com/>
www.esi.com
www.arpotech.com.au/slshelp.htm
www.trumpf.com/3.laserforming_proc_main.html
www.twi.co.uk/j32k/getFile/dmd_index.html
www.crumetals.com (Crucible Specialty Metals)

APPENDIX A

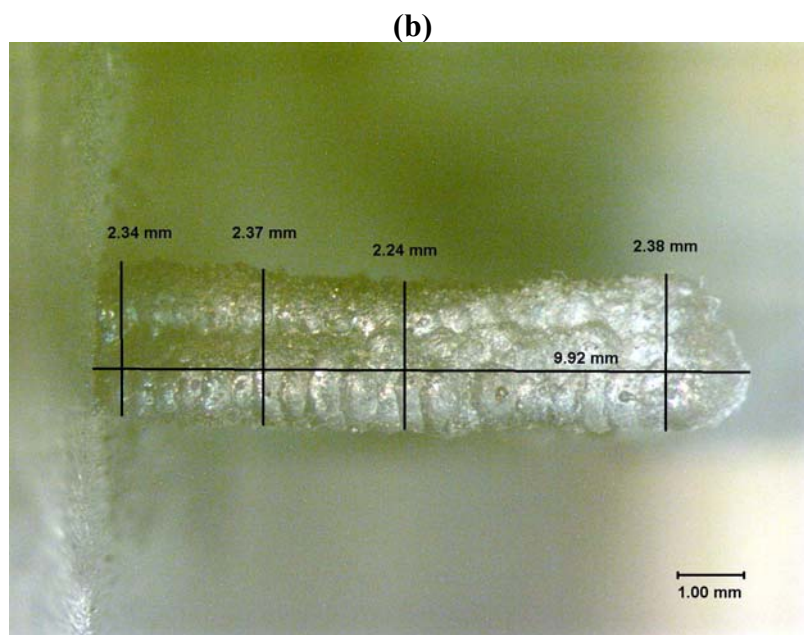
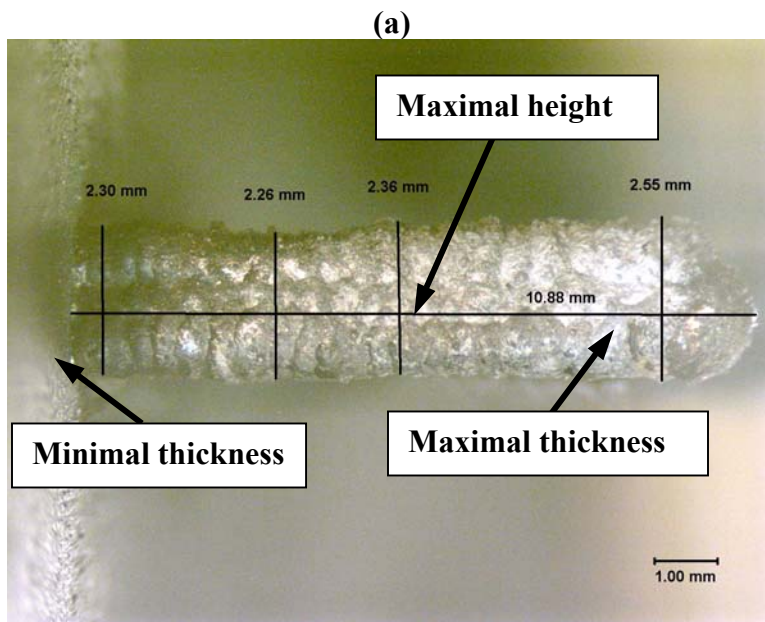
Geometry of the vertical walls fabricated by DMD from NiTi powder during the factorial design of experiments.

Figures A.1-A.6 show optical microscope measurements of the geometry of NiTi vertical walls built by DMD. Height, thickness, width and other geometrical parameters were measured. The heights and thicknesses of all walls are shown in Figures A.1, A.2, A.3 and A.4. They were measured at the points where the magnitudes of the heights are maximal, and the magnitudes of the widths are minimal and maximal as shown in Fig. A.1a and Fig. A.3a. Measurements of the widths at the intermediate points between their maximal and minimal values in all the walls were also performed. The magnitudes of the measured heights at the intermediate points are shown in Figs. A.5 and A.6.

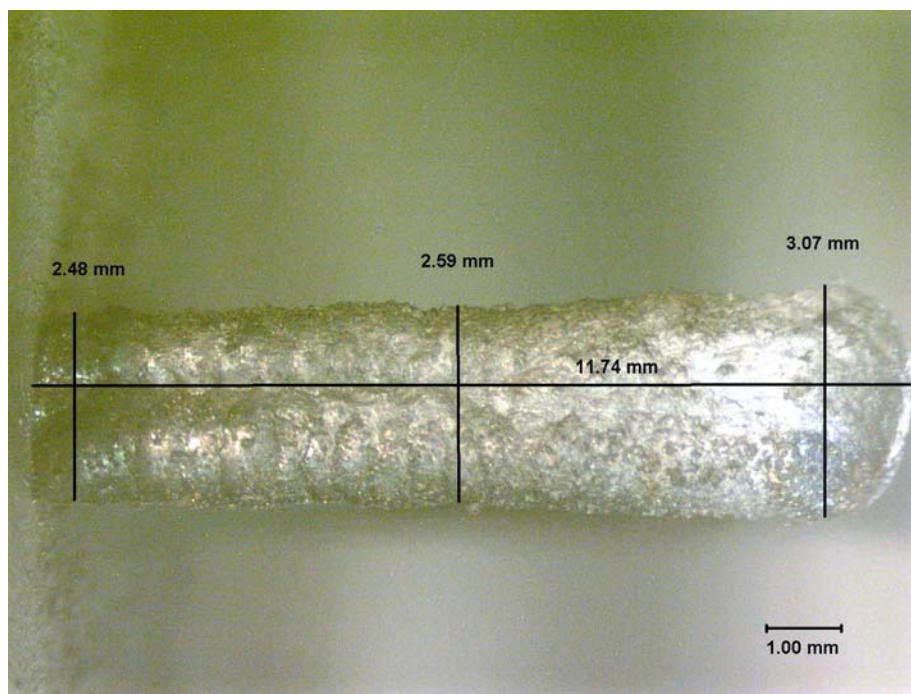
All the measurements were done to conduct a statistical analysis. The statistical analysis was aimed at the estimation of the influence of three factors (laser power, powder feeding rate and coolant flow rate) in the factorial design of experiments in Chapter 3. Based on the statistical analysis, it was concluded, that the most influential factor affecting wall geometry in a DMD process is the magnitude of the laser power.

The influence of the powder flow rate and the coolant flow rate on the geometry varied with the walls' height. For example, at the very bottom of a wall at the substrate, the coolant flow rate's influence on wall geometry was maximal. Larger magnitudes of the coolant rate

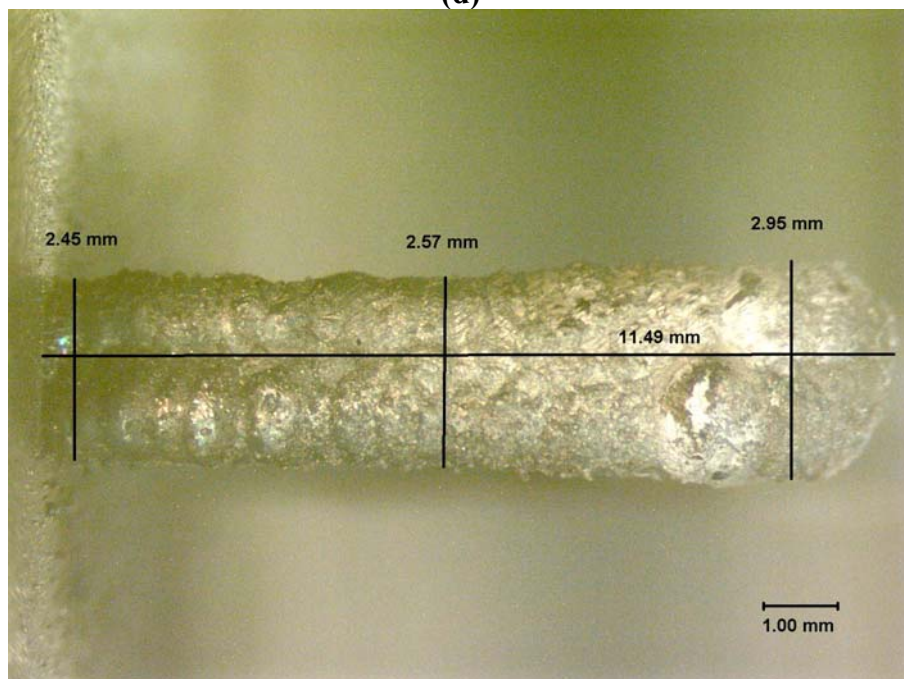
provided thinner walls due to the improved heat sink conditions at the substrate. The corresponding plots that show this influence are given in Chapter 3 and Appendices B and C.



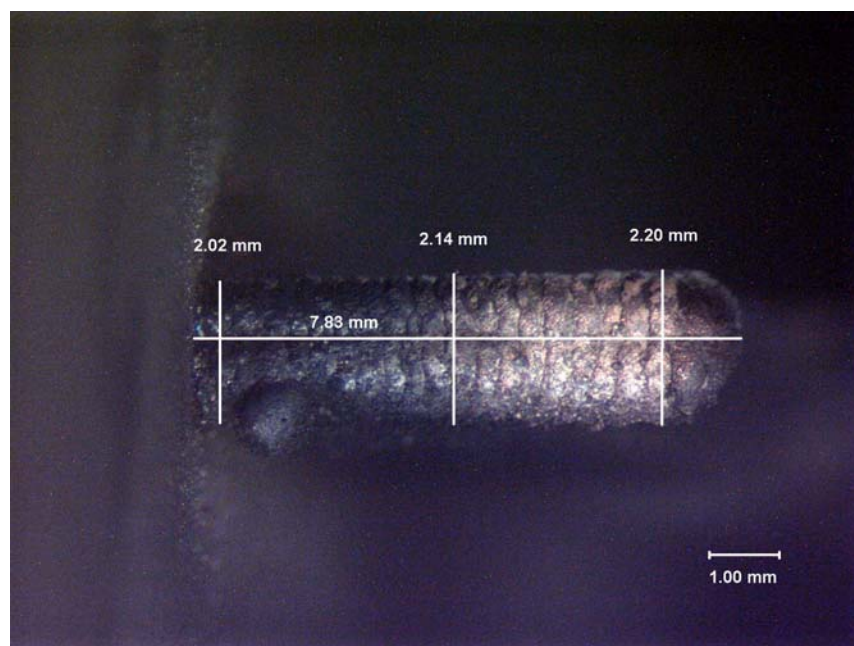
(c)



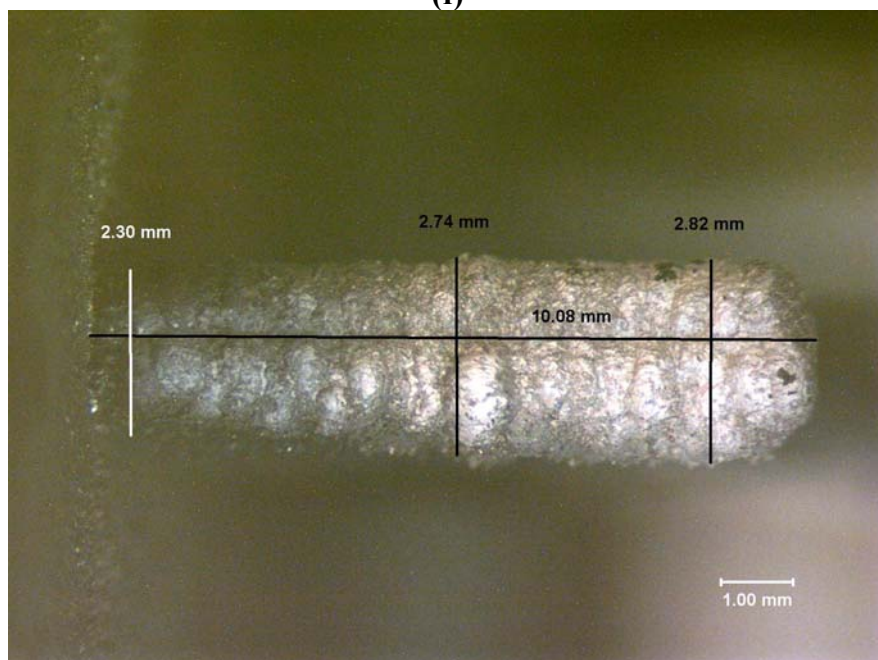
(d)



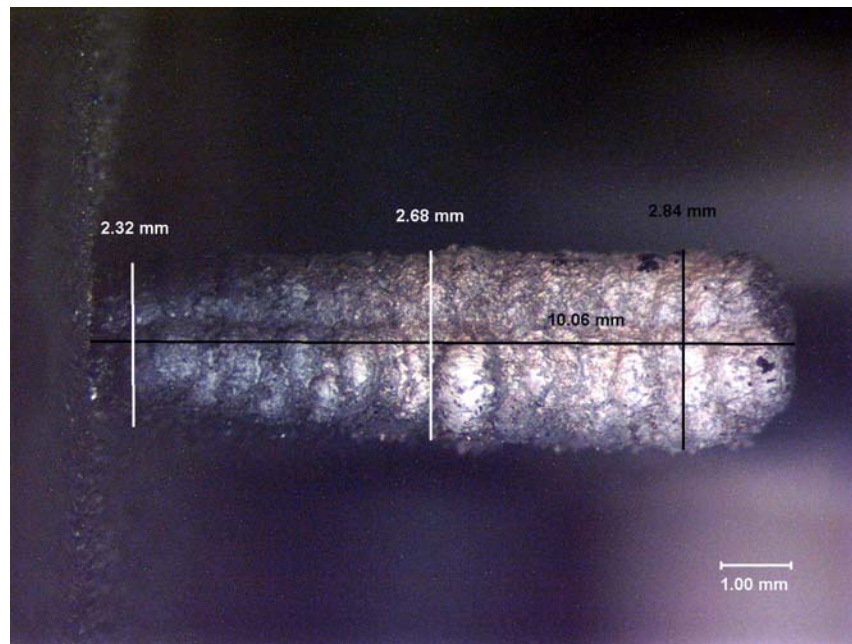
(e)



(f)



(g)



(h)

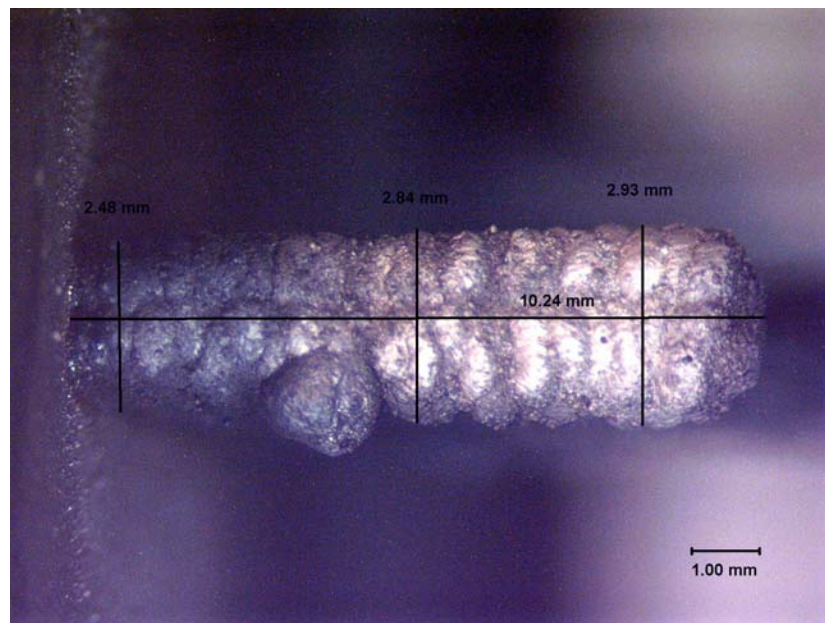
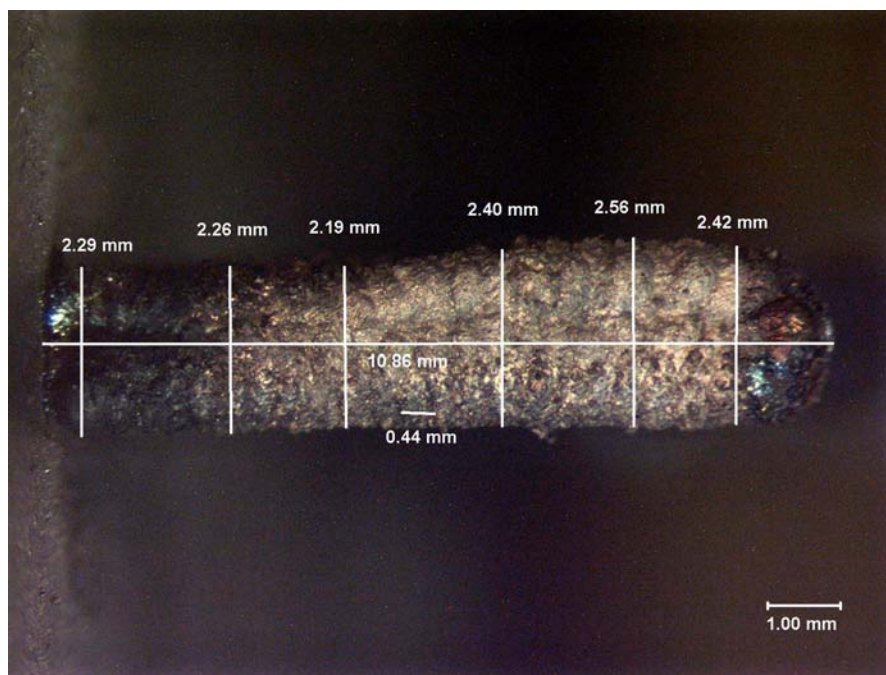
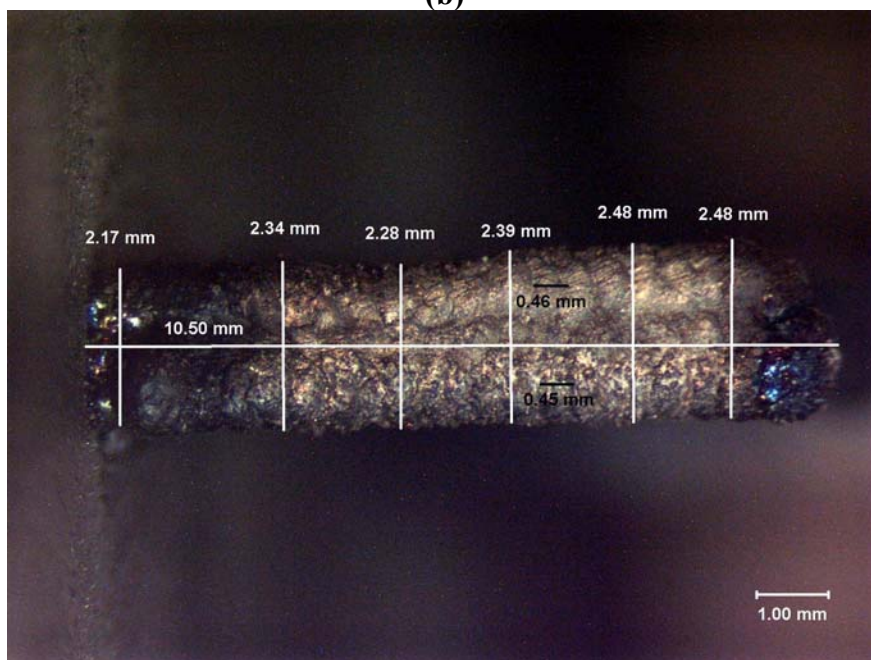


Figure A.1: Side view of DMD built NiTi vertical walls from Batch #1: (a) wall 1, (b) wall 2, (c) wall 3, (d) wall 4, (e) wall 5, (f) wall 6, (g) wall 7, (h) wall 8

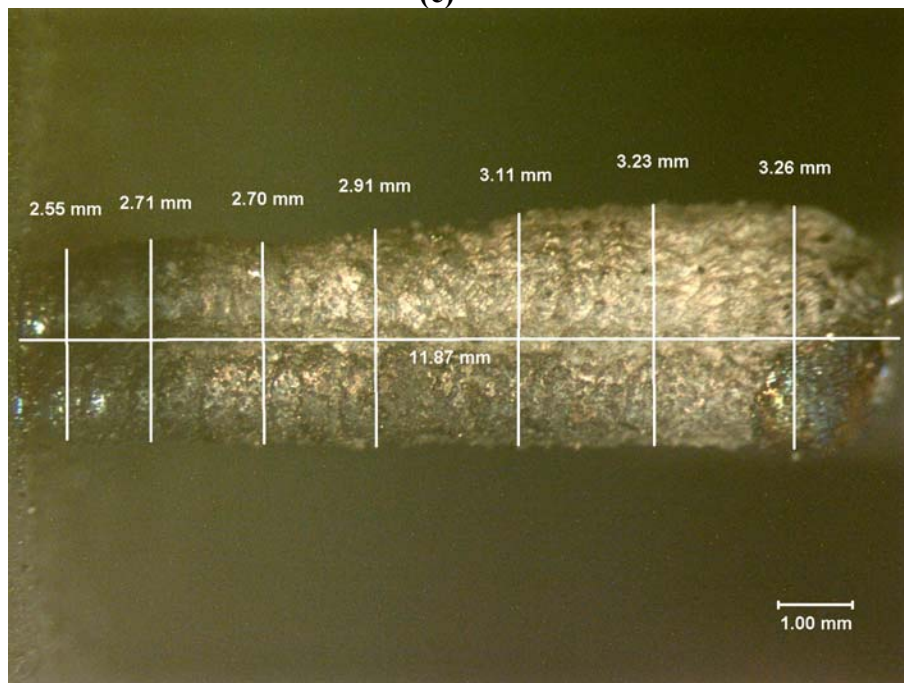
(a)



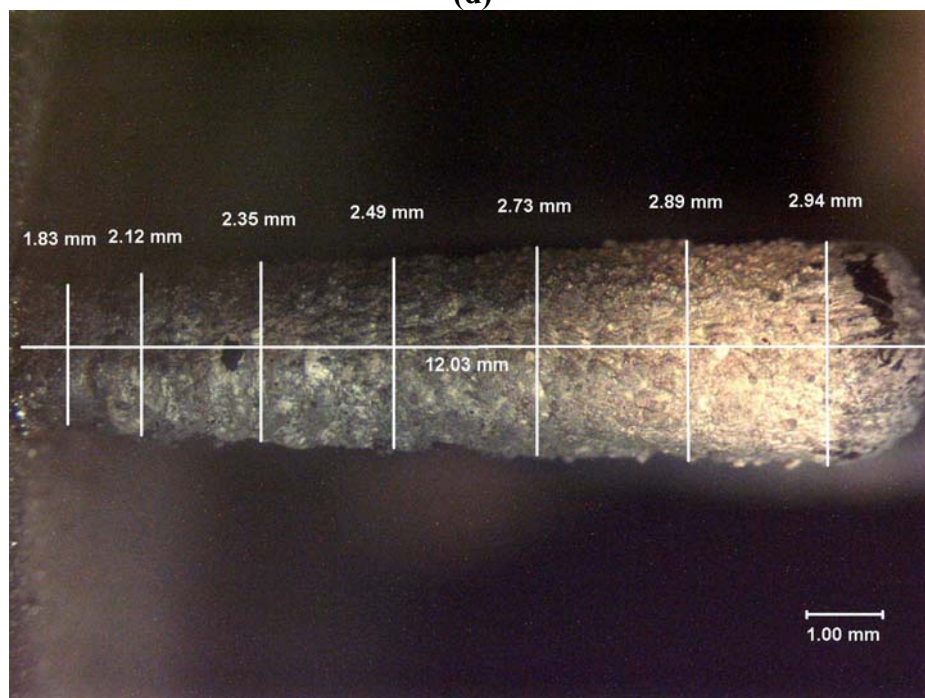
(b)



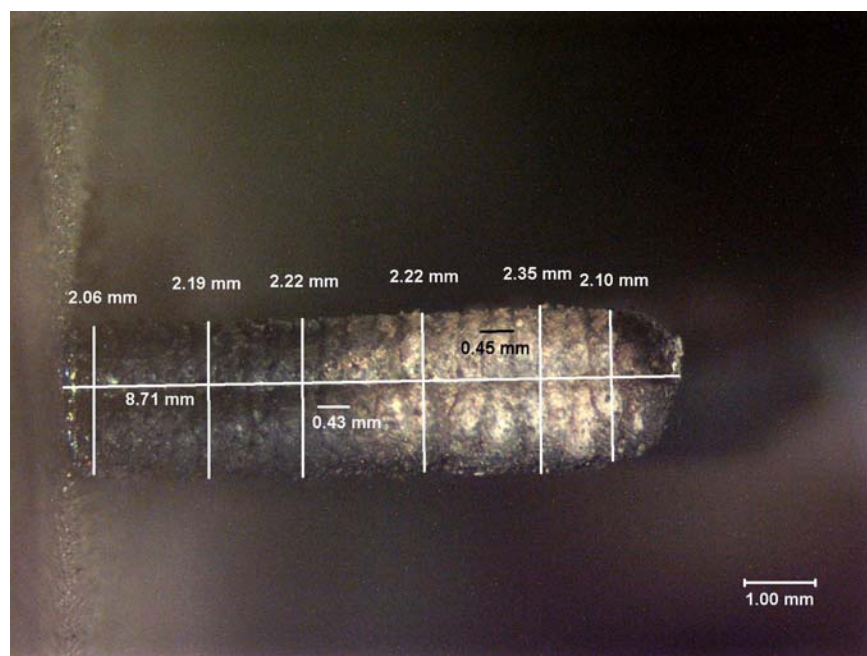
(c)



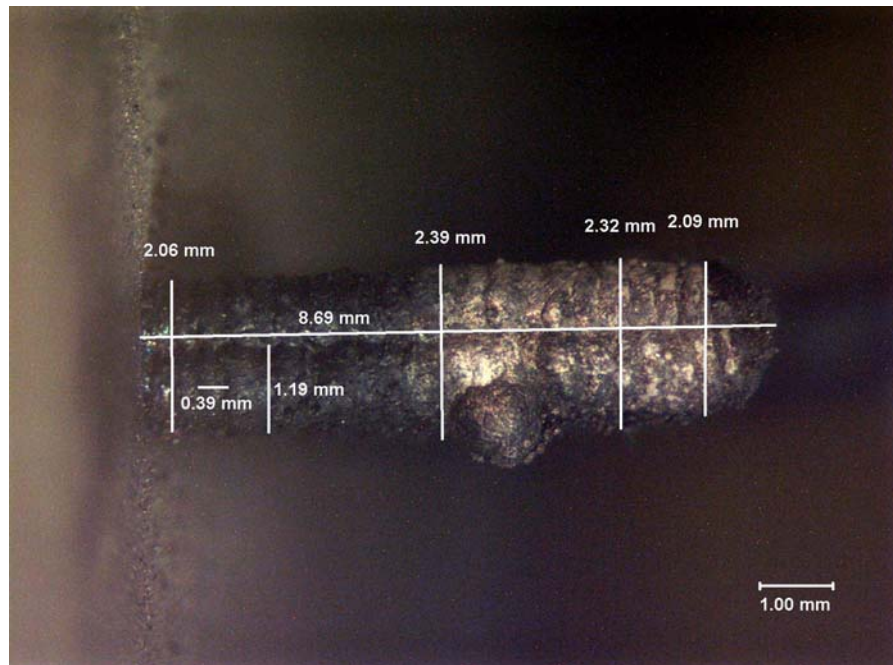
(d)



(e)



(f)



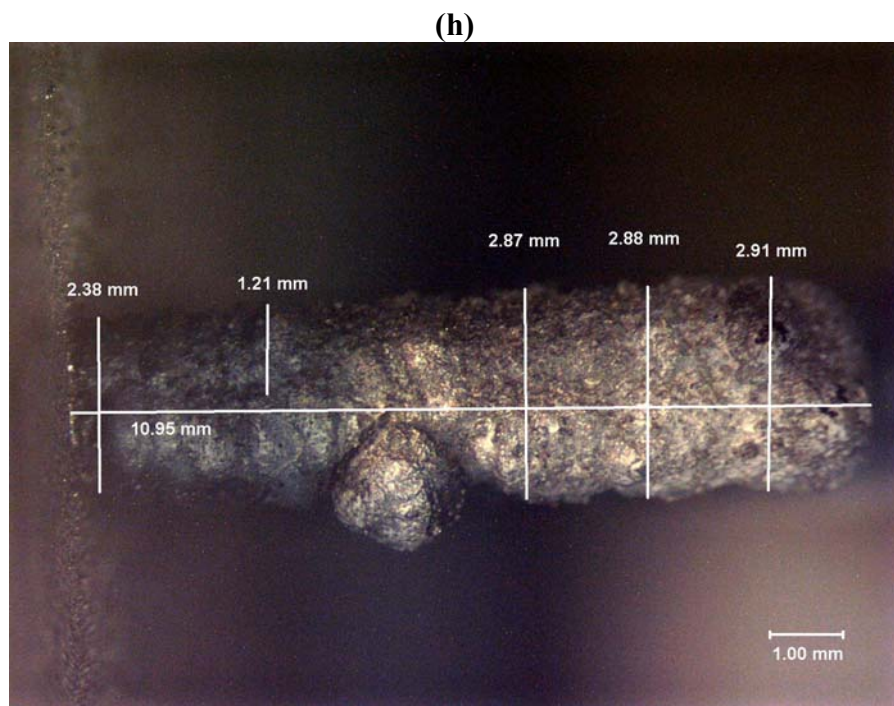
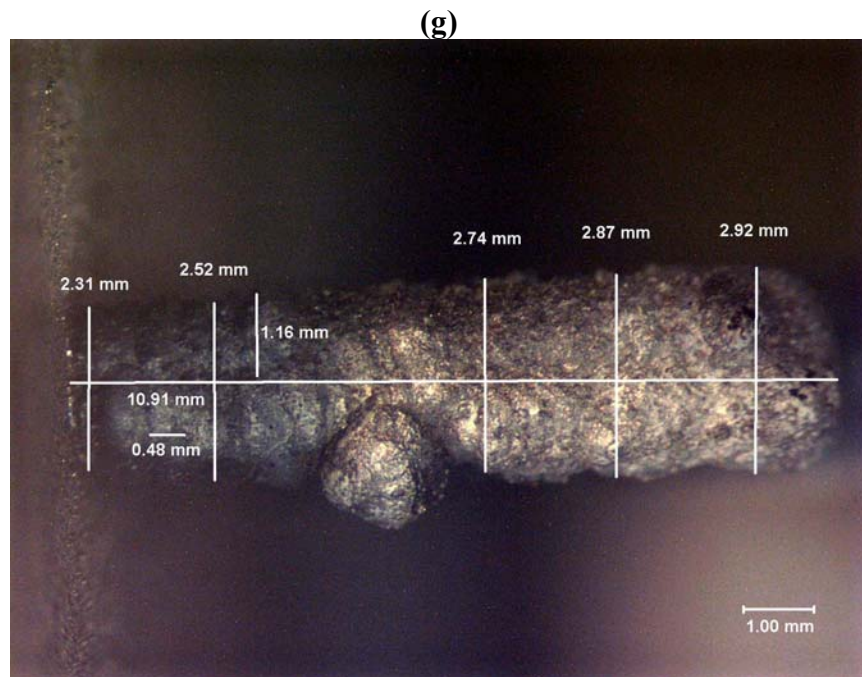
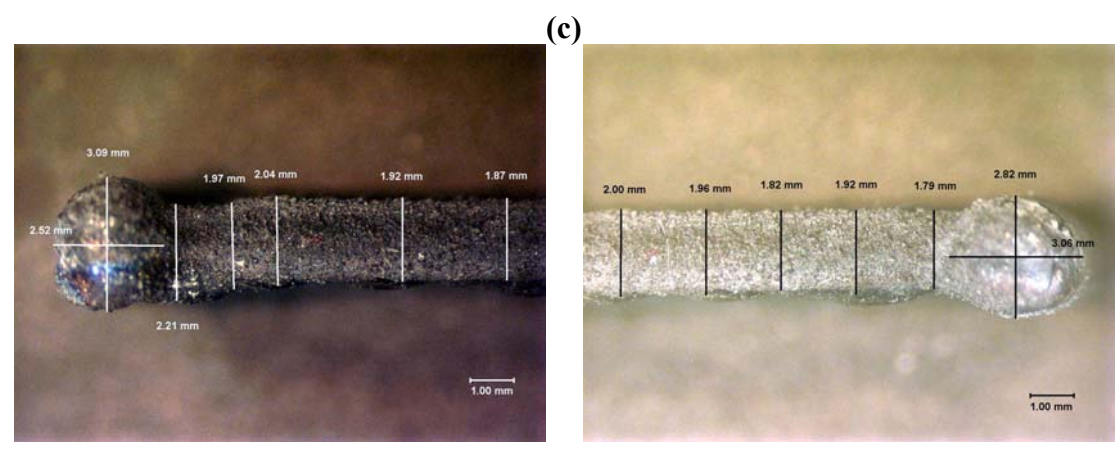
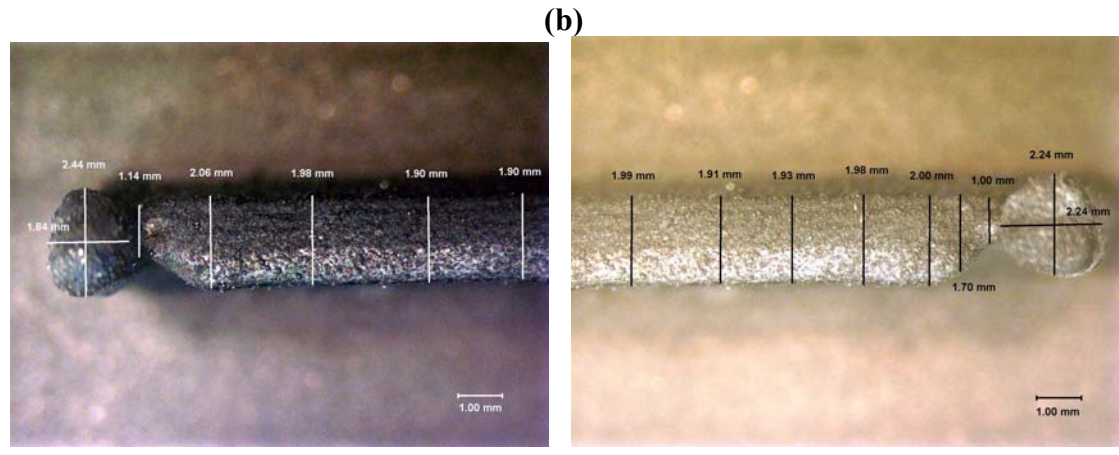
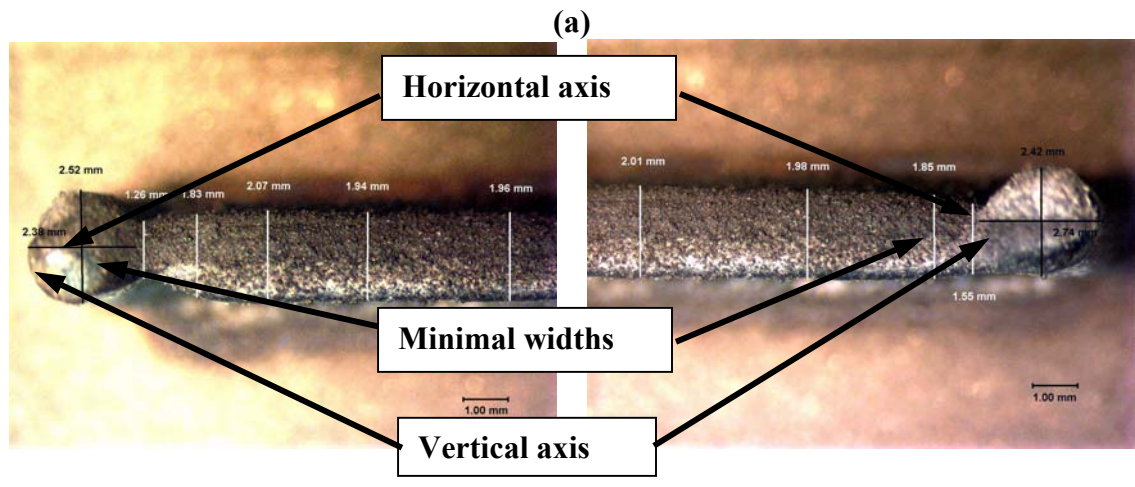
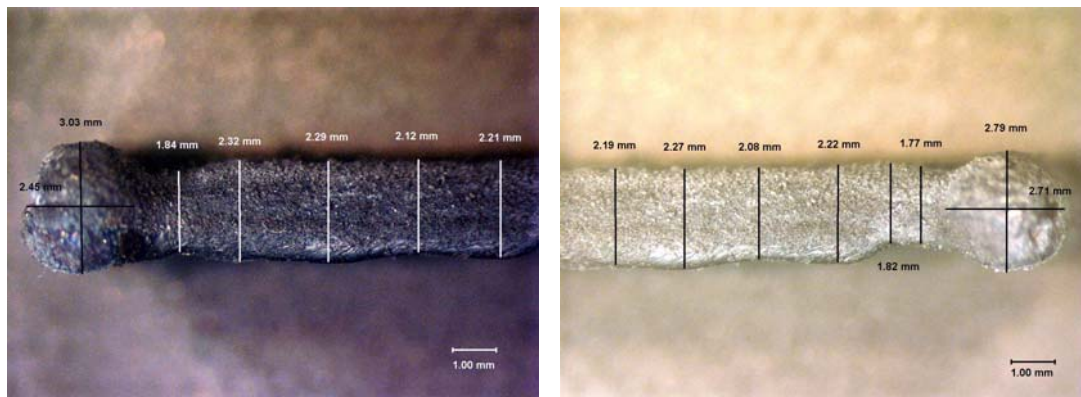


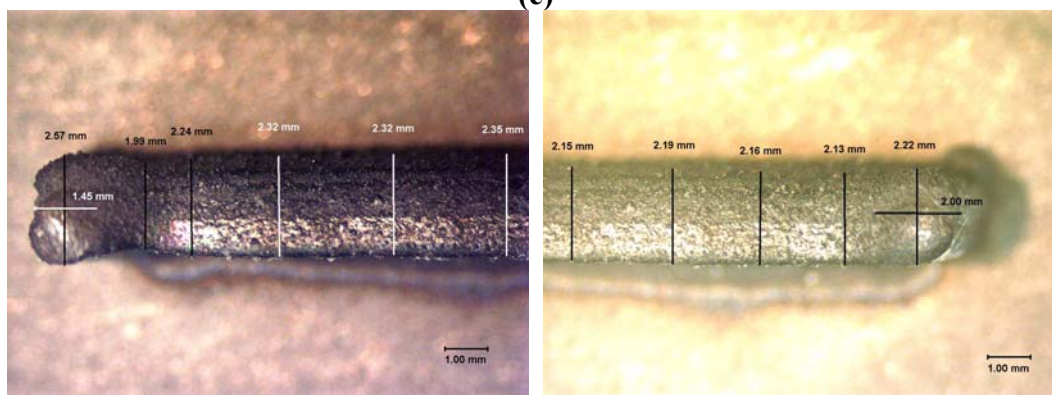
Figure A.2: Side view of DMD built NiTi vertical walls from Batch #2: (a) wall 1, (b) wall 2, (c) wall 3, (d) wall 4, (e) wall 5, (f) wall 6, (g) wall 7, (h) wall 8



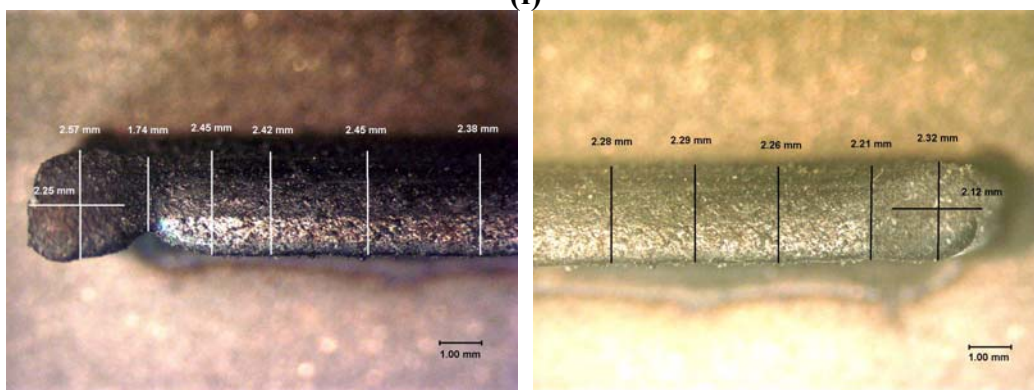
(d)



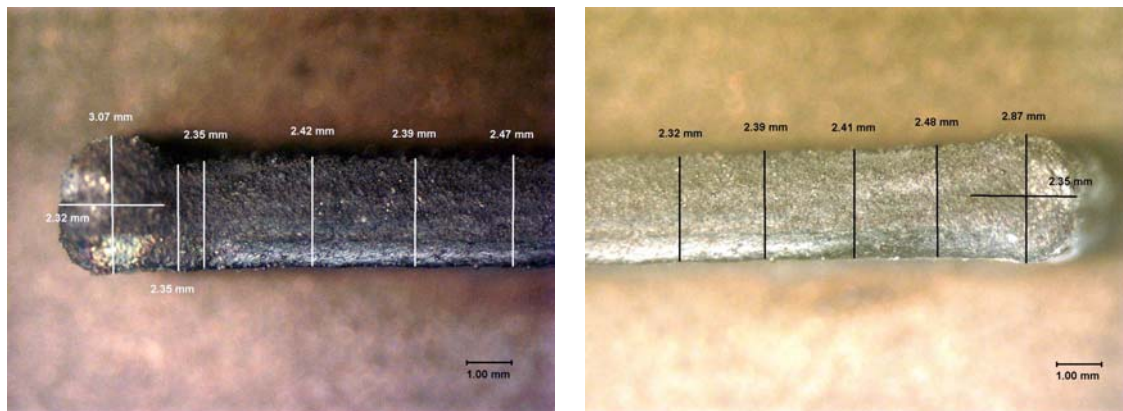
(e)



(f)



(g)



(h)

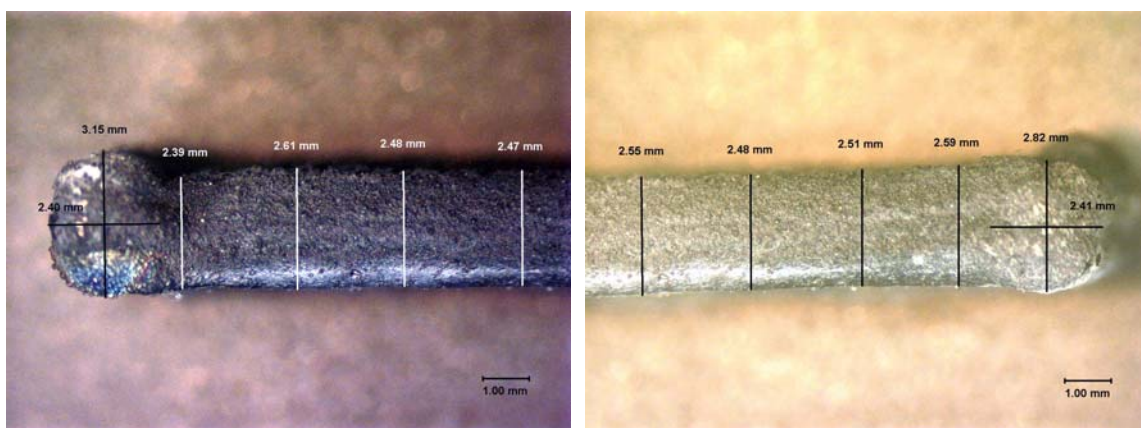
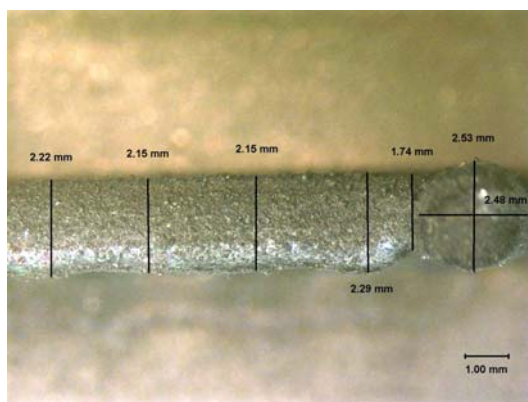
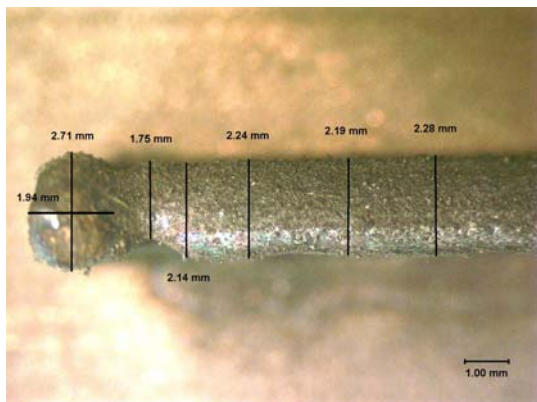
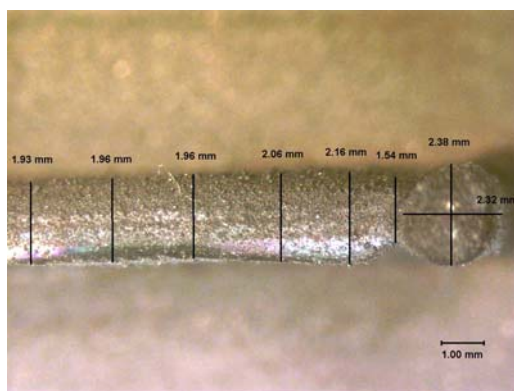
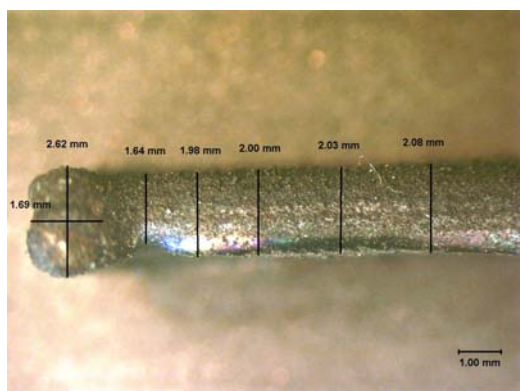


Figure A.3: Top view of DMD built NiTi vertical walls from Batch #1, left- and right- hand side: (a) wall 1, (b) wall 2, (c) wall 3, (d) wall 4, (e) wall 5, (f) wall 6, (g) wall 7, (h) wall 8

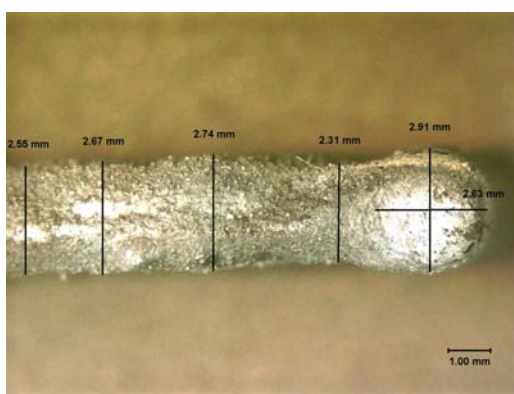
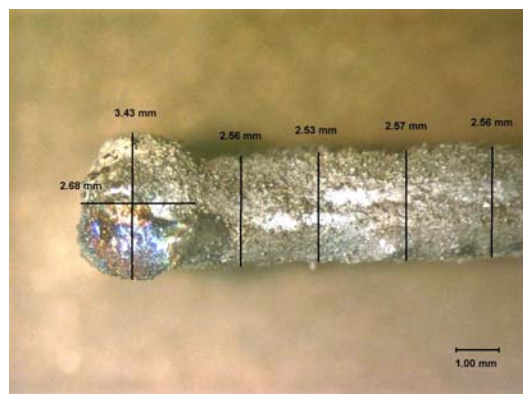
(a)



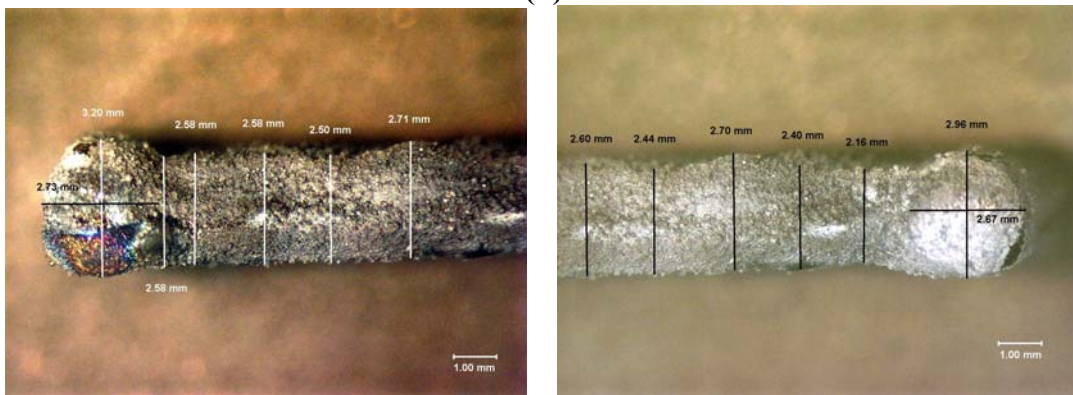
(b)



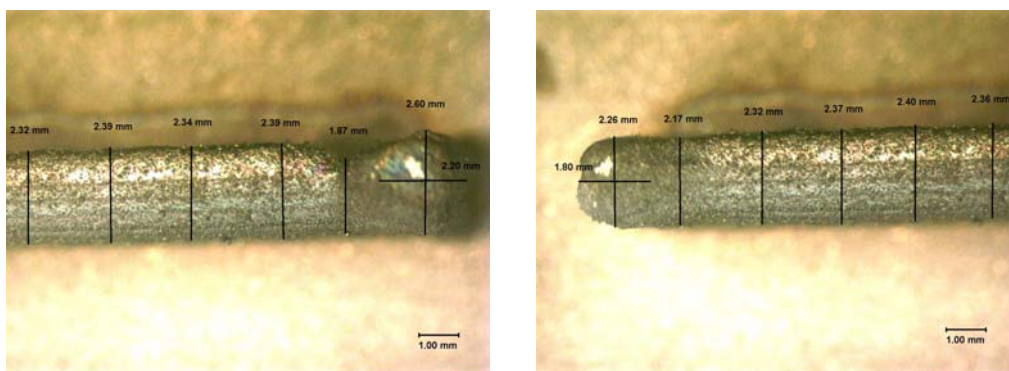
(c)



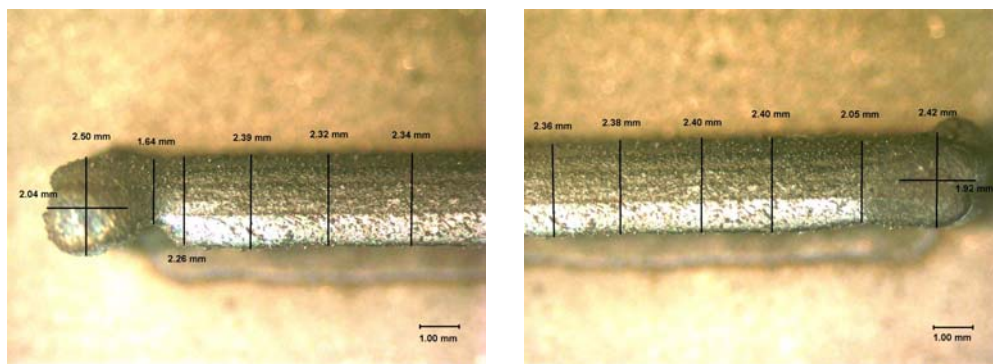
(d)



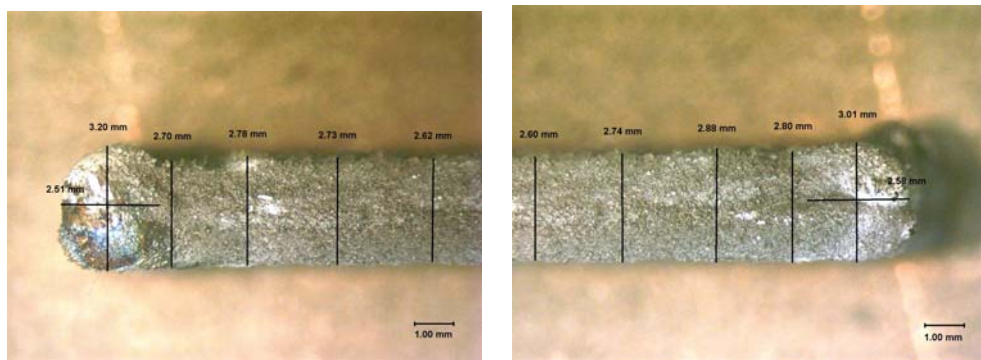
(e)



(f)



(g)



(h)

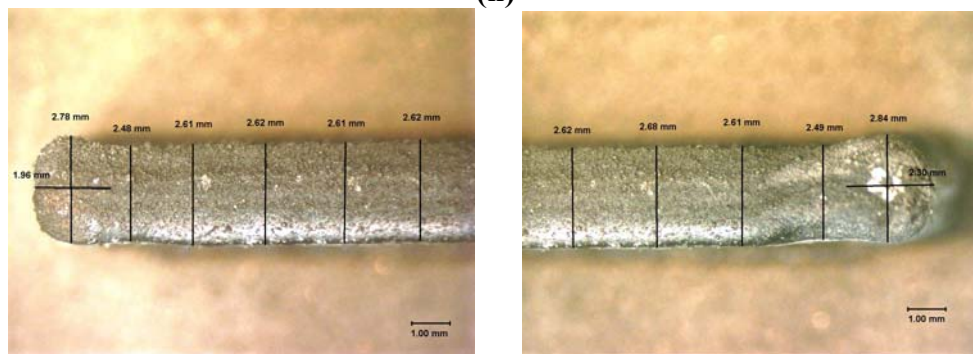
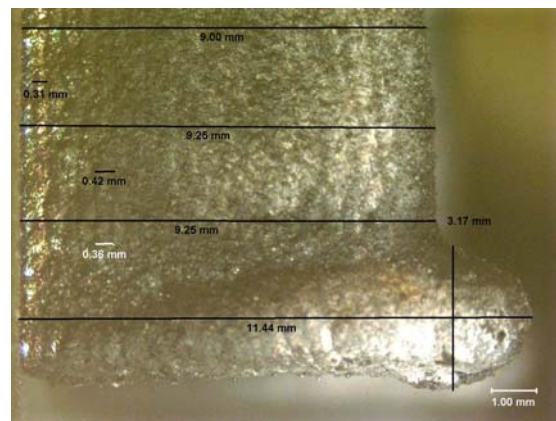
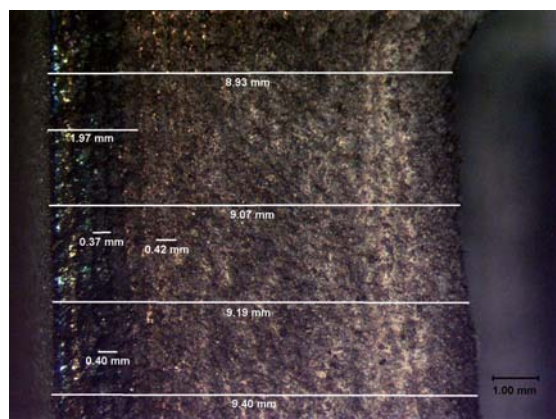
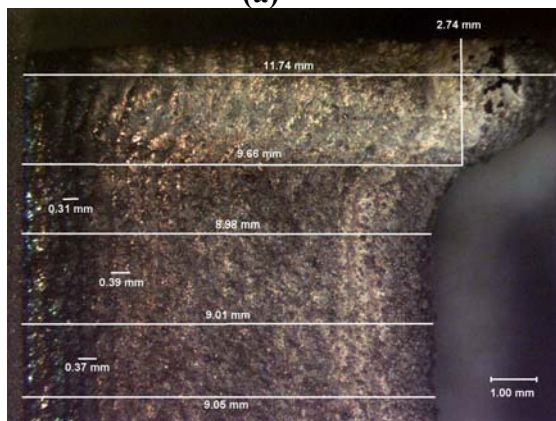
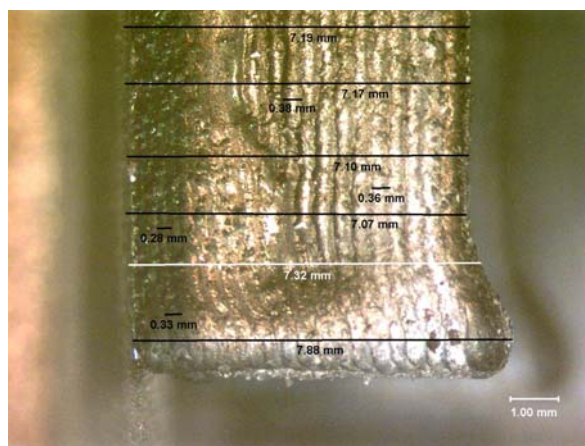
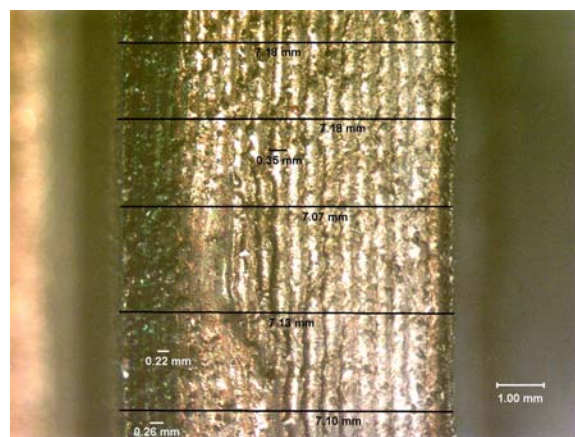
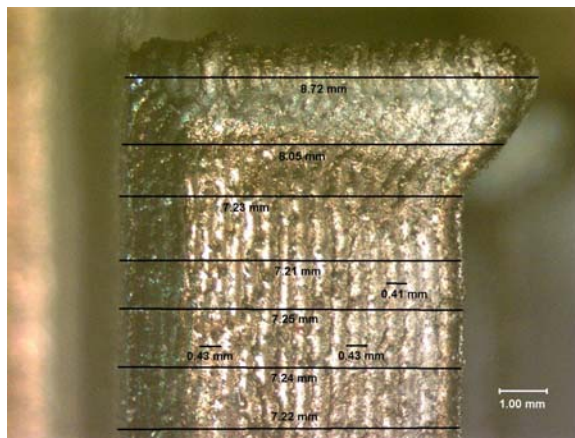


Figure A.4: Top view of DMD built NiTi vertical walls from Batch #2, left- and right- hand side: (a) wall 1, (b) wall 2, (c) wall 3, (d) wall 4, (e) wall 5, (f) wall 6, (g) wall 7, (h) wall 8

(a)



(b)

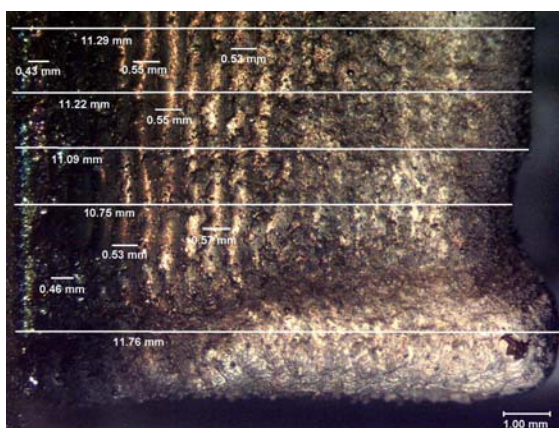
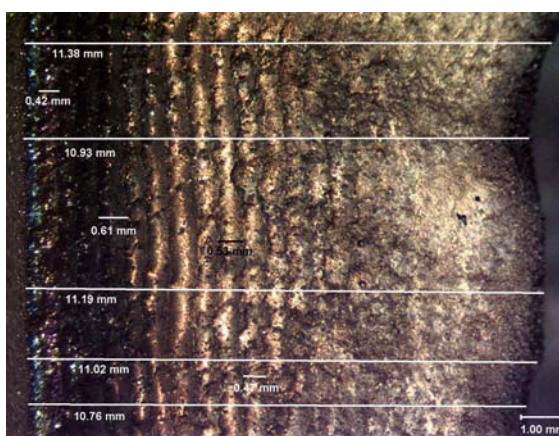
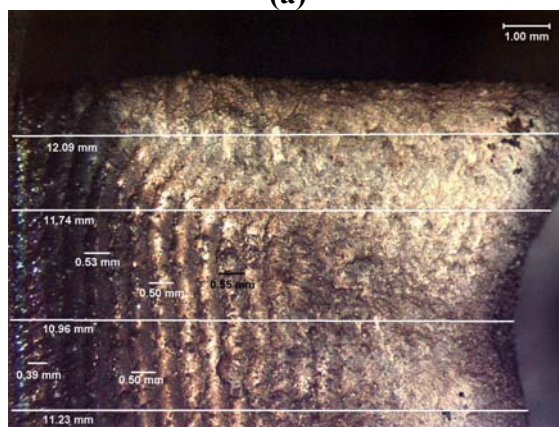


(c)

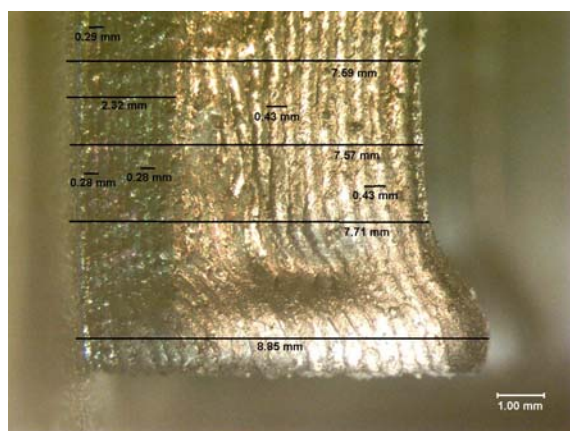
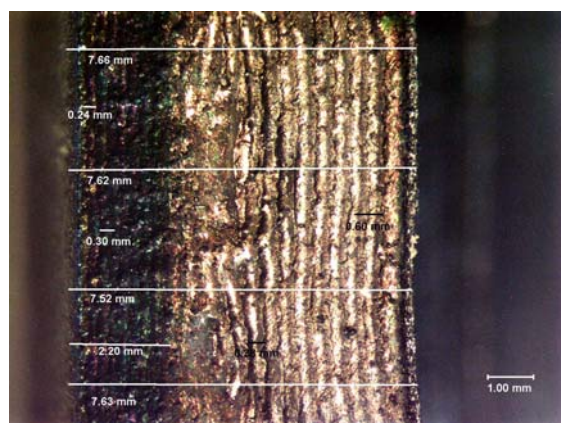
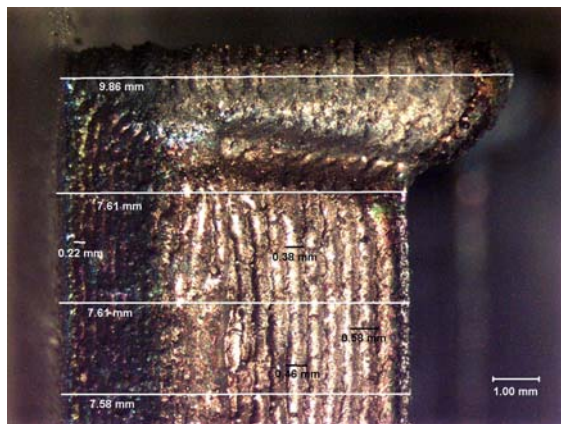


Figure A.5: Front view of DMD built NiTi vertical walls from Batch #1: (a) wall 4, (b) wall 5, (c) wall 8

(a)



(b)



(c)

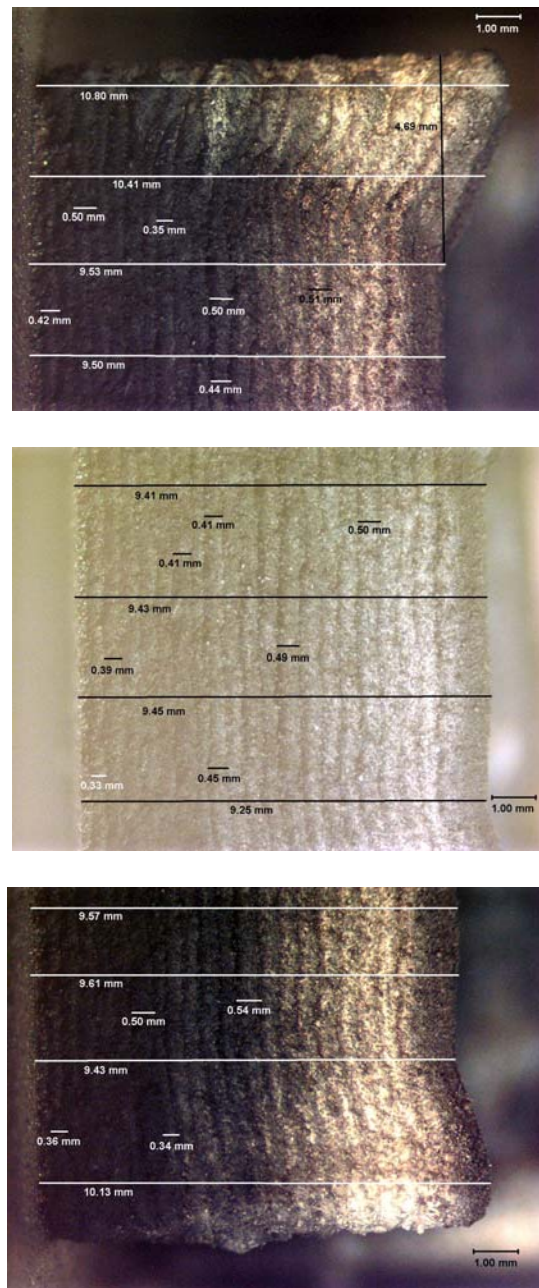


Figure A.6: Front view of DMD built NiTi vertical walls from Batch #2: (a) wall 4, (b) wall 5, (c) wall 8

APPENDIX B

Statistical estimation of the influence of laser power, coolant flow rate and powder flow rate on the geometry of DMD built NiTi vertical walls

Tables B.1-B.7 show the statistical estimates of the influence of laser power, powder feeding rate and coolant flow rate on the magnitudes of the walls' height, top width, bottom width, horizontal and vertical axis of the spherical build-ups according to Figures A.1-A.6 of Appendix A. The estimates were obtained based on the statistical analysis of the factorial experiments. In addition, the influence of the three parameters on the magnitude of the walls' roughness was also investigated. Roughness was measured by a mechanical stylus and an optical profilometer. The corresponding statistical estimates are given in Table B.9 and Table 8 in Chapter 3.

Table B.1: *Influence of laser power, powder flow rate and coolant flow rate on wall height*

Factor	Effect Estimate	Sum of Squares, SS	Percent Contribution, %
A (cooler)	0.13	0.0676	0.31199376
B (laser)	1.4775	8.732025	40.30084783
C (powder rate)	-1.4775	8.732025	40.30084783
AB	-0.0975	0.038025	0.17549649
AC	0.4825	0.931225	4.297875581
BC	0.235	0.2209	1.019518071
ABC	-0.405	0.6561	3.028093284
Pure error		2.2892	10.56532715
Total		21.6671	100

Table B.2: *Influence of laser power, powder flow rate and coolant flow rate on wall top width*

Factor	Effect Estimate	Sum of Squares, SS	Percent Contribution, %
A (cooler)	0.0175	0.001225	0.061975893
B (laser)	0.5975	1.428025	72.24744824
C (powder rate)	-0.155	0.0961	4.861945537
AB	-0.1075	0.046225	2.338641337
AC	0.155	0.0961	4.861945537
BC	-4.44089E-16	7.88861E-31	3.99105E-29
ABC	-0.025	0.0025	0.126481414
Pure error		0.3064	15.50156205
Total		1.976575	100

Table B.3: *Influence of laser power, powder flow rate and coolant flow rate on wall bottom width*

Factor	Effect Estimate	Sum of Squares, SS	Percent Contribution, %
A (cooler)	-0.04	0.0064	1.110003035
B (laser)	0.1575	0.099225	17.20938299
C (powder rate)	-0.06	0.0144	2.497506829
AB	-0.09	0.0324	5.619390366
AC	0.1675	0.112225	19.46407666
BC	0.105	0.0441	7.648614664
ABC	0.0775	0.024025	4.166847331
Pure error		0.2438	42.28417812
Total		0.576575	100

Table B.4: *Influence of laser power, powder flow rate and coolant flow rate on the left hand-side horizontal axis of the spherical build-up of a wall*

Factor	Effect Estimate	Sum of Squares, SS	Percent Contribution, %
A (cooler)	-0.08	0.0256	1.304126337
B (laser)	0.4725	0.893025	45.49286806
C (powder rate)	-0.1375	0.075625	3.852521651
AB	-0.0425	0.007225	0.368059093
AC	0.1225	0.060025	3.057819664
BC	-0.16	0.1024	5.216505349
ABC	-0.235	0.2209	11.2531839
Pure error		0.5782	29.45491594
Total		1.963	100

Table B.5: *Influence of laser power, powder flow rate and coolant flow rate on the left-hand side horizontal axis of the spherical build-up of a wall*

Factor	Effect Estimate	Sum of Squares, SS	Percent Contribution, %
A (cooler)	-0.1125	0.050625	3.363563883
B (laser)	0.5525	1.221025	81.12583881
C (powder rate)	-0.075	0.0225	1.494917281
AB	-0.045	0.0081	0.538170221
AC	0.0025	2.5E-05	0.001661019
BC	-0.0625	0.015625	1.038137001
ABC	-0.015	0.0009	0.059796691
Pure error		0.1863	12.37791509
Total		1.5051	100

Table B.6: *Influence of laser power, powder flow rate and coolant flow rate on the right-hand side horizontal axis of the spherical build-up of a wall*

Factor	Effect Estimate	Sum of Squares, SS	Percent Contribution, %
A (cooler)	-0.11875	0.05640625	3.347564346
B (laser)	0.38625	0.59675625	35.41593255
C (powder rate)	-0.42125	0.70980625	42.12515625
AB	-0.01375	0.00075625	0.044881472
AC	0.12375	0.06125625	3.635399241
BC	0.06375	0.01625625	0.96476619
ABC	-0.10125	0.04100625	2.433614368
Pure error		0.20275	12.03268558
Total		1.68499375	100

Table B.7: *Influence of laser power, powder flow rate and coolant flow rate on the right-hand side vertical axis of the spherical build-up of a wall*

Factor	Effect Estimate	Sum of Squares, SS	Percent Contribution, %
A (cooler)	-0.03375	0.00455625	0.367278462
B (laser)	0.52875	1.11830625	90.14645795
C (powder rate)	-0.03625	0.00525625	0.423705331
AB	-0.01625	0.00105625	0.085144115
AC	0.04375	0.00765625	0.617168883
BC	0.05125	0.01050625	0.84690685
ABC	-0.10375	0.04305625	3.470756271
Pure error		0.05015	4.042582134
Total		1.24054375	100

Table B.8: *Influence of laser power, powder flow rate and coolant flow rate on the wall roughness (half 1) measured by the optical profilometer*

Factor	Effect Estimate	Sum of Squares, SS	Percent Contribution, %
A (cooler)	0.072958333	0.021291674	0.028228907
B (laser)	-1.243625	6.186412562	8.202063854
C (powder rate)	-0.030958333	0.003833674	0.005082758
AB	0.453458333	0.82249784	1.090483336
AC	-1.058208333	4.479219507	5.938634716
BC	-0.084958333	0.028871674	0.038278616
ABC	-1.104875	4.882995063	6.473968055
Pure error		58.99994994	78.22325976
Total		75.42507194	100

Table B.9: *Influence of laser power, powder flow rate and coolant flow rate on the wall roughness (half 2) measured by the optical profilometer*

Factor	Effect Estimate	Sum of Squares, SS	Percent Contribution, %
A (cooler)	-1.267791667	6.42918284	18.92641972
B (laser)	1.217541667	5.92963084	17.45582368
C (powder rate)	-0.232458333	0.216147507	0.636301462
AB	-0.279541667	0.312574174	0.920165152
AC	-0.523208333	1.09498784	3.223457782
BC	0.480625	0.924001562	2.72010329
ABC	-0.524291667	1.099527007	3.236820316
Pure error		17.96330394	52.88090859
Total		33.96935572	100

The statistical analysis shows that laser power has the maximal effect (maximal percent contribution) on the walls' geometry. For example, Table B.2 shows that the magnitude of the walls width, at the very top of the walls, is affected at 72% by laser power, 4.86% by powder flow rate and 0.06% by coolant flow rate.

When approaching closer to the bottom of a wall, where the wall is attached to its substrate, the influence of the magnitude of the coolant flow rate (with the cooler beneath the substrate) and powder flow rate increases. Their joint effect increases as well as shown in Table B.3. For example, the laser power gives 17.2%, the powder flow rate - 2.5 %, the coolant flow rate 1%, and the joint effect from the coolant flow rate and powder flow rate is – 20%.

The obtained statistical data has practical applications when building structures by the DMD process from NiTi powder. It makes it possible to control the quality of the final DMD product by properly adjusting the DMD process parameters, such as laser power, the powder feeding rate and the coolant flow rate.

APPENDIX C

The distribution of the geometrical parameters of the thin NiTi walls built by DMD during the experimental factorial design.

The geometry of all 16 walls (8 walls in 2 DMD runs) was measured as shown in Appendix A. The geometrical parameters were the wall heights, widths, corner build-ups and roughness. The cumulative averaged trends in the distribution of these parameters are shown below in plots C.1 through C.7, and the plots in Figures 3.11, 3.12, and 3.13 in Chapter 3. There are two curves per plot. Each curve contains 8 points that correspond to 8 consecutive DMD single wall depositions with the DMD parameters (factors) varied according to Table 3 in Chapter 3. It is obvious to conclude, that points # 3, 4, 7, and 8 (Figs. C.1 – C.7) correspond to the maximal laser power values, cited in Table 3 (Chapter 3) while points # 1, 2, 5, and 6 correspond to the minimal laser power values. These results supports the fact, that the choice of laser power plays a major role in the DMD process as it was concluded in the statistical analysis given in Appendix B and Chapter 3. Although, it is anticipated, that the use of a more powerful cooler beneath the deposition substrate will impact the DMD process at a level similar to that of laser power does.

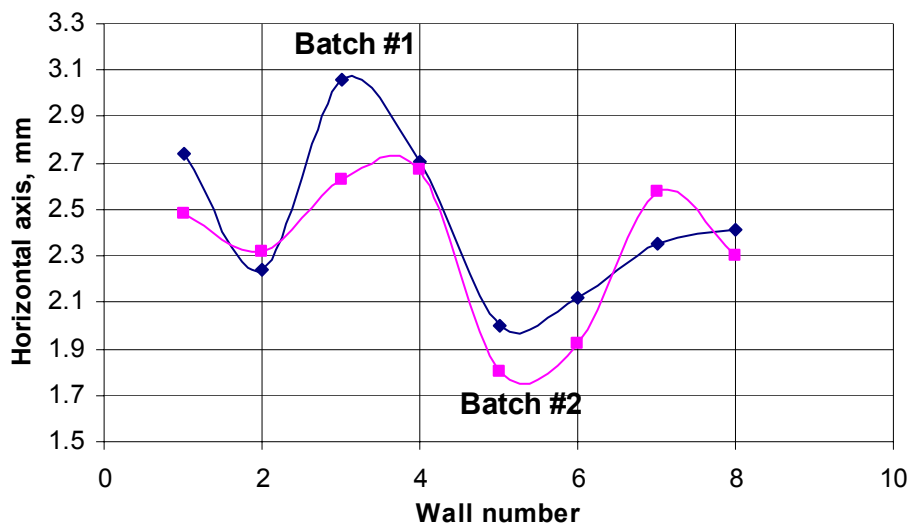


Figure C.1: *Distribution of the magnitudes of the horizontal dimension of the spherical build-ups at the right-hand side corner of the thin walls*

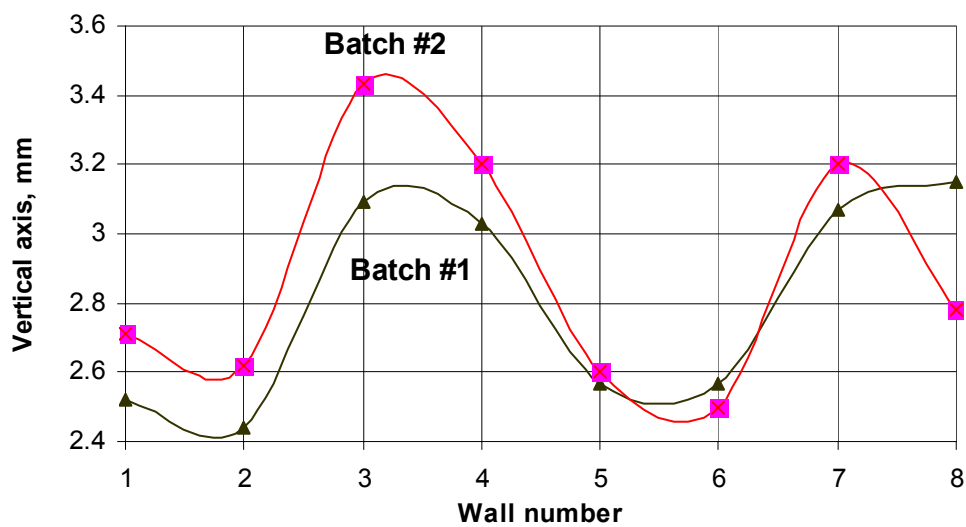


Figure C.2: *Distribution of the magnitudes of vertical dimension of spherical build-ups at the left-hand side corner of the thin walls*

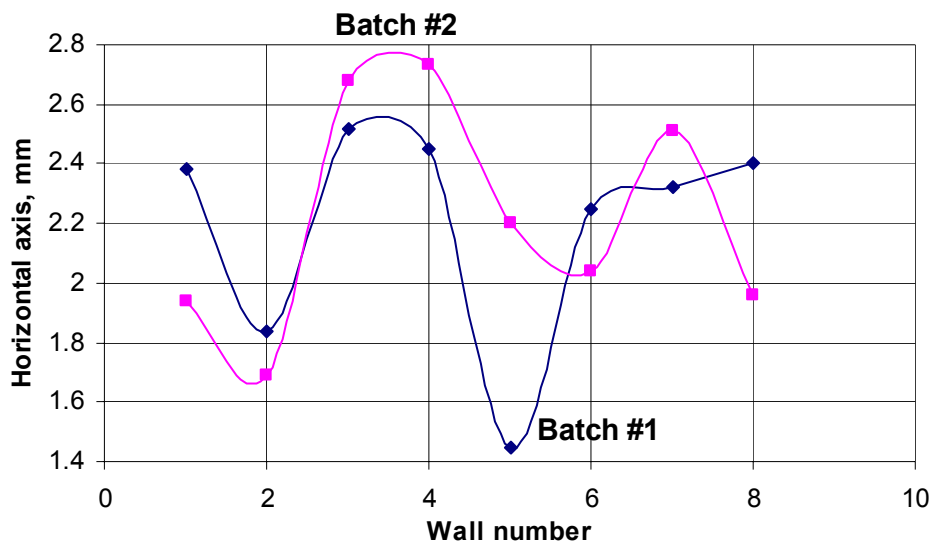


Figure C.3: Distribution of magnitudes of horizontal dimension of the spherical build-ups at the left-hand side corner of the thin walls

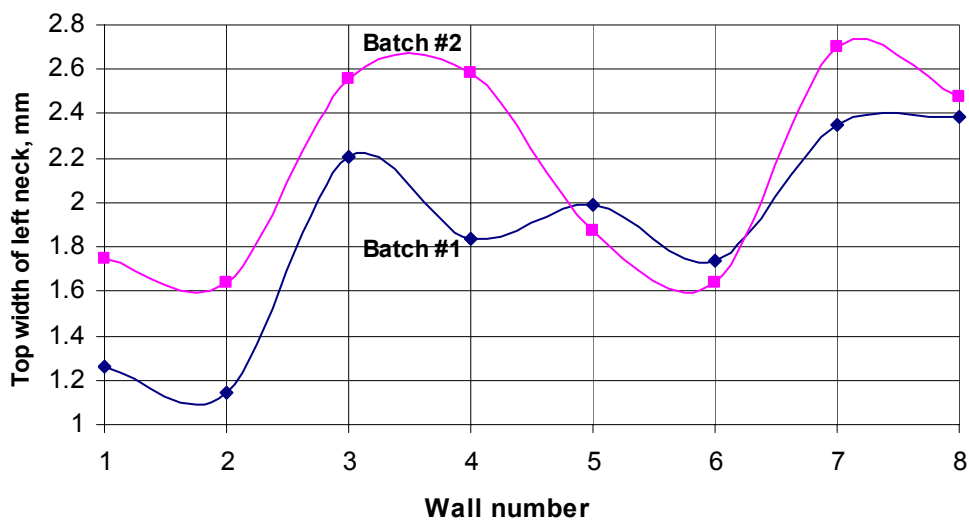


Figure C.4: Distribution of top widths of necks at the left-hand side corner of the thin walls

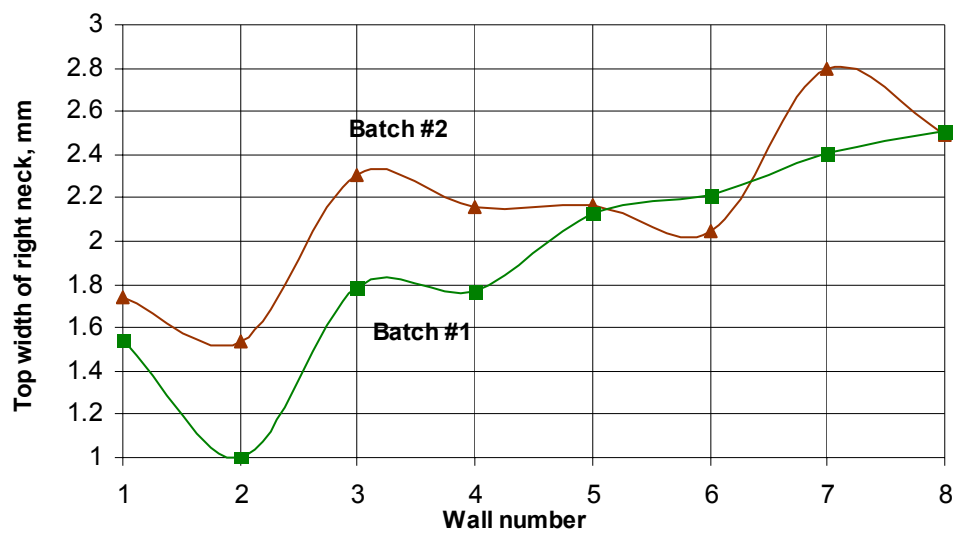


Figure C.5: Distribution of top widths of necks at the right-hand side corner of the thin walls

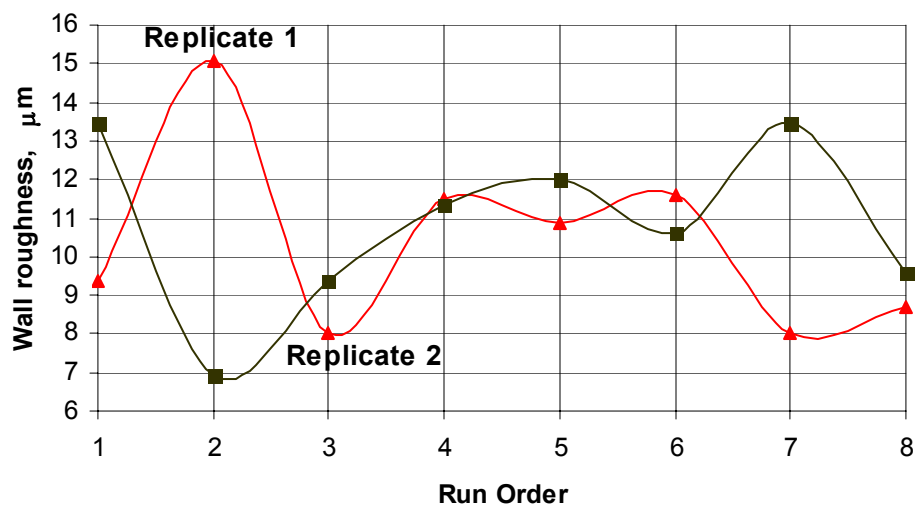


Figure C.6: Distribution of wall (half 1) roughness values from measurements by optical profilometer

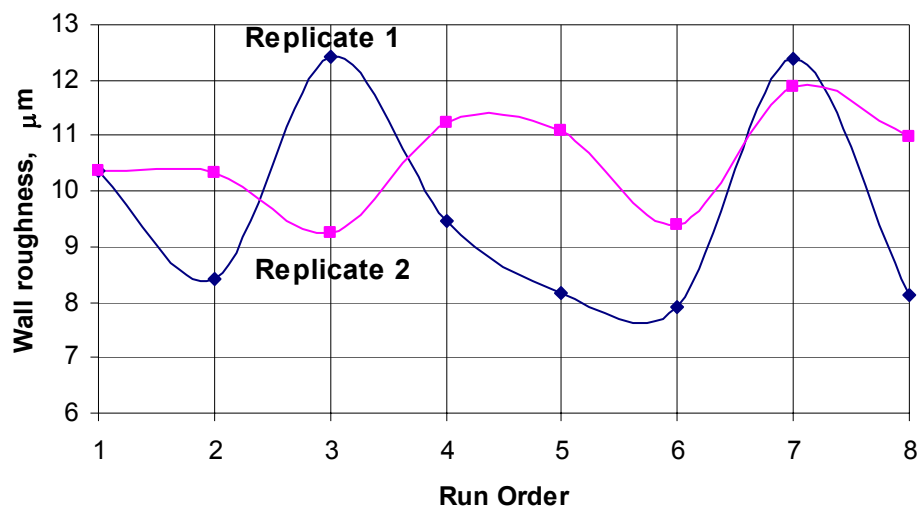


Figure C.7: *Distribution of wall (half 2) roughness values from measurements by optical profilometer*

APPENDIX D

Sensitivity and resolution data from the step response experiments with the thermally insulated SMA wire. The data are used in the analysis of the “self-sensing” principle.

Table D.1: *Sensitivity and resolution*

Experiment number	Sensitivity ($\mu\text{m}/\text{mV}$)	SMA wire Displacement Range (μm)	Resolution (μm)	Range – Resolution (μm)	Range + Resolution (μm)	Coefficient of determination, R ²
Exp43, section b, part 4	0.7434	17	1.8	15.2	18.8	0.8057
Exp57, section b, part 2	0.6394	20	1.6	18.4	21.6	0.7144
Exp46, section b, part 3	0.6254	23	1.5	21.5	24.5	0.8451
Exp43, section b, part 2	0.9121	24	2.3	21.7	26.3	0.7197
Exp46, section b, part 5	1.1334	27	2.8	24.2	29.8	0.5681
Exp43, section b, part 2	1.1082	29	2.7	26.3	31.7	0.4848
Exp57, section b, part 5	0.9418	30	2.3	27.7	32.3	0.5825
Exp57, section b, part 6	0.8395	30	2.1	27.9	32.1	0.5643
Exp43, section b, part 4	1.5154	32	3.7	28.3	35.7	0.7072
Exp43, section b, part 3	1.2616	36	3.1	32.9	39.1	0.4624
Exp53, section b, part 2	0.9975	39	2.4	36.6	41.4	0.5738
Exp57, section b, part 7	1.2667	40	3.1	36.9	43.1	0.4211
Exp43, section b, part 4	0.8352	41	2	39	43	0.925
Exp53, section b, part 5	1.087	42	2.7	39.3	44.7	0.7664
Exp	1.4	50	4	46	54	0.3517
Exp57, section b, part 1	1.3365	51	3.3	47.7	54.3	0.7058
Exp43, section b, part 7	1.5	53	3.6	49.4	56.6	0.8191
Exp53, section b, part 6	0.9516	59	2.3	56.7	61.3	0.8685
Exp53, section b, part 3	1.1439	66	3	63	69	0.7475

Table D.1: Sensitivity and resolution (continued)

Exp43, section b, part 8	2.1	75	5	70	80	0.7792
Exp41, section b, part 1	2.2747	76	5.6	70.4	81.6	0.7502
Exp43, section b, part 9	1.7666	86	4.3	81.7	90.3	0.769
Exp41, section a, part 3	2.4602	150	6	144	156	0.8248
Exp41, section a, part 2	2.4573	186	6	180	192	0.9244
Exp41, section b, part 1	2.7973	200	6.8	193.2	206.8	0.9255
Exp41, section a, part 4	2.704	210	6.6	203.4	216.6	0.9387
Exp41, section b, part 1	2.5994	220	6.3	213.7	226.3	0.9378

APPENDIX E

Transfer functions (TFs) derived from the step response experiments with the SMA wire

Table E.1: *Thermally non-insulated SMA wire*

Experiment Number	Discrete TF
arx111E28SmallStep1	0.001899/(z - 0.9912)
arx111E33LargeStep1	0.0003933/(z - 0.9967)
arx111E23LargeStep1	0.003045/(z - 0.9975)
arx111E35LargeStep1	0.002658/(z - 0.9894)
arx111E35LargeStep2	0.0005466/(z - 0.997)
arx111E30LargeStep1	0.0006429/(z - 0.9957)
arx111E32LargeStep3	0.001112/(z - 0.9981)
arx111E27LargeStep3	0.001221/(z - 0.9973)
arx111E32LargeStep2	0.001112/(z - 0.9981)
arx111E27LargeStep2	0.001885/(z - 0.9944)

Table E.2: *Thermally insulated SMA wire*

Experiment Number	Discrete TF
arx211E45step2	0.001708 $z/(z^2 - 0.6047z - 0.3939)$
arx211E45step1	0.001452 $z/(z^2 - 0.5055z - 0.4939)$
arx211E44step2	0.001447 $z/(z^2 - 0.9838z - 0.01315)$
arx211E44step1	0.0007117 $z/(z^2 - 0.973z - 0.02403)$
arx211E54step1	0.0006628 $z/(z^2 - 0.5635z - 0.4351)$
arx211E54step2	0.002835 $z/(z^2 - 0.7059z - 0.2923)$
arx211E53step1	0.002665 $z/(z^2 - 0.5229z - 0.4738)$
arx211E53step2	0.002323 $z/(z^2 - 0.5265z - 0.4712)$
arx211E53step3	0.002231 $z/(z^2 - 0.5422z - 0.4565)$
arx211E50	0.002257 $z/(z^2 - 0.6741z - 0.321)$
arx211E49	0.001175 $z/(z^2 - 0.6288z - 0.369)$
arx211E48	0.001843 $z/(z^2 - 0.8651z - 0.1324)$
arx211E48step2	0.001776 $z/(z^2 - 0.9619z - 0.03408)$
arx211E48step3	0.001608 $z/(z^2 - 0.8136z - 0.1817)$
arx211E46step1	0.001614 $z/(z^2 - 0.484z - 0.5146)$
arx211E46step2	0.002128 $z/(z^2 - 0.5518z - 0.4455)$
arx211E46step3	0.001917 $z/(z^2 - 0.5208z - 0.4768)$
arx211E45step3	0.001402 $z/(z^2 - 0.5197z - 0.4788)$
arx211E41step1	0.002695 $z/(z^2 - 0.7223z - 0.2757)$
arx211E41step2	0.001853 $z/(z^2 - 0.5582z - 0.4399)$
arx211E41step3	0.00315 $z/(z^2 - 0.8858z - 0.1121)$
arx211E43step1	0.001739 $z/(z^2 - 0.6619z - 0.3352)$
arx211E43step2	0.001845 $z/(z^2 - 0.8069z - 0.1896)$
arx211E43step3	0.003738 $z/(z^2 - 0.6928z - 0.3052)$

APPENDIX F

Experimental data from the step response experiments with the SMA wire.

Figures F.1 to F.4 show displacement-temperature plots from the experimental data obtained from the step response experiments with an SMA wire described in Chapter 7. The experiments were done to verify the mathematical model of the SMA transformation kinetics to be used in modeling the SMA actuator and its motion control. Each displacement step corresponds to a step in the temperature in the plots. Each increment (step) in the temperature in Figure F.1 corresponds to an increment in the applied voltage (electric current). Each pair of curves in Figures F.1 to F.4 presents a separate step response experiment. All the experiments were conducted independently from each other and analyzed in Chapter 7.

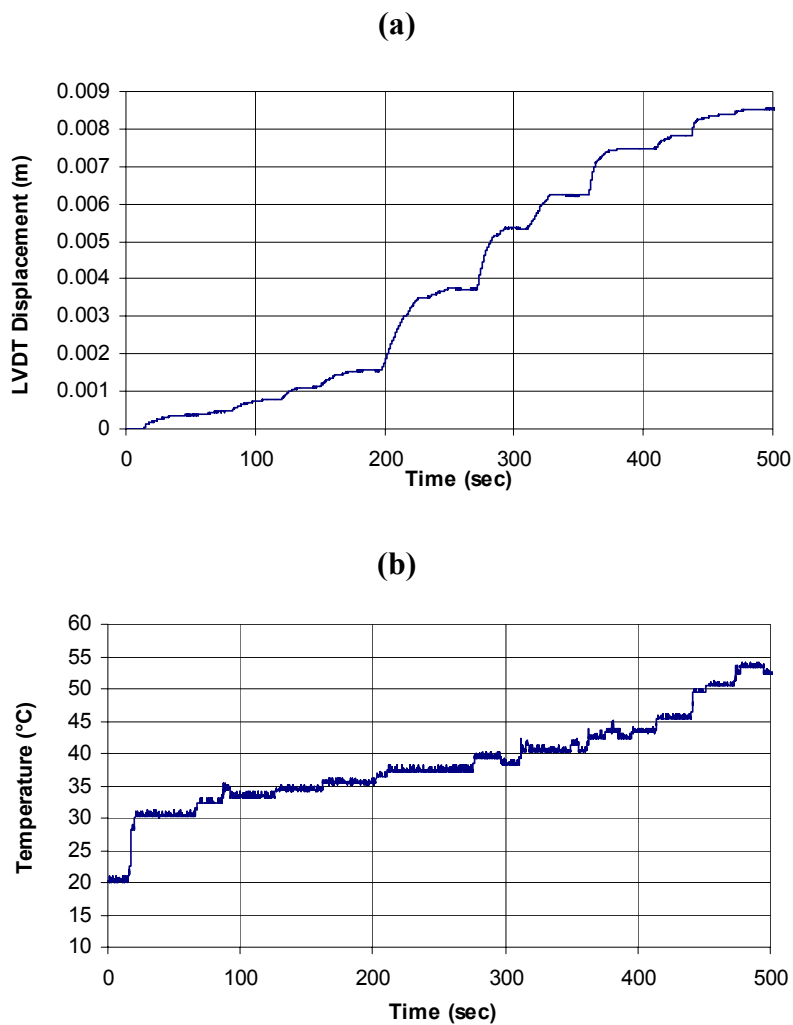


Figure F.1: *Experimental data set (Exp. 18) from SMA wire heating cycle: (a) SMA wire displacement, (b) SMA wire temperature*

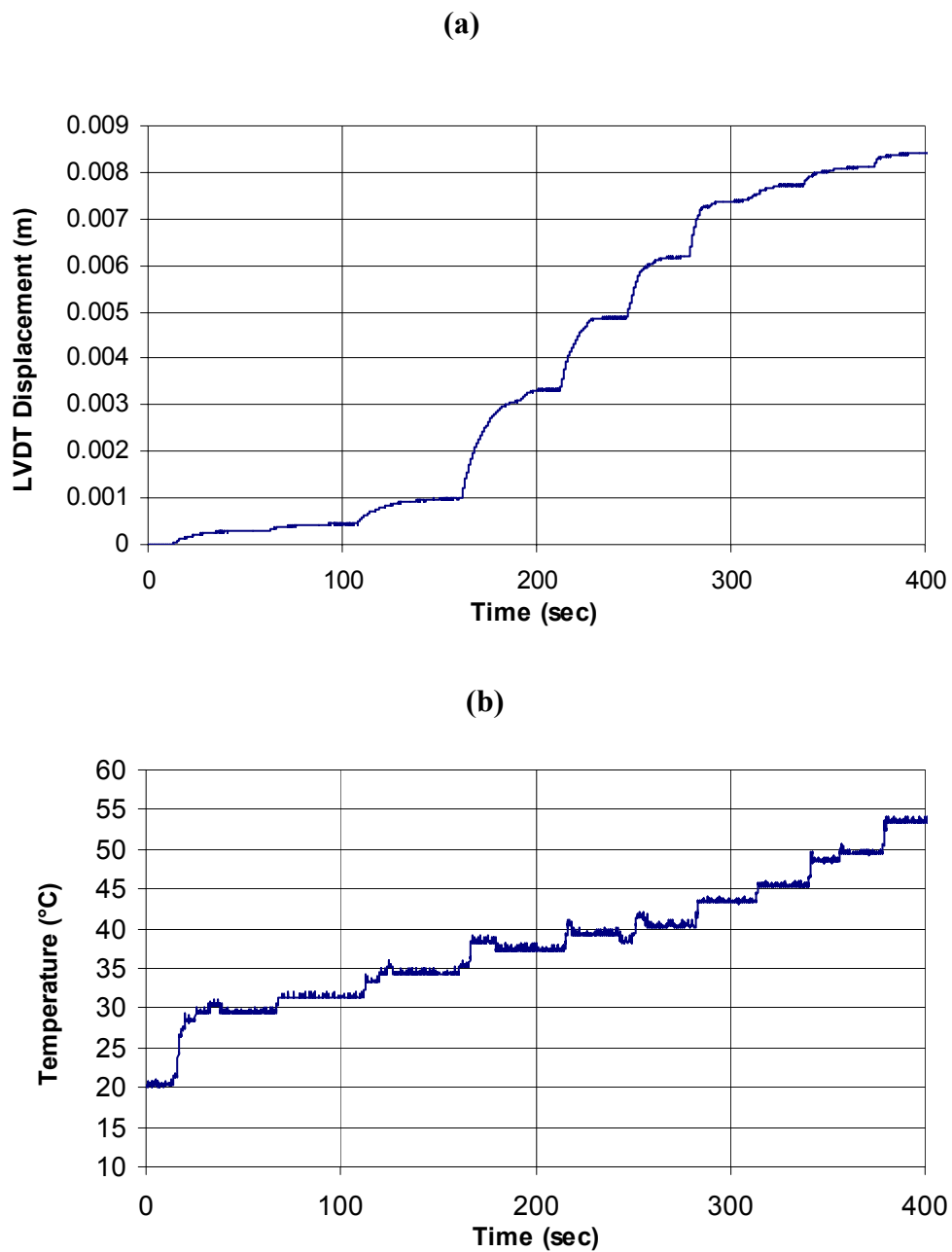


Figure F.2: *Experimental data set (Exp.20) from SMA wire heating cycle: (a) SMA wire displacement, (b) SMA wire temperature*

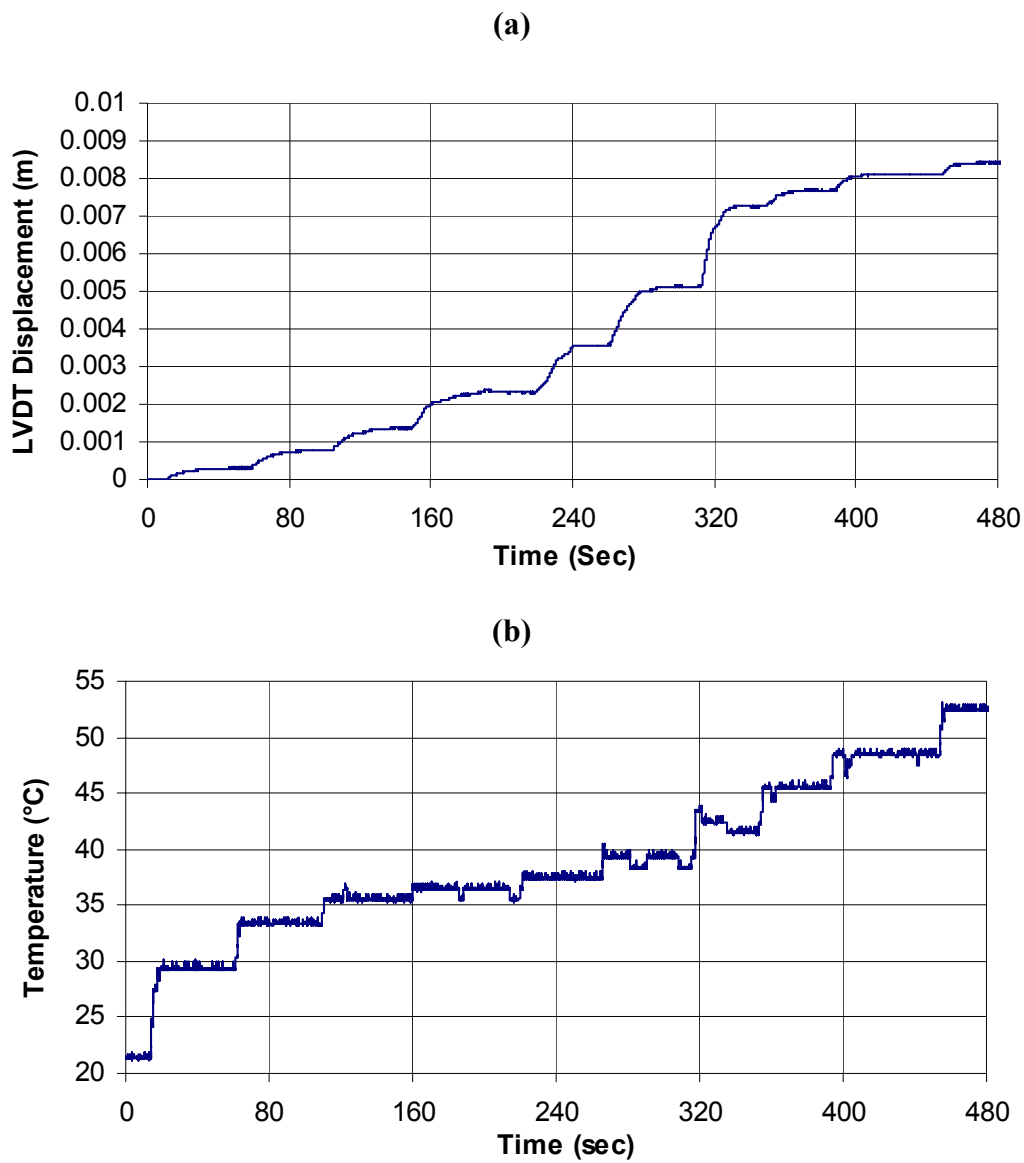


Figure F.3: *Experimental data set (Exp.21) from SMA wire heating cycle: (a) SMA wire displacement, (b) SMA wire temperature*

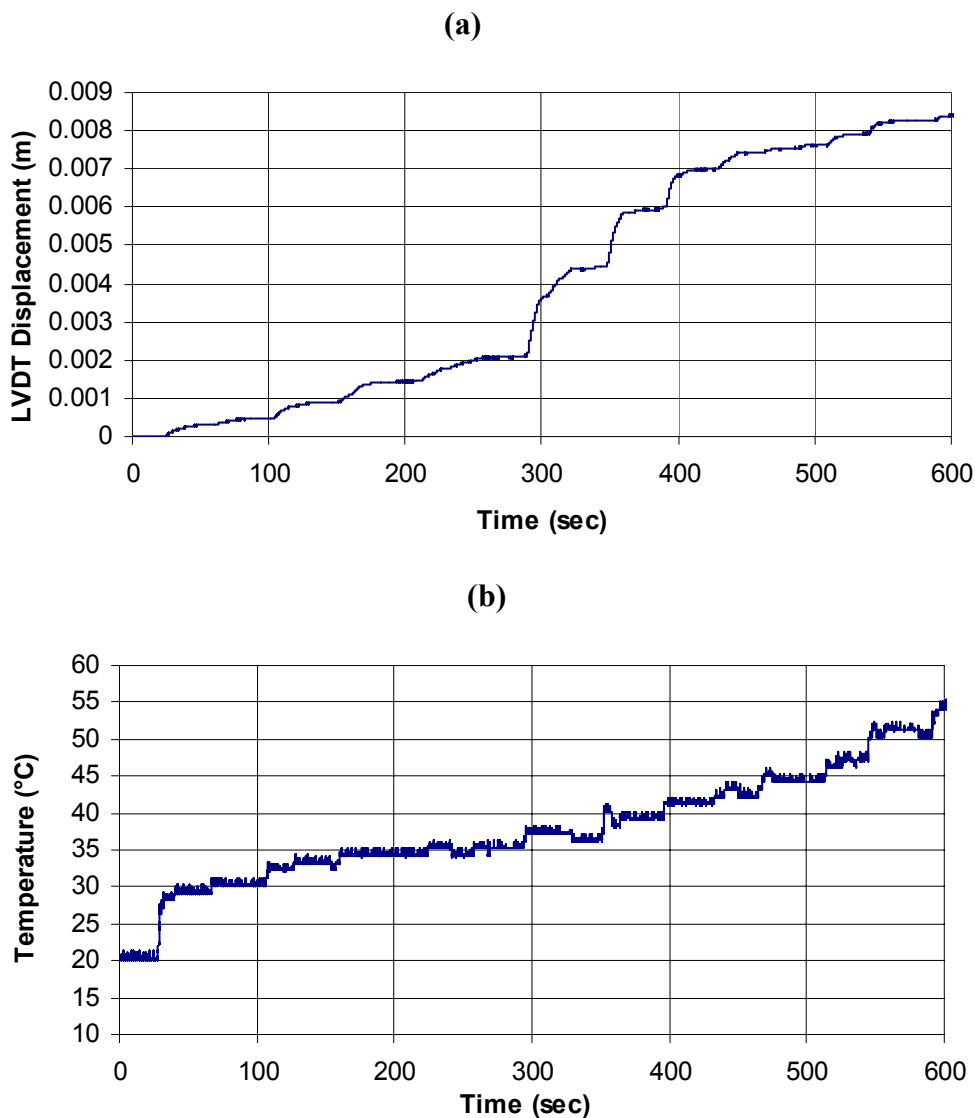


Figure F.4: *Experimental data set (Exp.22) from SMA wire heating cycle: (a) SMA wire displacement, (b) SMA wire temperature*

In order to compute the experimental austenite fraction values, all displacement curves were normalized, according to the procedure described in Section 7.5. The normalized experimental data-points were put into a cumulative plot, austenite fraction versus temperature, in Fig. 7.9, cited in Chapter 7.